

**AN INVESTIGATION INTO THE USE OF FLOW-FOCUSING  
ATOMIZATION WITH SPRAY DRYING FOR THE PRODUCTION OF  
NARROW PARTICLE SIZE DISTRIBUTIONS**

**Andrew Patrick Savage**

**A Thesis Submitted to the University of Birmingham**

**for the Degree of DOCTOR OF PHILOSOPHY**

**The School of Chemical Engineering**

**University of Birmingham**

**May 2015**

UNIVERSITY OF  
BIRMINGHAM

**University of Birmingham Research Archive**

**e-theses repository**

This unpublished thesis/dissertation is copyright of the author and/or third parties. The intellectual property rights of the author or third parties in respect of this work are as defined by The Copyright Designs and Patents Act 1988 or as modified by any successor legislation.

Any use made of information contained in this thesis/dissertation must be in accordance with that legislation and must be properly acknowledged. Further distribution or reproduction in any format is prohibited without the permission of the copyright holder.

The School of Chemical Engineering, University of Birmingham

**Investigation into the Use of Flow-Focusing Atomization with Spray Drying for the Production of Narrow Particle Size Distributions**

by

Andrew Patrick Savage

May 2015

**Summary**

Spray drying provides a rapid route to dry particles from a solution or suspension, and is an important unit operation in the food, chemical and pharmaceutical industries. The droplet size distribution produced by the atomization system within a spray dryer is vital in defining the output particle size distribution, which in turn can strongly influence the subsequent flow, dissolution, ingestion or bioavailability of the final product.

This thesis explores the capability of a simple atomizing system for the production of narrow droplet size distributions within an industrially-relevant spray dryer. The combination of constrained droplet size distribution, defined solute concentration and selected processing conditions has been evaluated to determine the influence upon the physicochemical properties of a model active pharmaceutical ingredient, and the dosing characteristics of formulated products.

A flow focusing atomizer was demonstrated to be capable of generating narrow droplet size distributions for solvents and solutions via the anticipated break-up mechanism.

Laser diffraction studies utilising water, ethanol and 2-propanol were undertaken and demonstrated the validity of the postulated control variables of the atomizer, however some systematic deviation from the theoretical droplet size proportional to the operating pressure was identified. Sodium chloride solutions up to 5 %w/w, and solutions of the corticosteroids fluticasone propionate and mometasone furoate up to 0.5 %w/w were then evaluated, showing good agreement with the results obtained for the solvents.

The control variables demonstrated to be important for droplet generation under quiescent conditions during the laser diffraction experiments were then demonstrated to be equally relevant in the dynamic environment within a spray dryer. A combination of target droplet size and sodium chloride concentration was used to produce batches of sodium chloride across a range of dry particle sizes. Subsequent laser diffraction analysis identified a linear relationship between predicted particle size and experimental results, suggesting the droplet formation mechanism confirmed initially was able to be translated to the spray dryer.

Designed experiments conducted using mometasone furoate indicate that droplet size, concentration and drying conditions are important in determining the particle size, texture and thermodynamic properties of the output powder. Average particle size results for spray dried mometasone furoate agree well with that anticipated from the combination of predicted droplet size and concentration. A systematic change in particle texture with operating conditions, notably inlet temperature and choice of solvent, was observed; correlations were also identified between spray drying operating parameters and thermal events for the output powder detected during thermal analysis. Analysis by



X-ray powder diffraction revealed all combinations of spray drying operating parameters yielded amorphous particles.

A capsule-based dry powder inhaler was used to understand the influence of spray dried mometasone furoate particle properties upon pharmaceutical performance. Analysis of formulations containing spray dried mometasone furoate particles with lactose monohydrate defined a clear link between the impaction profile in a cascade impactor and spray drying operating conditions. The combinations of droplet size and concentration utilised during spray drying, with the resulting differences in API particle size, were shown to demonstrate statistically significant relationships with respirable mass and emitted dose from the inhaler. Differences in the blend structure potentially attributable to the average size of mometasone furoate particles may have an influence on the relationship between emitted dose and airflow for capsule-based inhalers.

## **Acknowledgements**

The work that has resulted in this thesis would not have been possible without the advice and support of a number of people at both the University of Birmingham and GlaxoSmithKline. I would like to thank Philip Robbins and Mark Simmons at the University for their guidance on direction of the work, and patient supervision over the intervening years between initiation and completion.

I would like to thank Gino Martini, Keith Smith and David DeMagistris, formerly of Strategic Technologies within GSK R&D, for the opportunity to undertake PhD studies and for the necessary securing funding and to Gavin Bone for allowing me to revise my working schedule in order for the spray drying experiments to be undertaken. I would also like to express sincere gratitude to the various colleagues at GSK who have provided access to equipment and instruments, and provided advice regarding calibration and operation – Stephen Charles, Kenny Smith, Martin Hingle, Robyn Sadler, Rudolph Ismay, deserve particular mention regarding analysis, as do Les Ives, Ruth Murtagh and the Pilot Plant Operations team for being supportive with regard to the spray drying experiments.

Finally, and by no means least, to my wife Catherine for unwavering support, acting as a sounding board during the thesis and for being so understanding of the shared leisure time we've had to sacrifice over the last eight years.

## TABLE OF CONTENTS

1.	INTRODUCTION .....	8
1.1.	Objectives .....	11
1.2.	Spray Drying.....	14
1.2.1.	Spray drying equipment.....	15
1.2.2.	Pharmaceutical applications .....	28
1.3.	Droplet formation.....	34
1.3.1.	Flow focusing .....	38
1.4.	Inhaled drug delivery .....	42
1.4.1.	DPI Formulation .....	45
1.4.2.	Delivery system .....	59
1.4.3.	Aerodynamic particle size analysis of inhalation products .....	64
2.	EQUIPMENT AND MATERIALS .....	72
2.1.	Equipment.....	72
2.1.1.	Atomizing system .....	72
2.1.2.	Spray dryer.....	74
2.2.	Materials.....	76
2.2.1.	Solute properties .....	76
2.2.2.	Solvent and solution properties .....	77
2.3.	Conclusion .....	88
3.	CHARACTERISATION OF ATOMIZATION .....	89
3.1.	Droplet imaging .....	89
3.1.1.	Equipment configuration.....	90
3.1.2.	Experimental procedure .....	91
3.1.3.	Experimental conditions .....	92
3.1.4.	Results and discussion.....	92
3.2.	Droplet measurement.....	97
3.2.1.	Equipment configuration.....	99
3.2.2.	Experimental conditions .....	100
3.2.3.	Results and discussion.....	103
3.3.	Conclusion .....	127
4.	SPRAY DRYING.....	130
4.1.	Drying gas flow calibration.....	130
4.2.	In-situ atomizer validation using sodium chloride.....	131
4.2.1.	Methods .....	132
4.2.2.	Results and discussion.....	135
4.3.	Spray drying of active pharmaceutical ingredients.....	140
4.3.1.	Operating parameter ranges.....	142
4.3.2.	Methods .....	143
4.3.3.	Results and discussion.....	147
4.4.	Conclusion .....	167
5.	FORMULATION STUDIES.....	170
5.1.	Introduction .....	170
5.2.	Methods .....	179
5.2.1.	Manufacture of inhalation blends .....	179
5.2.2.	Cascade Impaction.....	180
5.2.3.	SEM characterisation .....	184
5.3.	Results and discussion.....	185

5.4.	Conclusion .....	197
6.	CONCLUSION AND FURTHER WORK.....	200
7.	APPENDICES.....	205
	Appendix 1 Images of droplet break-up.....	205
	Appendix 2 SEM images of spray dried NaCl.....	210
	Appendix 3 SEM images of spray dried MF .....	214
	Appendix 4 Thermal analysis results.....	227
	Appendix 5 X-ray powder diffractograms.....	241
	Appendix 6 Thermogravimetric analysis data.....	245
	Appendix 7 SEM images of MF-lactose blends .....	249
	Appendix 8 Droplet size, flow rate and pressure drop relationships for flow focusing atomization.....	255

## Table of figures

Figure 1.1	Schematic diagram of an open-cycle spray dryer.....	16
Figure 1.2	Variation in enthalpy or volume with cooling .....	32
Figure 1.3	Ohnesorge's classification of modes of disintegration .....	37
Figure 1.4	Flow focusing arrangement.....	39
Figure 1.5	Cascade impaction stage and plate arrangement .....	65
Figure 1.6	Cascade impactors .....	68
Figure 1.7	Cascade impaction configuration .....	69
Figure 1.8	The Electronic Lung .....	70
Figure 1.9	Cascade and Virtual Impactor Combination (CAVIC) .....	71
Figure 2.1	FFD atomizer .....	73
Figure 2.2	Spray drying configuration .....	75
Figure 2.3	Molecular structures of fluticasone propionate and mometasone furoate .....	76
Figure 2.4	Equilibrium molar solubilities of the API-solvent combinations .....	80
Figure 2.5	Equilibrium mass-fraction solubilities of the API-solvent combinations.....	81
Figure 2.6	Effect of droplet lifetime upon the surface tension of Fluticasone Propionate in ethanol .....	83
Figure 2.7	Effect of droplet lifetime upon the surface tension of Fluticasone Propionate in 2-propanol.....	84
Figure 2.8	Effect of droplet lifetime upon the surface tension of Mometasone Furoate in ethanol.....	84
Figure 2.9	Effect of droplet lifetime upon the surface tension of Mometasone Furoate in ethanol.....	85
Figure 2.10	Temperature dependence of surface tension of ethanol solutions.....	86
Figure 2.11	Temperature dependence of surface tension of 2-propanol solutions .....	87
Figure 3.1	Spraytec set up.....	100
Figure 3.2	Effect of atomizer to beam distance on droplet size distribution (150mbar, 2-propanol) .....	105

Figure 3.3	Effect of atomizer to beam distance on span (150mbar, 2-propanol) .....	106
Figure 3.4	Effect of pressure drop and liquid flow rate on droplet size for water.....	107
Figure 3.5	Effect of pressure drop and liquid flow rate on span for water .....	107
Figure 3.6	Effect of liquid flow rate on droplet size for 5%w/w aqueous sodium chloride solution .....	109
Figure 3.7	Effect of liquid flow rate on span for 5%w/w aqueous sodium chloride solution.....	109
Figure 3.8	Droplet size distributions for 5%w/w sodium chloride solutions .....	110
Figure 3.9	Effect of pressure drop and liquid flow rate on droplet size for 2-propanol, 25°C.....	111
Figure 3.10	Effect of pressure drop and liquid flow rate on span for 2-propanol, 25°C.....	112
Figure 3.11	Effect of pressure drop and liquid flow rate on droplet size for ethanol, 25°C .....	112
Figure 3.12	Effect of pressure drop and liquid flow rate on span for ethanol, 25°C .....	113
Figure 3.13	Effect of pressure drop and liquid flow rate on droplet size for 2-propanol, 50°C.....	115
Figure 3.14	Effect of pressure drop and liquid flow rate on droplet size for 2-propanol, 50°C.....	115
Figure 3.15	Effect of pressure drop and liquid flow rate on span for 2-propanol, 50°C.....	116
Figure 3.16	Effect of pressure drop and liquid flow rate on droplet size for ethanol, 50°C .....	116
Figure 3.17	Effect of pressure drop and liquid flow rate on droplet size for ethanol, 50°C .....	117
Figure 3.18	Effect of pressure drop and liquid flow rate on span for ethanol, 50°C .....	117
Figure 3.19	Variation of median droplet size standard deviation with average median droplet size for 2-propanol, 25°C .....	118
Figure 3.20	Variation of median droplet size standard deviation with average median droplet size for 2-propanol, 50°C .....	119
Figure 3.21	Variation of median droplet size standard deviation with average median droplet size for ethanol, 25°C .....	119

Figure 3.22	Variation of median droplet size standard deviation with average median droplet size for ethanol, 50°C .....	120
Figure 3.23	Effect of pressure drop and liquid flow rate on droplet size for 0.5%w/w API solutions in 2-propanol, 50°C .....	122
Figure 3.24	Effect of pressure drop and liquid flow rate on droplet size for 0.5%w/w API solutions in ethanol, 50°C.....	123
Figure 3.25	Effect of pressure drop and liquid flow rate on span for 0.5%w/w API solutions in 2-propanol, 50°C .....	123
Figure 3.26	Effect of pressure drop and liquid flow rate on span for 0.5%w/w API solutions in ethanol, 50°C.....	124
Figure 3.27	Comparison of solvent and solution droplet sizes .....	126
Figure 3.28	Droplet size distributions for 0.5%w/w mometasone furoate solutions in ethanol and 2-propanol .....	126
Figure 3.29	Droplet size distributions for 0.5%w/w fluticasone propionate solutions in ethanol and 2-propanol .....	127
Figure 4.1	Aspirator calibration .....	131
Figure 4.2	Comparison of measured median particle size to predicted size.....	136
Figure 4.3	Electron micrograph of sodium chloride produced at 1%w/w, c. 35µm droplet size .....	137
Figure 4.4	Electron micrograph of sodium chloride produced at 5%w/w, c. 70µm droplet size .....	137
Figure 4.5	Median size of sodium chloride produced at reduced dry gas flow rate .....	139
Figure 4.6	Experimental design - Gas flow value for each run are detailed within solvent identifier.....	141
Figure 5.1	Next Generation Impactor.....	181
Figure 5.2	Cascade impaction configuration .....	182
Figure 5.3	Batch comparison of average mometasone furoate emitted dose .....	185
Figure 5.4	Batch comparison of average mometasone furoate impactor sized mass.....	186
Figure 5.5	Batch comparison of average mometasone furoate respirable mass.....	186
Figure 5.6	Effect of mometasone furoate $X_{50}$ on Emitted Dose .....	191

## Symbols

B	Interaction energy
$C_{ae}, C_{pa}, C_{50}$	Cunningham slip correction factor
$C_p$	Heat capacity at constant pressure
d	Jet diameter
$d_0$	Orifice diameter
D	Droplet or particle diameter
E	Surface enrichment, ratio of surface to average concentration within solution mass
ED	Emitted dose
$\xi$	Surface charge density
F	Force
g	Acceleration due to gravity
H	Enthalpy
$\kappa$	Solvent evaporative flux
ISM	Impactor sized mass
l	Length
M	Mass
n	Molecular density
$\mu$	Viscosity (dynamic)
$\nu$	Viscosity (kinematic)
P	Pressure
Pe	Peclet number, ratio of solvent evaporative flux to solute diffusivity
Q	Flow rate
r	Radial position
R	radius
$r_n$	Normalised radial coordinate
Re	Reynolds number, ratio of inertial to viscous forces
RM	Respirable mass
$\rho$	Density
S	Distance
$\sigma$	Surface tension
St	Stokes number, ratio of stopping distance to characteristic dimension
t	Time
T	Temperature
$T_m$	Melting temperature
$T_g$	Glass transition temperature



u	Velocity
U	Internal energy
V	Volume
W	Mass fraction
We	Weber number, ratio of inertial to surface tension forces
X	Characteristic particle dimension
Z	Ohnesorge number, ratio of viscous to inertial and surface tension forces

## Abbreviations

2-PrOH	2-propanol
API	Active Pharmaceutical Ingredient – the component of the formulation responsible for eliciting a pharmacological response
APSD	Aerodynamic Particle Size Distribution of the API dose emitted from an inhaler
DPI	Dry Powder Inhaler
DSC	Differential Scanning Calorimetry
ED	Emitted Dose – the dose collected from all stages of the impactor, plus induction port and preseparator.
EtOH	Ethanol
FP	Fluticasone Propionate
HPLC	High Pressure Liquid Chromatography
ISM	Impactor sized mass – the dose collected from stages 2 to filter of the impactor
MF	Mometasone Furoate
NGI	Next Generation Impactor
pMDI	Pressurised Metered Dose Inhaler
RM	Respirable Mass – the fraction of the dose less than 5 $\mu\text{m}$ aerodynamic diameter collected from the cascade impactor
SEM	Scanning Electron Microscopy
TGA	Thermogravimetric Analysis
XRPD	X-ray Powder Diffraction

### 1. INTRODUCTION

The molecular arrangement within active pharmaceutical ingredient (API) particles and the efficiency of their delivery to the site of action are arguably the two most important factors in the administration of medicines to patients. The molecular arrangement determines the rate of release, likelihood and extent of physical change or chemical degradation, and the balance of adsorption and removal from the body following dosing. The molecular conformation and packing within the particle are a function of the timescale of particle formation and the rates of heat and mass transfer; the characteristics dimensions during particle formation will therefore strongly influence the relative position of the constituent molecules forming the particle.

At the smallest scale of scrutiny the packing of API molecules into a three dimensional arrangement will dictate the internal energy of the particle, and so the response of the particle to changes in the external environment. Traditional methods of API particle formation have relied upon crystallization from bulk solution, using cooling or the addition of a poor solvent to cause formation of a supersaturated solution and subsequent crystallization of API once the barriers to nucleation have been overcome (Mullin, 2001). The complexity of fluid flow, heat transfer and the balance of nucleation and growth kinetics make prediction of output particle size distribution problematic, resulting in the need for additional processes, such as comminution, to provide an acceptable particle size distribution for the intended route of delivery. Reduction in particle size by fracture and attrition, whilst undeniably effective, can induce inhomogeneities as different particles, and regions within each particle, experience varying degrees of stress during processing. Attrition processes can yield disrupted

## Introduction

regions that display different characteristics and propensities for chemical reaction or physical change when compared to the bulk (Mackin *et al.*, 2002). The surface of comminuted particles are particularly susceptible to disruption, being the focus of impact, hence a small structural change characterised by evaluation of the bulk may have a disproportionate effect upon the behaviour of the particulate system. An alternative approach is to produce particles at the size of interest by the generation and drying of droplets of suitable volume, thus avoiding the deleterious consequences of comminution. Precipitation or crystallization without additional attrition and fracture processes will reduce the energetic inhomogeneities across the particle surface, reducing the driving force for further unintended modification and limiting the range of interactions with other substrates. Atomic force microscopy studies have revealed a two-fold increase in adhesion force with lactose when using amorphous Zanamivir rather than the crystalline form (Berard *et al.*, 2002), suggesting variation of up to ten percent between API particle- excipient particle interactions for micronized APIs (Mackin *et al.*, 2002). In addition, compartmentalising solution into small volumes offers improved heat and mass transfer, constraining the possible particle size and potentially reducing the width of the particle size distribution compared to that obtainable by a combination of bulk crystallization and comminution.

The difficulty in obtaining the required particle characteristics from the manipulation of bulk quantities of API solution with additional processing has driven research into a number of alternative isolation technologies. The technology required for the production of repeatable and reproducible aliquots of matter is typically complex, often exploiting an imposed electric field or the regular oscillation frequency of a piezoelectric

## Introduction

crystal as the basis for droplet generation with low population variance (Basaran, 2002). Use of vibrating meshes driven by piezoelectric crystals is effective in generating narrow droplet distributions, however the average drop size formed is directly related to a small multiple of the mesh aperture size and so can lead to fouling issues where small droplets are required. Electrospray systems are widely used as the sample introduction system for mass spectrometers and have shown promise for monodisperse droplet formation, however the use of the technique is limited to liquids of suitable conductivity, with known issues for aqueous solutions (Ijsebaert *et al.*, 2001).

The drying step necessary to produce solid particles from monodisperse or narrow droplet distributions must be able to preserve the distribution throughout the evaporation process to be considered effective. Coalescence of droplets or the agglomeration of resultant particles will yield greater polydispersity, negating the atomization efficiency. The gas flow patterns and droplet or fluid ligament trajectory within the drying system are key parameters in preserving the distribution variance, governing the degree of droplet and particle co-association and wall impaction. The flow pattern and rate are additionally important in the extent of drying able to be achieved, and in conjunction with the operating temperature and droplet and solute physicochemical properties, are influential in defining the morphology of the dried particles.

Research has therefore centred upon the development of systems suitable for exploring fundamental hypotheses and demonstrating the benefits of reduced particle distribution widths in small-scale studies representative of potential industrial applications.

Assuming a narrow particle size distribution confers a benefit to finished product, a

## Introduction

decision on cost of process implementation and operation versus the incremental product quality benefit will determine the industrial viability. The costs associated with complex atomization systems of narrow applicability and bespoke drying systems may prove prohibitive in marginal cases, hence the development of robust atomization systems based upon simple operating principles coupled with established drying technology would be of value.

### **1.1. Objectives**

The primary objective of the studies described in this thesis is the to understand the particle property differences able to be obtained for active pharmaceutical ingredients by manipulation of spray drying operating conditions when using narrow droplet distributions. Previous research studies (Tajber *et al*, 2009; Prinn *et al*, 2002; Chawla *et al*, 1994) have demonstrated a link between operating parameters and output particle properties, but the elucidation of effect will inevitably have been compromised by the prevailing droplet distribution when using a two-fluid nozzle. The use of technology capable of generating narrow droplet distributions would allow the impact of operating conditions to be evaluated without the complicating effects of substantial droplet volume variance and the difference in processing pathway this can bring.

A second objective of the thesis is the evaluation of a simple atomizing technology for the production of narrow droplet distributions, and subsequently of the ability to translate the droplet distribution into meaningful differences in particle properties and dosage form quality using commercially available drying equipment. A configuration able to be readily industrialised would allow for processing benefits offered by the use of narrow droplet distribution drying to be rapidly realised, and may offer a path to a

## Introduction

relatively simple translation to manufacturing scale via a control framework of few impactful variables. The basis of droplet generation using the atomizer chosen for this work has been the subject of a number of studies over the past two decades (Ganan-Calvo *et al*, 1998; Ganan-Calvo *et al*, 2011), however to date no research into the possible beneficial effect for imparting preferred particle properties for inhaled delivery of pharmaceuticals has been conducted. The focus of this thesis is therefore to demonstrate the suitability of flow focusing for this purpose, rather than a further refinement to the mathematical basis for droplet formation.

The simple droplet formation technique introduced above, based on low pressure elongation of a liquid thread, has been explored in conjunction with a commercially available, small scale spray drying system to establish the viability of this processing approach. Comparison of experimental results with theoretical predictions has been performed to assess the suitability of the chosen atomizer, as described in Chapter 3. High speed videography and laser diffraction analysis of the droplet stream produced by the atomizer have been used to identify the droplet break-up regime, average droplet diameter and droplet distribution width and provide experimental verification of theoretical predictions, using solvent and solution properties defined in Chapter 2.

An inorganic solute, sodium chloride, has been used to validate the ability to translate the difference in droplet distribution characterised in a quiescent atmosphere to discernible particle differences using the spray dryer. Sodium chloride is known to produce crystals of low aspect ratio, reducing the potential impact of particle shape resulting from droplet drying upon analysis of the particle size. Model APIs have then been used to demonstrate systematic impact upon particle properties of droplet

## Introduction

formation and drying conditions. Two corticosteroid molecules, mometasone furoate and fluticasone propionate, have been spray dried and the physical and thermal properties evaluated to ascertain possible effects attributable to drying conditions.

The subsequent performance variation able to be obtained from a dosage form relevant to the particular APIs used, as described in Chapter 4. The APIs investigated within the spray drying experiments are routinely used for the treatment of lung disease and are commonly delivered topically using inhalation therapy. Selected particle batches for mometasone furoate have therefore been formulated with lactose monohydrate and delivered via a capsule-based dry powder inhaler to an inertial impactor in an attempt to link the particle properties imparted during drying to the aerodynamic particle size distribution generated via the inhaler. The formulation, testing and subsequent analyses performed are discussed in Chapter 5.

The following sections of the Introduction summarise the theoretical basis and development of the processing technology and formulation approaches used during the studies. The equipment configurational options in spray drying are discussed, with the suitability of processing options to particular scales of operation highlighted in order to position the choice of operating system used during the experimental studies in this thesis. A summary of the theoretical analysis of droplet drying, with reference to the relative movement of solute and solvent during this dynamic process, is then provided to frame the observations and subsequent discussion in Chapter 4. The likely implications of the kinetics of drying upon molecular arrangement within the dried particles are then outlined, as background to the discussions on thermal analysis and x-ray diffraction in Chapter 4. Droplet formation via the mechanisms relevant to atomizers is summarised,

## Introduction

with an additional section specific to flow-focusing – the particular variant of pneumatic atomizer employed during the experimental studies.

The final sections of the introduction provide background to the pharmaceutical aspects of the thesis, in particular the field of inhalation delivery using dry powder inhalers. The formulation approaches necessary to allow dispersion of the small API particles are summarised, alongside a description of the design of the primary packaging and delivery system that play an integral role in generating dose suitable for lung delivery. A description of the analytical systems necessary to identify and quantify the potentially inhalable portion of the liberated dose is then provided, to provide context for the studies described in Chapter 5.

### **1.2. Spray Drying**

Spray drying is a mature technology and is routinely used as part of industrial processes to manufacture products in the food, chemical and pharmaceutical sectors. The subdivision of a bulk liquid into droplets facilitates rapid drying and the production of particles of desired physical properties when an appropriately designed process is operated, providing the means for conversion of solution or suspension to dry solid in a single processing step. The first documented process is commonly recognised to be a patent published at the end of the nineteenth century (Percy, 1872), describing a process for simultaneously atomizing and desiccating fluid and solid substances to prevent destructive chemical change. The production of dried milk was the first commercial use of the technology, and the manufacture of whey powder, powdered milk and baby formula remain major spray drying applications. The need to preserve and reduce the transport burden for foodstuffs during World War II resulted in rapid development of the



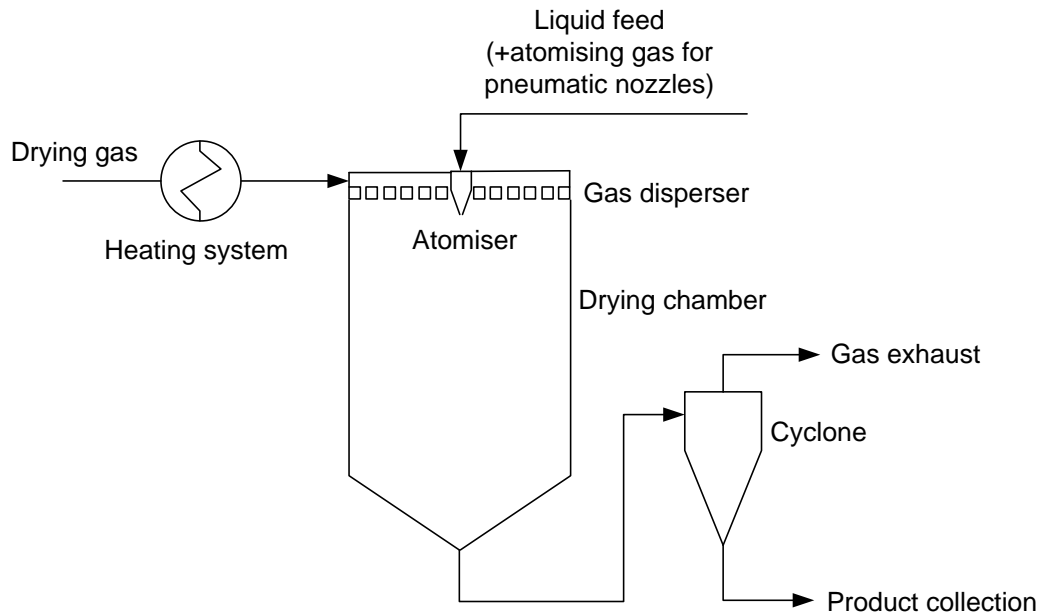
## Introduction

technique, supplemented after the war by the use of spray drying in the development of pharmaceuticals (Cal & Sollohub, 2010). At approximately the same time spray drying began to be used for the manufacture of APIs and excipients for pharmaceutical applications; antibiotics, analgesics and vitamins were some of the earliest spray drying processes developed within the pharmaceutical sector (Marshall, 1954). Spray drying remains an important processing route for pharmaceutical materials as it can readily form amorphous materials conferring preferential physical properties to excipients for direct compression tableting applications, and enhance dissolution rate compared to crystalline forms of API. The low temperatures experienced by APIs within the drying droplets and relatively small stresses imposed on molecules compared to milling processes have identified spray drying as an ideal process for the processing of biopharmaceuticals, with much current academic and industrial interest (Walters *et al.*, 2014).

### **1.2.1. Spray drying equipment**

The design of a spray drying installation is dictated by the characteristics of the feed and dry product and the value of the recovered material. A schematic diagram of a simple open-cycle system is presented as Figure 1.1.

## Introduction



**Figure 1.1 Schematic diagram of an open-cycle spray dryer**

The majority of spray drying processes use air as the drying gas, drawn in from the atmosphere via filters before being heated to the required temperature for use as the drying gas. The exhaust, comprising the inlet air, vaporised solvent and residual product with a particle size below that able to be collected by the separator, then passes back to atmosphere. Such open-cycle systems are only able to be used with non-volatile solvents and when the solute, when dried, offers little in the way of processing risk.

When an explosivity risk is present as a result of the liquid used as a solvent/ suspending agent or due to the dried product the process will typically be operated using an inerted atmosphere, such as the use of nitrogen as the drying gas rather than air. In some instances the solvent or product poses a direct risk to health and so requires both containment within the equipment and very efficient removal from the drying gas exhaust. Closed cycle systems are operated where the oxygen content of the drying gas

## Introduction

has to be limited due to flammability issues, incorporating a recycle system with a scrubbing system to remove solvent from the exhaust gas. Closed systems are constructed to prevent the leakage of gas, vapour or product and are usually operated at above ambient pressure to minimise the ingress of oxygen should a leak occur. If health risks are posed by the product or solution closed or semi-closed (powder-tight but not necessarily gas-tight) systems are often used; however the onus is really upon effective removal of the solvent or powder from the process exhaust so that open-cycle operation becomes a possibility. Semi-closed operation can also be used to reduce drying gas solvent content to an acceptable level whilst reusing some of the heat within the exhaust gas.

A number of methods for heating the drying gas are available depending on the particular drying application. Direct heaters, where the incoming gas stream is used to burn fuel and provide heat, give high thermal efficiencies by virtue of the high inlet temperatures generated. Directly heated systems can provide a route to an inert atmosphere without the need for a nitrogen feed if operated to efficiently consume the oxygen in the incoming gas stream. Semi-closed systems are often operated when the flammability risk is from the dried product as this allows efficient operation via heat recovery, however this configuration is not used for flammable solvents as solvent vapour will be recycled with the drying gas. Indirect heating is used where product would potentially be damaged upon contact with combustion products that will inevitably form in the case of direct heating. Electrical heaters are often used in the case of laboratory and pilot scale operations, where thermal efficiencies will inevitably

## Introduction

be low but are of low priority, and equipment and associated safety costs prevent the use of fired heaters.

The spray drying configurations outlined above share four common process objectives:

1. Conversion of the liquid feed into droplets to increase the available liquid surface area for evaporation, and to subdivide the liquid into droplets of an appropriate size to give the required output dried particle size distribution.
2. Efficient contact of the droplets and the drying gas of the required temperature and flow rate.
3. Provision of a suitably large drying volume affording sufficient residence time to enable the required degree of drying and maximise the fraction of product able to be recovered from the dryer.
4. Separation of the dried product from the fluid stream exiting the equipment without adversely impacting the physical or chemical properties of the product.

Specific considerations will influence the detail design of the equipment, for instance the need to operate intrinsically safe processes for dangerous substances and when using flammable solvents, or alternatively the need to protect the product when intended for consumption will dictate the design philosophy to a large extent.

### 1.2.1.1. **Atomization systems**

The design of spray drying atomizing systems can be divided into three groups; those that utilise the mechanical rotation of the atomizing device to impart the energy required to form droplets, atomizers that rely upon the relative movement of fluids to

## Introduction

cause subdivision of the liquid feed and the use of pressure in conjunction with a suitably sized orifice to form and disintegrate a liquid sheet or thread. The first group, the rotary atomizers, are the mainstay of industrial atomizer systems as they are able to cope with both solutions and suspension feedstocks, can accommodate a wide range of feed flow rates and the relationship between operating parameters and droplet size distribution is well understood. The second and third groups, the nozzle atomizers, can offer a wider range of droplet sizes, and tend to be the norm for small scale spray drying systems as a narrower drying chamber is required than for rotary atomizers.

Rotary atomizers exploit the momentum imparted to the liquid feed by the rotating wheel to form droplets by direct break-up of the sheet of liquid formed at the functional surface of the wheel, or by collapse of liquid ligaments generated as the liquid sheet projects away from the wheel edge. Simple flat discs are rarely used as slippage between the feedstock and disc surface occurs, leading to inefficient transfer of momentum from the wheel to the liquid and poor atomization. This problem can be partially overcome by employing a curved rather than flat surface, and distribution of feed onto the underside of an inverted-bowl wheel often leads to improved atomization as radial forces reduce slippage during wheel rotation. The most common approach to improved momentum transfer is however the use of vanes or channels at the wheel surface to minimise relative rotational movement between the wheel and liquid.

Droplet distributions obtained from rotary atomizers depend upon the combination of the properties of the solution/ suspension and atomizer characteristics. At constant operating conditions droplet size is known to be proportional to viscosity, surface tension and inversely proportional to liquid density. Wheel speed and feed rate

## Introduction

(inversely proportional and proportional relationships with droplet size respectively) are considered the key atomizer operating parameters. Prediction of droplet size from rotary atomizers is problematic, due to the complex droplet formation processes responsible for generation of the spray. Empirical prediction validated by measurement of the particle size of dried product has been used, however this approach is necessarily situation-specific and has been shown to give results of variable accuracy (Masters, 1991).

Two variants of nozzle atomizers are commonly available: pressure nozzles and pneumatic nozzles. Pressure nozzles convert pressure to kinetic energy, usually in the form of a swirling conical liquid sheet. The increase in edge diameter with distance from the atomizer results in a reduction in sheet thickness; interaction with the surrounding drying medium, surface tension, viscous and inertial forces disrupt the liquid sheet resulting in the formation of droplets. An increase in nozzle capacity is possible by reducing the volume occupied by the air core within the spray cone via increased axial motion of some of the liquid passing through the nozzle; the increase in capacity comes at the price of reduced droplet homogeneity however. Droplet size produced by pressure nozzles are a function of spray angle, pressure, and physical properties of the liquid feed. Wider spray angles result in smaller droplet sizes, however also result in a lower discharge coefficient and so less economical operation. Increasing operating pressure results in the transfer in more energy per unit mass to the liquid and leads to a reduction of droplet size at all but very high operating pressures. Liquid viscosity will impact upon both droplet size distribution and operating efficiency of the nozzle – increasing viscosity will result in a coarser droplet size distribution, but also a reduction

## Introduction

in the volume of the air core due to the reduced spray angle of the coarse droplets.

Surface tension increases will cause an increase in droplet size, however the magnitude of the surface tension range possible for successful pressure atomization is small and so the effect is small compared to that experienced as a result of changes in viscosity.

Prediction of average droplet size for industrial systems is subject to the particular nozzle design and application, however the correlation given as Equation 1.1 may provide a useful approximation (Masters, 1991):

$$D_{vs} = \frac{\mu \cdot 2774 Q^{\frac{1}{4}}}{\Delta P^{\frac{1}{2}}} \quad \text{Equation 1.1}$$

where  $Q$  is the feed flow rate ( $\text{m}^3 \text{s}^{-1}$ ),  $\mu$  is feed viscosity (Pa s) and  $\Delta P$  is the pressure drop across the nozzle (Pa). Pressure nozzles are cheap to manufacture and easy to maintain; multiplexing of nozzles is necessary to cope with increased throughput however accurate manufacturing of the component parts with small tolerances means the impact upon overall droplet size distribution is usually acceptable. The main drawbacks for pressure nozzles are the need for a high pressure feed system, usually requiring expensive pressure pumps, and a reduced capability to cope with suspended solids when compared to rotary or pneumatic atomizers – a consequence of the narrow flow geometries necessary for successful operation.

Pneumatic nozzles utilise the energy from a pressurised gas stream to impart the momentum to the liquid feed necessary for droplet production. Contacting the liquid feed with the high velocity gas stream results in a rapid increase in liquid surface area via friction, which subsequently breaks up into droplets from the jet or sheet initially formed, or is directly atomized under highly turbulent conditions. The physical

## Introduction

properties of the liquid feed, notably surface tension, viscosity and density, will influence the droplet size distribution produced (increase in these parameters will lead to an increased droplet size), however given that these properties are unlikely to be able to be modified greatly in the industrial setting, the velocity and density of the gas stream is of greater practical significance alongside the gas: liquid ratio.

Contact of the gas and liquid streams can be accomplished using a number of designs. A coaxial gas stream enveloping a jet can be used for low liquid flow rates; the narrow jet diameter allows for acceptable atomization when using a sufficiently rapid air flow. Increasing the liquid flow rates necessitates the conversion of the liquid bulk into a conical sheet to allow penetration of the air stream and efficient energy transfer. Formation of the sheet is achieved by rotating the liquid within the nozzle to form a liquid annulus, followed by coaxial contact with the gas stream to accelerate the liquid and then increase the diameter to reduce layer thickness and disintegrate the conical sheet into droplets. When atomizing using a single gas stream the contact with gas can occur within the nozzle (internal mixing), outside the nozzle head (external mixing) or, when using mechanical rotation to initially form the liquid sheet (pneumatic cup atomization) at the internal – external boundary.

The majority of the energy transferred from the gas stream to the liquid stream accelerates the liquid sheet, with less than 1 % of the energy being employed to cause droplet formation (Masters, 1991). The transfer of energy is maximised when using internal mixing nozzles, however independent control of the gas and liquid streams is not possible with this design, reducing the operational influence able to be exhibited upon the atomization process.



## Introduction

The gas: liquid ratio is of greatest importance in controlling the droplet size distribution obtained from pneumatic atomizers. Increasing the relative gas flow will reduce the droplet size produced, and also reduce the spray angle of the conical liquid sheet, although the variation in spray angle possible across the operating range is not appreciable. Droplet size has been correlated with operating characteristics using Equation 1.2 (Nukiyama & Tanasawa, 1940):

$$D_{average} = \frac{A}{(u_{rel}^2 \rho_a)^\alpha} + B \left( \frac{M_{gas}}{M_{liq}} \right)^{-\beta} \quad \text{Equation 1.2}$$

Where:  $u_{rel}$  = initial relative gas: liquid velocity ratio,  $M_{gas}/M_{liq}$  = gas: liquid mass ratio; A and B are constants reflecting nozzle design and liquid properties,  $\alpha$  and  $\beta$  are exponents characteristic of nozzle design.

Gas: liquid ratios of 0.1 to 10 are usual, with incomplete atomization and inefficient energy expenditure encountered below and above the ratios indicated. Increasing gas density at constant velocity reduces average droplet size, a consequence of increased energy transfer to the liquid feed.

The contact of gas and liquid streams is normally accomplished using either a single gas flow concentrically arranged to envelope a central liquid flow or an annular liquid flow with both inner and outer gas flows. The former arrangement, known as a two fluid nozzle, is most commonly used and capable of efficient atomization in the majority of applications. The latter design, the three-fluid arrangement, is beneficial for atomizing high-viscosity feeds when penetration of the liquid sheet from one side is problematic, or where very fine droplet size distributions are required.

### **1.2.1.2. Droplet and drying gas contact**

The average velocity and velocity distribution of drying gas within a drying chamber of fixed volume determine the residence time available to accomplish drying and the extent of deposition upon the inner surfaces of the drying chamber and connective pipe-work.

Recirculation flows will influence the temperature distribution within the drying chamber and so affect the drying profile of the droplets whilst passing through the chamber.

Drying gas enters the drying chamber through the air disperser which induces the initial motion and trajectory of the gas stream. The optimal gas flow pattern is dependent upon the required droplet movement, and in turn will depend upon the operating characteristics of the atomizer and the atomizer-drying gas flow arrangement. The position of the disperser within the drying chamber depends upon the mode of operation. Entry of drying gas from the chamber roof is commonplace for co-current spray and drying gas configurations; this can have the additional benefit of reducing wall deposition when using a rotary atomizer if drying gas entry is through the majority of the cross sectional area of the chamber roof. Concentration of the drying gas flow around the atomizer has been employed for spray nozzles to give more rapid drying. Side entry of the drying gas results in a rotary gas flow, giving a longer droplet residence time than for roof entry gas flow; splitting the gas flow between wall and roof entry to the chamber gives a compromise between residence time and wall deposition, allowing the technique to be used for optimising rotary atomization.

Counter-current operation is usually effected using bottom entry of the drying gas flow, with the gas entry point being situated at the junction between the cylindrical and conical sections of the chamber. Most counter-current configurations have a plenum at

## Introduction

the chamber base imparting a rotary motion to the incoming gas; gas entry via a central conduit and wall entry of the drying gas are alternative disperser designs. Introduction of drying gas to mixed flow design dryers depends upon the position of the atomizer and the overall flow pattern required; splitting of the inlet gas can be used, particularly in the case of mixed flow dryers incorporating a fluidised bed where part of the inlet gas is employed to fluidize the powder mass.

### 1.2.1.3. **Drying chamber**

The drying chamber aspect ratio for small to medium-sized equipment is determined by the choice of atomization system and drying gas flow; wide chambers are favoured for use with rotary atomizers due to the high radial velocity component imparted to the droplets when compared to nozzle atomizers. Tall form dryers with a relatively narrow diameter but substantial length are commonplace industrially and for smaller units when using nozzle atomizers with co-current gas flow as spray angles from pressure and pneumatic atomizers are usually narrow and the gas flow acts to minimise transverse droplet movement.

The dimensions chosen for the chamber will be based upon estimation of the gas flow and droplet movement within the chamber by calculation or modelling. The chamber configuration chosen should provide a droplet residence time sufficiently long to allow complete drying but not expose the dry product to excessive heat, whilst maximising product collection by minimising wall deposition. Once the atomizer type and average droplet size has been identified indicative calculations can be undertaken to evaluate the likely deposition on the chamber wall and so the expected level of product loss. In reality droplets will usually follow the drying gas flow pattern within six diameters of the

## Introduction

atomizing wheel for rotary atomizers, so for all but laboratory or pilot scale equipment direct impingement of droplets or wet product on the dryer wall is not an overriding concern. Where rotary atomizers are used with small spray drying units the radial distance of droplet projection ( $S_h$ ) expected can be estimated using the relationship below (Lapple & Shepherd, 1940):

$$S_h = \frac{D^2 \rho_l u_h}{18 \mu_g} \quad \text{Equation 1.3}$$

Where  $D$  = droplet size (m),  $u_h$  = initial radial velocity ( $\text{m s}^{-1}$ ),  $\rho_l$  = liquid density ( $\text{kg m}^{-3}$ )  $\mu_g$  = drying gas viscosity (Pa s).

Estimation of chamber size to ensure optimum drying time is relevant to all configurations, but is complex given the temporal and spatial variation in chamber temperature and humidity, gas velocity and droplet size and density (Langrish, 2007). A simplified approach is therefore typically used which assumes plug flow of drying gas and a constant droplet diameter to estimate residence time. The effect of droplet velocity imparted by the atomizer upon residence time is small but the deceleration time for droplets to slow to the velocity of the drying gas stream can be estimated for nozzle atomizers using Equation 1.4 (Masters, 1991):

$$t = \int_{Re_1}^{Re_2} \left( \frac{D \rho_g (\rho_s - \rho_g) g}{\mu_g \rho_l} - \frac{1.5 \mu_g}{D^2 \rho_l} \left( \frac{R'}{\rho_g u^2} \right) Re^2 \right)^{-1} dRe \quad \text{Equation 1.4}$$

Where  $Re_1$  is the initial droplet Reynolds number,  $Re_2$  is droplet Reynolds number at time  $t$ ,  $D$  is droplet size (m),  $\rho_s$ ,  $\rho_l$  and  $\rho_g$  are solid, feed and atomizing gas densities respectively ( $\text{kg m}^{-3}$ ),  $\mu_g$  is the drying gas viscosity (Pa s),  $R'$  is the drag force per unit area acting on the droplet ( $\text{N m}^{-2}$ ) and  $u$  is droplet velocity ( $\text{m s}^{-1}$ ). As the Reynolds number is

a function of the droplet velocity, calculation of the time required for the droplet Reynolds number to change between known values will give the deceleration rate, hence iterative integration will allow calculation of the increased path length required to give the necessary drying residence time.

### **1.2.1.4. Particle collection**

When the spray drying operation produces large or very dense particles, gravitational settling into the base of the drying chamber may form the primary product collection; however the small particle sizes often encountered in spray drying usually require a purpose-designed particle collection system downstream of the drying chamber. Efficient separation of dry product particles from the drying gas stream beyond the drying chamber is important to ensure a cost-effective process and to minimise particulate exhaust emissions. The optimal collection system will depend upon the aerodynamic size of the particles to be collected, their mechanical robustness and the economic value of the product. The common technologies employed for particle collection for spray drying are cyclones, bag filters, electrostatic precipitators and wet scrubbers. Cyclone collectors present the least operationally complex solution, giving continuous collection of dry material for up to 99 % of particles in the exhaust air stream. Bag filters offer higher efficiencies in terms of collection, however blinding of the filter media increases resistance to air flow requiring pulsing of the bag with a reversed air flow or vibration to de-occlude the surface. The additional operational complexity of bag filters increases the running costs and unblinding the filter bags causes fluctuations in air flow which can increase product variability. Wet scrubbers have very high collection efficiencies and are particularly useful when collecting product that strongly adheres to

equipment surfaces, however the product will then require a secondary separation to allow recovery from suspension. Electrostatic precipitators again have high collection efficiencies and do not result in gas flow fluctuations, similarly to cyclones. Installation and operating costs are higher than for cyclones, and so would not be favoured over cyclones except for expensive or polluting products, or where abrasive products would lead to cyclone damage. Where a spray drying operation has environmental or operator safety concerns a secondary collection system may be used in addition to cyclones, which form the primary separation system.

### 1.2.2. Pharmaceutical applications

Spray drying has been heavily utilised to produce particles to enhance API targeting and control the rate of release (Re, 2006). The subdivision of bulk liquids into droplets, compartmentalising the content has been exploited to generate particle structure at the micrometer or nanometre scale, using the relative difference in solute solubility and component diffusivity to form layers and voids, or to combine nanoparticles into multicomponent particles of larger dimension. An analysis by Vehring and co-workers (Vehring *et al.*, 2007) quantifies the contribution of the diffusivity of each solute to the surface enrichment under the conditions of a receding liquid surface, as encountered during spray drying. The Peclet number, defined for each solute as Equation 1.5, is used to provide a relative measure of the concentration of each solute at the surface:

$$Pe_i = \frac{\kappa}{8D_i}, \quad \text{Equation 1.5}$$

where  $\kappa$  is the solvent evaporative flux ( $\text{m}^2 \text{s}^{-1}$ ) and  $D_i$  is the diffusion coefficient of solute  $i$  ( $\text{m}^2 \text{s}^{-1}$ ). An exact solution for  $C_{s,i}$ , the surface concentration of solute  $i$  from the bulk concentration is possible via Equation 1.6 and Equation 1.7:

## Introduction

$$\beta_i = \int_0^1 r_n^2 e^{\left(\frac{Pe_i}{2} r_n^2\right)} dr_n \quad \text{Equation 1.6}$$

$$C_{s,i} = \frac{C_{m,i}}{3\beta_i} e^{\left(\frac{Pe_i}{2}\right)} \quad \text{Equation 1.7}$$

where  $C_{m,i}$  is the average droplet solute concentration and  $r_n$  is the normalised radial coordinate,  $\frac{r}{r_s}$ , where  $r$  is the radial position (m) and  $r_s$  is the droplet radius (m). A practically useful estimate of the surface enrichment,  $E_i$ , as defined in Equation 1.8, can however be obtained using Equation 1.9:

$$E_i = \frac{C_{s,i}}{C_{m,i}} \quad \text{Equation 1.8}$$

$$E_i = 1 + \frac{Pe_i}{5} + \frac{Pe_i^2}{100} + \frac{Pe_i^3}{4000} \quad \text{Equation 1.9}$$

The differential mobility of solutes, and the difference between solute diffusivity and solvent evaporation rates provide an insight into the mechanisms of layering and the formation of hollow particles. The low particle density generated by producing hollow particles offers advantages for pulmonary delivery, and the interest in this sector is illustrated by the body of work conducted using biodegradable polymer and phospholipid materials to produce particles with voidage, often in the form of crumpled shells (Edwards *et al.*, 1997, Kawakami *et al.*, 2014, Liang *et al.*, 2015, Parsian *et al.*, 2014, Vanbever *et al.*, 1999).

More complex solid foam structures are possible if emulsion systems, rather than solutions, are used as the feed liquid. Voidage can be achieved by producing an emulsion where the dispersed phase is of submicron dimension and has a lower

## Introduction

evaporation rate than that of the continuous phase containing the solute. Upon spray drying, the continuous phase will evaporate first, precipitating the solute in the form of a solid foam with the subsequent removal of the dispersed phase producing the voids.

This approach to particle formation has been employed for the generation of Pulmosphere™ formulations (Dellamary *et al.*, 2000), using a fluorocarbon in water emulsion to produce a phospholipid framework to incorporate API as either a molecular dispersion or as embedded nanoparticles.

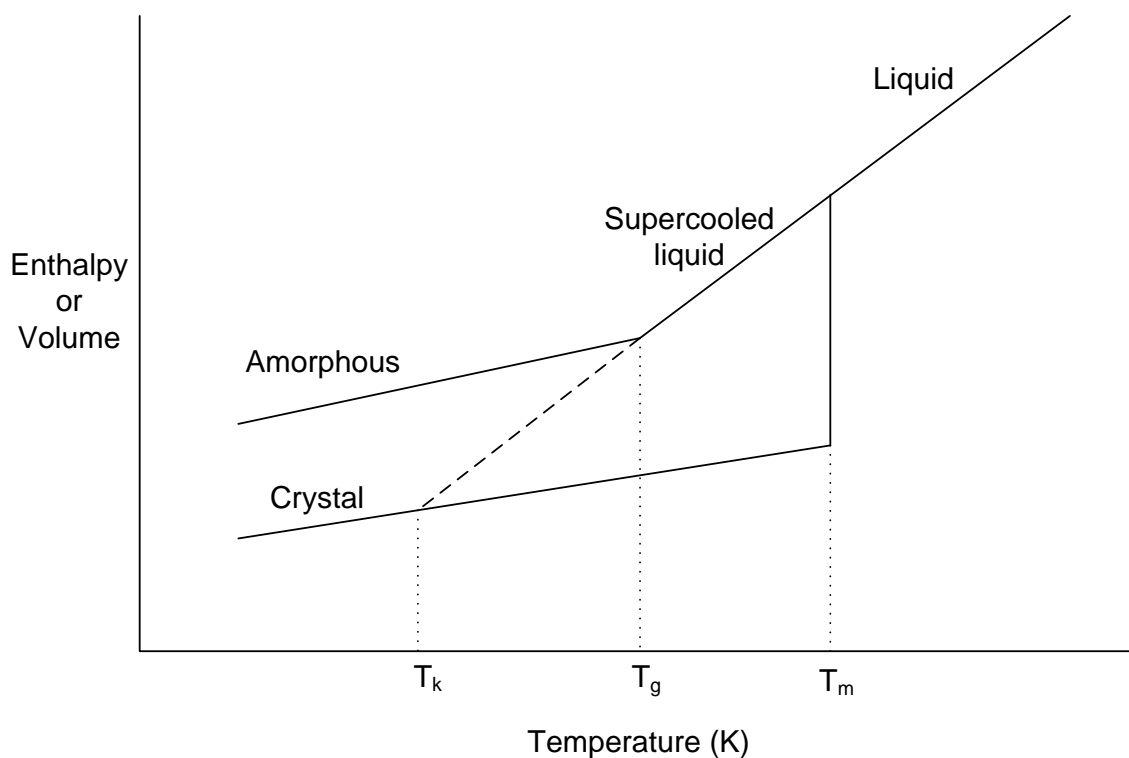
Narrow particle size distribution is of primary importance in API delivery for a number of dosage forms. Particle dimension in intravenous therapy is important for both therapeutic effect and to avoid harmful side effects, such as formation of embolisms or blood clots (Wissing *et al.*, 2004). Size and monodispersity have been demonstrated to be key in providing predictable controlled release from biodegradable polymers for ocular delivery (Barzegar-Jalali *et al.*, 2012); similarly predictable increases in the oral bioavailability of low solubility APIs by the use of monodisperse polymer matrices has been described (Bohr *et al.*, 2011). Cellular uptake of biopharmaceuticals and the ability to cross membranes, such as the blood-brain barrier, are inextricably linked to the morphology of particles and much research is underway to further explore and advance this therapeutic route (Davis *et al.*, 2008, Panyam & Labhasetwar, 2003).

The examples provided above exemplify the importance of compartmentalising the API or polymer matrix in a reproducible volume to provide consistent particle shape and size, however rate of solvent evaporation and molecular mobility of solutes also has consequences for particle structure beyond particle morphology. The molecular arrangement of solutes will be a function of the time available for the adoption of



## Introduction

preferential conformations, and so the drying conditions used will directly impact the crystallinity of the resulting dried particles. Where evaporative timeframes are short in comparison to crystal nucleation and growth an absence of long range molecular order can be expected. The processing pathway and resulting material state can be illustrated with reference to Figure 1.2; if the generation of supersaturation occurs at a sufficiently slow rate a crystalline phase will be formed at the melting temperature  $T_m$ , with a step change reduction in enthalpy and volume via heat transfer as a first order transition. If supersaturation is generated at a rapid rate in comparison to molecular relaxation then the preferential molecular conformations necessary for crystallizations are not attained, and with the loss of translational molecular movement a supercooled liquid is formed. Further reduction in temperature will result in the glass transition temperature ( $T_g$ ) being reached, denoted by the loss of rotational molecular motion with a reduction in specific volume; a consequent reduction in heat capacity can be seen as the change in gradient of  $\frac{dV}{dT}$  or  $\frac{dH}{dT}$ , as shown in Figure 1.2 (Hancock & Zografi, 1997):



**Figure 1.2** Variation in enthalpy or volume with cooling

The value of the glass transition temperature,  $T_g$ , identified during analysis is dependent upon experimental factors, during both material preparation and measurement. An absolute limit for  $T_g$  is the intersection with the crystal enthalpy or volume curve,  $T_k$  (known as the Kaufman temperature), as this represents enthalpy equivalence between the amorphous and crystalline states. The variable nature of the glass transition has been the subject of debate, primarily as to whether this represents separate thermodynamic states or a relaxation continuum. Thermodynamically separate states have been postulated previously, however only under widely differing processing conditions, such as large differentials in pressure (Angell, 1995). The range of conditions possible in the case of pharmaceutical API isolation is more modest, so differences in the properties of amorphous materials are most likely due to differing molecular relaxation

## Introduction

resulting from process-related kinetic differences, such as cooling or precipitation rate rather than being due to polyamorphic forms.

An additional effect is also known to influence the experimentally identified glass transition. Trace amounts of solvent retained during precipitation or environmental water absorbed during cooling can act as plasticisers, reducing the glass transition temperature. The reduction in glass transition is understood to be proportional to the mass fraction of the retained / absorbed liquid, and is described by the Gordon-Taylor equation developed during the study of polymer blends (Hancock, 2002):

$$T_{g1,2} = \frac{(W_1 T_{g1} + W_2 T_{g2} K)}{(W_1 + W_2 K)} \quad \text{Equation 1.10}$$

Where  $T_{g1}$ ,  $T_{g2}$ ,  $T_{g1,2}$  are the glass transitions temperatures of component 1, 2 and the mixture respectively (K),  $W_1$  and  $W_2$  are the mass fractions of components 1 and 2, and  $\Delta C_{p1}$  and  $\Delta C_{p2}$  are the differences in heat capacity ( $\text{J kg}^{-1}$ ) above and below the glass transition temperature for components 1 and 2. The term K is defined as presented in Equation 1.11:

$$K = \frac{\Delta C_{p2}}{\Delta C_{p1}} \quad \text{Equation 1.11}$$

The amorphous state can confer therapeutic advantages compared to crystalline forms. The higher internal energy of amorphous forms results in more rapid dissolution than for the crystalline version, increasing bioavailability giving more effective treatment, or a reduction in dosage. The pharmaceutical industry and regulatory authorities have however been reticent to adopt amorphous forms of APIs with preferential adoption of crystalline forms usually encountered. The inherent physical instability may lead to

conversion to a crystalline form under suitable environmental conditions, which could result in an uncontrolled change in the dosing characteristics of a medicine after dispensing. Whilst thermodynamic instability is necessarily the case for all amorphous forms compared to crystals, the rate of transformation varies and for a number of APIs the kinetics are sufficiently slow that little risk of conversion within a meaningful timeframe is present. A margin of 50K between storage temperature and glass transition has been suggested as appropriate (Hancock & Shamblin, 2001), however, as discussed above, the possibility of lowering of the  $T_g$  via plasticisation by absorbed water should be considered and mitigated.

### **1.3. Droplet formation**

The formation of droplets by the atomizer is the key step in defining the particle size distribution of the dried product. The droplet size distribution generated depends upon the variability in the dimension of the fluid ligaments produced by the atomizer which act as precursors to droplets. Additionally the environment into which the droplets are dispersed may influence the final droplet distribution, either by further break up (secondary atomization) or by coalescence as a result of differing droplet velocities. A large body of information on droplet formation has been generated by researchers over the 180 years since Savart identified the proportionality between breakup length and jet velocity at constant orifice diameter, and orifice diameter at constant jet velocity (Eggers & Villermaux, 2008). Plateau's analysis of 1849 demonstrated that the surface area of a cylindrical jet exceeds that of two droplets of equivalent volume if the length of the cylinder is greater than the jet circumference; hence the surface energy of the liquid is reduced by the formation of droplets. Rayleigh provided insight into the dynamics of the

## Introduction

transition from a jet to droplets, recognising the role of growth of perturbations of the jet surface in the eventual breakup of the jet and the defining influence of perturbation wavelength in the size of droplets formed.

Rayleigh showed that the growth rate of the dominant disturbance,  $q_m$  is dependent upon the surface tension as shown in Equation 1.12:

$$q_m = 0.97 \left( \frac{\sigma}{\rho d^3} \right)^{\frac{1}{2}} \quad \text{Equation 1.12}$$

where  $\sigma$  is the surface tension ( $\text{N m}^{-1}$ )  $d$  is the jet diameter (m), and subsequently that the dominant wavelength can be defined as per Equation 1.13.

$$\lambda_m = 4.51d \quad \text{Equation 1.13}$$

Assuming a portion of the jet of this length transforms into a droplet of diameter  $D$  (m), then  $\lambda_m$  and droplet size  $D$  can be predicted using Equation 1.14 and Equation 1.15:

$$\frac{\pi d^2}{4} \cdot 4.51d = \frac{\pi D^3}{6} \quad \text{Equation 1.14}$$

$$D = 1.89d \quad \text{Equation 1.15}$$

Rayleigh's description of surface tension-driven breakup was developed further by a number of contributors (Lefebvre, 1988). Weber (1931) included the effects of viscosity upon the droplet formation process. Weber's analysis defines two characteristic wavelengths for an inviscid disturbed cylindrical jet for the minimum wavelength of

## Introduction

disturbance able to be propagated and the optimal wavelength of disturbance respectively, as given in Equation 1.16 and Equation 1.17:

$$\lambda_{min} = \pi d \quad \text{Equation 1.16}$$

$$\lambda = \sqrt{2\pi}d \quad \text{Equation 1.17}$$

In the case of viscous jets  $\lambda_{opt}$  is revised as given in Equation 1.18, with  $\mu_l$  representing liquid viscosity (Pa s), so an increase in liquid viscosity would be expected to increase the size of droplets produced at breakup.

$$\lambda_{opt} = \sqrt{2\pi}d \left( 1 + \frac{3\mu_l}{\sqrt{\rho_l \sigma d}} \right)^{0.5} \quad \text{Equation 1.18}$$

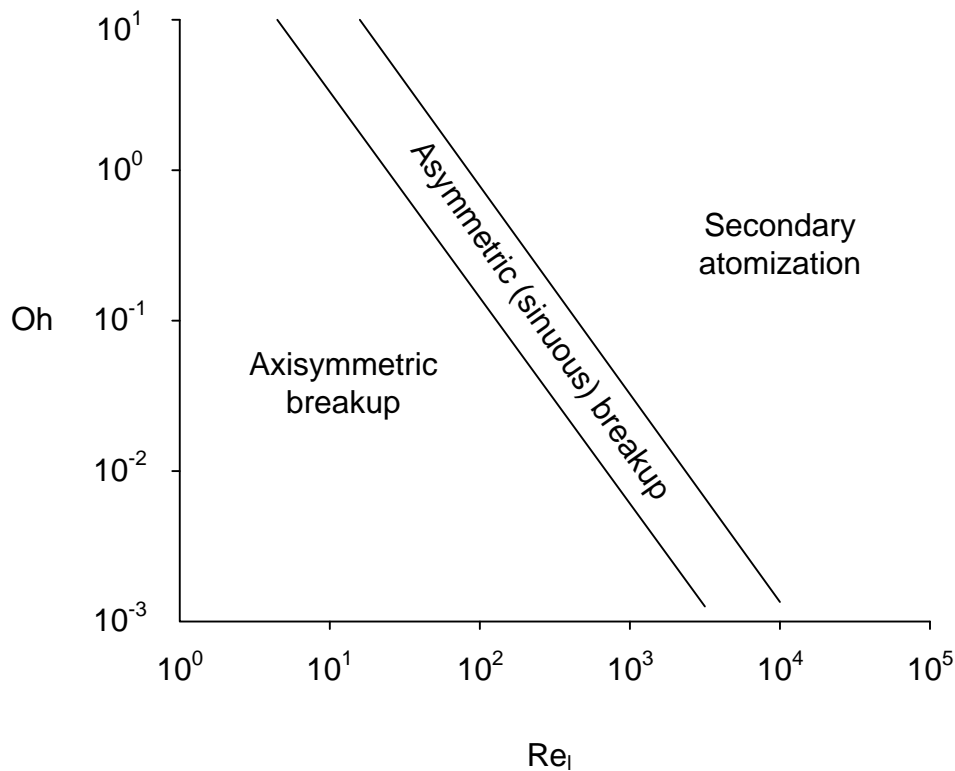
A number of researchers have investigated the effect of gas friction on the disintegration of liquid jets. Increasing the relative jet to ambient air velocity leads to wave formation at the jet surface, augmenting or supplanting the effects of surface tension on the breakup process. Haenlein (1932) described four separate regimes of increasing influence as jet velocity increases within a stagnant air environment, ranging from surface tension being the dominant factor to disintegration of the jet at the nozzle orifice. Ohnesorge (1936) adopted an analytical approach to the impact of aerodynamic forces, using dimensional analysis to characterise operating space. Ohnesorge defined a dimensionless number  $Z$ , the stability number or viscosity group, latterly referred to as the Ohnesorge number, and plotted this against the Reynolds number to establish the

## Introduction

dominant mechanism of atomization. The Ohnesorge number,  $Z \left( \frac{\sqrt{We}}{Re} \right)$ , is calculated as shown in Equation 1.19:

$$\frac{\mu_l}{(\rho_l \sigma d_0)^{0.5}} \quad \text{Equation 1.19}$$

Where  $d_0$  is the orifice diameter (m), so is constant for a liquid jet issuing from a fixed nozzle geometry at constant temperature, with variation in operating parameters being reflected in the changing Reynolds number. Ohnesorge's classification of jet breakup is reproduced as Figure 1.3



**Figure 1.3** Ohnesorge's classification of modes of disintegration

Increasing the jet velocity progressively will change the mode of disintegration from surface tension-driven axisymmetric as described by Rayleigh, to an air friction

## Introduction

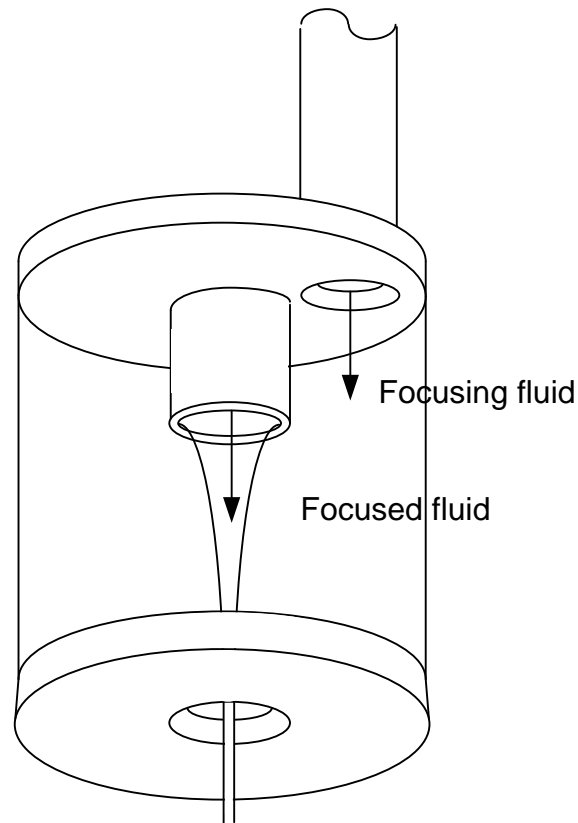
dominated non-axisymmetric sinuous wave mode predicted by Weber and observed by Haenlein. Increasing the jet velocity further reduces the breakup length to the nozzle exit with chaotic droplet formation.

The approach to characterising jet breakup devised by Ohnesorge has been further developed by Reitz (1978) with an increase in the range covered for sinuous breakup, and a separation of this mode into two classes. The first of the two classes, at lower Reynolds numbers for a given Ohnesorge number, is characterised by a combined surface tension and air friction effect, producing droplets of similar diameter to the jet. The second class depicts an increased effect of air friction to give shorter wavelength disturbances at the jet surface leading to droplets smaller than the jet diameter.

### **1.3.1. Flow focusing**

Flow focusing is the generation of a narrow-diameter liquid jet by use of a fast-flowing coaxial fluid stream. Flow focusing devices consist of a liquid conduit through which the focused liquid is introduced into the centre of a chamber, an additional conduit through which the focusing fluid is fed, and an exit orifice of circular cross-section through which both the focussed and focusing fluids exit. A diagram of a generalised flow-focusing arrangement is shown as Figure 1.4.





**Figure 1.4** Flow focusing arrangement

When operated optimally, a liquid jet with a diameter significantly smaller than that of the focussed fluid conduit can be produced under conditions of turbulence sufficiently low that subsequent break-up conforms to the Rayleigh ideal, resulting in narrow droplet size distributions (Ganan-Calvo, 1998).

Analysis of the forces during jet generation has led to a description of jet momentum and subsequently to an estimate of droplet diameter following break-up. Energy is supplied to the liquid by the fact-moving gas stream as viscous stress and through the pressure distribution at the liquid surface, resulting in the generation of additional surface area as the jet is produced, coupled with kinetic energy as the momentum of the jet increases.

The relationship has been described by Equation 1.20, which has been observed to

## Introduction

provide accurate results when used to evaluate jet diameters beyond the discharge orifice (Ganan-Calvo *et al.*, 2011a):

$$\frac{2\tau}{R_j} - d_z P_g = d_z \left( \frac{\sigma}{R_j} + \frac{\rho_l Q_l^2}{2\pi^2 R_j^4} \right) + \frac{6\mu_l Q_l}{\pi R_j^2} d_z (R_j^{-1} d_z R_j) \quad \text{Equation 1.20}$$

$\tau$  is the tangential viscous stress on the liquid surface caused by the gas stream ( $\text{N m}^{-2}$ ),  $P_g$  is the pressure exerted at the liquid surface by the gas stream (Pa),  $R_j$  is the jet radius (m),  $Q_l$  is the focused liquid flow rate ( $\text{m}^3 \text{s}^{-1}$ ),  $\sigma$  is the interfacial tension ( $\text{kg s}^{-2}$ ) and  $\mu_l$  is the liquid viscosity (Pa s).

The energy dissipation by the interfacial energy increase is considered small, and when considering low viscosity liquids the viscous dissipation and viscous stress terms become small, hence the three terms can be neglected, as shown in Equation 1.21, to give an acceptably accurate estimate of jet radius:

$$d_z \left( \frac{\rho_l Q_l^2}{2\pi^2 R_j^4} - P_g \right) = 0 \quad \text{Equation 1.21}$$

Integration of Equation 1.21 provides an estimate of the jet radius at the point of break up given the low rate of radial change beyond the orifice plate, Equation 1.22:

$$R_j \approx R = \left( \frac{\rho_l Q_l^2}{2\pi^2 \Delta P_g} \right)^{\frac{1}{4}} \quad \text{Equation 1.22}$$

Equation 1.22 is also able to be derived with reference to Bernoulli theorem, as can be seen from the similarity in form to Equation 1.21. The two variable terms within Equation 1.21 are consistent with the Bernoulli equation, as given as Equation 1.23 (Coulson & Richardson, 1999),

$$\frac{P}{\rho} + \frac{1}{2}u^2 + gz = \text{constant} \quad \text{Equation 1.23}$$

The formation of the liquid jet can therefore be described using a conservation of energy argument; the acceleration of the liquid jet results in a reduction in pressure within the liquid and, by continuity, within the adjacent gas phase.

The formation of droplets from the jet is driven by surface tension acting upon disturbances in the liquid surface generated at the nozzle exit, with resulting droplet size predicted by Equation 1.15. A spectrum of disturbance wavelengths are evident at the liquid surface, however only the disturbances with a wavelength greater than the circumference of liquid jet are observed to propagate downstream. The fastest-growing disturbance predominates at the point of break-up; disturbances with a circumference: wavelength ratio of 0.697 (the 'Rayleigh mode') have been observed to have the dominant effect on droplet break-up and thus the size of the droplets produced (Eggers, 1997).

The flow rates for the focusing and focused fluid, and focused fluid conduit and exit orifice diameters and separation are therefore critical process parameters for successful operation. Axisymmetric disturbances are understood to be the precursor to quasi-monodisperse droplet formation, and the Weber number, as defined in Equation 1.24, has been used to describe the limit for formation of axisymmetric disturbances.

$$We = \frac{D\Delta P}{\sigma} \quad \text{Equation 1.24}$$

## Introduction

An upper limit of  $We = 40$  (Ganan-Calvo, 1998) has been proposed for generation of narrow droplet size distributions by growth of the Plateau-Rayleigh instability; outside this region sinusoidal ('whipping') disturbances increasingly dominate, resulting in both a larger droplet size than predicted and increased polydispersity. A lower limit is also evident, due to the formation of a recirculation flow that disrupts the formation of the jet surface below a minimum liquid flow rate (Ganan-Calvo *et al.*, 2011b).

Target operating parameters for the experiments described in Section 3.2 were identified using an iterative approach employing the above equations. Flow rates and pressure drops for a required droplet size were identified, and then the Weber number was defined to allow comparison with the scientific literature. An Excel spreadsheet was produced to allow calculation of size and associated Weber number across the experimental space of flow rate and pressure drop for each of the liquids atomized.

### **1.4. Inhaled drug delivery**

The respiratory tract has long been used as a treatment route for a variety of diseases, often of pulmonary origin. Vapours, aerosols and fumes of plant extracts, organic liquids and minerals were inhaled from primitive vessels or rudimentary mechanical systems to provide relief from a range of conditions including cough and asthma (Anderson, 2005). Efficient delivery of API to the lung was first achieved using pressurised metered dose inhaler devices (pMDIs) in the 1950s, utilising a combination of chlorofluorocarbon (CFC) propellants to aerosolize the formulation upon actuation of a metering valve (Bell & Newman, 2007). Two therapeutic agents were initially delivered, adrenaline and isoprenaline, as separate formulated products, using ethanol as a cosolvent to form a solution. The pMDI rapidly became the mainstay of portable inhaled therapy, with

## Introduction

industrial quantities of CFC propellants being available as a result of their use in refrigerant systems, and metering valves having been developed for the cosmetic fragrance sector. The use of one of three surfactants, oleic acid, sorbitan trioleate or lecithin, expanded the formulation space to include micronised particles, reducing aggregation and making dispersed, inhalable particles possible rather than relying upon droplets to ensure respirable size for the API; use of the surfactants also conferred the additional benefit of lubricating the metering valve. The ozone-depleting potential of CFCs was recognised with the ratification of the Montreal Treaty in 1987, requiring the eventual replacement of CFC systems with alternatives of lower depleting potential. Hydrofluoroalkanes (HFAs) were identified as a suitable replacement to CFCs and have become the continuous phase of choice for modern pMDI development, however some technical issues remain. No surfactant system has yet been identified for use in HFA-based pMDIs, resulting in the need for expensive contingencies, such as coated inner valve and canister surfaces, to stabilise suspension formulations. The two predominantly used propellants, HFA134a (1,1,1,2-tetrafluoroethane) and HFA227ea (1,1,1,2,3,3,3-heptafluoropropane) have low boiling points, requiring the use of expensive pressurised manufacturing systems to produce and fill the formulations. From a patient perspective however the lower enthalpy of vaporisation of the propellants compared to the CFC systems tends to allow for a more comfortable dose delivery. The pMDI remains the predominant portable delivery system, however difficulty in coordination of dose release and inhalation manoeuvre for patients, exacerbated by the technical difficulties associated with the CFC to HFA transition has led to the development of alternative inhaler variants.

## Introduction

Dry powder inhaler devices (DPIs) entered the market in 1971 with the introduction of Fison's Spinhaler, delivering agglomerated sodium cromoglycate from a capsule employing a system of blades to spin the capsule ejecting the powder and subsequently disrupt the agglomerates to produce a respirable/ fine particle fraction - the proportion of the dose considered efficacious with an aerodynamic diameter less than 5  $\mu\text{m}$  (Bell *et al.*, 1971). A series of capsule based inhalers have followed, for instance Rotahaler (Glaxo), Aerolizer (Novartis), Cyclohaler (Teva) and Handihaler (Boehringer Ingelheim), all operating on the same base principle of using the patient's inspiratory effort to entrain and deagglomerate the dose within the capsule (Newman & Busse, 2002; Prime *et al.*, 1997). The need to reload the device after each actuation was partially circumvented by the Aerohaler (Boehringer Ingelheim), using a magazine of six capsules to reduce the frequency of patient intervention, however similar levels of convenience to those associated with pMDIs were only realised with the development of reservoir and multiple unit dose devices. Reservoir devices, such as the Turbuhaler (AstraZeneca), Twisthaler (Schering Plough), Jethaler (Ratiopharm), Clickhaler (Vectura), Novolizer (Meda), Skyehaler (Skyepharma) and Eazyhaler (Orion) use an internal container of API or formulation as blend, spheronized API or compressed disk from which an aliquot is metered as a dose for the patient upon preparation of the device for actuation. A substantial number of patient doses (up to 200) can be obtained from a single device; however concerns around dose reproducibility have hampered entry into some markets, primarily the US. Multiple unit dose devices contain premeasured doses filled into individual dose units at the manufacturing facility, requiring the patient to advance the blister strip (Ellipta and Diskus, GlaxoWellcome) or disk (Diskhaler, GlaxoWellcome) to obtain the dose immediately prior to inhalation.

## Introduction

All currently marketed DPIs are passive, rather than active devices, utilising the patient's inspiratory flow through the device to provide the energy required to liberate respirable particles. Formulation and device design therefore needs to be carefully considered to make best use of the patient's inspiratory manoeuvre, allowing an efficacious respirable fraction to be generated under flow conditions achievable by the target patient population.

### **1.4.1. DPI Formulation**

The small particle size required for API particles to reach the central and peripheral lung, acknowledged to be an aerodynamic diameter of between 1 and 5  $\mu\text{m}$  provides a technical challenge with respect to dispersion of API particles from the agglomerated state. Deaggregation of API particles within the airflow through a device requires the forces acting upon the particles to overcome the autoadhesive forces holding the agglomerate together. The adhesion forces acting between particles in respiratory formulations can be subdivided into those arising from interactions between the molecules of neighbouring particles at narrow particle separation, referred to as van der Waals forces, electrostatic forces imposed during powder transport and handling, and capillary forces due to the adsorption of water in the interstices between particles. The relative contribution of each of these adhesion mechanisms will depend upon the prevailing environmental conditions. Van der Waals forces are short range forces, resulting from electromagnetic interaction between the protons and electrons of molecules in close proximity to the contact zones between the particles. The quantum mechanical nature of this interaction, coupled with the additional complexity of surface roughness of interacting particles currently prohibits accurate prediction for real

## Introduction

particulate systems, however useful estimates of the magnitude of forces are considered achievable by the evaluation of simplified cases.

Interactions between molecules that leave their chemical identities unchanged arise from dipole-dipole (Keesom interaction), dipole-induced dipole and induced dipole - induced dipole (London or dispersion) interactions. The potential,  $V$ , of these interactions is approximated by Equation 1.25:

$$V = -\frac{C}{S^6} \quad \text{Equation 1.25}$$

where  $S$  is the particle separation (m). The constant of proportionality,  $C$ , is specific for each of the interactions as defined in Equation 1.26, Equation 1.27 and Equation 1.28 (Atkins, 1998):

**Dipole-dipole:**

$$C = \frac{2\mu_1^2\mu_2^2}{3(4\pi\epsilon_0)^2kT} \quad \text{Equation 1.26}$$

**Dipole-induced dipole:**

$$C = \frac{\mu_1^2\alpha_2}{\pi\epsilon_0} \quad \text{Equation 1.27}$$

**induced dipole- induced dipole:**

$$C = \frac{2}{3}\alpha_1\alpha_2\frac{I_1I_2}{I_1 + I_2} \quad \text{Equation 1.28}$$

where  $\mu$ ,  $\alpha'$  and  $I$  are the dipole moment (D), polarizability volume ( $\text{m}^3$ ) and ionisation energies (J) of the two molecules involved in the interaction. Differentiation of the potential provides an expression for the attractive force, presented as Equation 1.29:

$$F = \frac{C}{6S^7} \quad \text{Equation 1.29}$$



## Introduction

The force therefore declines rapidly with intermolecular distance, hence only the molecules in very close proximity to those in a neighbouring particle will contribute significantly to the intermolecular interaction. Consideration of the combined effect of the molecules in a small spherical particle with the face of a larger faceted particle leads to Equation 1.30 (Finlay, 2001),

$$F_{vdW} = A \frac{d}{12D^2} \quad \text{Equation 1.30}$$

where  $A$  is the Hamaker constant for the interacting materials defined by Equation 1.31:

$$A = \pi^2 B n_{mp} n_m, \quad \text{Equation 1.31}$$

where  $B$  describes the interaction energy ( $\text{J m}^6$ )  $n_{mp}$  and  $n_m$  are the molecular density in the particle and wall respectively.  $D$  and  $d$  represent the interparticle separation and particle diameter (m).

Analysis by Finlay (2001) demonstrates that for a particle with a diameter of five microns 95 percent of the van der Waals force is contributed by molecules within  $0.0005d$  (2.5 nm) of the adhesional contact, or 0.00008 percent of the particle mass. Given the sensitivity of the force to such a small area around the contact point, the texture of the surfaces of the adhering particles is of paramount importance to adhesion by this mechanism.

Increasing the moisture content of the atmosphere surrounding adjoining particles will eventually lead to condensation of liquid water into the interstices. The Kelvin effect predicts that the vapour pressure above a concave liquid meniscus will be reduced compared to that above a flat surface, hence preferential condensation will be expected

## Introduction

at the contact points of solid surfaces of substances wetted by water (Adamson, 1982).

The adhesion force attributable to capillary condensation emanates from the surface tension of the condensed water acting to oppose increase in the meniscus surface area.

The increase in adhesion force can be estimated for the adhesion of a particle and flat surface of the same material using Equation 1.32:

$$F_{cap} = 2\pi d(\sigma_{23}\cos\theta + \sigma_{12}) \quad \text{Equation 1.32}$$

where  $d$  is the particle diameter (m),  $\sigma_{23}$  is the air-water surface tension ( $\text{N m}^{-2}$ ),  $\theta$  is the contact angle, and  $2\sigma_{12}$  is the work of adhesion (J) resulting from van der Waals forces at the particular environmental conditions (e.g. including the presence of water at surfaces).

Assuming a typical value for interparticle spacing on contact of 0.4 nm, capillary adhesion would be expected to occur within inhaled formulations where hydrophilic surfaces are present (Finlay, 2001) and capillary forces would be expected to be the major contributor to adhesion above 65 percent relative humidity (%RH). Atomic force microscopy (AFM) studies performed at greater than 50 %RH demonstrated increased adhesion forces compared to measurements generated using dry atmospheres (Sedin & Rowlen, 2000, Xu *et al.*, 2013). Studies relevant to inhaled API and excipients conducted by Podczec demonstrated an increase in adhesion force beyond 75 %RH for micronised lactose particles on a compacted lactose surface, however no similar increase was observed when hydrophobic micronised salmeterol xinafoate particles were used (Podczec *et al.*, 1996). AFM was used to assess the impact of increasing relative humidity on lactose-budesonide and lactose-salbutamol formulations (Price *et al.*, 2002), demonstrating the dependence of the effect upon the particular molecule used. Two

## Introduction

orders of magnitude difference in interaction energy were encountered between the APIs, and differing interaction energy trends were observed. Capillary adhesion was interpreted as being significant for both molecules above 30 %RH, but with a large rise in adhesion noted above 60 %RH for salbutamol, compared to a linear increase in adhesion force with relative humidity for the less hydrophilic budesonide. Capillary effects became dominant for both APIs beyond 65 %RH. The effects of capillary condensation have been observed to be reversible, however where particles exhibit aqueous solubility this may result in dissolution and the formation of permanent solid bridges upon removal of the condensate by drying.

Relative movement of particles during powder handling and transport can result in triboelectrification, with a resulting increase in adhesion if dispersion is attempted before the charge has decayed sufficiently. An experimental design was conducted to evaluate the charge generated by blending of lactose for 30 minutes in a Turbula mixer using an aluminium container then filled into gelatin capsules, compared to that imparted during aerosolisation (Chow *et al.*, 2008). A range of air flow rates and ambient humidities were evaluate during inhaler testing, and the impact of repeated use of the test inhaler was examined. Larger charges were seen to be developed upon aerosolisation than during processing and filling (of the order of  $10 \text{ nC g}^{-1}$  versus  $1 \text{ nC g}^{-1}$  respectively), however an increase in charge with handling was noted. Increased charging was observed when handling or aerosolising powders at low humidities and when aerosolising at higher flow rates, and an increased rate of charge dissipation was noted at higher relative humidity attributed to increased charge transport in humid air and condensed liquid in the particle interstices rapidly dissipating static charge. The

## Introduction

impact of adding API to lactose on the charge developed during blending in a Turbula mixer in containers of different materials of construction was considered by Elajnaf and co-workers (Elajnaf *et al.*, 2006). A large change in the charge developed by addition of small quantities of API was noted, with polarity of charge developed for each material attributed to the relative position in a triboelectrical series of each particulate. The material of construction of the blending container was observed to play a significant role in the charge developed, but generation of a powder layer on the surface of the container reduced the charge imparted to the powder. Charge densities of magnitude  $10 \text{ nC g}^{-1}$  were generated for API blends at  $20 \text{ }^\circ\text{C} / 45 \text{ \%RH}$ . The impact of particle size and crystallinity on the development of charge was evaluated for lactose monohydrate (Carter *et al.*, 1998). Increased charge was measured on larger particles within the particle size range 45 to  $180 \text{ }\mu\text{m}$ , however little impact of crystallinity upon results was noted. Work performed using processing containers made of a variety of materials demonstrated a lack of impact upon the aerosolisation of spray dried mannitol, despite powder charge differences of  $-96 \text{ nC g}^{-1}$  for stainless steel to  $93 \text{ nC g}^{-1}$  for Teflon being imparted to the powder (Adi *et al.*, 2010).

The adhesion force attributable to contact of two particles with charged surfaces can be estimated by Equation 1.33:

$$F = \frac{\pi d^2 \xi_1 \xi_2}{4\epsilon_0} \quad \text{Equation 1.33}$$

where  $\xi$  is the surface charge density ( $\text{C m}^{-2}$ ) of the adhering particles, and  $\epsilon_0$  is the vacuum permittivity ( $\text{C}^2 \text{ N}^{-1} \text{ m}^{-2}$ ). Studies conducted on the adhesion force for micronised salmeterol xinafoate particles on lactose surfaces revealed a mean adhesion force of 2.4

## Introduction

$\times 10^{-11}$  N (Podczeck *et al.*, 1997). An analysis by Finlay based upon the above relationship for autoadhesion of lactose particles of diameter 3  $\mu\text{m}$  using an adhesion force of  $1.5 \times 10^{-11}$  N concluded a charge density of greater than  $2 \text{ nC g}^{-1}$  would be necessary to have a significant impact upon adhesion (Finlay, 2001). The discrepancy between this value and the charges generated during experimental studies on charges generated indicates that no observable impact upon triboelectrification by processing should be expected, consistent with the findings of Adi *et al.* (2010), where tumbling blending has been used to prepare formulations.

Charging is also possible during powder entrainment upon inhalation by contact with inhaler surfaces and other particles within the emitted powder cloud. Using an electrical Next Generation Impactor (eNGI) Hoe and co-workers evaluated the contribution of formulation and inhaler components to the charging of the aerosolised powder cloud (Hoe *et al.*, 2010). Charge densities between 100 and  $2294 \text{ nC g}^{-1}$  were measured within the induction port across the 30 to  $90 \text{ L min}^{-1}$  airflow used, orders of magnitude greater than that attributed to processing. The distribution of charge with impacted salbutamol sulphate charge was seen to be bimodal, with net negative charge measured below 2.82 and above  $8.04 \mu\text{m}$ ; increasing net charge with flow rate was seen, but not proven to be statistically significant due to data variability. The impact of storage humidity on aerodynamic particle size distribution and charge was investigated using a Next Generation Impactor (NGI) and an Electrical Low Pressure Impactor (ELPI) (Young *et al.*, 2007). Results from both impactors demonstrated a similar trend of fine particle fraction of salbutamol sulphate with humidity, with a maximum at 60 %RH; results from the ELPI showed a consistent decrease in the charge carried by the impacted powder with

## Introduction

increasing humidity. A multifactorial study considering the relative effects of formulation ingredients and contact materials on the generation of charge and subsequent impact on deposition was performed by (Telko & Hickey, 2014). Two standard entrainment tubes of differing specific resistance were used rather than different devices, so effects attributable to materials of construction could be separated from that of resistance. The use of different contact materials to contain the formulation prior to actuation had little impact upon the charge profile generated, suggesting triboelectrification during blending and subsequent charge exposure upon particle separation was the predominant mechanism. Storage effects were observed upon the charge profile and stage deposition, with differences in performance apparent for a formulation retested after a two week storage interval. The charges generated upon aerosolisation were detected when dosing using the entrainment tubes at up to 95 %RH, indicating that charge generation in DPIs is a clinically-relevant phenomenon. The charges developed on the API and excipients were observed to be dependent upon their relative position in the triboelectric series, as anticipated, and reducing the drug concentration decreased the fine particle fraction (consistent with active site theory, as described later in this section) with an increase in charge per particle. The actuation conditions demonstrated an unexpected trend, with the magnitude of charge per particle decreasing with increasing specific resistance and turbulence. The authors attributed this counterintuitive trend to the increase in particle collisions likely to occur with a higher resistance, as a denser powder cloud is likely to result. An increase in particle collision would promote charge transfer, and provide an opportunity for back flow of charge. The magnitude of charge generated during the study was greater than

## Introduction

previously considered likely, with potentially tens of thousands of charges per particle possible and therefore a possible influence on particle trajectory and site of deposition.

Once aerosolised, separation of particle agglomerates containing the API particles is necessary in order for a sufficiently small aerodynamic size for lung delivery to be achieved. The lift and drag forces experienced by a particle are proportional to the area presented to the laminar airstream, whilst the adhesional force is proportional to the particle diameter. An agglomerate comprised of API particles will therefore be inherently difficult to separate using aerodynamic forces, requiring additional energy or modification of the adhesion forces to generate a meaningful respirable fraction. Inhaler devices with a means of generating deagglomerating forces other than by patient inspiratory effort, known as active inhalers, have been developed however have not yet attained acceptance in clinical practice. Devices such as the Turbuhaler and Twisthaler employ formulations containing spheronized pellets of API that are dispersed using a tortuous airflow path (Wetterlin, 1988; Yang *et al.*, 2001), however questions have been raised regarding the dose reproducibility of such devices (Chrystyn, 2007). The most widely used approach for assuring acceptable respirable fraction is to mix the API with an excipient of larger particle size, and exploit the difference in inertia to promote separation via drag or during impact with the internal surfaces of the inhaler. A high carrier to API mass ratio is typically used to increase the likelihood of API-carrier interactions; the size disparity between API and carrier particles necessitates a high mass ratio as the probability of API: API interaction versus API: carrier interaction will be dictated by the number, rather than mass, ratio. The use of dilute API concentrations has the added benefit of allowing dosing of milligram quantities of powder blend rather

## Introduction

than microgram quantities of API, reducing the impact of nominal dose weight variability on the uniformity of delivered API dose. The use of adhesive mixtures, also known as ordered or interactive mixtures, were employed previously in pharmaceutical dosage forms to provide an approach to improved blend homogeneity (Staniforth, 1987). The key difference with DPI formulations is the need for the adhesion to be reversible in order to generate the respirable fraction of the API within the formulation. The most widely used excipient for inhaled formulations is lactose (4-( $\beta$ -D-galactosido-)-D-glucose), usually in the form of the  $\alpha$ -monohydrate, however other sugars such as mannitol, glucose, trehalose and sorbitol have been evaluated and provide a practical alternative (Kou *et al.*, 2012). The influence of the physical characteristics of the lactose carrier upon the aerodynamic particle size distribution and emitted or delivered dose is well recognised, and has been the subject of study for numerous research groups over the past three decades. The characterisation of lactose carrier distributions has usually employed the median particle size and fines content (defined most frequently as the weight percentage of particles with a diameter less than 15  $\mu\text{m}$ ) as descriptors. Manipulation of the fines content has been shown to have a profound effect on the respirable fraction of API able to be obtained from a DPI formulation with a proportional effect between increasing fines content and increasing respirable fraction (Adi *et al.*, 2006, Islam *et al.*, 2004a, Kinnunen *et al.*, 2014, Zeng *et al.*, 2001); however the mechanism behind this effect remains the subject of debate. Two theories have been proposed: the occlusion of active sites on larger carrier particles, and the formation of fine agglomerates of lactose and API particles that enhance the API fine particle mass by providing a structure more amenable to separation than single API particles; it is considered likely that a combination of the two factors will be important in determining



## Introduction

the fraction of API released from the carrier (Jones & Price, 2006). The level of fines necessary to maximise respirable fraction appears to be dependent upon the particular system under study; the physical properties of the API and other formulation ingredients in combination with the device used will influence the optimal fines content.

Consideration of the entire carrier particle size distribution has led a number of authors to evaluate the optimal median carrier particle size. A number of factors other than dispersibility of API from the carrier surface require consideration, such as good powder flow to allow for ease of filling and the ability to retain the dosing characteristics on storage (Guenette *et al.*, 2009), hence the ideal distribution will be defined with respect to the properties of the API and the formulation process. Typically carriers with median particle size in the range 63 to 90  $\mu\text{m}$  have been used for formulation studies employing lactose (Jones & Price, 2006).

Lactose surface properties are an important factor in the generation of the respirable dose, and, whilst a degree of modification is possible by lactose processing, research groups have been exploring the possibility of using small amounts of alternative excipients to change the adhesional contact. Two approaches are possible: the use of alternative fine particles to replace or supplant the lactose fines within the formulation (Louey & Stewart, 2002, Tee *et al.*, 2000), or the coating of the carrier or API with a ternary excipient to modify the surface properties (Begat *et al.*, 2009, Stank & Steckel, 2013). Large differences in emitted dose (the dose or fraction of dose released during actuation) and respirable fraction (the proportion of the dose considered efficacious, generally considered to be fraction with an aerodynamic diameter (Equation 1.34) less

## Introduction

than 5  $\mu\text{m}$ ) are able to be obtained by these approaches, however additional excipients and processing steps are required increasing the complexity of manufacture.

The mixing process employed to produce the formulation can have a profound influence upon the behaviour of dry powder formulations. Two approaches to the formation of adhesive mixtures are in general use – the use of tumbling blenders or the use of an impeller blade to aerate the blend and induce roping flow (Litster *et al.*, 2002), often referred to as low and high shear blending respectively. The comparatively low energy input when using tumbling blending can lead to extended mixing times being necessary to achieve suitable blend homogeneity (Zeng *et al.*, 2000), whilst increasing the processing time for high shear blending can suppress the available lactose fines (Bridson *et al.*, 2007) and increase the adhesion force between API and carrier particles (De Boer *et al.*, 2012).

The physical properties of the API within an inhaled formulation are probably the key determinants of the delivered dose. The aerodynamic diameter (Telko & Hickey, 2005) of the liberated API particles is the primary property in deposition within the respiratory tract (Biddiscombe *et al.*, 2006), defined in Equation 1.34:

$$D_{ae} = D_{eq} \sqrt{\frac{\rho_p}{\rho_0 \chi}} \quad \text{Equation 1.34}$$

where  $\rho_p$  and  $\rho_0$  are the particle and unit densities respectively ( $\text{kg m}^{-3}$ ), and  $\chi$  is the dynamic shape factor determined experimentally to account for deviations from sphericity. Particle density therefore has a profound influence upon the site of deposition in the respiratory tract, and as modification of the particle density will change

## Introduction

the geometric size for a given aerodynamic size, can change the balance of adhesion and drag forces. Single compound crystalline particles offer little opportunity for density modification given the repeating molecular motif. Amorphous or partially amorphous particles however, particularly those with multiple components, offer the opportunity for density reduction by the incorporation of voids or production of hollow particles. Porous Pulmosphere™ particles, produced using the endogenous lung surfactant DSPC (distearoylphosphatidylcholine) are reported to offer a number of related formulation approaches, acting either as a carrier for crystalline API or as with the API dissolved within the DSPC matrix. Lung doses of up to 60 percent of label claim have been reported, compared to less than 20 percent for conventional API-carrier blends, with reduced dose variability (Weers & Tarara, 2014). Hollow particles, usually produced by spray drying, have been used to increase the respirable fraction. Bosquillon and co-workers (2001) described increases by using a combination of lactose, DPPC (dipalmitoylphosphatidylcholine) and albumin, compared to similar formulation using trehalose or mannitol in place of lactose, and highlighted the inclusion of albumin as having a large influence upon both particle morphology and fine particle fraction. The same research group used similar formulations to deliver human growth hormone to male Wistar rats, demonstrating superior delivery compared to instillation of solution, with a threefold increase in adsorption. The use of DPPC as an excipient, primarily to promote formation of low density particles using an endogenous lung material, had the additional benefit of acting as a permeation enhancer. In a study delivering human parathyroid hormone (PTH) to Wistar rats using a DPPC-based formulation (Codrons *et al.*, 2003) high respirable fractions (c. 60 %) and emitted doses (c. 90 %) were observed from a Spinhaler for the low density particles generated by spray drying. Two

## Introduction

formulations were then reported to show improved adsorption over subcutaneous injection, and the inclusion of albumin within the formulation allowed a similar in-vivo effect with a ten-fold reduction in dose.

The geometric size of aerosol droplets and particles has been demonstrated to directly affect the site of deposition in the lung. A review conducted by Stahlhofen *et al* (1989) describes the effect of particle size upon the deposition of radiolabelled particles of differing size in the lung in the context of inspiratory flow rate and in consideration of the rate of clearance, suggesting that an aerodynamic diameter of 6  $\mu\text{m}$  gives highest deposition for the combination of impaction, sedimentation and diffusion mechanisms (Stahlhofen *et al.*, 1989). Studies using salbutamol sulphate solution droplets demonstrated an increased improvement in patient FEV<sub>1</sub> (forced exhalatory volume in 1 second) for droplets with an aerodynamic particle size of 6  $\mu\text{m}$  compared to 3 and 1  $\mu\text{m}$  comparators (Usmani *et al.*, 2005), despite greater lung deposition for smaller particle sizes. The evaluation of 1.5, 2.8 and 5  $\mu\text{m}$  droplets of ipratropium bromide revealed that 5  $\mu\text{m}$  particles were less efficacious (Zanen *et al.*, 1995). Narrow distributions of solid API particles have also been reported to improve the delivery characteristics of DPI devices. Radiolabelled mannitol delivered from an Aerolizer device of mean particle sizes 2.7, 3.6 and 5.4  $\mu\text{m}$  showed a doubling of lung dose upon size reduction from 5.4 to 3.6  $\mu\text{m}$ , however little further difference in effect upon reduction in size to 2.7  $\mu\text{m}$  (Glover *et al.*, 2008). The particles were not monodisperse however (GSD of 2.6, 2.4 and 2.7  $\mu\text{m}$  with increasing average size) so the distribution width may be partially responsible for the lack of change. Spray dried mannitol (Chew & Chan, 1999) and disodium cromoglycate (Chew *et al.*, 2000) were used to understand the effect of

increasing flow rate upon respirable fraction of different size fractions from two inhaled devices. An interaction between flow rate, device and API size was noted however a clear trend of increased respirable fraction with reducing particle size was observed.

### **1.4.2. Delivery system**

The interaction between the delivery system and formulation is of paramount importance in determining the proportion of the API within the formulation that is able to be delivered to the lung. Separation of the API particles from the carrier is dependent upon the turbulence generated within the inhaler at the point of dose emission (Clark & Hollingworth, 1993) characterised by the device resistance, which can be assessed by measurement of the pressure difference necessary to maintain a specific air flow through the device. The detail design of the DPI being used will dictate the resistance generated at a particular flow rate (Srichana *et al.*, 1998), hence use of a standardised pressure difference rather than flow rate has been proposed as a more rigorous basis for device comparability (Steckel & Muller, 1997).

The airstream passing through the DPI first entrains the powder, the mechanism being dependent upon the configuration of the primary dose container (Dunbar *et al.*, 1998). In the case of static dosing systems, such as blisters and reservoir devices, shear fluidization is understood to be the dominant mechanism, whilst mechanical effects are the major contributor in DPIs utilising spinning or vibrating capsules. Shear fluidization can occur under either laminar or turbulent regimes, dependent upon the air velocity and geometry of the inhaler. In the case of turbulent shear, the energy for entrainment is provided by turbulent eddies generated within the airstream penetrating the boundary layer above the powder surface. The lift force provided by turbulent eddies has been

## Introduction

estimated using the relationships presented as Equation 1.35, Equation 1.36 and Equation 1.37 (Finlay, 2001):

$$F_L = 20.9 \rho_{fluid} v^2 \left( \frac{d^+}{2} \right)^{2.31} \quad \text{Equation 1.35}$$

$$d^+ = \frac{u_\tau d}{\nu} \quad \text{Equation 1.36}$$

$$u_\tau = \sqrt{\frac{\tau_w}{\rho_{fluid}}} \quad \text{Equation 1.37}$$

$\tau_w$  is the mean shear stress at the wall ( $\text{kg m}^{-1} \text{s}^{-2}$ ),  $d$  is the particle diameter (m),  $\nu$  is the kinematic viscosity ( $\text{m}^2 \text{s}^{-1}$ ) and  $\rho_{fluid}$  is the gas density ( $\text{kg m}^{-3}$ ). For DPIs  $d^+$  is understood to be below 100, resulting in estimated lift forces between  $10^{-9}$  and  $10^{-6}$  N across the particle diameter range 3 to 60  $\mu\text{m}$ , compared to adhesional forces of  $10^{-12}$  and  $10^{-8}$  N.

Entrainment by shear fluidization in DPIs is believed to be more likely to occur in the laminar regime (Finlay, 2001) as a Reynolds number below  $10^5$  is expected for an airflow path of cross sectional area larger than 6  $\text{mm}^2$ . The lack of turbulent eddies to provide the kinetic energy necessary for fluidization indicates reliance on alternative mechanism being responsible, with saltation being unlikely due to the short path length for impact-driven entrainment.

The lift force provided by a passing laminar airstream is a result of the fluid viscosity, causing asymmetry in airflow at the leading and trailing edges of particles. The lift force can be estimated by Equation 1.38

$$F_L = C_L \frac{1}{2} \rho_{fluid} A_F v^2 \quad \text{Equation 1.38}$$

with the coefficient of lift,  $C_L$ , able to be expressed as functions of the particle Reynolds number,  $Re_p$ , and the ratio of the particle diameter to the boundary layer thickness,  $\frac{d}{\delta_{99}}$ ;  $A_F$  ( $m^2$ ) and  $v$  ( $ms^{-1}$ ) are the face area presented by the particle to the airstream and the airstream velocity respectively. In the case of  $Re_p \ll 1$  and  $\frac{d}{\delta_{99}} \ll 1$ ,  $C_L$  is estimated as 5.87 (King & Leighton, 1997). Some doubt exists whether the inequalities stated are satisfied for DPIs operating at patient relevant flow rates, and alternative values for  $C_L$  below 0.4 have been suggested. The lift force has been demonstrated to dominate the adhesion force and particle weight for carrier particles, however is considered insufficient to cause direct entrainment of inhalable particles (Finlay, 2001).

Following entrainment, the dry powder inhaler influences the deaggregation of powder agglomerates via three mechanisms:

1. Impaction upon the inner surfaces of the inhaler
2. Particle separation by the direct effect of aerodynamic forces
3. Differential acceleration experienced by primary particles within the agglomerate

Most DPIs have features within the device designed to increase the turbulence of the inspired air and to provide a structure to promote deagglomerating impacts, either directly or indirectly. Commonly this is in the form of a grid upstream of the entrainment point of the powder; however the primary mechanism of deagglomeration attributable to such design features may be dependent upon the particular device design. A study conducted by Voss and Finlay concluded that impaction upon the bars of the grid was an

## Introduction

ineffective method of deaggregation using a test rig (Voss & Finlay, 2002), however alternative studies have suggested the presence of the grid promotes impaction upon device surfaces, increasing the respirable fraction (Coates *et al.*, 2004, Suwandecha *et al.*, 2014). The increase in turbulence generated by the grid structure and other air flow path features is accepted as having a beneficial effect upon the reduction of agglomerates. The eddies generated within the DPI result in localised differences in air velocity which can exhibit stresses across agglomerates, the magnitude of which is dependent upon eddy size and energy. Eddy size in such systems is commonly described by categorisation into one of three scales: integral, inertial subrange and Kolmogorov. Integral scale eddies are the largest, containing the majority of the kinetic energy in a turbulent system and probably are the most effective in terms of agglomerate disruption. A measure of the velocity of integral scale eddies can be gained from estimation of the turbulent energy dissipation rate,  $\epsilon$ , with an estimate eddy size using Equation 1.39

$$\epsilon = \frac{u_i^3}{l} \quad \text{Equation 1.39}$$

where  $u_i$  is the integral velocity scale ( $\text{m s}^{-1}$ ) and  $l$  is the eddy length scale (m). Where a grid is used to promote turbulence the relationships presented as Equation 1.40 and Equation 1.41 can be used with  $S$  being values for the spacing between bars of the grid (m),  $u$  is the mean upstream velocity ( $\text{m s}^{-1}$ ),  $x_0$  and  $x$  are the grid and turbulence measurement positions and  $c_1$  and  $n$  are constants for the particular arrangement under study.



## Introduction

$$\frac{u_i}{u} = c_1 \left( \frac{x}{S} - \frac{x_0}{S} \right)^n \quad \text{Equation 1.40}$$

$$\frac{l}{S} = \frac{-\sqrt{c_1}}{2n} \left( \frac{x}{S} - \frac{x_0}{S} \right)^{\frac{n+2}{2}} \quad \text{Equation 1.41}$$

Knowledge of the size and energetics of the integral scale eddies subsequently allows extrapolation of the length  $\eta$  (m), time  $t_K$  (s) and velocities  $v_K$  ( $\text{m s}^{-1}$ ) associated with the Kolmogorov scale by the relationships given as Equation 1.42, Equation 1.43 and Equation 1.44:

$$\frac{\eta}{l} \approx \left( \frac{u_i l}{v} \right)^{-\frac{3}{4}} \quad \text{Equation 1.42}$$

$$\frac{t_K}{t_i} \approx \left( \frac{u_i l}{v} \right)^{-\frac{3}{4}} \quad \text{Equation 1.43}$$

$$\frac{v_K}{u_i} \approx \left( \frac{u_i l}{v} \right)^{-\frac{1}{4}} \quad \text{Equation 1.44}$$

In the range of Reynolds numbers usually associated with DPI systems, the inertial subrange lengths, times and velocities can be considered intermediate between the integral and Kolmogorov scales.

A comparison of forces has been used to estimate the relative contributions of direct aerodynamic forces versus stress imposed on agglomerates by integral scale eddies in the removal of small particles from carriers (Finlay, 2001). Assuming an adhesion force of  $10^{-11}$  N, larger forces for drag ( $10^{-9}$  N) and lift ( $10^{-10}$  N) are likely making these viable mechanisms (along with impaction of inhaler surfaces) for deaggregation; in contrast the forces generated upon agglomerates by the turbulent airstream were calculated as being

of similar magnitude to the adhesion forces therefore suggesting this mechanism plays a minor role in the generation of the respirable fraction.

### **1.4.3. Aerodynamic particle size analysis of inhalation products**

The characterisation of inhaled formulations and devices relies predominantly upon techniques that utilise inertial impaction to separate the emitted/ delivered dose into size fractions, followed by chemical analysis of the deposited mass. Test methodology has typically used cascade impactors originally introduced for the evaluation of airborne dust or contaminant concentrations, however more recently purpose-designed impaction systems for inhaled product testing have become available (Marple *et al.*, 2003). The use of carrier-based formulations in the majority of dry powder formulations, and the dynamic nature of the droplets formed during actuation of metered dose inhalers make the use of laser-based systems difficult, given the inability to distinguish between particles of different compositions. Sophisticated characterisation systems employ laser diffraction in combination with inertial impaction have however been described (Mitchell *et al.*, 2006).

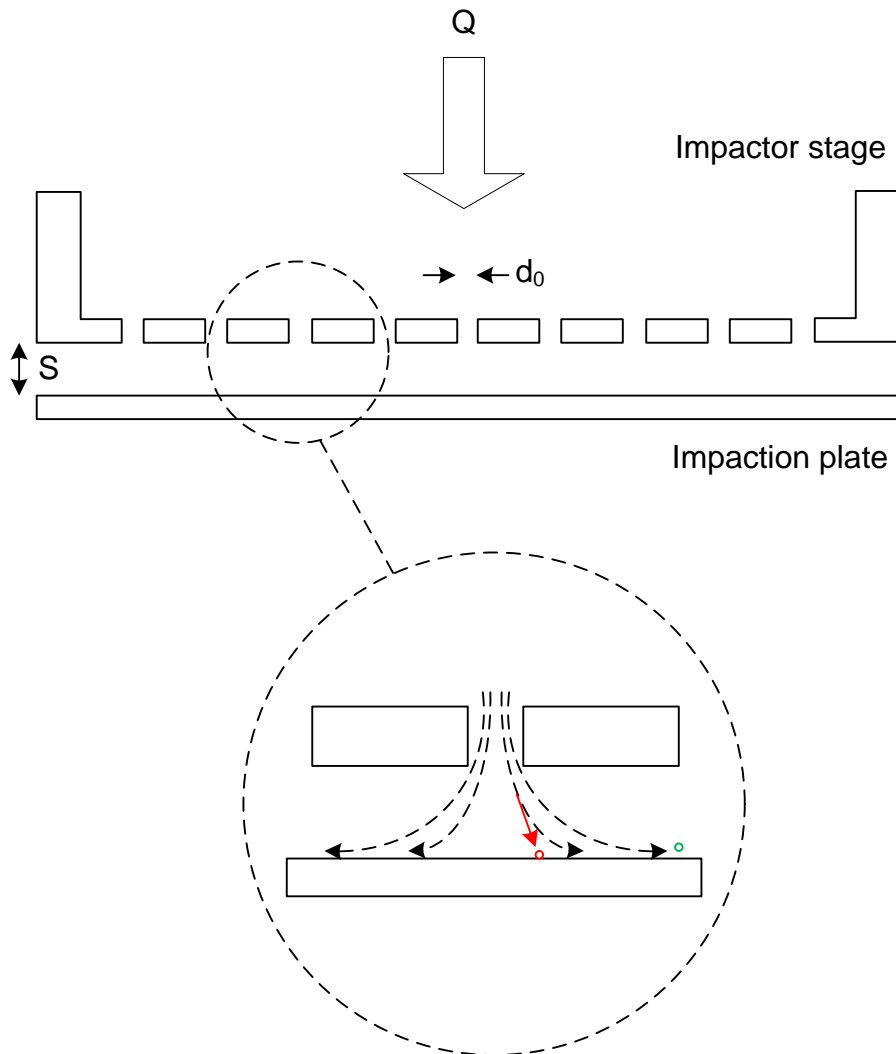
Cascade impaction relies upon inertial forces acting upon particles entrained in the airstream to fractionate the particle size distribution. The flow path of particle-laden gas within the impactor is arranged to cause changes in direction; with particle inertia determining whether the particle remains travelling with the gas stream or deviates on a separate path. A series of flow orifices, also known as nozzles, and adjacent impaction plates are employed to collect sequentially finer fractions of the overall particle distribution from the gas stream. The combination of orifice diameter and number are used to define the gas velocity through the stage, and in conjunction with the orifice

## Introduction

stage to collection plate ratio is used to define the aerodynamic size able to be collected.

A schematic arrangement of a collection stage within a cascade impactor is given as

Figure 1.5; hashed arrows indicate gas flow streamlines and red and green circles depict impacting versus uncollected particles respectively:



**Figure 1.5 Cascade impaction stage and plate arrangement**

Flow conditions within impactors are described with reference to Stokes law. The Stokes number ( $St$ , the ratio of particle stopping distance to a characteristic dimension) at each stage can be calculated using Equation 1.45 (Mitchell & Nagel, 2003)

## Introduction

$$St = \frac{\rho_p C_{pa} D_p^2 U}{9\mu d_0} = \frac{\rho_0 C_{ae} D_{ae}^2 u}{9\mu d_0} \quad \text{Equation 1.45}$$

where  $d_0$  is the average orifice diameter for the particular stage (m),  $D_p$  and  $D_{ae}$  are the particle geometric and aerodynamic diameters (m),  $\rho_p$  and  $\rho_0$  are the particle and reference densities ( $\text{kg m}^{-3}$ ),  $u$  is the average gas velocity through the impactor nozzles ( $\text{m s}^{-1}$ ),  $C_{pa}$  and  $C_{ae}$  are the Cunningham slip factors ( $\approx 1$  for  $d_p > 1 \mu\text{m}$ ) and  $\mu$  is dynamic viscosity of air (Pa s) at the test temperature. The efficiency of collection at the stage is a sigmoidal function of  $St$ ; 50% efficiency is defined as the cut size,  $D_{50}$ , of the stage (also known as the effective cut-off diameter, ECD), and for simplicity all particles larger than  $D_{50}$  are assumed to be collected on the stage with all smaller particles assumed to carry over to the next impaction stage. Considering a volumetric flow  $Q$  ( $\text{m}^3 \text{s}^{-1}$ ) the ECD can be calculated using Equation 1.46, where  $n$  is the number of nozzles present in the impactor stage.

$$D_{50} = \left( \frac{9\pi\mu n d_0^3}{4\rho_0 C_{ae} Q} \right)^{\frac{1}{2}} \cdot \frac{\sqrt{St_{50}}}{\sqrt{C_{50}}} \quad \text{Equation 1.46}$$

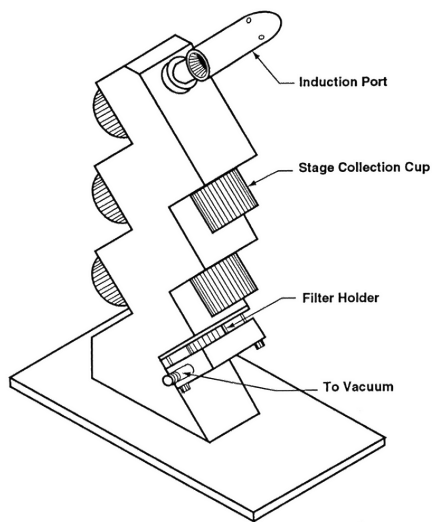
To maximise collection efficiency, the Reynolds number for flow through the nozzle orifice of diameter is maintained between 500 and 3000, hence the combination of  $n$  and  $d_0$  is carefully defined across the stages of the impactor to give the required series of cut points within the aerodynamic distribution. The ratio of nozzle to plate distance,  $S$ , and  $d_0$  should be between one and 10 for good stage efficiency, and an optimum value of 0.495 has been suggested for  $\sqrt{St_{50}}$  (Marple *et al.*, 2003).

The cascade impactors commonly used for characterisation are described in the US and European Pharmacopeia, for example the Multi-Stage Liquid Impinger (Apparatus C

## Introduction

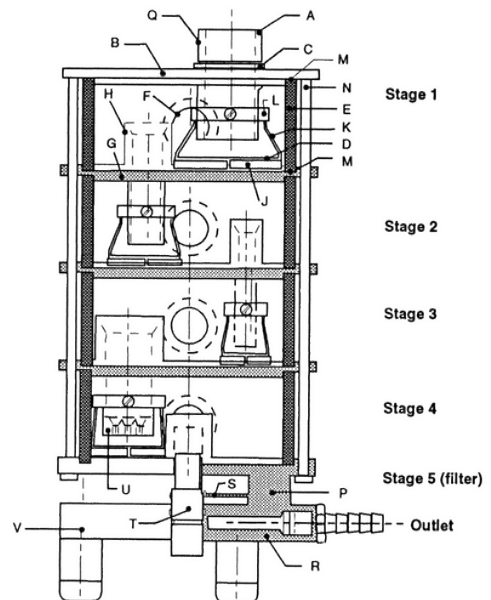
(USP) and Apparatus 4 (Ph Eur)), Anderson Cascade Impactor (Apparatus D and Apparatus 1, 3) and the Marple Miller (Apparatus 2, Ph. Eur only). The most recently developed impactor, the Next Generation Impactor (Apparatus E and Apparatus 5, 6), has been designed for ease of analytical work-up and incorporation into automated systems. Example schematics of the impactors are presented as Figure 1.6 (United States Pharmacopeia Convention, 2014).

Marple-Miller



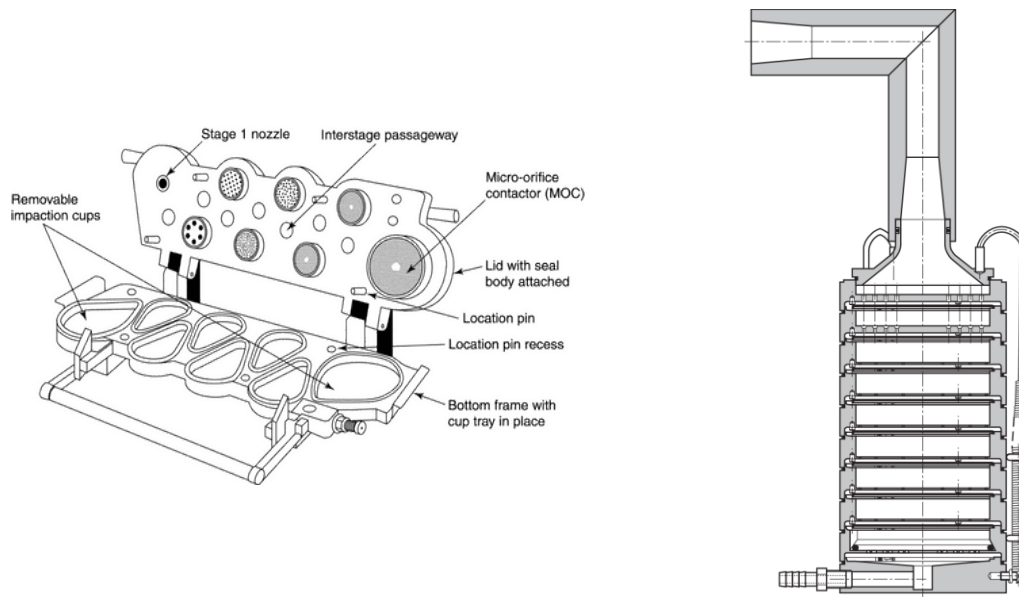
Next Generation Impactor

Multi-Stage Liquid Impinger



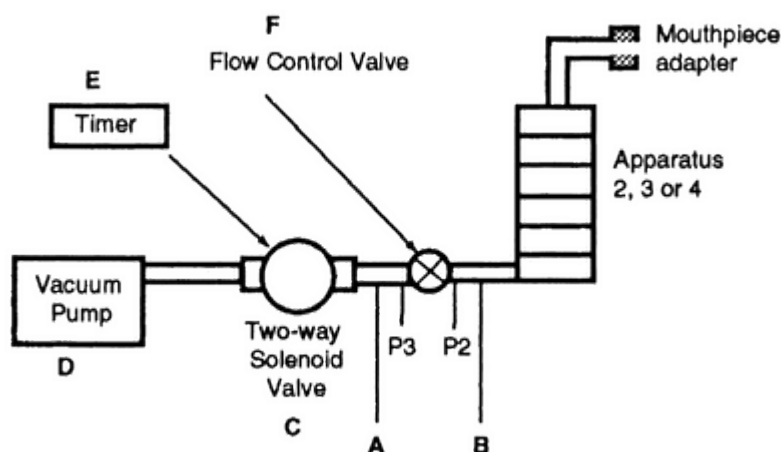
Anderson Cascade Impactor

## Introduction



**Figure 1.6 Cascade impactors**

The impaction systems configuration used depends upon the information required. Simple vacuum pumps capable of generating a sufficiently large peak flow rate are typically used to distinguish between devices or different formulations, and are the mainstay of analysis for the release of commercial or clinical products for human use. The pump is usually used in conjunction with a timed switching valve, so a particular flow volume can be routed through the inhaler at peak flow. An example of an equipment configuration for this purpose is presented as Figure 1.7 (United States Pharmacopeia Convention, 2014).

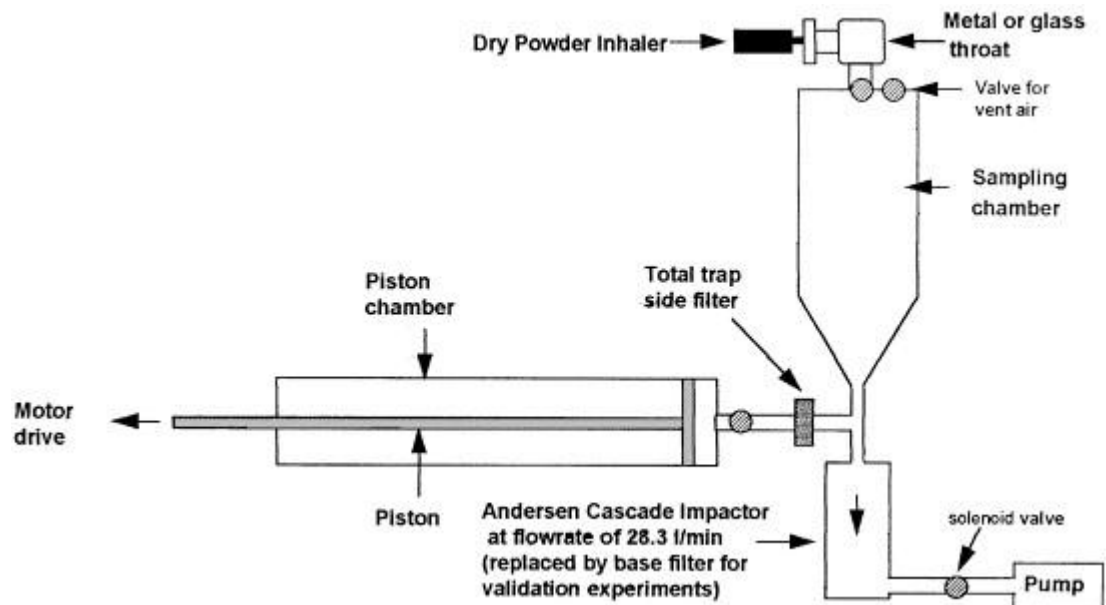


**Figure 1.7 Cascade impactor configuration**

Stable flow conditions within the impactor are achieved using a flow control valve to regulate the pressure ratio  $P3/P2$ . A pressure ratio of 0.5 or lower ensures critical flow through the impactor, reducing the impact of flow fluctuations caused by variation in pumping rate (Mohammed *et al.*, 2012).

Coupling the cascade impactor to a more complex actuation system offers the potential to increase the patient-relevance of the information obtained. The Electronic Lung (Burnell *et al.*, 1998), as shown in Figure 1.8, uses a computer-controlled servo motor to move a piston in response to an inhalation profile previously recorded for a patient. The dose is therefore entrained from the device using a realistic flow profile into the sampling chamber; valves then allow the inhaler to be isolated from the chamber. The aerosolised dose is subsequently drawn through the cascade impactor using the standard 'square wave' flow profile at the required test flow rate to allow fractionation of the dose via impaction and derive the aerodynamic particle size distribution of API.

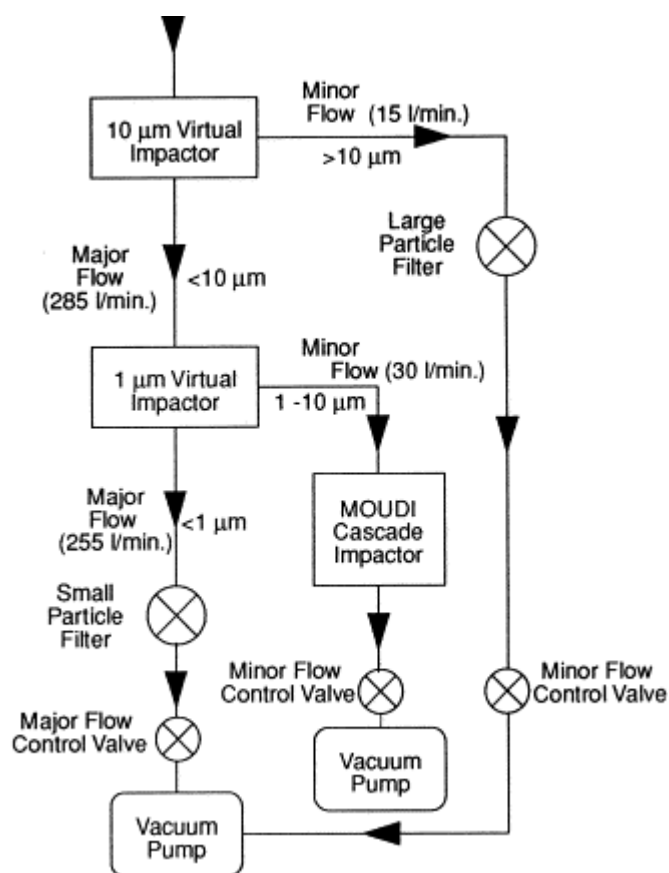
## Introduction



**Figure 1.8** The Electronic Lung

An alternative to the Electronic Lung system was proposed in the form of a combined cascade and virtual impactor combination (CAVIC). This device, which incorporates an anatomical throat profile to mimic the human oropharyngeal cavity, uses a similar breathing simulator to the electronic lung but pushes, rather than draws the airflow through the inhaler and combines this with an additional, larger airstream to remove the need for a separate holding chamber (Finlay & Gehmlich, 2000). Two 'virtual' impactors are used to reduce the particle size distribution range to 1 to 10  $\mu\text{m}$ , and to reduce the flow through the cascade impactor to 30  $\text{L min}^{-1}$  to allow impaction and sizing of particles in the respirable range. A schematic diagram of the CAVIC system is presented as Figure 1.9.





**Figure 1.9 Cascade and Virtual Impactor Combination (CAVIC)**

The complex systems illustrated with the two examples above are typically employed to understand the result of device modification, such as a change in specific resistance upon the likely deposition in patients. Assessment of the effect of particle manipulation is typically performed using the simpler pharmacopeial systems presented at the beginning of this section (Donovan & Smyth, 2010, Young *et al.*, 2011, Zeng, Martin, Marriott, & Pritchard, 2001), hence a Next Generation Impactor configured according to Figure 1.7 has been used to evaluate the API particles generated during the studies presented in this thesis.

## **2. EQUIPMENT AND MATERIALS**

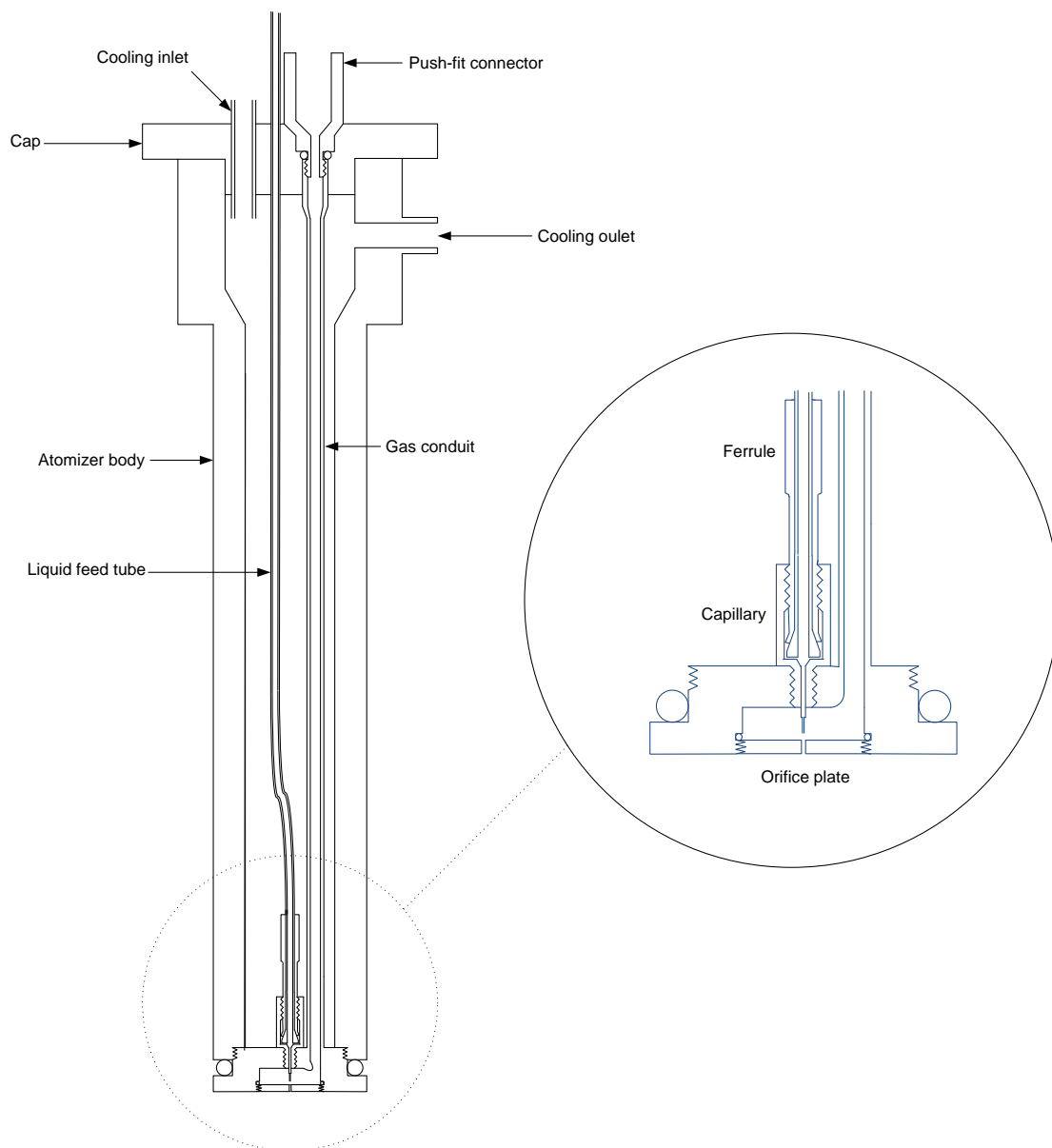
### **2.1. Equipment**

#### **2.1.1. Atomizing system**

Atomization by flow-focusing was performed using an FFDryer atomizer (Ingeniaticas Tecnologias, Seville, Spain). The atomizer is designed to fit into the atomizer port of a Buchi B-290 spray dryer and provides separate conduits for the focused liquid and focusing gas. The body and cap of the atomizer have 6 mm push-fit connectors fitted to allow connection to a liquid temperature-regulating circuit using pneumatic tubing. The liquid feed conduit consists of a 1.6 mm feed tube connected to stainless steel capillary of internal diameter 150  $\mu\text{m}$ . The capillary is mounted into a chamber at the end of the atomizer body also housing the atomizing gas conduit. The chamber is closed by a plate containing a 150  $\mu\text{m}$  orifice and sealed by a thread to compress an o-ring to give a gas tight seal. Marks on the atomizer chamber external surface and orifice plate are aligned to give the required distance of 100  $\mu\text{m}$  between the capillary tip and inner surface of the orifice plate. Gas is supplied to the atomizer via a 6 mm push-fit pneumatic connector attached to the entrance of the gas conduit. The atomizing gas supply is regulated using a needle valve (SS-4MG-MH, Swagelok, King's Langley, U.K.) and digital manometer (LEO1, Keller-Druch, Winterthur, Switzerland). The liquid for atomization is supplied by a Syringe pump (Isco 260D, Teledyne Isco, Lincoln, U.S.A.) in order to give consistent flow across the range of flow rates evaluated. The integrated PLC system of the Isco pump was used to regulate the liquid flow rates during the droplet size distribution and spray drying experiments. Liquid is drawn into the pump via a non-return valve connected to the pump piston by 3.2 mm outside diameter stainless steel

## Equipment and Materials

tubing, and discharged through 1.6 mm outside diameter stainless steel tubing connected to the FFD atomizer liquid conduit. A diagram of the FFD atomizer is presented as Figure 2.1.



**Figure 2.1** FFD atomizer

## Equipment and Materials

A liquid-jacketing system connected to a recirculating bath (LTD 6, Grant Instruments, Cambridge, U.K.) was used to regulate the temperature of the liquid within the atomizing system. A circuit was assembled using the integral jacket surrounding the pump piston, the atomizer body, and a coaxial jacket around the stainless-steel liquid feed tubing constructed using 8 mm pneumatic tubing. A thermocouple was inserted into the cooling circuit at the atomizer cooling outlet port and connected to data logger (5100e, Eurotherm Ltd, Worthing, U.K.) to allow the temperature within the atomizer to be monitored. The set-point of the recirculating bath was adjusted manually during experiments in order to obtain the desired atomizer temperature.

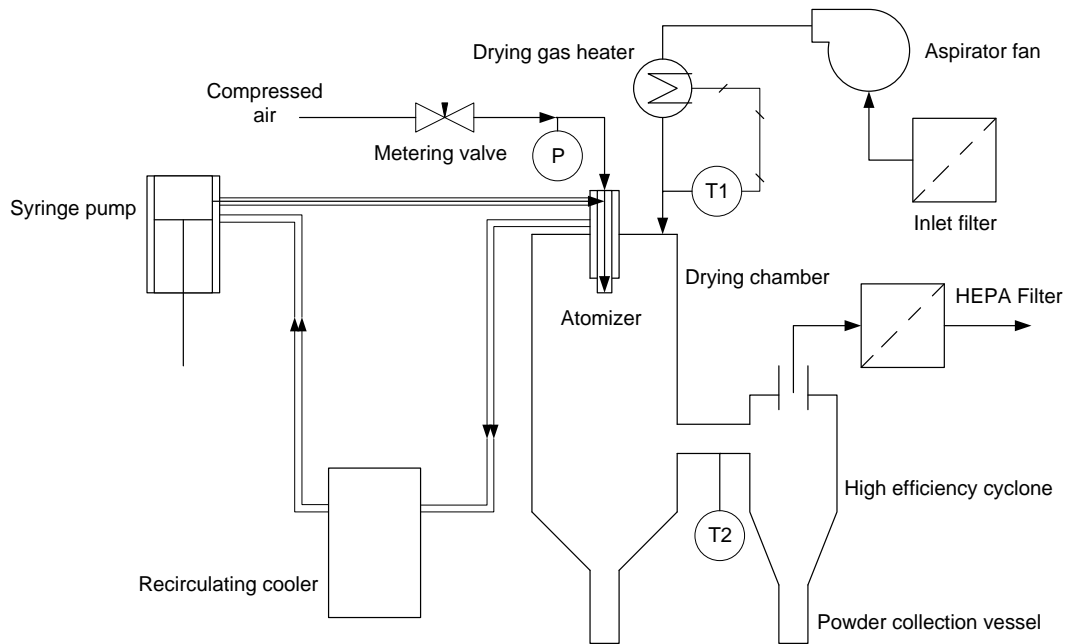
### **2.1.2. Spray dryer**

A B-290 spray dryer (Buchi Labortechnik, Flawil, Switzerland) was used to dry solution droplets produced by the FFDryer atomizer and collect the resulting solute particles. Buchi spray dryers have been extensively used in research, particularly for the evaluation of organic compounds. Langrish and co-workers have used the B-290 extensively in the study of sugars during spray drying. The B-290 was used to compare models describing the impact of process parameters on the crystallization kinetics of spray dried lactose solutions, identifying inlet air temperature as the dominant parameter (Chiou & Langrish, 2008). Langrish also describes a similar impact of inlet air temperature upon crystallinity for lactose and sodium chloride, demonstrating that the effects of processing parameters upon crystallinity are not limited to organic molecules (Langrish, 2009). The B-290 was used to provide amorphous lactose particles which were subsequently used in the validation of rate of change models to describe the transition from the amorphous to crystalline state (Das & Langrish, 2012). The B-290 has also been used with APIs;

## Equipment and Materials

amorphous salbutamol sulphate particles were produced for use in recrystallization studies (Grisedale *et al.*, 2011), and the successful production of composite particles of budesonide and formotorol fumarate using the B-290 has been demonstrated (Tajber *et al.*, 2009).

The spray dryer used within this work was fitted with a high efficiency cyclone (Buchi, Flawil, Switzerland) to maximise the collection of small particles. The spray dryer was used in open-cycle 'blowing' mode given the negligible risk of over-pressurising the spray dryer by blinding the outlet HEPA filter. Air was used as the atomizing and drying gas throughout the spray drying experiments. A diagram of the spray dryer configuration is presented as Figure 2.2.



**Figure 2.2** Spray drying configuration

## 2.2. Materials

### 2.2.1. Solute properties

Fluticasone propionate and mometasone furoate are corticosteroid molecules commonly used for the treatment of lung diseases, notably asthma and chronic obstructive pulmonary disease (COPD), and are structurally similar as a consequence of both being derivatives of cortisol. Corticosteroids induce relaxation of the smooth muscle that forms part of the airway structure when delivered topically (the molecules exhibit low oral bioavailability) and are commonly dosed to patients using DPIs and pMDIs (Patton & Byron, 2007).

The molecules share the androstane 3-ring structure common to all steroid molecules, however substituent groups differ, most notably at in the ester groups at C-17 but also with respect to the halogen at C-9 and the lack of a halogen atom at C-6 for mometasone furoate (Crim *et al.*, 2001). The structures of fluticasone propionate and mometasone furoate are presented as Figure 2.3.

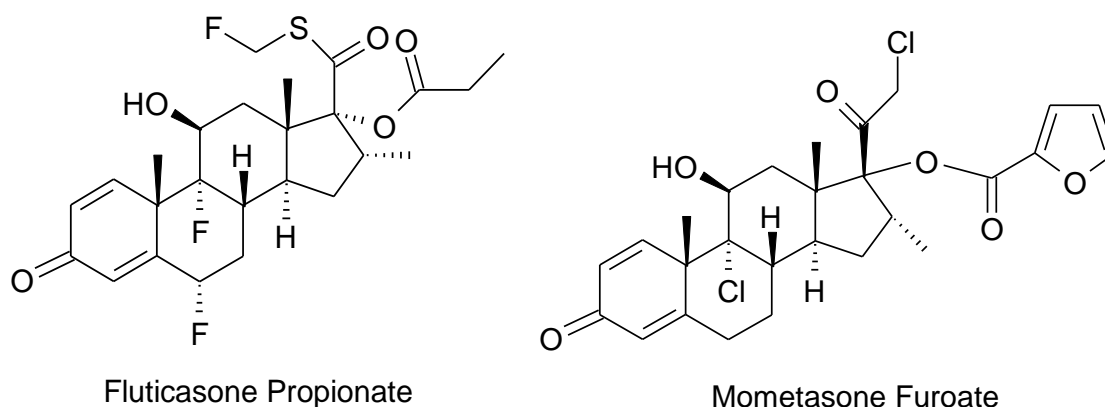


Figure 2.3 Molecular structures of fluticasone propionate and mometasone furoate

## Equipment and Materials

The structural difference between the molecules translates to differences in the solid state. Two crystalline forms of mometasone furoate are known; a stable anhydrous form designated form 1 and a monohydrate form produced in the presence of sufficient water during nucleation. The monohydrate is able to be converted to a second anhydrous form, designated form 2, at temperatures above 130°C. Form 2 readily reconverts to a monohydrate form at room temperature with sufficient humidity and shows similar crystal packing to the monohydrate. Form 1 appears to be stable as an anhydrate; no presence of a hydrated form was detected following storage at 97 %RH for 3 months. The monohydrate is suspected to be the stable form at low temperature with sufficient humidity; however the distinctly different molecular packing of the two forms presents a significant energy barrier to conversion between forms (Chen *et al.*, 2005).

Two forms of fluticasone propionate are known to exist, both of which are non-solvated. Form 2 has only been produced at elevated pressures using supercritical fluid crystallization and has been seen to be metastable at room temperature, converting to form 1 in the order of 6 months (Su *et al.*, 2011). Thermal analysis of form 1 shows no events until the melt decomposition commencing at 280°C; an exothermic event was observed at 150°C to 180°C for form 2 attributed to conversion to form 1. The exothermic transition was observed to be irreversible during cooling and reheating, typical of a monotropic relationship between forms (Cooper, 2003).

### **2.2.2. Solvent and solution properties**

The physical properties of the liquid being focused by the FFDryer atomizer will have a significant influence on the size and polydispersity of the droplets generated. The density of the focused fluid, in combination with the focusing gas pressure drop, is

## Equipment and Materials

paramount in determining the liquid jet diameter at the point of break up. The liquid density, in conjunction with the liquid surface tension and focusing gas pressure drop defines the balance of inertial and capillary forces that characterise the mode of break-up, as denoted by the Weber number (Ganan-Calvo & Riesco-Chueca, 2006). The density and surface tension must therefore be known to an appropriate degree of precision in order to accurately predict the size of droplets produced. The identification of a value for surface tension can be additionally complicated in the case of solutions containing a surface-active solute. Under these circumstances the value derived for surface tension becomes dependent upon the rate at which the surface under measurement is produced, as a consequence of differing solvent and solute diffusivity (Eastoe & Dalton, 2000). The surface tension value employed to characterise such solutions undergoing dynamic processing will therefore need to reflect the timescale of the unit operation in order to reflect the apparent value.

The characteristics of the solid particles resulting from drying of solution droplets produced by the atomizer are a function of the saturation, solute diffusivity and drying rate, as described in Section 1.2.2 of the Introduction. Estimation of the saturation level during drying requires knowledge of the solubility of the solute at temperatures relevant to the drying process, particularly the saturation concentration. Studies were therefore undertaken to understand the solubility and surface tension of mometasone furoate and fluticasone propionate in ethanol and 2-propanol. The solubility studies demonstrated that only low concentrations of solute are possible for the solutes and solvents used, as is often the case for relatively large, non-polar organic molecules dissolved in organic solvents. The density of such systems is suitably similar to that of the solvent that the



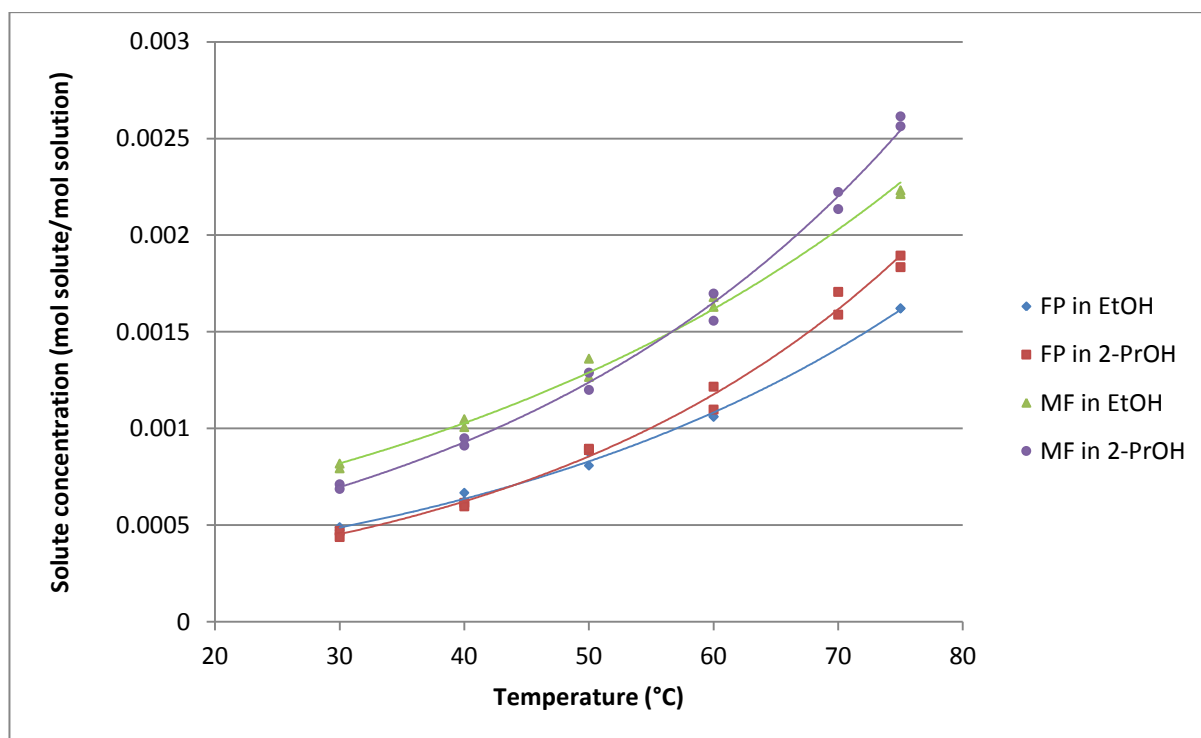
solvent density provides a suitably accurate approximation of the solution density. The solution density was therefore represented by literature values for the relevant solvent (Haynes, 2012) at the temperature of interest.

### **2.2.2.1. Solubility**

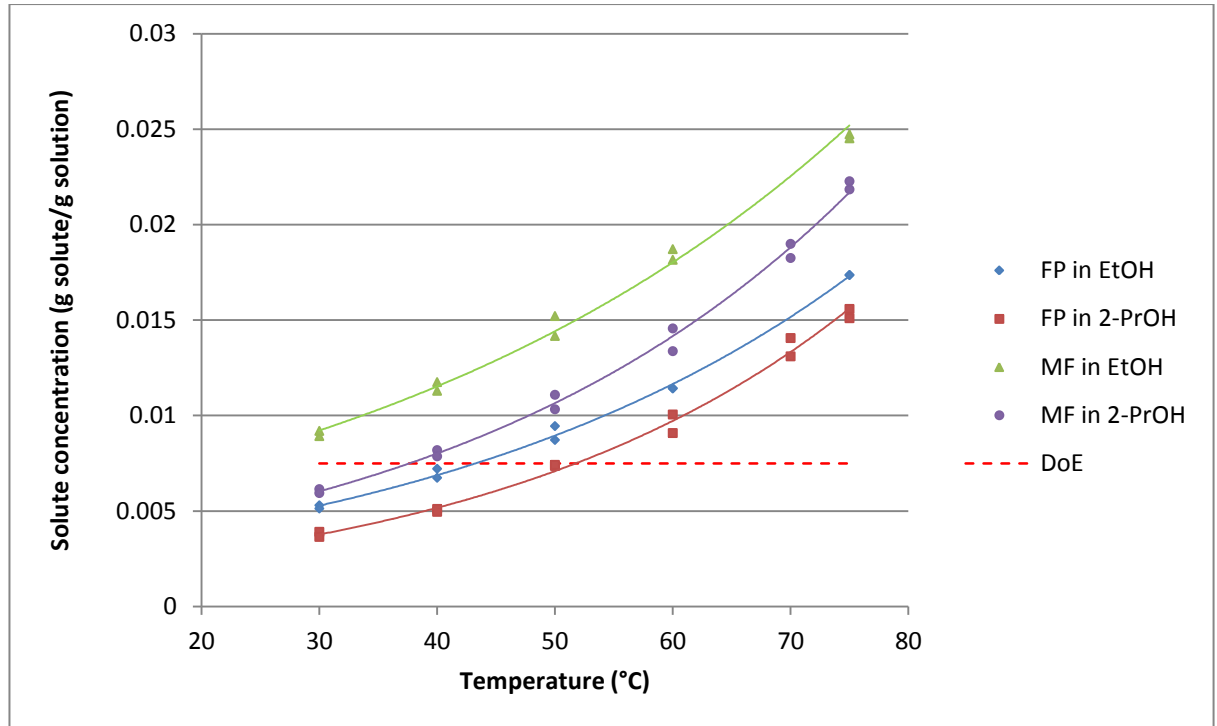
Equilibrium solubility was determined between 30°C and 75°C by the evaluation of filtered solution aliquots taken from saturated solutions containing an excess of solute (Mullin, 2001). Two 50 mL vials containing 2 g of API and 20 g of solvent were prepared for each solute-solvent combination and placed in a Reaction Station (Stem RS1000, Electrothermal, Rochford, UK). A magnetic stirrer bar was placed in each vial and the contents agitated at the required temperature for 48 hours in order to form saturated solutions. 10 ml plastic syringes (BD Plastipak, Becton Dickinson, Madrid, Spain) fitted with 0.2 µm syringe filters (Millex GV, Millipore, Co. Cork, Ireland) were sealed inside a plastic bag and immersed in a thermostatically controlled bath (LTD 6, Grant Instruments, Cambridge, U.K.). The bath was set to the same temperature set-point as the Reaction station and the syringes were left to equilibrate for at least 2 hours to attain a temperature equivalent to the solution samples. Once the required time period had elapsed a syringe and filter were removed from the bag and the solution vial opened. Approximately 2 mL of solution was withdrawn from the vial into the syringe, the filter was then removed and the sample was discharged to waste. The filter was then replaced onto the syringe and a further approximate 2 mL of solution was withdrawn. The filter was removed and the sample was discharged into a preweighed vial, then sealed with a lid and the vial and contents were weighed so the mass of solution could be determined. A second syringe and filter combination were then selected and the

## Equipment and Materials

sampling process described above was repeated for the second saturated solution vial to give a second solution sample. The lids were removed and the open vials were placed in a vacuum oven at 40°C for 24 hours to remove the solvent; at the end of the drying period the vials were weighed to allow the mass of dry solute to be calculated. Solution sample concentrations were then calculated and are presented on both a molar and mass basis as Figure 2.4 and Figure 2.5. (Note: the final set of sample concentrations was evaluated at 70°C; insufficient sample remained to allow results for the two APIs in ethanol to be generated).



**Figure 2.4** Equilibrium molar solubilities of the API-solvent combinations



**Figure 2.5** Equilibrium mass-fraction solubilities of the API-solvent combinations

A clear difference in the solubilities of the two APIs is evident with higher equilibrium concentrations being achieved for mometasone furoate than for fluticasone propionate for both solvents used.

A range of solution concentrations are required during the spray drying experimental design study to evaluate the effect of this parameter upon the physical properties of the dried particles produced. A maximum solute concentration of 0.0075 was required to complete the spray drying experimental design study described in Section 4.3; hence with reference to Figure 2.5 (required concentration signified by dotted line marked as 'DoE') the temperature of the API solutions for spray drying will need to be maintained above 50°C to avoid possible precipitation of solute before atomization.

### 2.2.2.2. Surface tension measurement

Surface tension data for mometasone furoate and fluticasone propionate in ethanol and 2-propanol have been generated to aid understanding of the droplet generation and drying processes. Measurements were performed using a T60 bubble pressure tensiometer (Sita Messtechnik GmbH, Dresden, Germany). Maximum bubble pressure tensiometry is often used to provide information when liquids are to be used in processes with short characteristic timescales, where liquid surface is created at rapid rate (Beckett, 1996). The technique is most beneficial when studying the behaviour of surfactant systems, where the speed at which surfactant molecules are able to migrate to an expanding interface will have an impact upon the surface tension (Miller *et al.*, 1994). Maximum bubble pressure tensiometers utilise the relationship between the interfacial tension / surface energy of an expanding bubble and the pressure required to cause the expansion. The maximum pressure will be attained where the bubble radius equals the radius of the capillary used to generate the bubble; the dynamic surface tension can then be calculated via a modified Young- Laplace equation shown as Equation 2.1:

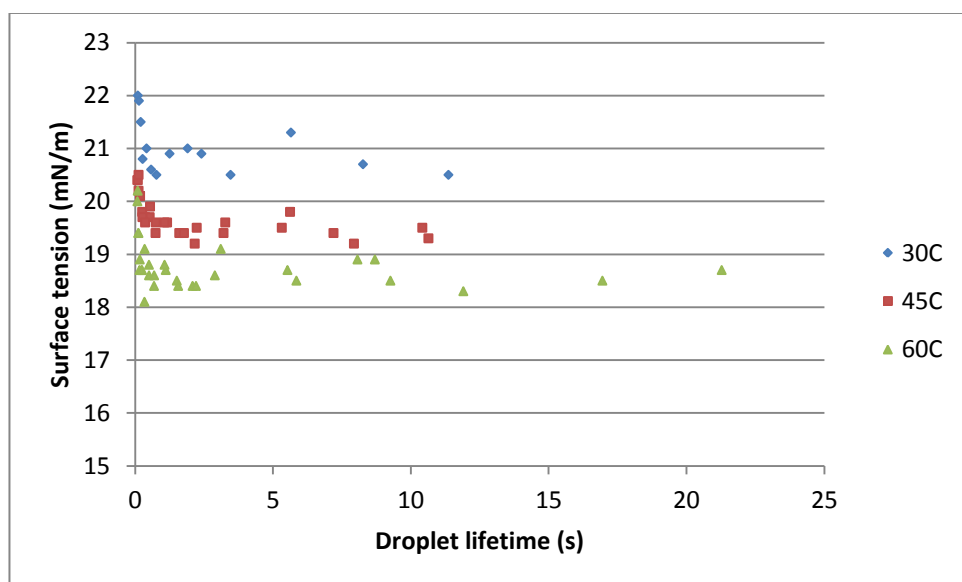
$$P = \frac{2\sigma}{r} + \rho gh + \Delta p \quad \text{Equation 2.1}$$

Where  $P$  is pressure within the bubble ( $\text{N m}^{-2}$ ),  $r$  is the bubble radius (m),  $\rho$  is the liquid density ( $\text{kg m}^{-3}$ ),  $\sigma$  is the dynamic surface tension ( $\text{N m}^{-1}$ ),  $h$  is the immersion depth of capillary in liquid (m) and  $\Delta p$  (Pa) is a correction term for hydrodynamic effects.

## Equipment and Materials

The characteristic timescale for maximum bubble pressure tensiometry is considered to be the lifetime of the bubble, corresponding to the time required for the bubble to reach maximum pressure from the commencement of expansion (Fainerman *et al.*, 1994).

Measurement of surface tension was performed in duplicate for each solution system at temperatures of 30°C, 45°C and 60°C. A solute concentration of 0.5 %w/w was used for each solute-solvent system. A range of bubble lifetimes from approximately 0.1 to 10 s were evaluated. Solutions were contained in clean 20 mm diameter glass tubes and the temperature was regulated using a Stem RS1000 Reaction Station (Electrothermal, Rochford, UK). Figure 2.6 to Figure 2.9 show a decrease in surface tension with temperature for the four solution systems; in addition a decrease in measured surface tension with lifetime is apparent between the minimum lifetime value evaluated and a lifetime of approximately 1 second.



**Figure 2.6** Effect of droplet lifetime upon the surface tension of Fluticasone Propionate in ethanol

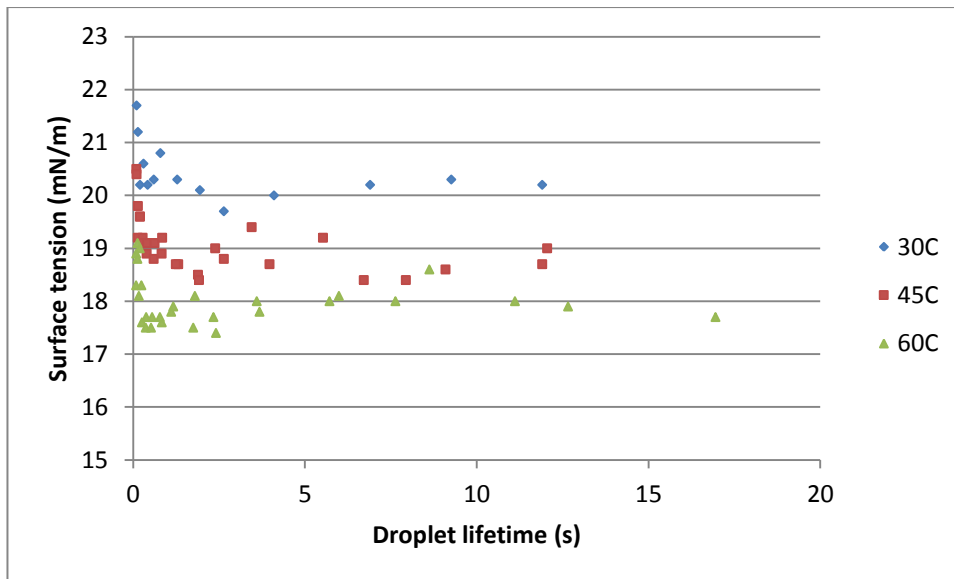


Figure 2.7 Effect of droplet lifetime upon the surface tension of Fluticasone Propionate in 2-propanol

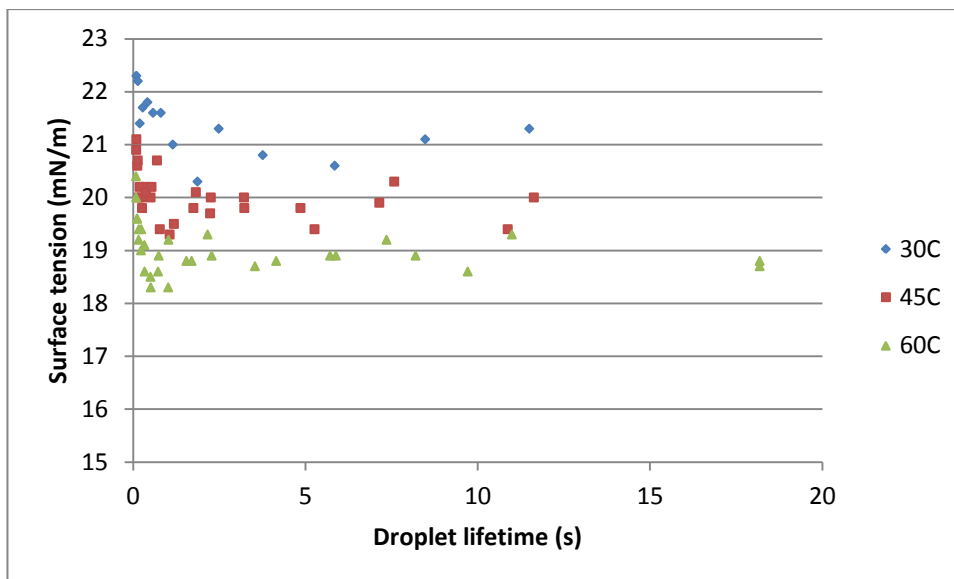
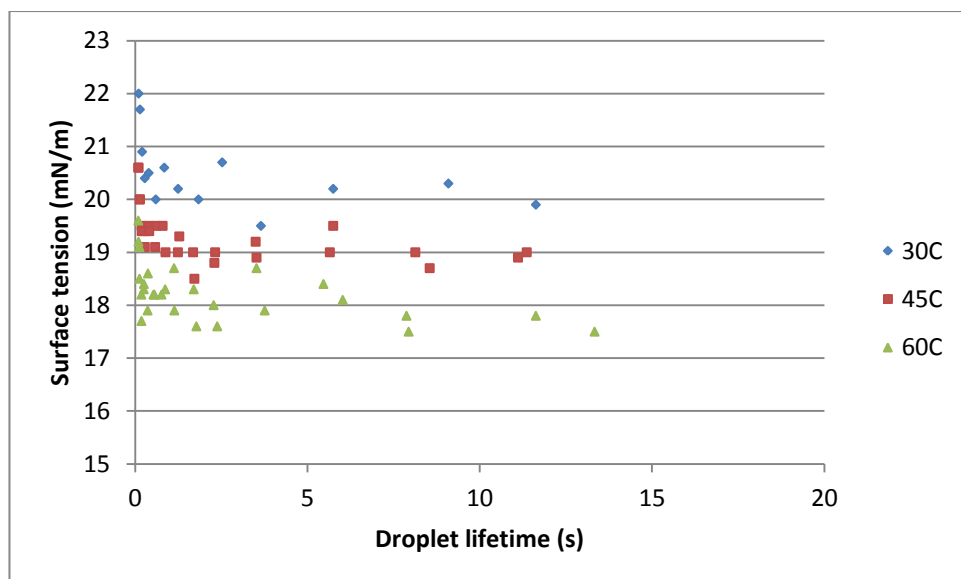


Figure 2.8 Effect of droplet lifetime upon the surface tension of Mometasone Furoate in ethanol



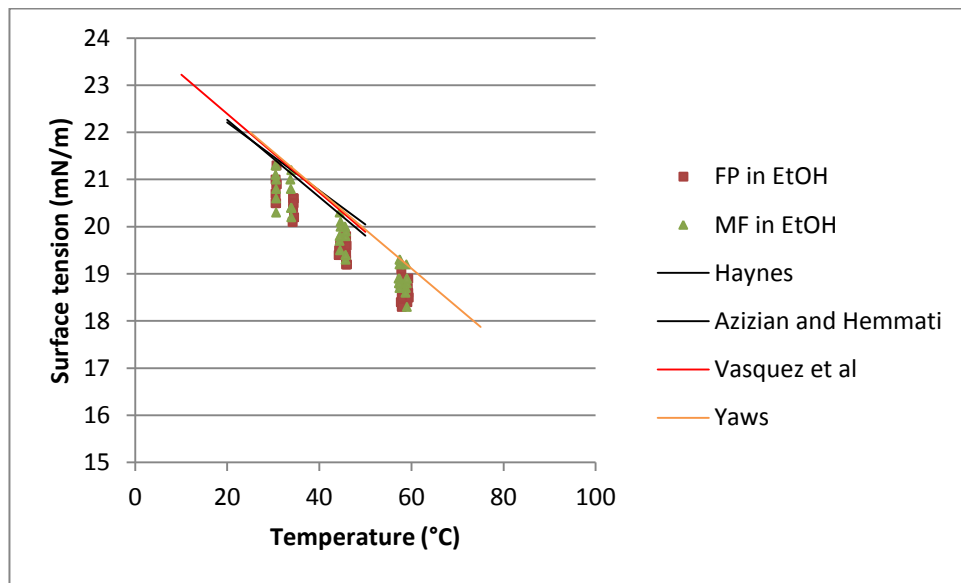
**Figure 2.9** Effect of droplet lifetime upon the surface tension of Mometasone Furoate in ethanol

Although a reduction in surface tension with lifetime is evident at small lifetime values, the change of surface tension with lifetime is not typical of that expected for a solution containing a surface active solute. In the case of surface activity, the maximum surface tension (that of the solvent) is the observed at low lifetimes; the surface tension then decreases to an asymptotic value as sufficient time is allowed for the surfactant molecules to migrate to the emerging bubble surface. Solution surface tensions for the four solution systems approach that of the solvents at longer lifetimes, typically in excess of one second, for all three temperatures evaluated. The higher than expected values for surface tension at short droplet lifetimes may be attributed to the measurement technique; long, narrow capillaries are used with the Sita T60 instrument and measurement geometries such as this have been associated with pressure differences between the reservoir in the instrument and the developing bubble. This has been

## Equipment and Materials

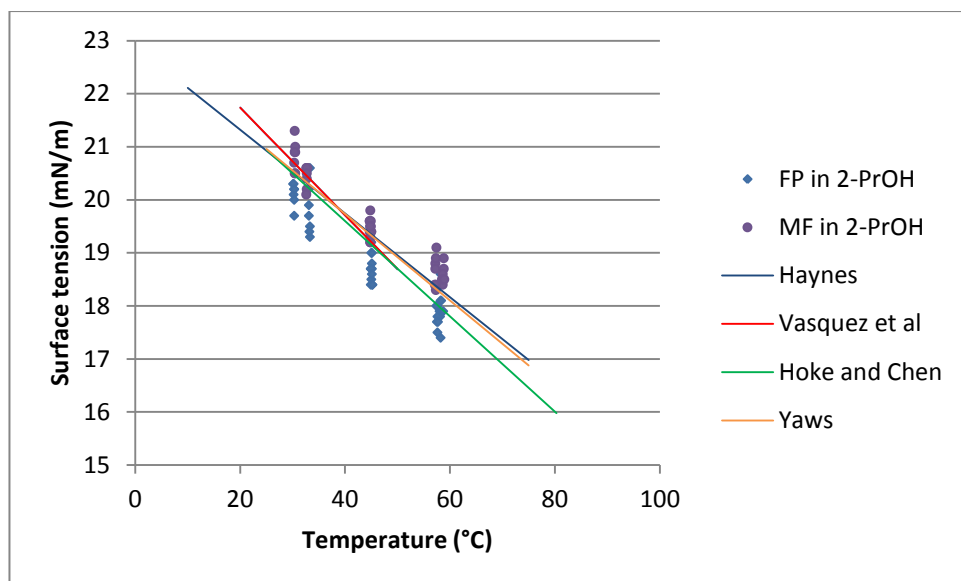
observed to result in an overestimation of surface tension at short bubble lifetimes (Kovalchuk & Dukhin, 2001).

A comparison of the surface tension results obtained for solutions at 45°C is presented below. Figure 2.10 and Figure 2.11 contain individual values for each of two frequency sweeps from >1 to approximately 10 s; surface tension values obtained at droplet lifetimes of less than one second have been omitted for the reasons given above. The results for the solutions have been compared with literature values for the respective solvents (Azizian & Hemmati, 2003, Haynes, 2012, Hoke & Chen, 1991, Vazquez *et al.*, 1995, Yaws, 2012) in Figure 2.10 and Figure 2.11.



**Figure 2.10** Temperature dependence of surface tension of ethanol solutions





**Figure 2.11** Temperature dependence of surface tension of 2-propanol solutions

Some difference is observed in the literature values for the two solvents, however the rate of change of surface tension with temperature is observed to be similar for solvents and solutions. The surface tension values measured for fluticasone propionate and mometasone furoate solutions in ethanol are lower than those published in the scientific literature. The short timescale of the atomization process and the likely difference in diffusivity of the solute and solvent, given the approximately tenfold difference in molecular mass, it is unlikely that the solute would cause a significant deviation in surface tension from that of the solvent (Loubiere & Hebrard, 2004).

The lack of surface activity of the solutes, coupled with the small impact of the low concentration and likely slow diffusivity, indicates that solvent values for surface tension are appropriate for use in characterising the droplet formation process in flow focusing. Literature data (Yaws, 2012) was used to provide surface tension values for the

experimental sections within this work as this reference provides information for all operating temperatures of interest.

### **2.3. Conclusion**

Evaluation of equilibrium solubility of the two corticosteroid molecules with temperature demonstrates similar trends and concentrations with respect to order of magnitude.

Mometasone furoate exhibits a consistently higher absolute solubility across the temperature range in both of the alcohols, probably as a consequence of the differing substituent groups given the similarity in molecular weight and structure between the two molecules. The molar solubilities of each corticosteroid in the two alcohols are seen to be equivalent, resulting in an increased mass fraction solubility in ethanol. The equilibrium solubility studies have allowed processing conditions for API spray drying to be identified.

The surface tensions measured for the four solute-solvent combinations are typical of non-surface active solutes, as the stable values for solutions are similar to those taken from the scientific literature for the solvents used. Solvent data therefore should provide an appropriate basis for calculation of flow focusing parameters.

### **3. CHARACTERISATION OF ATOMIZATION**

#### **3.1. Droplet imaging**

The successful production of low-polydispersity droplet distributions using flow-focusing is dependent upon the use of appropriate nozzle geometry and suitable operating parameters, as described in Section 1.3.1. The FFDryer atomizer has been designed to comply with the dimensional requirements necessary for successful flow focusing (Rosell-Llompart & Ganan-Calvo, 2008), however to be certain that any trends between predicted droplet size and concentration and subsequent dry powder properties are genuine, assurance is required that the particular atomizer being used does produce droplets by the break-up of a liquid jet by the intended mechanism (Ganan-Calvo, 1998). An evaluation of droplet formation was performed using high-speed photography for each of the solvent systems intended for use in the spray drying experiments.

High speed photography is a common technique in the study of atomization, giving a clear insight into the process of spray generation. The key mechanisms responsible for formation of droplets are readily identified, allowing additional analytical techniques to be selected appropriate to the timescales and nature of the break-up process. High speed photography followed by Phase Doppler Anemometry was used to characterise the formation of droplets produced by a twin fluid atomizer (Kufferath *et al.*, 1999). A Nanolite spark system provided illumination; the 20 ns duration was sufficiently brief to allow capture of clear images of spray plumes from this dynamic process characterised by high Reynolds numbers. Mayer employed high-speed cinematography and flashlight photography to study the atomization of cryogenic propellants, demonstrating significant differences between atomization and mixing in under subcritical and

supercritical conditions (Mayer, 1994). The use of magnifying lenses with high speed imaging has allowed the study of individual droplets, rather than spray plumes, when evaluating liquid jet break-up. Brenn, Helpio and Durst used a CCD camera fitted with a magnifying lens to study droplet formation from a novel, multiple atomizer array producing droplets from circular jets via piezoelectric oscillation (Brenn *et al.*, 1997). The authors used an LED-based stroboscope to illuminate the image capture, synchronised to the oscillator. Image processing was then employed to yield information on the droplet size distribution produced by the array. Ganan-Calvo used high speed videography to demonstrate the operating principles of a flow-focusing atomizer, employing a 70 ns shutter time with an unspecified light source to confirm operating conditions for obtaining monodisperse droplets (Ganan-Calvo, 1998).

An imaging system comprising a high speed videography system, a magnifying lens and a high-intensity light source was assembled to evaluate the FFDryer atomizer and used to obtain images of droplet formation across and beyond the Weber number range postulated to encompass successful operation.

### **3.1.1. Equipment configuration**

Images of jet break-up were collected using a high speed video camera (Motionpro 10000, Redlake, San Diego, USA) fitted with a microscope lens (Linos, Göttingen, Germany). Illumination was provided by an image processing strobe (BVS-II Wotan, Polytec GmbH, Waldbronn, Germany) triggered by collection of images by the camera. Light from the strobe was directed via a fibre-optic conduit arranged to back-light the liquid jet from the atomizer. The camera was mounted onto a tripod with vertical adjustment to allow the point of droplet generation to be accurately imaged; the

distance between lens and droplet stream was maintained throughout the experimental runs at approximately 5mm.

### **3.1.2. Experimental procedure**

Images were captured using an exposure time of 2  $\mu$ s at a shutter speed of 10000 frames per second. The short exposure time, necessitated by a droplet generation rate of the order of  $10^5$  droplets per second, requires intense light to obtain a clear image. The strobe unit is able to produce the necessary intensity, however only as a single pulse within the timeframe of image capture. The very short exposure time also made synchronisation of image capture and strobe activation challenging, resulting in a number of instances of underexposed images if only a single frame was captured. The recording of a sequence of ten frames upon triggering ensured one of the images was acceptably clear; the remaining nine underexposed images were discarded.

Ten acceptable images were obtained for each set of atomizer operating conditions to determine whether droplet formation by axisymmetric break-up was taking place. Each image was analysed using ImagePro software (Version 4.5, Media Cybernetics Inc, Maryland, USA) to provide a characteristic droplet diameter for each droplet image present within the main image. A graticule (Pyser-SGI Ltd. Kent, UK) was used to calibrate the Imagepro software in order that measurements could be performed. Larger droplets were observed to be non-spherical in shape, so an average size was calculated based upon the maximum and minimum dimensions of the droplet to give a more representative characteristic diameter. Droplet size distributions were then calculated from the droplet images to allow comparison of image analysis results to those predicted by theory.



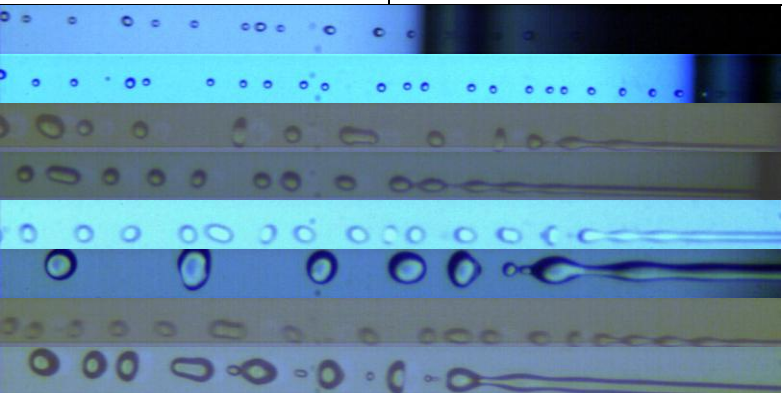
**3.1.3. Experimental conditions**

Droplet images were captured for water, ethanol and propanol across and beyond the Weber number range postulated for axisymmetric break-up. The flow rates, and pressure drops used are given in Table 3.1, Table 3.2 and Table 3.3.


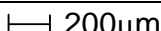
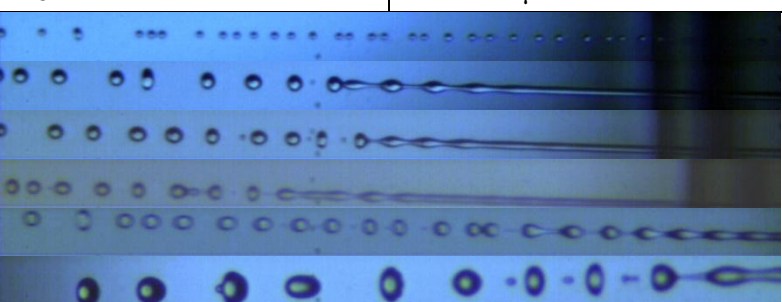
**3.1.4. Results and discussion**

A representative image is presented for each condition for water, ethanol and propanol in Table 3.1, Table 3.2 and Table 3.3 respectively. The remaining images captured are presented as Appendix 1.

**Table 3.1 Droplet formation images for water**

Flow rate (mL/h)	Pressure drop (mbar)	Direction of flow: 	
		Image	
7	60		
10	130		
27	60		
32	80		
40	130		
62	60		
63	300		
80	100		

**Table 3.2 Droplet formation images for Ethanol**

Flow rate (mL/h)	Pressure drop (mbar)	Direction of flow: 	
		Image	
10	100		
20	25		
22	30		
28	50		
40	100		
64	50		

**Table 3.3 Droplet formation images for 2-propanol**

Flow rate (mL/h)	Pressure drop (mbar)	Direction of flow: ←	
		Image	200µm
5	25		
7.5	55		
12	150		
20	25		
24	35		
30	55		
35	75		
40	100		
49	150		

A comparison of median droplet diameter ( $D_{50}$ ) measured from the images to the droplet size predicted by Equation 1.15 is presented as Table 3.4, Table 3.5 and Table 3.6.

**Table 3.4 Droplet size analysis results for water**

Flow rate (mL h <sup>-1</sup> )	Pressure Drop (mbar)	We	Predicted $D_{50}$ (µm)	Image analysis $D_{50}$ (µm)
7	60	3.9	45	38
10	130	8.3	44	38
27	60	7.6	88	85
32	80	10	89	88
40	130	17	88	93
62	60	11	133	164
63	300	39	90	91
80	100	19	133	141

## Characterisation of Atomization

**Table 3.5 Droplet size analysis results for ethanol**

Flow rate (mL h <sup>-1</sup> )	Pressure Drop (mbar)	We	Predicted D <sub>50</sub> (μm)	Image analysis D <sub>50</sub> (μm)
10	100	23	44	Not recorded
20	25	11	89	77
22	30	13	89	74
28	50	21	88	72
40	100	43	89	77
64	50	32	133	129

**Table 3.6 Droplet size analysis results for 2-propanol**

Flow rate (mL h <sup>-1</sup> )	Pressure Drop (mbar)	We	Predicted D <sub>50</sub> (μm)	Image analysis D <sub>50</sub> (μm)
5	25	6.2	44	50
7.5	55	14	44	41
12	150	37	43	50
20	25	12	88	88
24	35	17	88	84
30	55	27	88	97
35	75	37	88	100
40	100	50	88	97
49	150	74	88	91

Weber number values below 40 are understood to be required to ensure axisymmetric break-up of the liquid jet and give the narrowest possible droplet size distribution (Ganan-Calvo, 1998, Ganan-Calvo, 2008, Rosell-Llompарт & Ganan-Calvo, 2008). The critical Weber number has been exceeded for two of the three liquids evaluated and axisymmetric break-up has been observed to occur up to Weber numbers of 39, 43 and 74 for water, ethanol and 2-propanol respectively when operated at conditions postulated to generate droplet with a diameter of approximately 90 μm. No evidence of



## Characterisation of Atomization

an asymmetric mode of break up was observed above  $We = 40$  during imaging of the liquids evaluated which appears in contradiction of the accepted threshold for flow-focusing, however axisymmetric break-up above this threshold value has been previously reported (Gordillo *et al.*, 2001a). Atomization driven by hydrodynamic, rather than capillary forces, has been postulated as the mechanism for axisymmetric droplet formation at  $We > 40$ . The authors note that transition to helicoidal (asymmetric) break-up is likely to occur with increasing  $We$ , however no evidence of this was seen during imaging, up to a maximum of  $We = 74$  evaluated for 2-propanol.

Liquid jet break-up generally occurs too close to the atomizer aperture to make identification of the break-up mode possible when operating at a target droplet size below  $50\mu\text{m}$ . Images obtained for 2-propanol at  $12\text{ mL h}^{-1}$  liquid flow, 150 mbar pressure drop appear to show axisymmetric break-up; the similar trajectory of the droplets produced at break-up in all images indicates axisymmetric break-up is the likely mechanism as transition to a helicoidal, asymmetric mode would be expected to cause a wider range of droplet trajectories.

Larger than predicted droplet sizes are observed at operating conditions encompassing relatively high liquid flow compared to pressure drop across the atomizer orifice; this is particularly evident when water was used as the focussed fluid at conditions of  $62\text{ mL h}^{-1}$  liquid flow, 60 mbar pressure drop and  $80\text{ mL h}^{-1}$  liquid flow, 100 mbar pressure drop. Given the close proximity of the droplets to the point of break-up in the images, coalescence after break-up is unlikely to be the cause of the large droplet size. A more likely explanation is a wider than predicted jet diameter at the point of jet detachment, leading to a proportionally large droplet after break-up. Measurement of the jet

## Characterisation of Atomization

diameter at break-up for  $62 \text{ mL h}^{-1}$  liquid flow, 60 mbar pressure drop gives a jet radius of  $77 \text{ }\mu\text{m}$ , approximating to a droplet size of  $145 \text{ }\mu\text{m}$  compared to a predicted value of  $133 \text{ }\mu\text{m}$ .

The short exposure times used necessitated opening the aperture of the lens to the maximum extent to best use the light produced by the strobe unit. The depth of field becomes small under such operating conditions, and this combined with the rapid movement of the droplets results in some loss of definition of the droplet edge within the images. Measurement using image analysis will therefore be subject to a degree of error. The results and predicted droplet diameter do however agree well, hence it would appear that a combination of low pressure drop and high liquid flow may result in droplet size being under-predicted. Effects attributable to flow ratios have been observed during previous flow focussing studies (Gordillo *et al.*, 2001a), however were attributed to the effect of hydrodynamic forces when operating at  $We > 40$  rather than at the low Weber number conditions prevalent at high liquid: gas flow ratios.

Satellite droplets are evident in a number of the images, a known consequence of this mode of droplet formation (Lefebvre, 1988). These have occurred across the range of conditions evaluated; however they are at least an order of magnitude smaller in diameter than droplets formed from detachment of the perturbation rather than the neck between two perturbations. Solid material produced from satellite droplets during spray drying of solutions should therefore be readily identifiable and their impact on subsequent test results should be able to be explained.

### 3.2. Droplet measurement

Laser diffraction has become established as a key technique for the characterisation of particle and droplet size distributions. The technique exploits the relationship between the diffraction angle of a light beam and the particle size of the object causing the diffraction to provide an estimate of the particle size. Modern laser diffraction measurement systems employ a collimated beam of laser light and a concentric detector arrangement to provide a scattering pattern from a particulate sample which is then deconvoluted using Fraunhofer or Mie algorithms to yield a volume-based size distribution. The ability to characterise an entire particulate distribution coupled with a sampling rate of up to  $2500 \text{ s}^{-1}$  make laser diffraction systems a powerful tool for the evaluation of dispersed systems (Mitchell *et al.*, 2006).

A number of applications of laser diffraction for the study of spray generation are noted in the relevant literature. The technique has been used to quantify the output from continuous sprays such as fuel injectors and spray dryer atomizers and also transient sprays, for example those produced by aerosol devices fitted with metering valves or pumps. The particular laser diffraction system employed during this work, the Malvern Spraytec, has been used to evaluate continuous spray generation in a number of instances. An analysis of water mist sprays for fire suppression systems (Santangelo, 2010) demonstrated the ability of the measurement system when used to characterise high velocity droplets. A study of droplet production from a spray dryer atomizer (Thybo *et al.*, 2008) notes the changing average droplet size with distance from the atomizer, attributed to coalescence within the turbulent spray produced by a two-fluid atomizer. The Malvern Spraytec was used as part of an investigation to correlate droplet and

resulting particle size distributions for spray pyrolysis (Wang *et al.*, 2008). Good correlation was observed between solution droplet distribution measured using the Spraytec and the resulting dry particle size distribution of the solute determined by image analysis of scanning electron micrographs.

Extensive use of the Malvern Spraytec in the characterisation of aerosol device output is evident in the literature. The effect of formulation ingredients upon droplet size distribution was investigated for nasal spray devices (Dayal *et al.*, 2004) and use of the Spraytec allowed elucidation of the impact of changing physicochemical properties upon spray characteristics. Laser diffraction was used to provide information for a computational fluid dynamics (CFD) model describing delivery from a novel liquid inhaler (Worth *et al.*, 2009). The Spraytec was employed to measure the droplet sizes generated immediately beyond the inhaler mouthpiece and provide the initial conditions for the CFD model, which was subsequently validated using inertial impaction.

Two notable studies have been conducted to evaluate the measuring capabilities of the Spraytec system. The ability of the Spraytec to evaluate multi-modal droplet distributions was investigated (Triballier *et al.*, 2003) and the measurement system was observed to successfully characterise the bi- and trimodal distributions used within the study. A second part of this study, also evaluated in a further experiment (Dumouchel *et al.*, 2009) challenged the capability of the software algorithm to deconvolute the effect of multiple scattering which can lead to under-sizing of dense sprays. Automotive fuel injection systems were used within both studies; multiple injectors and a protecting tube were used to change the spray density without changing the droplet size distribution. Results demonstrated a narrowing of the distribution when light transmission falls below

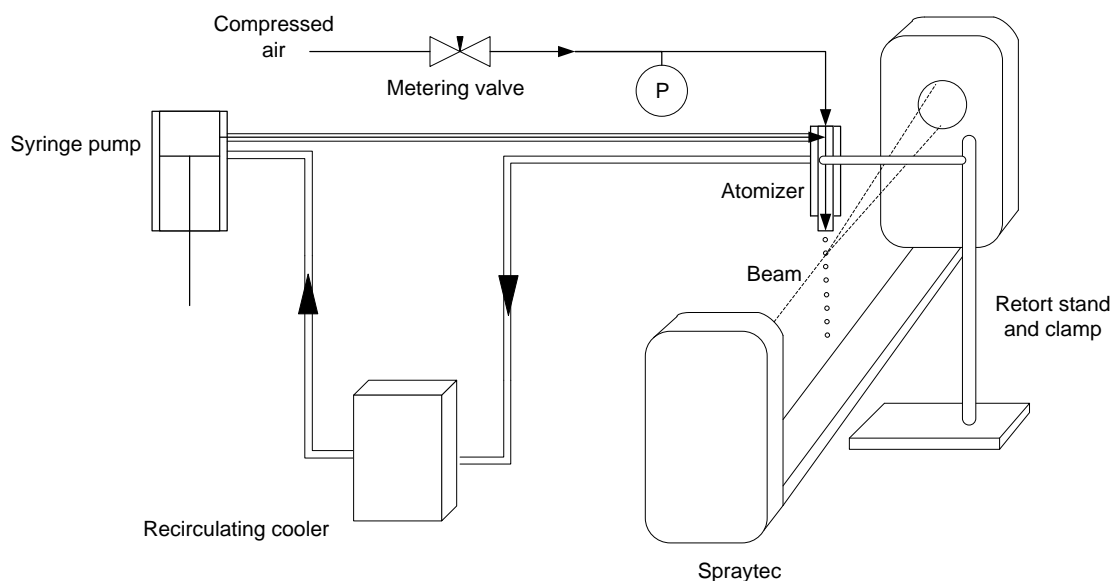
40% interpreted by the authors as the software algorithm being unable to fully correct for the under-sizing of the droplet distribution.

The droplet distribution produced by flow focusing-based devices is typically monomodal (Ganan-Calvo, 1998) and droplet density would be expected to be low given the modest liquid flow rates for flow focusing devices compared to spray dryer two fluid atomizers, automotive fuel injectors or fire suppression systems. The Malvern Spraytec should therefore be capable of determining droplet size distributions produced by the FFD atomizer.

### **3.2.1. Equipment configuration**

Droplet size distribution measurement was performed using a Spraytec laser diffraction instrument (Malvern Instruments, Worcestershire, UK) fitted with a 300 mm lens. The lens has a minimum working distance of 150 mm and is capable of measuring droplets within the range 0.1 to 900  $\mu\text{m}$  (Malvern Instruments, 2005). The FFDryer atomizer was suspended directly above the laser beam, maintaining a defined gap between the lowest point of the atomizer orifice plate and the top of the beam. A retort stand and clamp were used to suspend the FFDryer atomizer in order that the atomizer could be removed from the vicinity of the beam during the background measurement step that preceded each droplet distribution measurement. A distance of 50 mm between the centre of the atomizer orifice plate and the Spraytec detector window was used for all experimental runs to avoid vignetting (Triballier *et al.*, 2003). An illustration of the experimental set up is presented as Figure 3.1.

## Characterisation of Atomization



**Figure 3.1** Spraytec set up

### 3.2.2. Experimental conditions

A standard operating procedure (SOP) was written based on the default continuous spray SOP provided within the Spraytec software in order to ensure measurements of different experimental runs were performed under similar conditions. Refractive indices specific to each of the liquids under test were used for data analysis; refractive indices for solutions were assumed to be identical to those for the solvent as a result of the low concentration of solute present. A curve-fitting model was not selected for use with the data analysis software as no knowledge of the droplet size distribution produced by the atomizer was available prior to the Spraytec evaluation (Triballier *et al.*, 2003).

Background measurement was performed before each measurement run, once completed the FFDryer atomizer was aligned as detailed in section 3.2.1 and the flow rate and pressure drop set as required. Droplet production from the atomizer was then allowed to stabilise for five minutes before commencing measurement. The droplet

distribution was then measured for five minutes, capturing a scattering pattern every second during this period.

Droplet generation was characterised for water, ethanol and propanol, and also for solutions of sodium chloride in water and mometasone furoate and fluticasone propionate in ethanol and 2-propanol.

Three groups of measurements were undertaken to demonstrate the suitability of the FFDryer atomizer and measurement configuration for investigating the API behaviour during spray drying:

1. Data generated to define the atomizer-to-beam distance to be used during characterisation.
2. Data generated to establish the effect of atomizer operating parameters upon droplet size distribution and agreement of data with control theory.
3. Evaluation of the impact of inclusion of solute on droplet size distribution compared to solvent only.

### **3.2.2.1. Atomizer to beam distance**

The dried particle size generated during spray drying is dependent upon the droplet size at the point of atomization; hence an accurate measurement of droplet size is essential to understand drying behaviour. The laser beam used for droplet size measurement is collimated to a width of approximately 10 mm so a change in droplet size during measurement is possible if the drying kinetics under the conditions of measurement are sufficiently rapid, resulting in the detection of an artificially wide droplet distribution. In

addition, coalescence of droplets will change the droplet distribution; if this were to occur beyond the point of measurement the droplet size distribution collected would underestimate the true droplet sizes being produced. Jet break up was observed to occur at less than 3mm from the orifice plate of the FFDryer atomizer during droplet imaging experiments; measurement at intervals beyond this range should therefore allow coalescence to be identified by an increasing droplet size with increasing distance (Thybo *et al.*, 2008). Droplet size measurements were performed at atomizer to beam distances of 5, 10 and 15 mm for the same droplet generation conditions using 2-propanol to determine the impact of droplet age upon size at ambient conditions.

### **3.2.2.2. FFDryer atomizer characterisation**

Evaluation of atomizer parameters was performed to define sets of operating conditions relevant to use with the Buchi B-290 spray dryer. The small length of the drying chamber within the Buchi unit results in a short droplet residence time, hence droplet diameters less than 100  $\mu\text{m}$  for water are required in order to allow drying of droplets to completion. Pressure drop and flow rate values postulated to give droplet sizes of 10 to 100  $\mu\text{m}$  were identified using the relationships established by Ganan-Calvo (1998) for water, ethanol and 2-propanol. Initial experiments were conducted at room temperature employing as low a pressure drop as possible in order to operate at the minimum Weber number, and therefore to operate as close as possible to the preferred operating region postulated in the literature. Further runs were then performed using higher pressure drops of 150 to 400 mbar for ethanol and 2-propanol, and 150 to 900 mbar for water, to evaluate maximising the atomizer throughput and therefore maximising the yield of solute upon spray drying for a fixed period.



## Characterisation of Atomization

Additional experiments were then conducted on ethanol and 2-propanol using a jacketing temperature of 50°C to determine the impact of the change of operating temperature upon droplet generation. Solution temperatures in excess of 50°C are necessary to ensure operation below the saturation limit for mometasone furoate and fluticasone propionate solutions in ethanol and 2-propanol at the solution concentration chosen, as defined in Section 2.2.2.1.

Finally runs were conducted with solute at a representative concentration – 5 %w/w for sodium chloride in water at 25°C, and 0.5 %w/w for mometasone furoate and fluticasone propionate in ethanol and 2-propanol at 50°C – in order to confirm consistency between operation using solvents and associated solutions.

### 3.2.3. Results and discussion

To allow comparison of the effect of operating parameters within a complex experimental space, droplet size information obtained during the atomizer evaluation is represented using the normalised values described below. Summary graphs of the input data, detailing droplet size versus liquid flow rate at fixed pressure drop, are presented in Appendix 8.

- the ratio of measured median droplet diameter to predicted droplet size -

$$\left( \frac{D_{50}}{D_{\text{predicted}}} \right)$$

- The measured average span, calculated as the difference between the ninetieth and tenth percentiles divided by the median size -  $\left( \frac{D_{90} - D_{10}}{D_{50}} \right)$

## Characterisation of Atomization

Both values have been calculated as the mean of the value recorded at intervals of one second over the measurement period. An additional graph has been included for data sets where outlying results have necessitated a large ordinate scale and made interpretation of the remaining data difficult; in this case the additional graph has a reduced scale excluding the outlying results. Additional summary figures are given defining the impact of increasing Weber number upon droplet size.

To allow comparison of data the solvent / solution flow rate through the atomizer has been expressed using the predicted droplet size, which appears as the ordinate in many of the following figures. The jet diameter at the point of break-up can be estimated using Equation 3.1 and Equation 3.2 below, with resulting droplet size given by Equation 1.15:

$$We = \left(\frac{8}{\pi^2}\right)^{\frac{1}{4}} \left(\frac{\rho_l Q^2 \Delta P^3}{\sigma^4}\right)^{\frac{1}{4}} \quad \text{Equation 3.1}$$

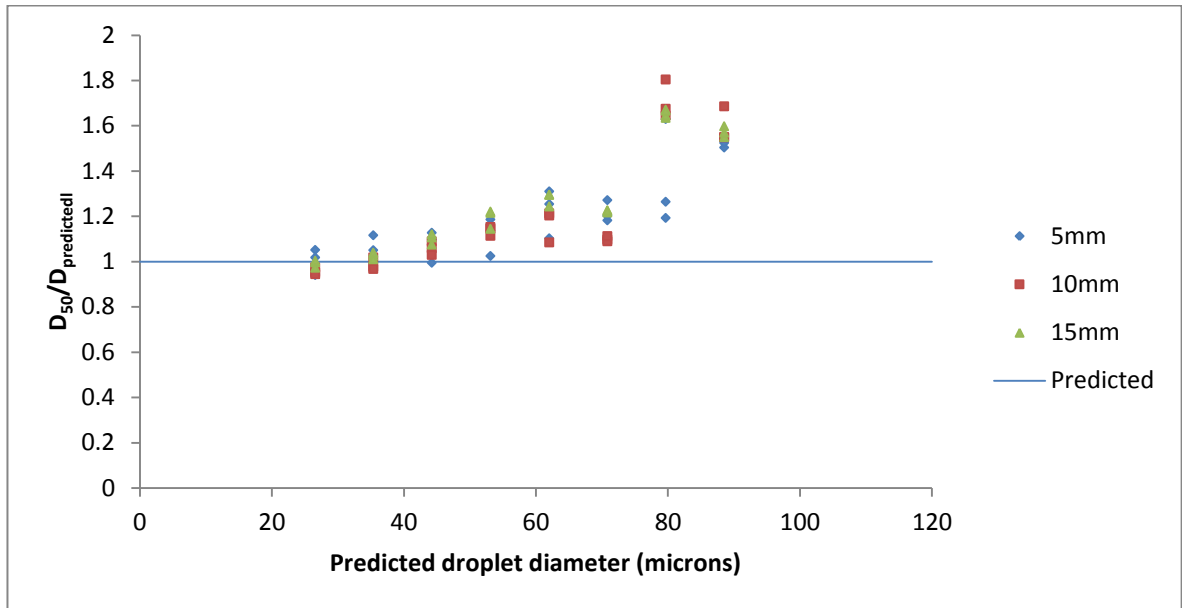
$$D_j = \frac{We \cdot 2\sigma}{\rho_g u_g^2} \quad \text{Equation 3.2}$$

At a defined pressure the predicted size will therefore reflect the liquid flow rate, as all other variables will be constant for a particular solution/ solvent and operating temperature. The actual droplet size produced during the experiment is represented as the ratio of the median size ( $D_{50}$ ) to the predicted size to again allow cross comparison of data where numerous of variables are subject to change.

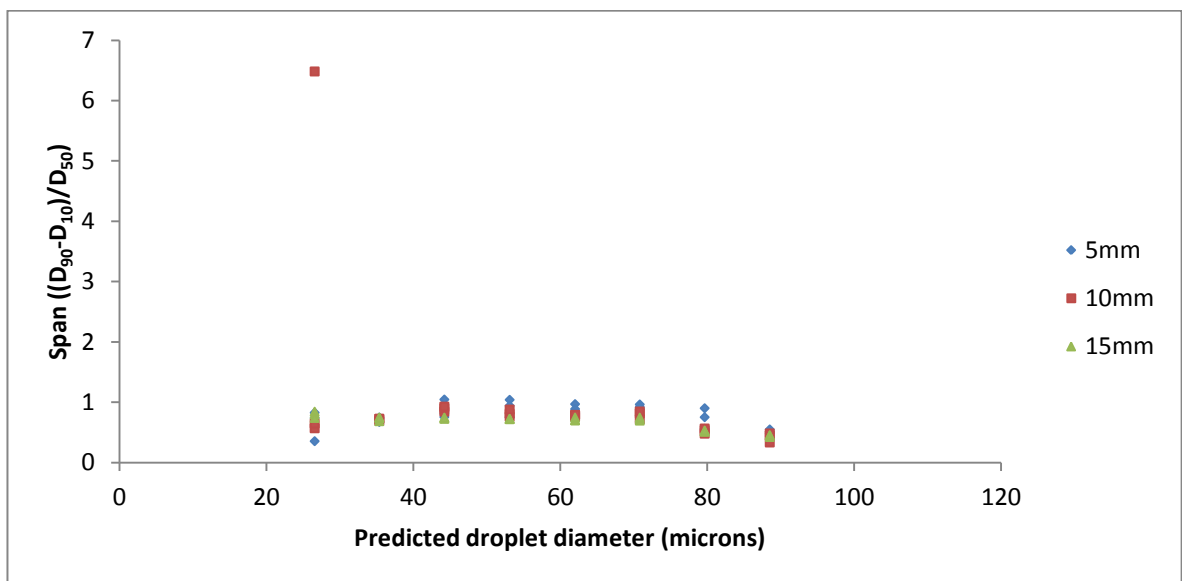
**3.2.3.1. Atomizer to beam distance**

The impact of varying atomizer to beam distance upon average droplet size and span is presented as

Figure 3.2 and Figure 3.3:



**Figure 3.2 Effect of atomizer to beam distance on droplet size distribution (150mbar, 2-propanol)**



**Figure 3.3 Effect of atomizer to beam distance on span (150mbar, 2-propanol)**

Close agreement is observed between measurements made at atomizer to beam distances of 5, 10 and 15 mm with respect to both particle size and span. Two of the three measurements for 5 mm distance at a target droplet size of 80  $\mu\text{m}$  yielded a significantly lower size than the remaining measurement and those for 10 mm and 15 mm runs. Poor reproducibility between runs at target size of 80  $\mu\text{m}$  and greater was evident throughout the evaluation using the Spraytec, hence the difference in results at 80  $\mu\text{m}$  is likely to be as a result of poor reproducibility rather than atomizer to beam distance. The high value for span at 10 mm atomizer to beam distance, target size 30  $\mu\text{m}$  is caused by a high 90<sup>th</sup> percentile value, frequently observed during measurement of droplet generation using low flow rates at relatively large pressure drops. This effect is either a consequence of coalescence subsequent to initial jet break-up, or possibly as a result of periodic helicoidal-type break-up of longer wavelength than for the axisymmetric mode (Gordillo *et al.*, 2001a).

The results indicate a stable droplet size distribution over the distance evaluated, consequently 10 mm atomizer to beam distance was chosen for subsequent Spraytec evaluation experiments.

### **3.2.3.2. Atomizer operation characterisation**

#### **3.2.3.2.1. Water and aqueous sodium chloride atomization**

Comparison of a dimensionless actual: predicted median diameter over the predicted droplet diameter range for water at pressure drops between 200 and 300 mbar is

## Characterisation of Atomization

summarised in Figure 3.4; the associated span is presented as Figure 3.5. A minimum of two runs per flow rate at a pressure drop were undertaken.

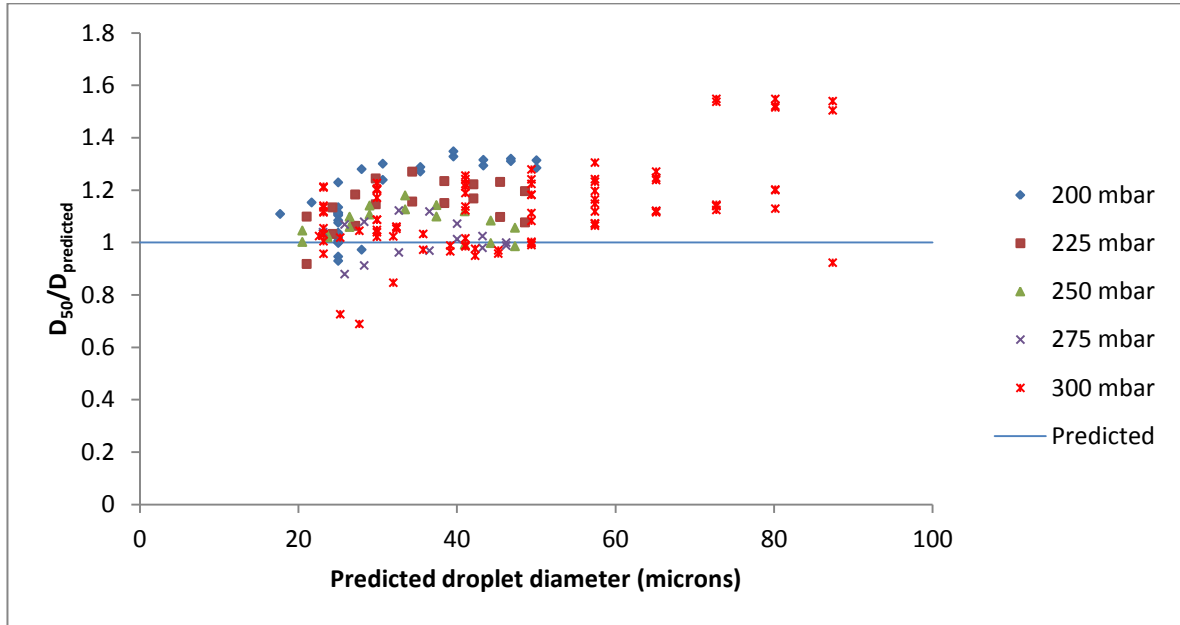


Figure 3.4 Effect of pressure drop and liquid flow rate on droplet size for water

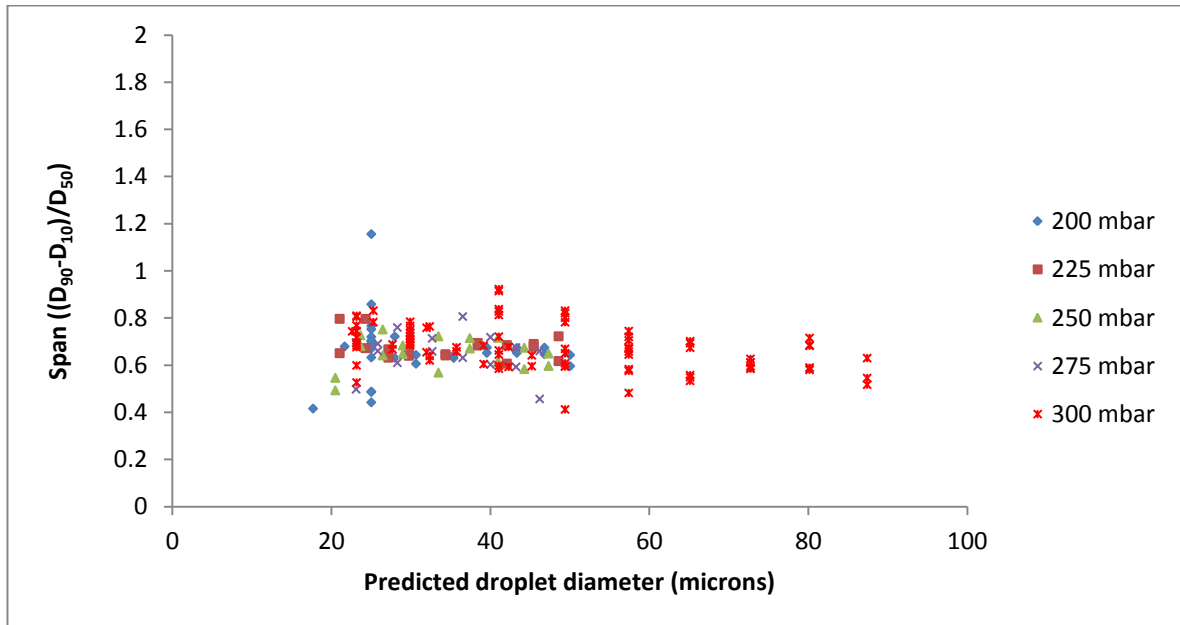


Figure 3.5 Effect of pressure drop and liquid flow rate on span for water

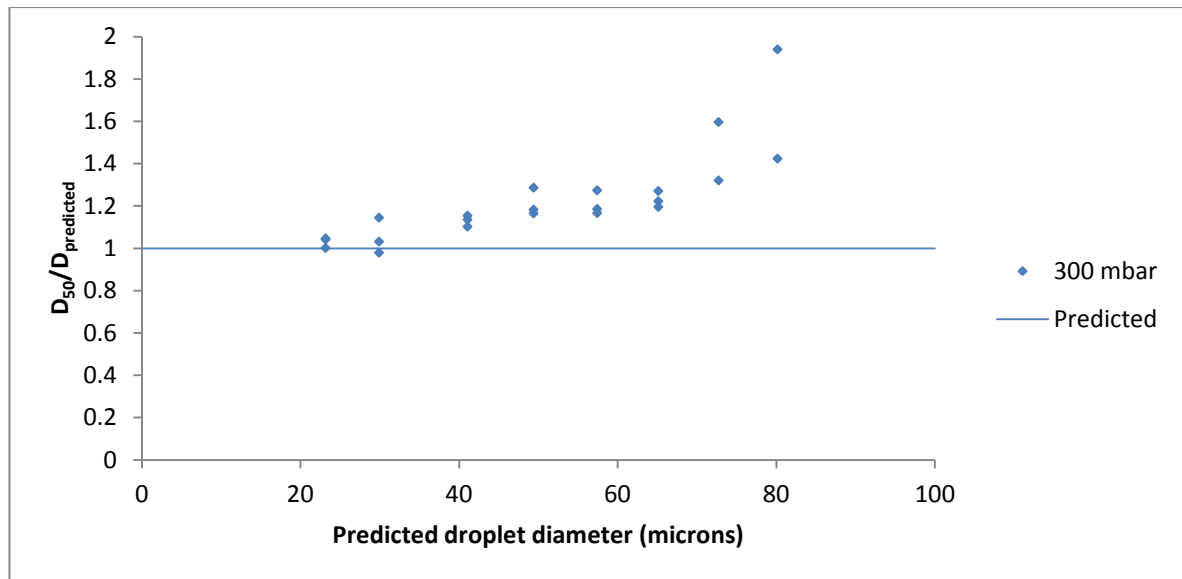
## Characterisation of Atomization

Some evidence of a trend of reducing  $\frac{D_{50}}{D_{\text{predicted}}}$  with increasing pressure can be observed, however the inherent variability between runs at nominally the same operating conditions results in the relationship being difficult to discern. Substantial between-run variability when using water is apparent in the span values in Figure 3.5; it would appear that the width of the distribution as well as the midpoint is subject to significant variability when using water as the focussed fluid.

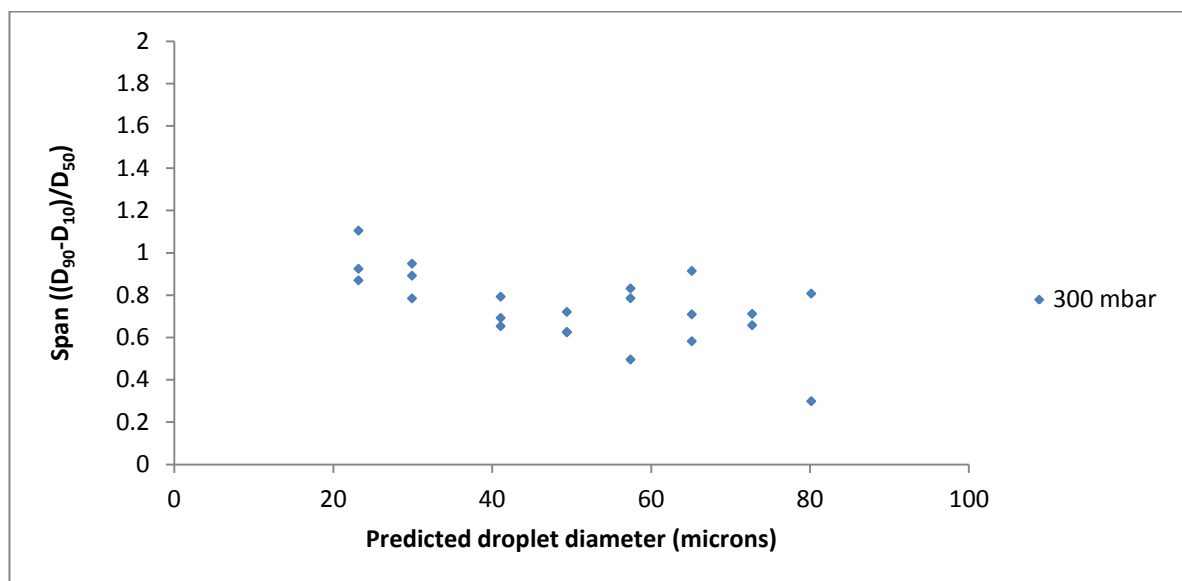
Little difference in span or median size standard deviation is observed for water over the range 200 to 300 mbar pressure drop, corresponding to  $We = 7$  to 38. Further experiments were conducted up to a 900 mbar pressure drop in an attempt to maximise process efficiency for a required droplet size, however no deterioration in performance with regard to span and  $\frac{D_{50}}{D_{\text{predicted}}}$  was observed. Operational issues were encountered at pressure drops above 500 mbar; leakage occurred at the joint between the atomizer capillary and solution feed tube so a pressure drop of 300mbar was chosen for further evaluation.

Sodium chloride solutions at 5 % w/w were used to evaluate the atomizer further as this is the maximum concentration proposed for spray drying runs to characterise the in-situ performance of the atomizer with the Buchi B-290 spray dryer. Repeat runs ( $n=3$ ) were undertaken at the flow rates evaluated previously for water,  $\frac{D_{50}}{D_{\text{predicted}}}$  and span with increasing predicted droplet size are presented as Figure 3.6 and Figure 3.7.

## Characterisation of Atomization



**Figure 3.6** Effect of liquid flow rate on droplet size for 5%w/w aqueous sodium chloride solution

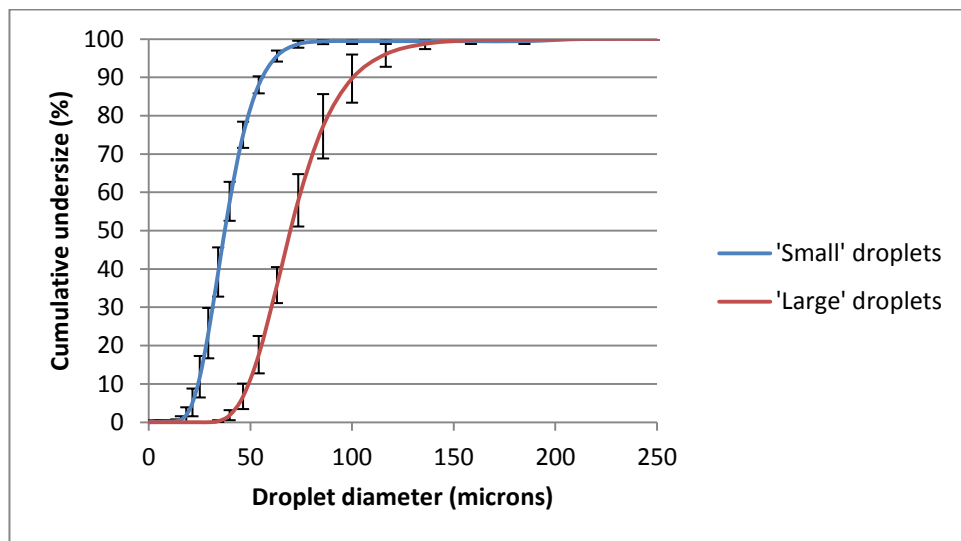


**Figure 3.7** Effect of liquid flow rate on span for 5%w/w aqueous sodium chloride solution

Good agreement with the results produced for water is observed for both droplet size and span when using 5 %w/w sodium chloride solution. Two separate droplet sizes below 100  $\mu\text{m}$  are required for the spray drying experiments using sodium chloride solutions. The repeatability between runs reduces at predicted sizes above 70  $\mu\text{m}$  (see

## Characterisation of Atomization

Figure 3.6), corresponding to a flow rate of  $41 \text{ mL h}^{-1}$ , so the larger of the two solution flow rates was restricted to at or below this threshold. An increase in actual droplet size compared to predicted droplet size with increasing droplet size was again observed for the sodium chloride solution runs, as noted in previous experiments, hence the operating conditions to be used were chosen on the basis of experimental data.  $25.8$  and  $7 \text{ mL h}^{-1}$  flow rates were selected for the spray drying experiments as they correspond to droplet diameters of approximately  $70$  and  $35 \mu\text{m}$  respectively and should produce an acceptable difference in droplet size whilst giving a reasonable spray drying run time. Droplet size distributions for the selected conditions are shown as Figure 3.8, with error bars representing the standard deviation.

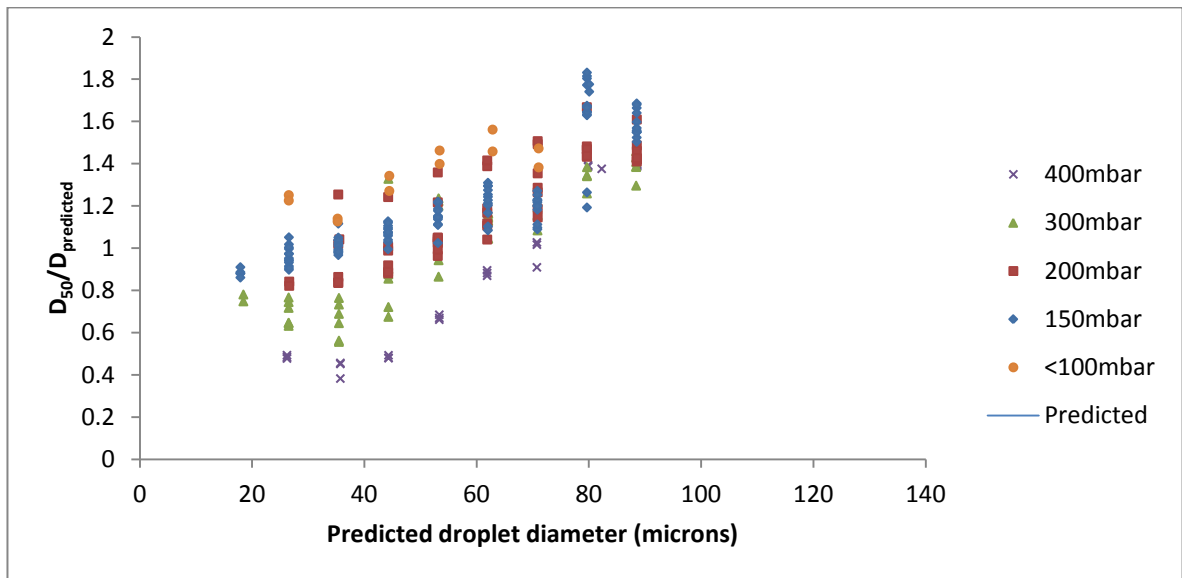


**Figure 3.8** Droplet size distributions for 5%w/w sodium chloride solutions



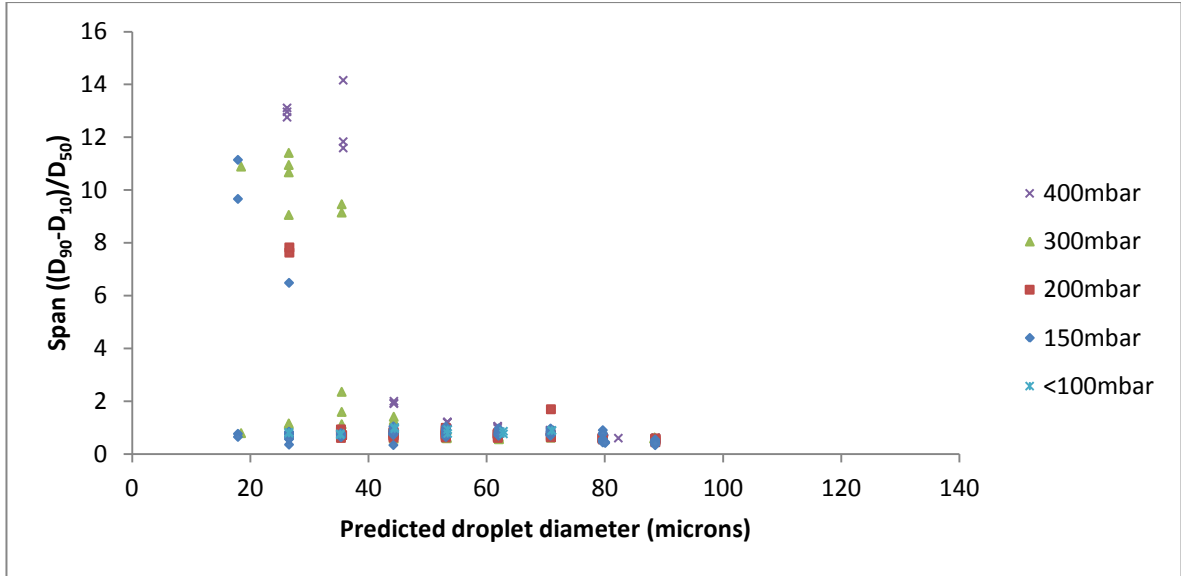
**3.2.3.2.2. Atomization of ethanol and 2-propanol**

A wide pressure drop range was explored to define suitable operating parameters for atomization alcohols and associated solutions. Initially pressure drops from 70 to 400 mbar, with flow rates of 2 to 80 mL h<sup>-1</sup> were evaluated at 25°C to identify an acceptable compromise between distribution width and spray drying run time.  $\frac{D_{50}}{D_{\text{predicted}}}$  and span relationships with predicted droplet diameter across the pressure drop range are summarised in Figure 3.9 to Figure 3.12.

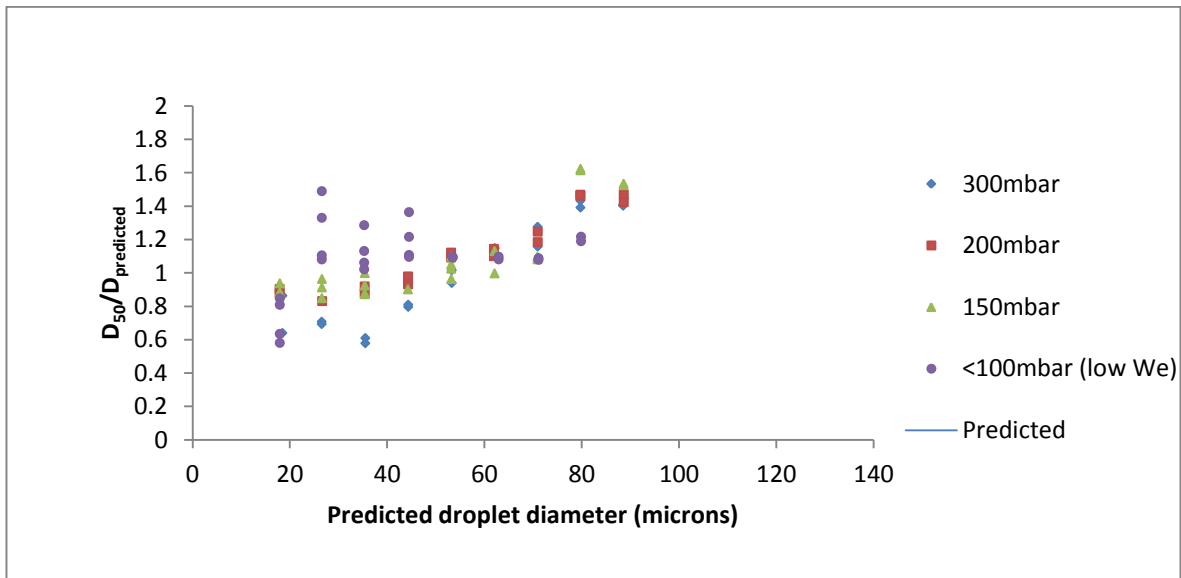


**Figure 3.9** Effect of pressure drop and liquid flow rate on droplet size for 2-propanol, 25°C

## Characterisation of Atomization

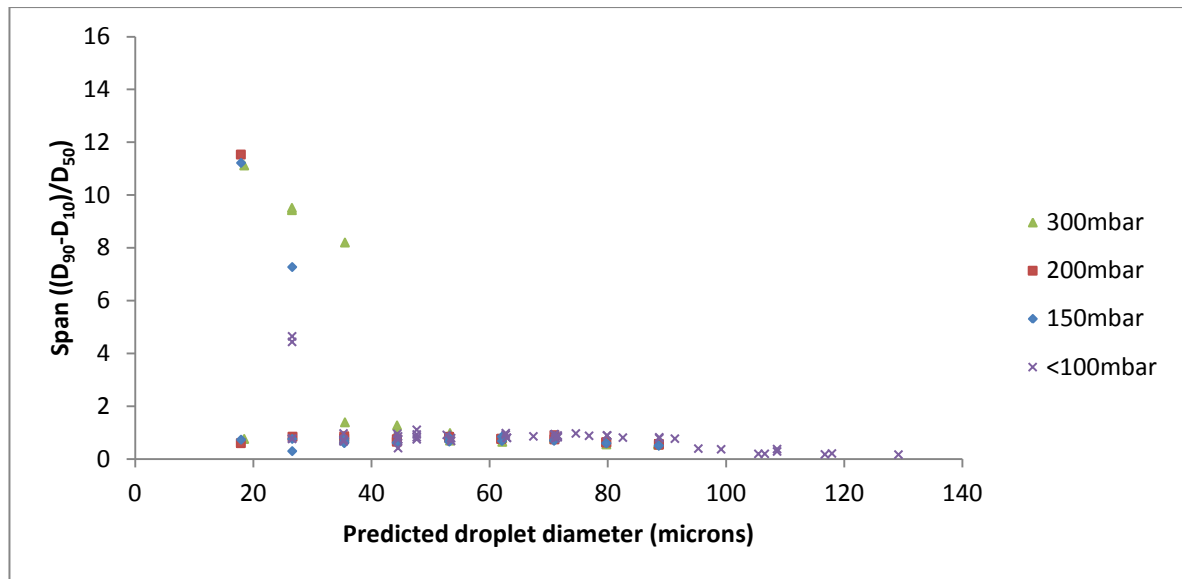


**Figure 3.10** Effect of pressure drop and liquid flow rate on span for 2-propanol, 25°C



**Figure 3.11** Effect of pressure drop and liquid flow rate on droplet size for ethanol, 25°C

## Characterisation of Atomization



**Figure 3.12** Effect of pressure drop and liquid flow rate on span for ethanol, 25°C

A clear relationship between pressure drop and the difference between actual and predicted droplet size is evident for 2-propanol and ethanol. Smaller than anticipated droplets are observed in the case of predicted diameters less than 40  $\mu\text{m}$  with a minimum in the relationship between predicted versus actual size and pressure drop observed at approximately 35  $\mu\text{m}$ . No further inflection is observed beyond the minimum; as droplet size increases the offset is observed to reduce and approaches and then exceeds the predicted size. The droplet size at which actual and predicted sizes coincide is pressure drop dependent, being larger for higher pressure drops. The under-prediction of droplet size at higher flow rates is consistent with the observations made during the high speed videography studies detailed in Section 3.1.4. The production of undersize droplet diameters at higher Weber numbers is consistent with theoretical considerations and experimental evidence presented by Gordillo, Perez-Saborid and Ganán-Calvo (Gordillo *et al.*, 2001b). Perturbations formed at the surface of the liquid jet as a result of hydrodynamic forces have higher growth rates than those resulting from

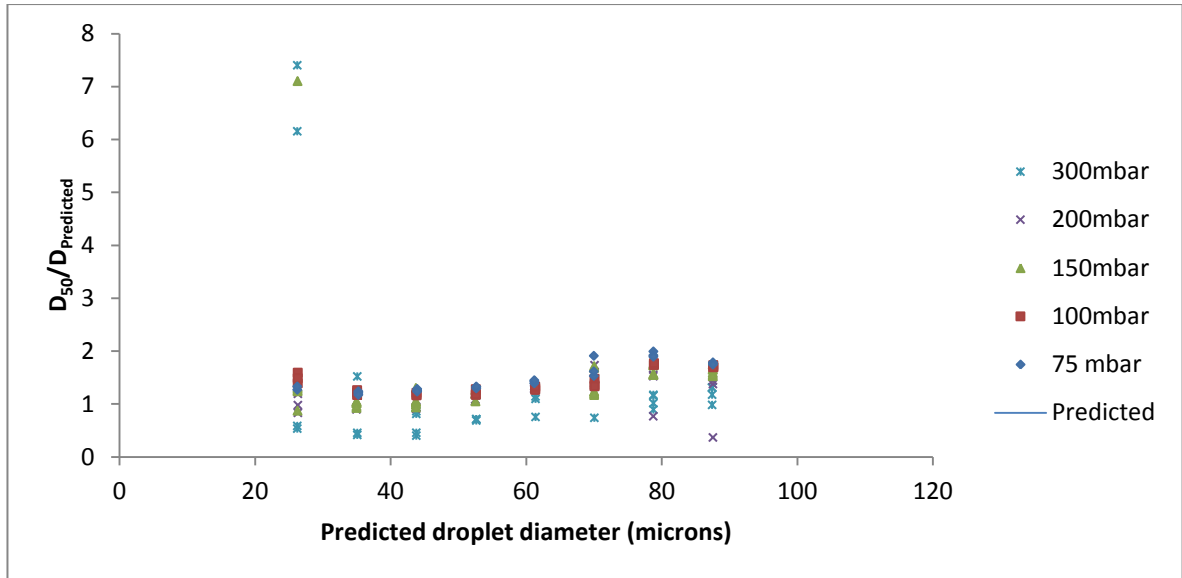
## Characterisation of Atomization

capillary forces at  $We > 40$ . The wavelength of the perturbations formed as a result of the action of the gas stream is shorter than that predicted for capillary action; hence a smaller droplet size will result. Droplet size is expected to be inversely proportional to pressure drop under such circumstances, as has been seen during the characterisation studies performed to characterise the FFDryer atomizer. Additionally, the applicability of Bernoulli theory to the operation of the atomizer, as described in Section 1.3.1, suggests that the viscous drag imparted by the high velocity gas stream is not considered within the control theory. The shearing effect at the liquid surface is likely to additionally elongate the liquid thread, thus providing an explanation for the offset in droplet size noted.

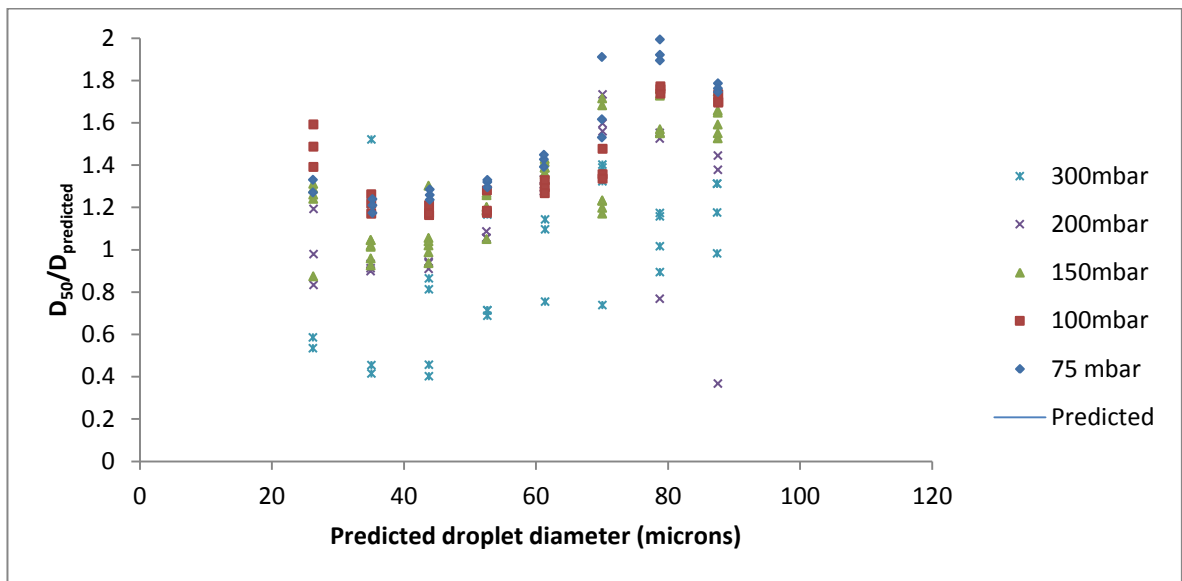
Instances of increased span are observed when operating at conditions chosen to give a predicted size below  $40\ \mu\text{m}$  resulting from high average ninetieth percentile values observed at low liquid flow rates. The root cause of the high values is unclear; either coalescence is occurring before the point of sizing, or disruption to axisymmetric break-up results in the droplet formation mechanism deviating from that expected.

Additional runs were conducted at  $50^\circ\text{C}$ , the jacketing temperature to be used in the spray drying runs; the data from these runs is summarised in Figure 3.13 to Figure 3.18.

## Characterisation of Atomization

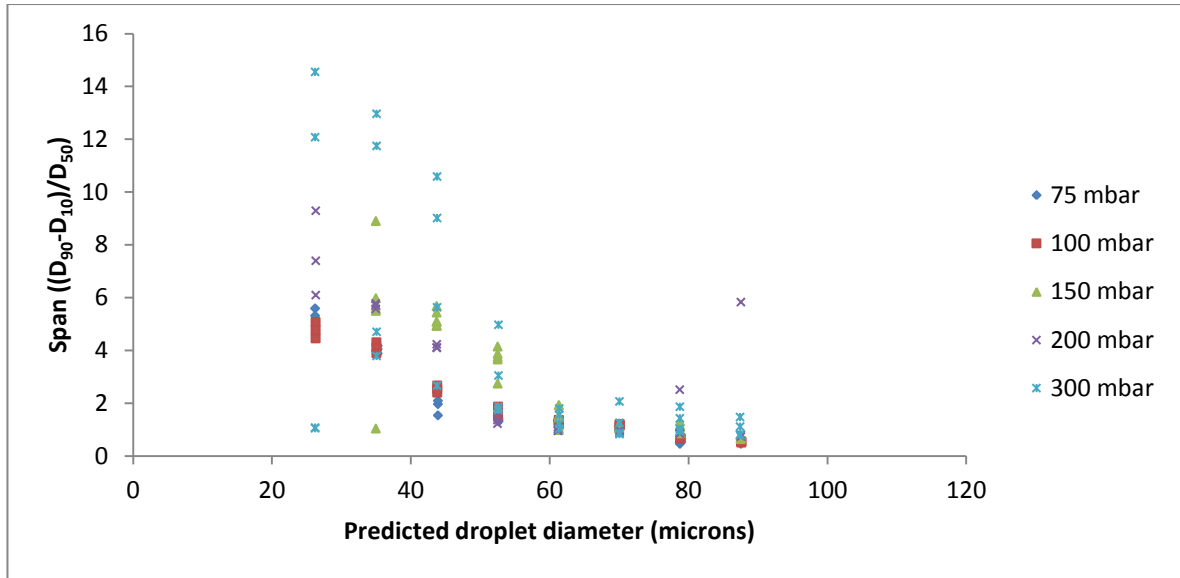


**Figure 3.13** Effect of pressure drop and liquid flow rate on droplet size for 2-propanol, 50°C

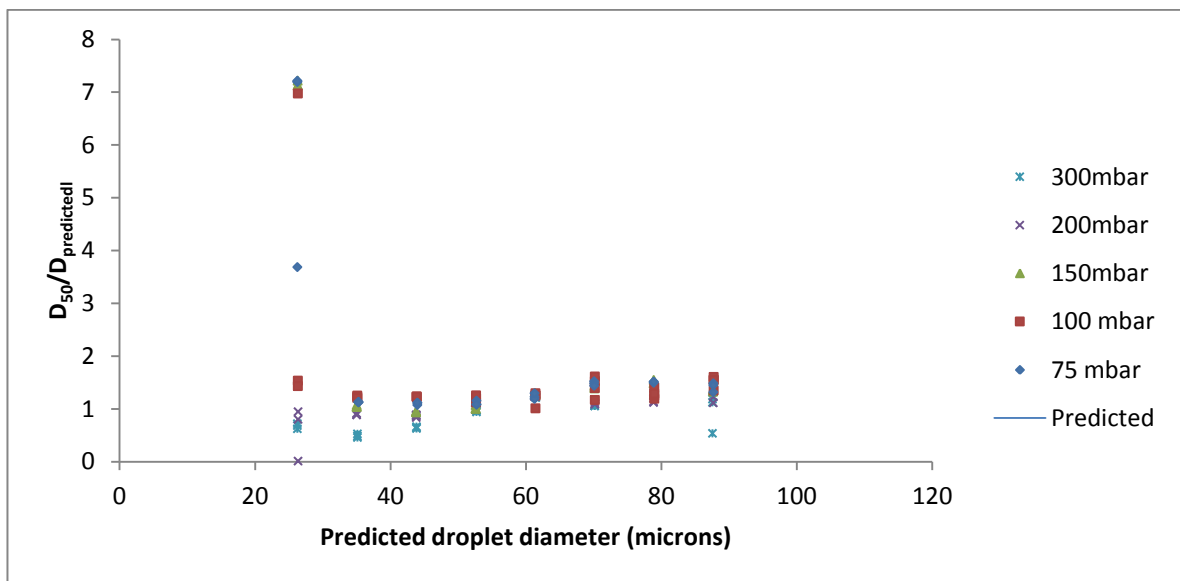


**Figure 3.14** Effect of pressure drop and liquid flow rate on droplet size for 2-propanol, 50°C

## Characterisation of Atomization

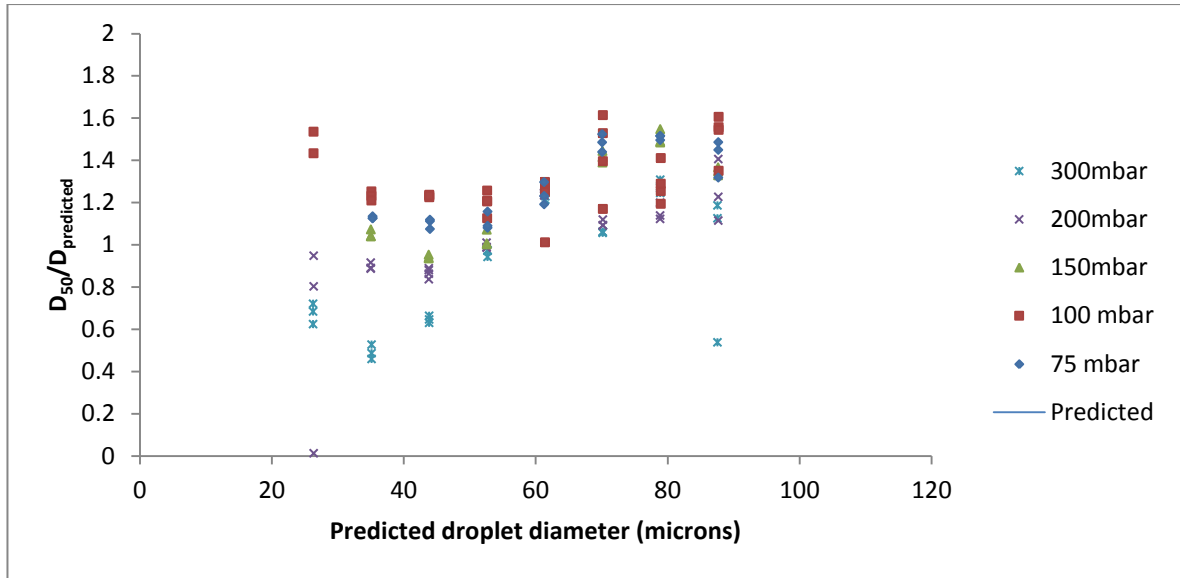


**Figure 3.15** Effect of pressure drop and liquid flow rate on span for 2-propanol, 50°C

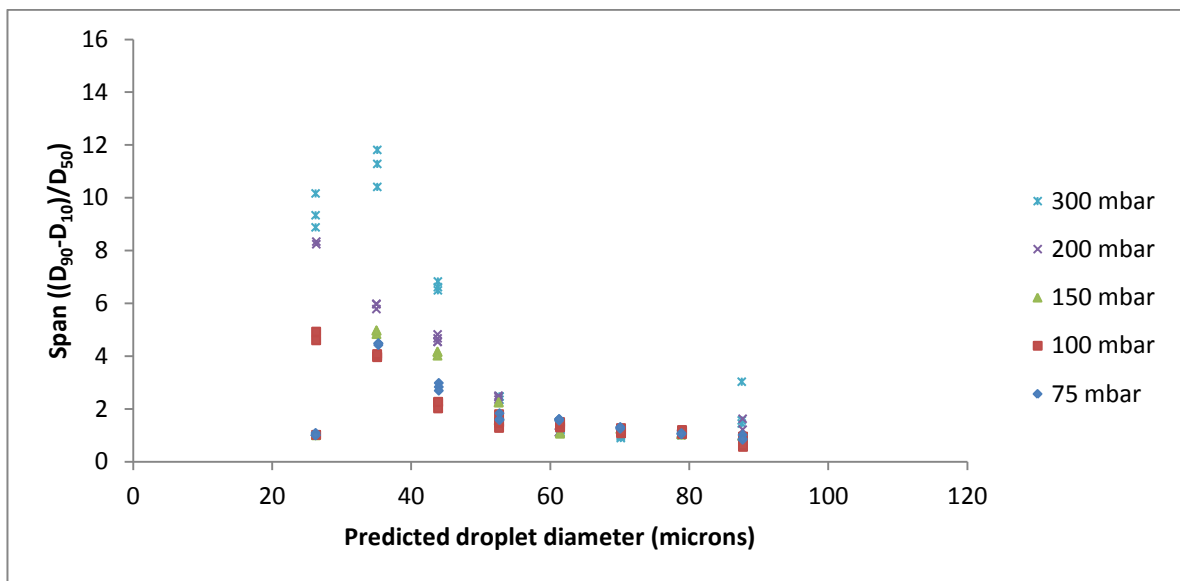


**Figure 3.16** Effect of pressure drop and liquid flow rate on droplet size for ethanol, 50°C

## Characterisation of Atomization



**Figure 3.17** Effect of pressure drop and liquid flow rate on droplet size for ethanol, 50°C



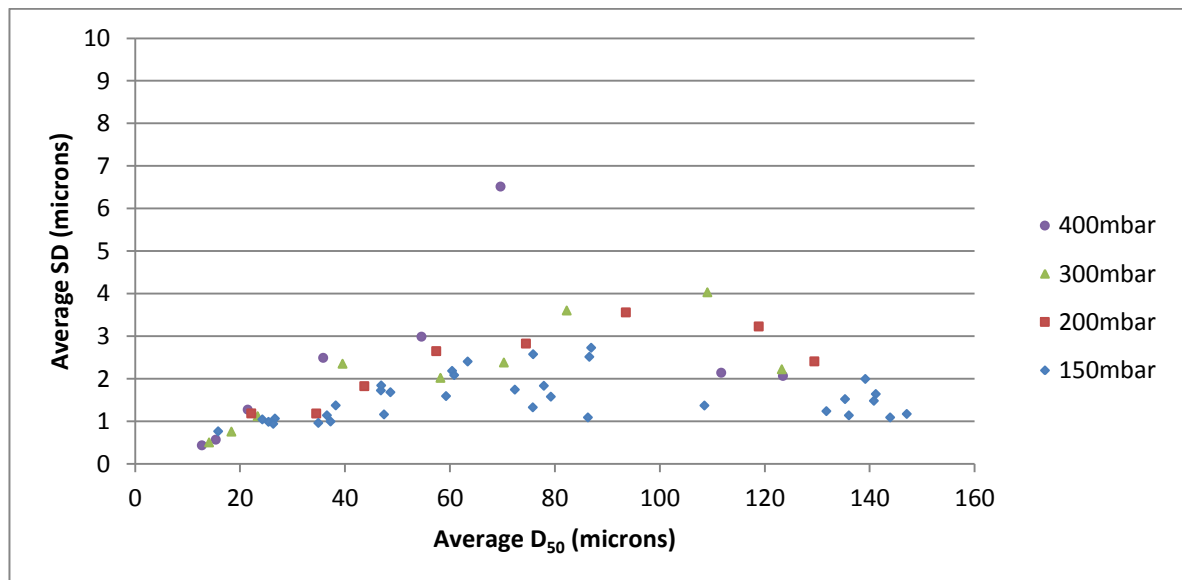
**Figure 3.18** Effect of pressure drop and liquid flow rate on span for ethanol, 50°C

A consistent pattern of change in results from those obtained at 25°C is observed for both alcohols. Average  $D_{50}$  values at the smallest predicted droplet size conditions are variable, with some runs yielding average  $D_{50}$  values of approximately seven times that of runs performed at nominally identical conditions. At larger target droplet sizes a

## Characterisation of Atomization

general pattern of under-prediction of droplet size at higher pressure drops is again evident, similarly to the 25°C data, however at the higher temperature inter-run variability is seen to increase over that observed previously. Span values at low predicted droplet sizes show large values, similarly to the low temperature data, however span values below one are observed across the droplet size range at pressure drops above 150 mbar.

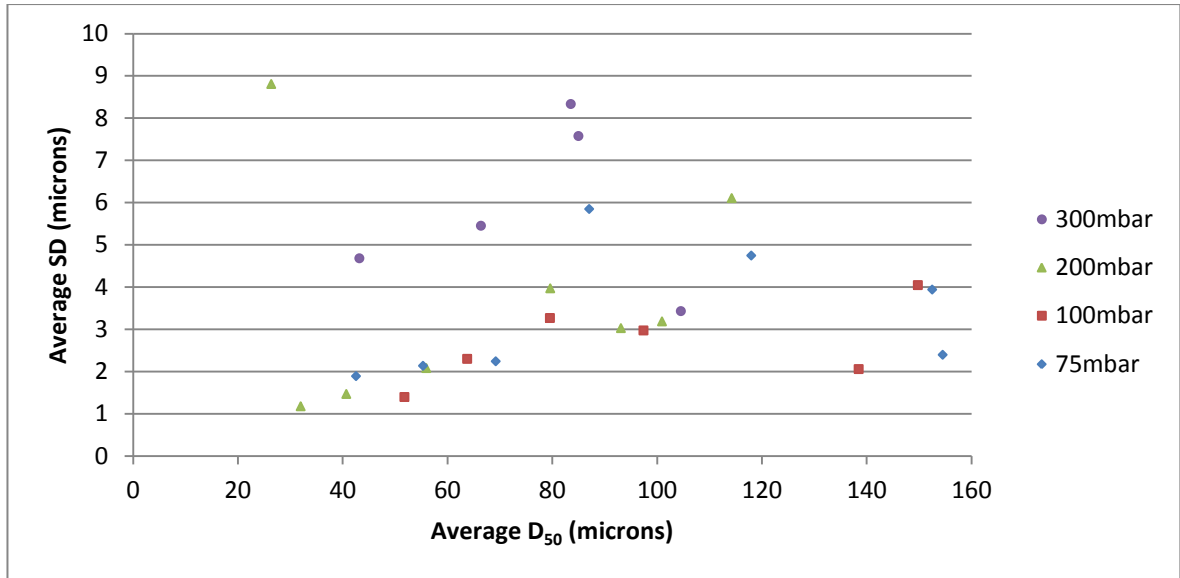
Further characterisation of the variability over the pressure drop range at the two operating temperatures is possible by evaluating the variance of the 300  $D_{50}$  measurements taken over the course of the five minute duration of each of the measurement runs. Figure 3.19 to Figure 3.22 summarise the predicted size standard deviation values for the experimental runs performed at the pressure-drop – temperature combinations.



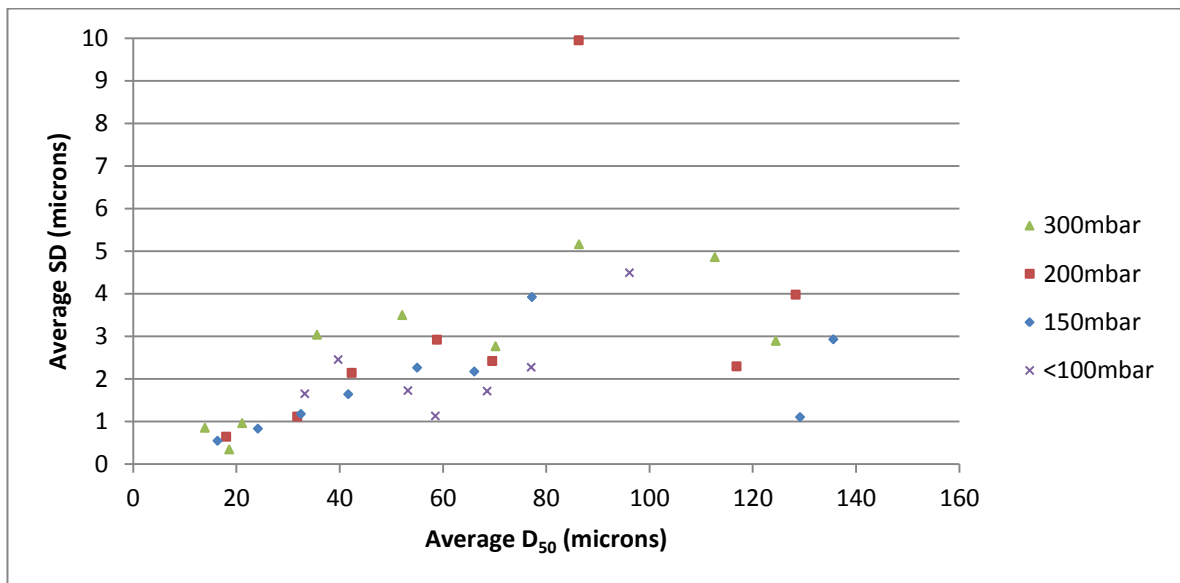
**Figure 3.19** Variation of median droplet size standard deviation with average median droplet size for 2-propanol, 25°C



## Characterisation of Atomization

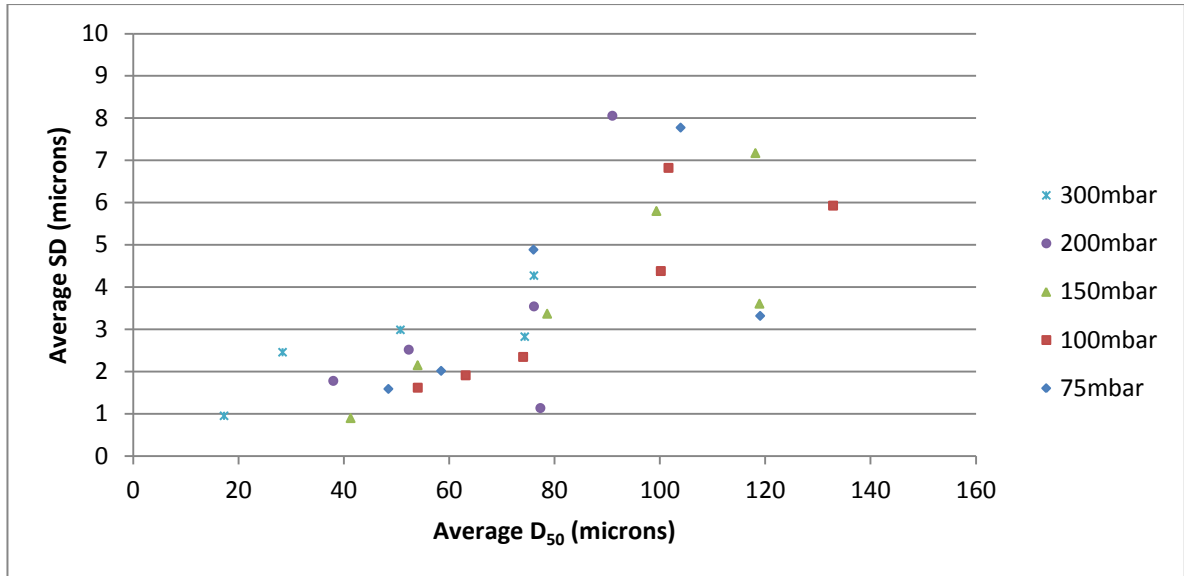


**Figure 3.20** Variation of median droplet size standard deviation with average median droplet size for 2-propanol, 50°C



**Figure 3.21** Variation of median droplet size standard deviation with average median droplet size for ethanol, 25°C

## Characterisation of Atomization



**Figure 3.22** Variation of median droplet size standard deviation with average median droplet size for ethanol, 50°C

Consistent with the observations for the  $D_{50}$  and span values, a pattern is evident between the alcohols for standard deviation. Standard deviation of less than 3  $\mu\text{m}$  is apparent at 25°C with a pressure drop of 200 mbar or less for both alcohols at predicted droplet sizes less than 80  $\mu\text{m}$ . When considering the entirety of the data ethanol was seen to give larger standard deviations than 2-propanol at the higher pressure drops, and an increase in standard deviation with predicted droplet size is seen. Increasing the operating temperature to 50°C causes an increase in standard deviation, however for both alcohols standard deviations less than 4  $\mu\text{m}$  are able to be obtained when operating at 100 to 200mbar pressure drop at predicted droplet sizes below 80  $\mu\text{m}$ . Outside this range standard deviations between 5 and 9  $\mu\text{m}$  can be experienced, particularly at higher pressure drops. The increase in standard deviation for droplets would translate to an increased variance of the dried particle size distribution, hence an upper limit of 80  $\mu\text{m}$  was imposed during the particle formation activities described in Chapter 4.

Interestingly the standard deviation appears to reach a maximum in the vicinity of 100  $\mu\text{m}$  median size, corresponding to Weber numbers in excess of 50. The increase in standard deviation at this point is in agreement with the accepted theory for flow focussing; however the subsequent decrease in standard deviation with increasing liquid flow indicates that the Weber number may not be the only parameter of interest when atomizing liquids by this method.

### **3.2.3.2.3. Atomization of mometasone furoate and fluticasone propionate solutions**

An evaluation of the reproducibility for repeat runs was conducted for solvent and solvent with solute. The difference between maximum and minimum average  $D_{50}$  was used as the basis for a t-test, and a 95% confidence interval constructed using the associated standard deviations (Mason, 2003). Standard deviations were assumed to be unequal between samples and standard errors calculated accordingly. Significant difference is observed between the repeat runs in almost all cases; the few exceptions are due to large standard deviations rather than close similarity between median sizes. As noted earlier a degree of polydispersity was observed for all experimental runs and is apparent in the median droplet size standard deviation data presented as Figure 3.19 to Figure 3.22. The significant difference between runs is therefore not a result of a very small standard error but due to real difference in the droplet distribution produced between experimental runs conducted under nominally identical conditions. As optimal operating conditions were unable to be identified using statistical analysis, evaluation of the span and median size standard deviation and process efficiency was used to identify operating conditions for spray drying experiments. The observed effect of operating

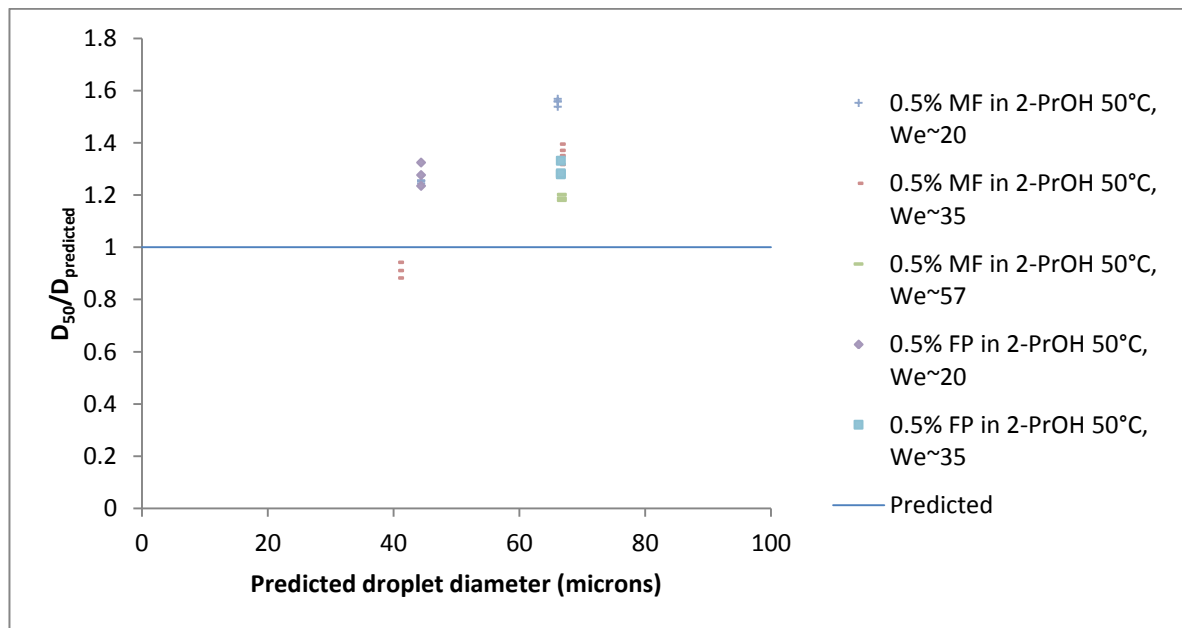
## Characterisation of Atomization

pressure upon both span and reproducibility of droplet production resulted in a limit of 150 mbar pressure drop being employed for use in subsequent API solution experiments

Two distinct droplet distributions are required to characterise the behaviour of the two APIs during spray drying, as was the case for aqueous sodium chloride solutions. The need to maintain the solution temperature at 50°C also limits the minimum predicted droplet size to 40 µm in order to avoid increased span and consequent issues with wide particle size distributions. Three liquid flow rate and pressure drop combinations were selected at each of two target predicted droplet sizes for evaluation with API solutions.

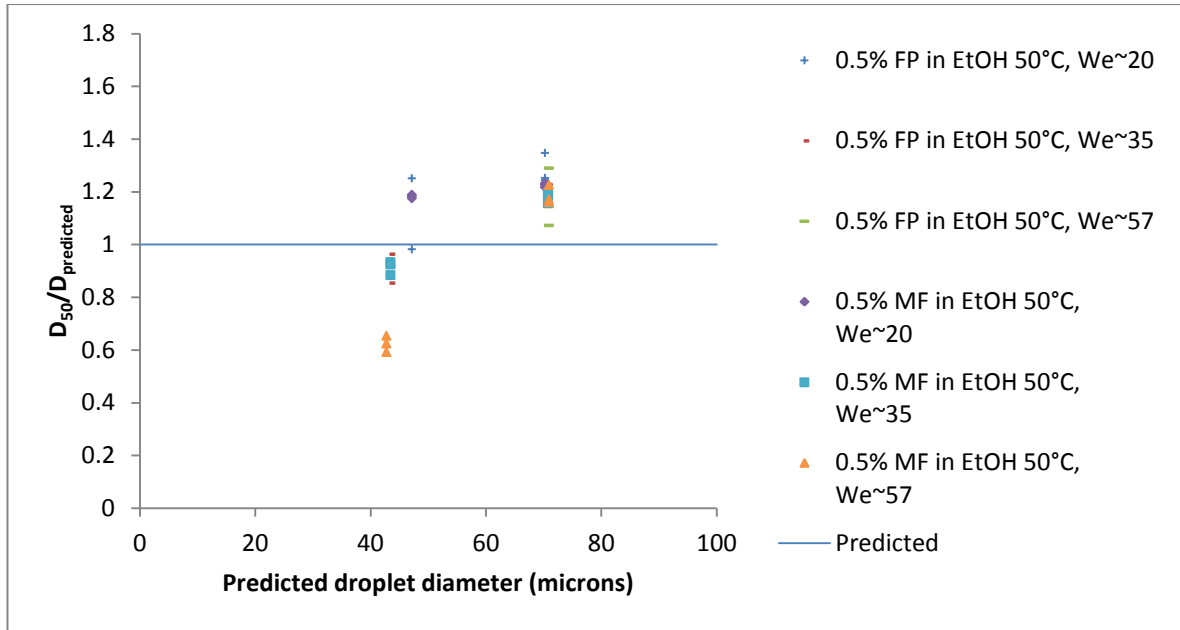
$\frac{D_{50}}{D_{\text{predicted}}}$  and span data produced by the experimental runs are summarised in Figure

3.23 to Figure 3.26.

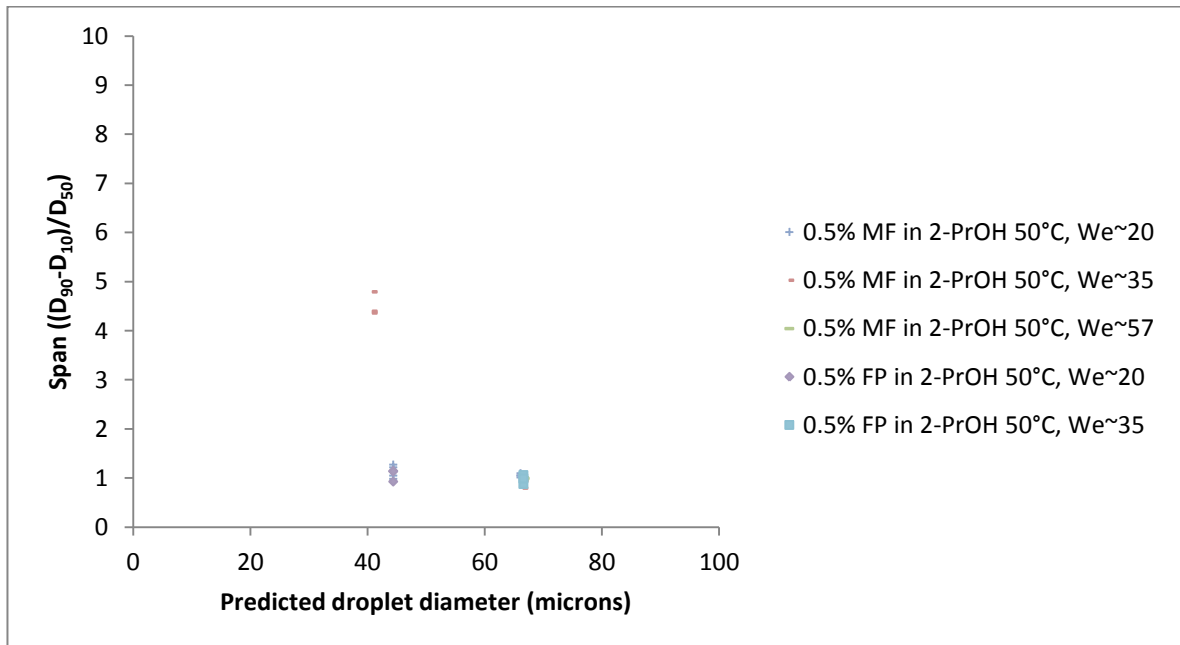


**Figure 3.23** Effect of pressure drop and liquid flow rate on droplet size for 0.5%w/w API solutions in 2-propanol, 50°C

## Characterisation of Atomization

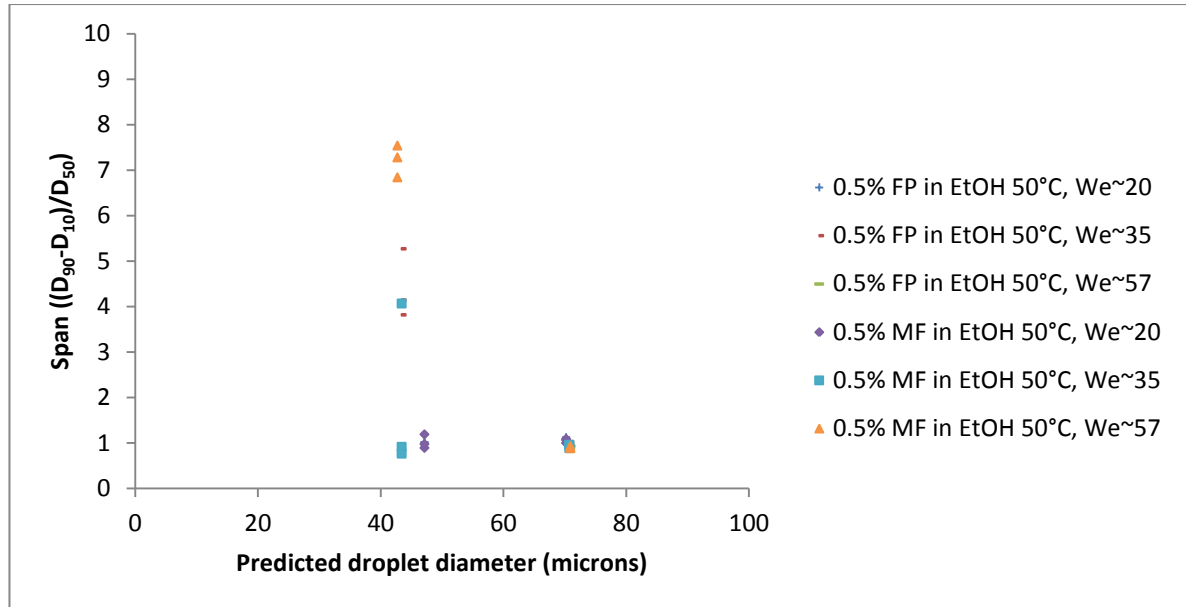


**Figure 3.24** Effect of pressure drop and liquid flow rate on droplet size for 0.5%w/w API solutions in ethanol, 50°C



**Figure 3.25** Effect of pressure drop and liquid flow rate on span for 0.5%w/w API solutions in 2-propanol, 50°C

## Characterisation of Atomization



**Figure 3.26** Effect of pressure drop and liquid flow rate on span for 0.5%w/w API solutions in ethanol, 50°C

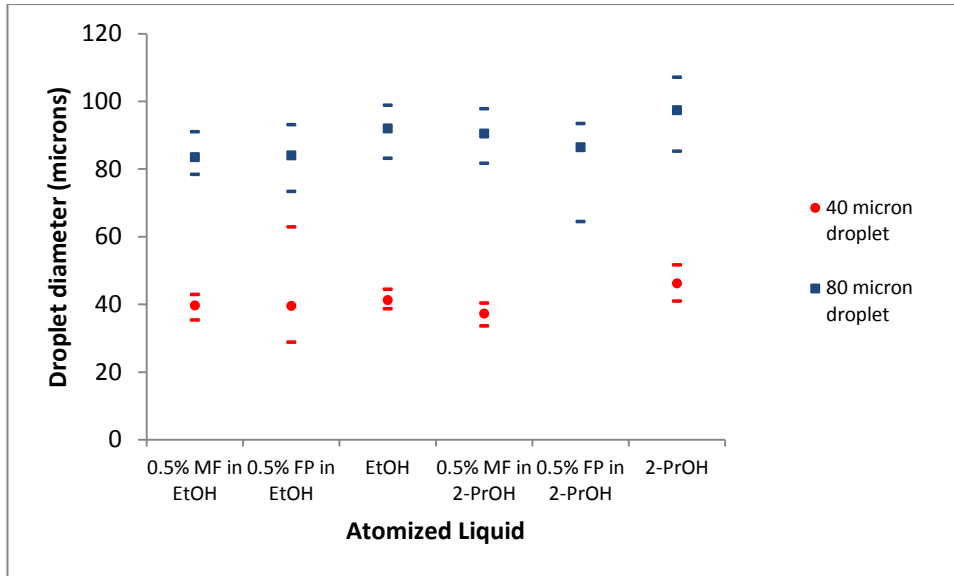
Conditions at each target droplet size were chosen to give Weber numbers of approximately 20, 35 and 60, however following the first set of evaluation runs using mometasone furoate in ethanol the smaller target droplet size condition at  $We = 60$  was abandoned as a cone spray, rather than liquid jet, was formed at the atomizer orifice. Formation of a cone spray resulted in a large increase in span, characterising a wide distribution of droplets being of little use in the spray drying evaluation. Selection between the remaining two conditions at the smaller target droplet size was a compromise between actual droplet size and span. At  $We = 20$  a small span is produced, however the median droplet size of approximately  $55 \mu\text{m}$  will result in a significant degree of droplet distribution overlap with that of the larger size with median droplet sizes of  $82$  to  $94 \mu\text{m}$  being produced across the three conditions evaluated. Operation using conditions characterised by  $We = 35$  results in a median size of approximately  $40 \mu\text{m}$ ; the span however did increase to approximately 4 in a number of the evaluation

## Characterisation of Atomization

runs. Analysis of the droplet distribution data (as shown in Figure 3.28) reveals a bimodal distribution for  $We = 35$  conditions with two distinctly separate modes at approximately 40 and 200  $\mu\text{m}$ . The distribution around the 40  $\mu\text{m}$  mode is narrow and gives a good droplet distribution for generation of spray dried API. Material produced as a result of droplets drying from the mode at approximately 200  $\mu\text{m}$  should be readily recognisable during characterisation of dried material and so the impact of such particles upon analytical results can be accounted for.  $We = 35$  conditions of  $12 \text{ mL h}^{-1}$  solution flow and 150 mbar pressure drop were therefore selected for use in API spray drying studies.

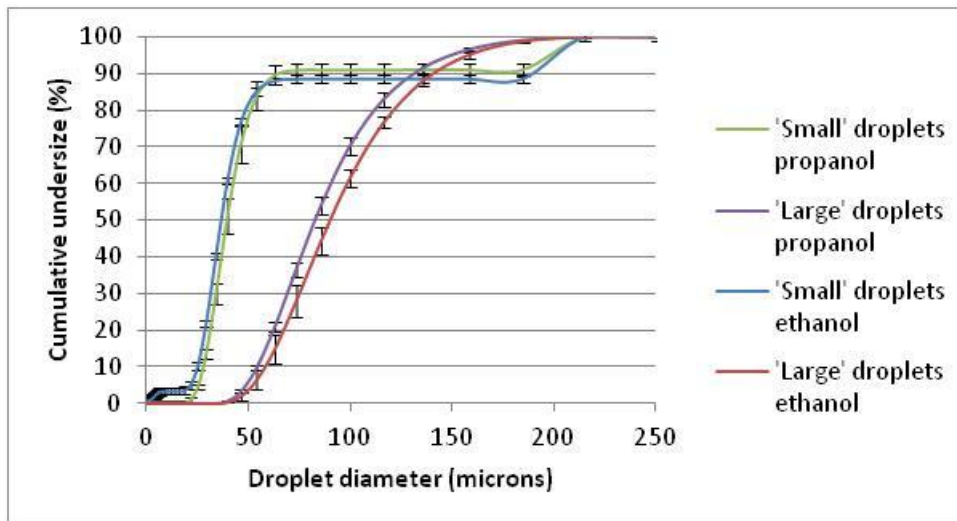
Very similar values for span are observed for the three sets of operating conditions evaluated for generation of the larger droplet size. The  $We = 20$  condition produced the largest median droplet size, however some lateral movement of the jet was observed during measurement, raising concerns regarding the jet stability when used within the spray dryer. Operating conditions used to give  $We = 57$  resulted in the generation of a smaller median droplet size and poorer reproducibility as evident in Figure 3.23 and Figure 3.24. The  $We = 35$  operating condition of  $26 \text{ mL h}^{-1}$  liquid flow rate and 100mbar pressure drop producing approximately 80  $\mu\text{m}$  diameter droplets was therefore selected for the API spray drying evaluation. A comparison of the average droplet diameters produced at the target sizes is presented for the solvents and solutions as Figure 3.27, with minimum and maximum bars for the mean values indicated.

## Characterisation of Atomization



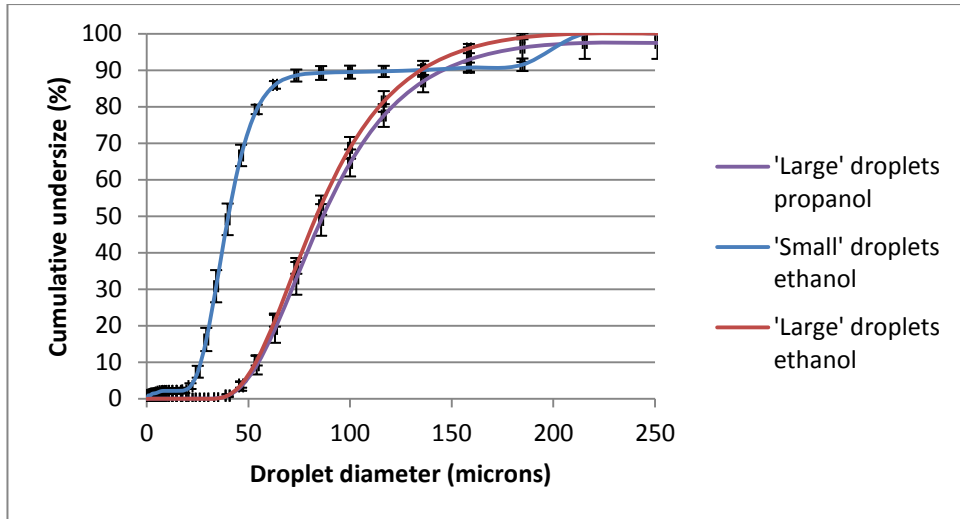
**Figure 3.27 Comparison of solvent and solution droplet sizes**

The average droplet size distributions with standard error bars generated for mometasone furoate and fluticasone propionate solutions at the chosen spray drying conditions are shown as Figure 3.28 and Figure 3.29 respectively.



**Figure 3.28 Droplet size distributions for 0.5%w/w mometasone furoate solutions in ethanol and 2-propanol**





**Figure 3.29** Droplet size distributions for 0.5%w/w fluticasone propionate solutions in ethanol and 2-propanol

### 3.3. Conclusion

The high speed imaging demonstrates that the FFD atomizer, under appropriate operating conditions, is capable of generating a droplet train of narrow polydispersity. Additionally the operating window within which reproducible droplet generation is possible encompasses a droplet size range of substantial volume difference. The Weber number calculated for the particular experimental conditions effectively describes the important operating characteristics of the system, however the liquid: gas ratio would also appear to be important, with images suggesting increasing variance with increasing relative flow of liquid. Reduction in the liquid: gas flow ratio beyond a critical value is known to induce changes in the droplet formation mode, attributed to meniscus instability recognisable by changing position of the meniscus with time. The meniscus of the liquid thread appears relatively stable for the liquid: gas flow ratios evaluated, with no large change in position with time, however at the more extreme conditions chosen for imaging some movement of the meniscus is evident. A transition to dripping from jetting is known to occur at low liquid: gas volume flow ratios, of the order 0.0001

however no information is available regarding the stability of droplet formation at high ratios. At some point the required droplet formation mechanism will become unsustainable and formation may be taking place at the limits of stability for the extreme cases evaluated here, however continuous droplet formation is observed at liquid: gas flow ratios as high as 0.01, demonstrating the wide operating range of the atomization technique.

Successful flow focusing beyond the postulated Weber number limit of 40 would also appear possible from the perspective of preserving axisymmetric break-up of the liquid stream. Droplet formation under conditions encompassed by the Weber number range 6 to 74 is observed to occur with apparently stable liquid thread, with no evidence of helicoidal motion. Some difference in the nature of droplet formation is however apparent, identified by the use of laser diffraction. A systematic variation in the droplet size predicted by Equation 3.1, Equation 3.2 and Equation 1.15 is observed with pressure drop; an increase in pressure drop results in a progressively smaller droplet size compared to the value predicted. An additional trend of over-prediction then under-prediction of droplet size is seen with increasing droplet size at a single pressure drop, with some evidence of an over-prediction minimum within the range. This may indicate additional factors or interactions being important in the control of droplet formation, worthy of further exploration. The effect is partially explained by the work of Gordillo (Gordillo *et al.*, 2001b), which accounts for the impact of higher pressure drops and increasing Weber number, however the under-prediction at lower pressure drop and Weber number remains unexplained.

## Characterisation of Atomization

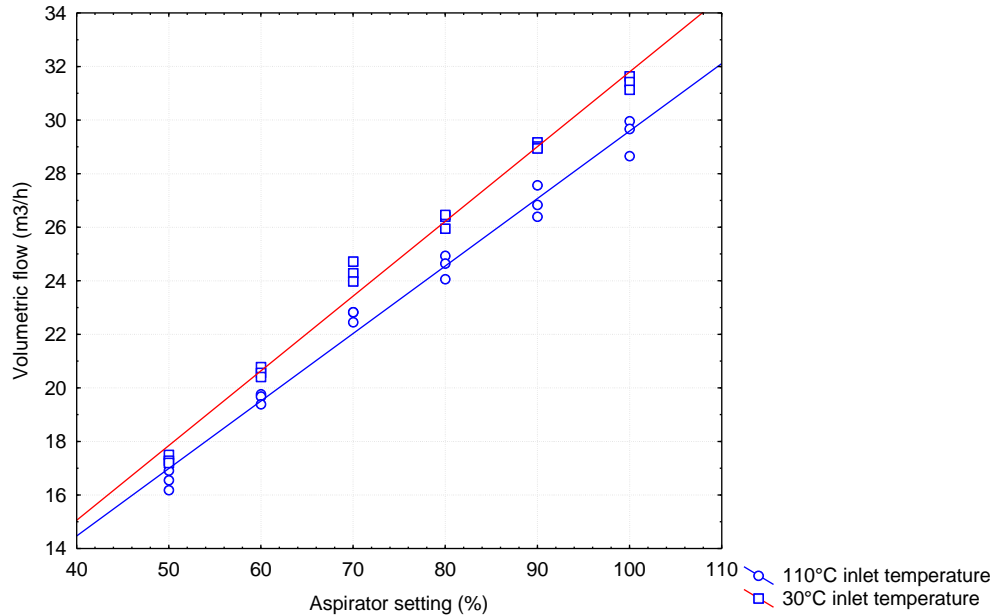
Atomization of water or aqueous sodium chloride solutions yielded results with greater variability than for alcohols or alcoholic solutions, particularly at small droplet sizes with an average coefficient of variation of 4.5% for aqueous sodium chloride compared to 2.8% for mometasone furoate in 2-propanol. The wider spread may be indicative of additional factors attributable to either the increased surface tension or viscosity unaccounted for in the current control theories. Repeatability of atomization from the nozzle used was also observed to be poorer than expected, with a statistically significant difference in median droplet size apparent between nominally identical runs. An appreciable range of median values for the droplet size distributions was observed for both sodium chloride and mometasone furoate solutions; as with the within run results aqueous sodium chloride solutions were observed to be more variable than mometasone furoate in alcohol. Average median droplet sizes for nominally identical runs ranged from 29.3 to 38.7  $\mu\text{m}$  and 67.0 to 74.0  $\mu\text{m}$  for the 35 and 70  $\mu\text{m}$  sodium chloride solution droplet sizes, compared to 38.4 to 40.5  $\mu\text{m}$  and 81.9 to 84.7  $\mu\text{m}$  for 0.5% w/w mometasone furoate in ethanol at the 40 and 80  $\mu\text{m}$  droplet sizes respectively. Whilst still being able to produce the difference in droplet size distribution and subsequent particle size distribution required within this work, the variability may make the differences in output particle properties more difficult to discern. A robust analysis of the repeatability of flow focussing systems is not available, hence it is not possible to determine whether the observations made are generic or a feature of the particular atomizer used.

## **4. SPRAY DRYING**

### **4.1. Drying gas flow calibration**

Drying gas flow on the Buchi B-290 is regulated using a fan speed controller incremented in percent, rather than being described using linear or volumetric gas flow. In order to define the drying gas flow rate range described by the scale, and to check the linearity of the response, calibration was performed across the flow rate range at two temperatures. A hot wire anemometer (Testo AG, Lenzkirch, Germany) was used to measure air velocity within the measurement pipe recommended by the manufacturer (Buchi Labortechnik, Flawil, Switzerland) connected to the cyclone outlet. The velocity was measured across the control range of the aspirator (50 to 100 %) in increments of 10 %. The rate was measured in ascending aspirator setting, and repeated a further two times at each measurement temperature. Velocities were measured at 30 and 110°C (the maximum operating temperature of the anemometer) and converted volumetric flow rate to understand the impact of temperature on flow and linearity. Results for the calibration are presented as Figure 4.1.

## Spray Drying



**Figure 4.1 Aspirator calibration**

Linear regression analysis was performed using Statistica 8 (Statsoft Inc., Tulsa, USA) for volumetric flow rate data at each temperature. The correlation coefficient of 0.99 for both temperatures demonstrates good linearity of response of volumetric flow rate with the aspirator scale, and shows the linearity is unaffected by operating temperature across the range evaluated.

### **4.2. In-situ atomizer validation using sodium chloride**

The operating conditions optimised for droplet size and distribution width identified in Chapter 3 were defined for jets issuing into stagnant air, however the environment within the spray dryer involves a drying gas stream. A number of runs were therefore conducted using sodium chloride solutions to evaluate the impact of droplet production within a dynamic environment. Two sets of operating conditions were defined in section 3.2.3.2.1 capable of producing droplets with average sizes of approximately 35 and 70  $\mu\text{m}$ ; use of solutions of different sodium chloride concentration should produce a range

## Spray Drying

of dried sodium chloride particle sizes that can be correlated to droplet size and concentration assuming the atomizer performs similarly within the spray dryer. Sodium chloride was chosen as the solute as it is known to produce solid crystals of low aspect ratio when spray dried (Tang *et al.*, 2006). The high growth rate relative to nucleation rate (Mullin, 2001) of small inorganic molecules increases the likelihood of a single crystal being produced under the range of conditions evaluated (Langrish, 2009); if multiple viable nuclei did grow the drying droplet would ensure agglomeration, resulting in a single particle of low aspect ratio being formed from the spherical droplet at the latter stages of evaporation.

Solution concentrations of 0.01, 0.03 and 0.05 mass fraction sodium chloride were spray dried using an inlet temperature of 160°C and an aspirator setting of 100 %. The temperature of the atomizer, feed tubing and syringe pump was regulated at 25°C to ensure droplet generation conditions were as intended. Run times of between ninety minutes and six hours were necessary to produce sufficient material for laser diffraction analysis to be performed and to allow scanning electron micrographs to be collected. Spray drying runs and subsequent laser diffraction sizing were performed as defined below.

### **4.2.1. Methods**

#### **4.2.1.1. Spray drying**

The required mass of sodium chloride was weighed into a beaker using a 4 decimal place analytical balance to a 0.1 % weight tolerance. The required mass of deionised water was added to the beaker and the contents agitated for 30 minutes to ensure dissolution. The pump was flushed twice with deionised water and the solution drawn into the pump

## Spray Drying

by withdrawing the piston. The atomizer was located into the top of the drying chamber and connections were made to the pump outlet and atomizing gas regulation valve. The temperature regulation circuit was connected and the bath was switched on to circulate the regulation fluid. The Inlet temperature and aspirator set points were entered and the aspirator fan was switched on. Once the aspirator was operational the heating element was switched on and the outlet temperature was allowed to stabilise. The pressure indicated on the atomizer gauge was noted, and the needle valve adjusted to approximately 60 mbar below the target pressure value. Once the pressure reading had stabilised, with further adjustment of the needle valve if necessary, pumping of solution was commenced. An abrupt increase in pressure was noted as liquid atomization commenced, at which point the needle valve was adjusted iteratively to reach a pressure within 5 mbar of the setpoint. Initial atomization was of water only, as the remainder of the rinse was present within the tubing at the pump outlet. A brief drop in pressure was observed prior to atomization of solution, attributed to an empty portion of tubing at the pump outlet emptied when the cylinder was withdrawn prior to refilling with solution after the second solvent flush. Upon atomization of solution the atomizer pressure, atomizer temperature, spray dryer inlet temperature and outlet temperature were recorded, and subsequently recorded at 15 minutes, 30 minutes and at 30 minute intervals until completion of the spray drying run. At completion of spray drying the pump was stopped and the atomizing gas flow stopped by closing the needle valve. The spray dryer heater was switched off, but the aspirator left running at setpoint until the outlet temperature had fallen below 70°C, at which point the aspirator was stopped. Particles were recovered by disconnecting the cyclone collection pot and pouring the recovered sodium chloride into a pre-weighed collection vial via a powder funnel, with

## Spray Drying

gentle tapping of the side of the collection pot to encourage flow. The vial was weighed to determine the mass of powder recovered and the vial was covered with a filter paper secured with a cable tie and placed in a sealed desiccator containing 4A molecular sieve to minimise exposure to moisture until analysis was able to be performed. The product-contact components of the spray dryer were disassembled and washed down to remove any adhered sodium chloride, and the pump, connecting tubing and atomizer liquid conduit were thoroughly flushed twice with deionised water.

### **4.2.1.2. Particle size measurement**

Laser diffraction analysis was performed using a Sympatec Helos instrument, fitted with Vibri feed and Rodos/M dispersion systems (Sympatec GmbH, Claustal, Germany). The pressure drop used to ensure dispersion of the sample was selected by evaluating a range of pressures whilst maintaining a gap of 2 mm. A plateau region was identified in a plot of pressure against median particle size of spray dried sodium chloride for a single batch of spray dried material, the midpoint of the plateau (3 bar pressure drop) was selected for measurements to provide the best compromise between dispersion and particle attrition. Measurements were performed using the R2 lens (working range 0.25 to 87.5  $\mu\text{m}$ ); the R1 lens was evaluated initially however the upper limit of the working range of the lens is 35  $\mu\text{m}$  which may be insufficient to fully characterise all of the sodium chloride batches generated. Samples were measured in duplicate and were fed using a Vibri feed rate setting of 50 % until 5 seconds after the optical concentration fell below 1.0 %. A template was used to ensure a similar mass of powder was aligned optimally for feeding. The template consisted of a steel plate of 3 mm thickness with a 55 mm x 3.5 mm rectangular slot removed from the centre. The template was placed on



## Spray Drying

the vibrating platform of the feeder, powder loaded in and smoothed using a steel spatula until the slot was full with a powder surface level with the top of the plate. The plate was then removed to leave a loose compact ready for sizing.

### 4.2.2. Results and discussion

Results of the sizing are summarised in Figure 4.2. The  $X_{50}$  value obtained from Sympatec analysis is plotted against the predicted particle diameter,  $X$ , based on the diameter of a sphere produced from the mass of sodium chloride present within a droplet of the target particle size, calculated using Equation 4.1:

$$X_{pred} = \left( \frac{d^3 \cdot Y \cdot \rho_d}{\rho_s} \right)^{\frac{1}{3}} \quad \text{Equation 4.1}$$

Where  $d$  is the target droplet diameter (m),  $Y$  is the mass fraction of solute within the solution, and  $\rho_d$  and  $\rho_s$  are the droplet and solute densities respectively. Linear regression analysis was performed using Statistica 8 (Statsoft Inc., Tulsa, USA). The correlation coefficient ( $R^2$ ) of 0.9384 shows a good relationship between expected and actual particle size. Median sizes measured using laser diffraction are consistently smaller than predicted so either the droplet size produced within the spray dryer is smaller than that generated when generating jets in stagnant air, or the dimension evaluated by laser diffraction is not consistent with that used to characterise the droplet. Electron micrographs are presented for the spray-dried sodium chloride batches in Appendix 2; two micrographs representing the extremes of solute concentration and droplet size are shown as Figure 4.3 and Figure 4.4.

## Spray Drying

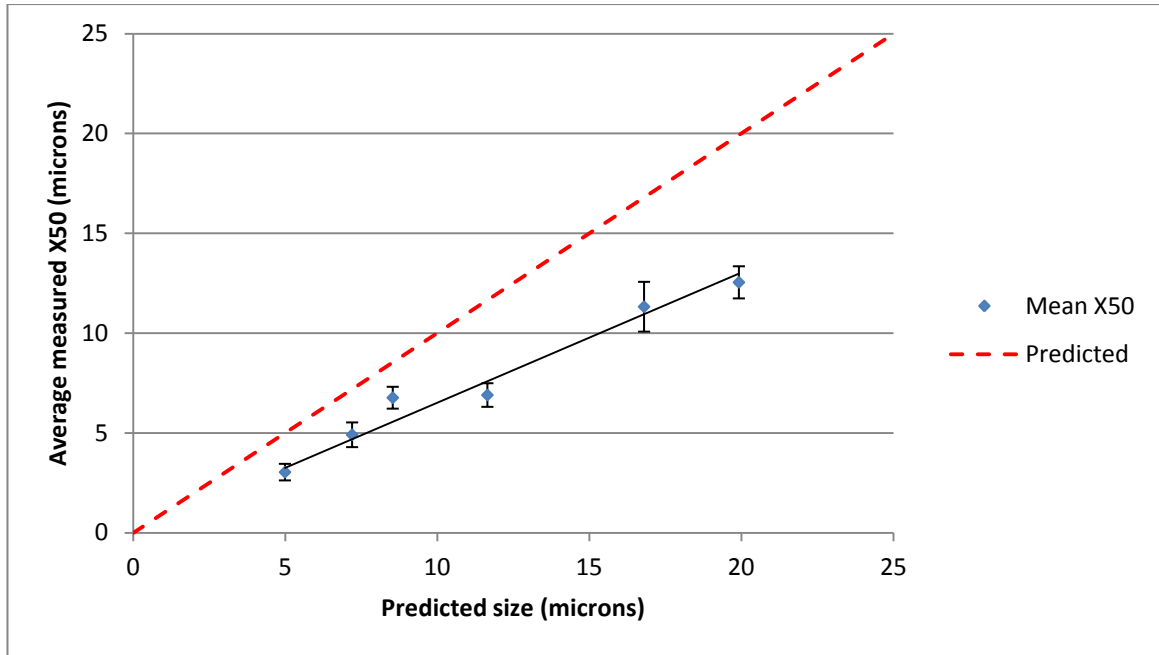
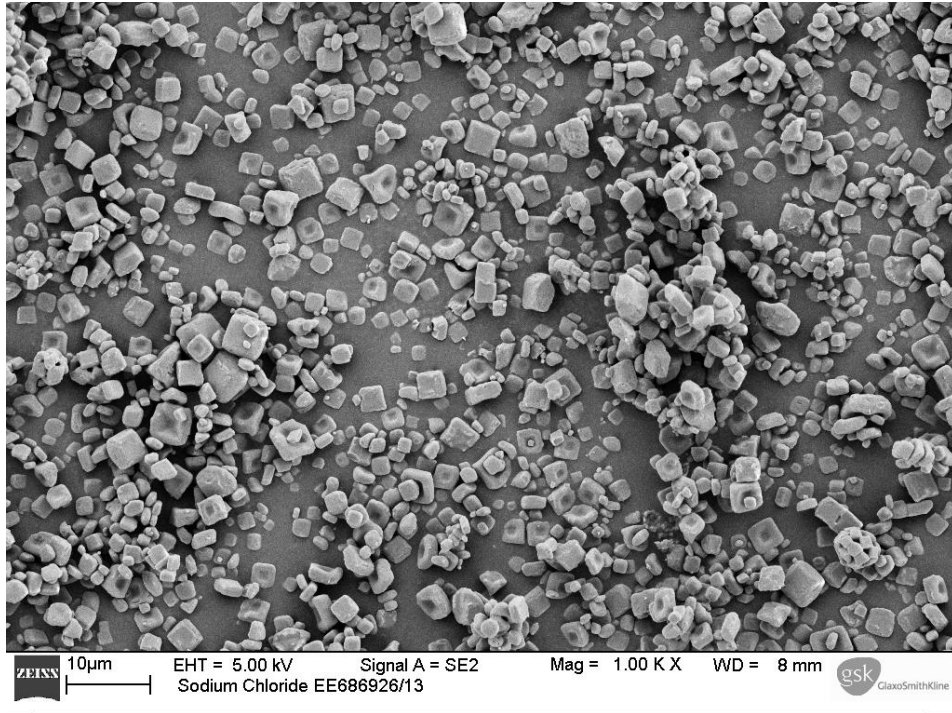
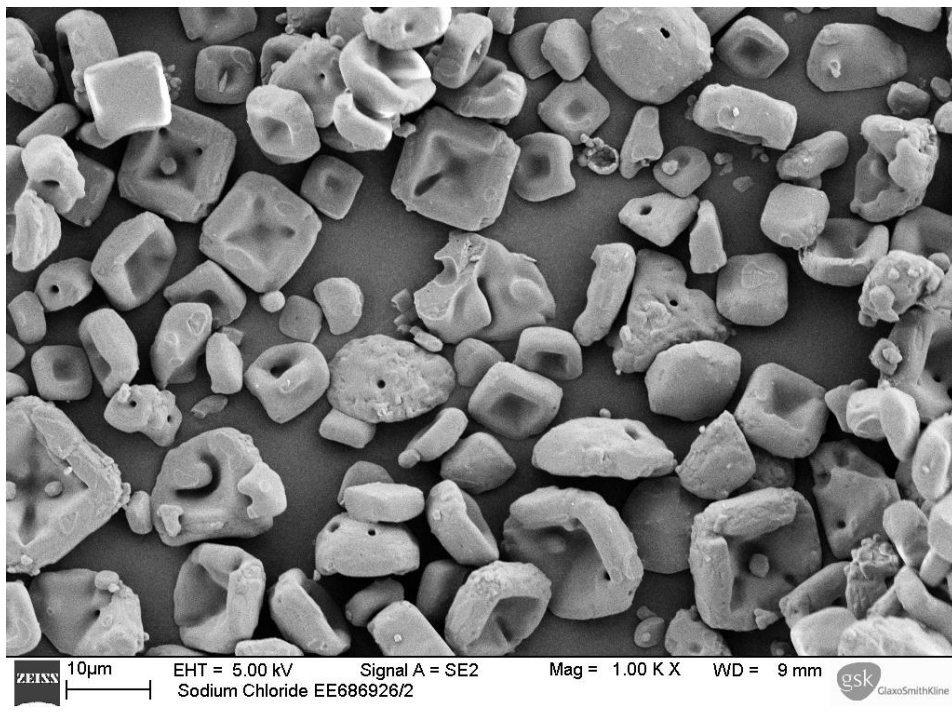


Figure 4.2 Comparison of measured median particle size to predicted size.

## Spray Drying



**Figure 4.3** Electron micrograph of sodium chloride produced at 1%w/w, c. 35µm droplet size



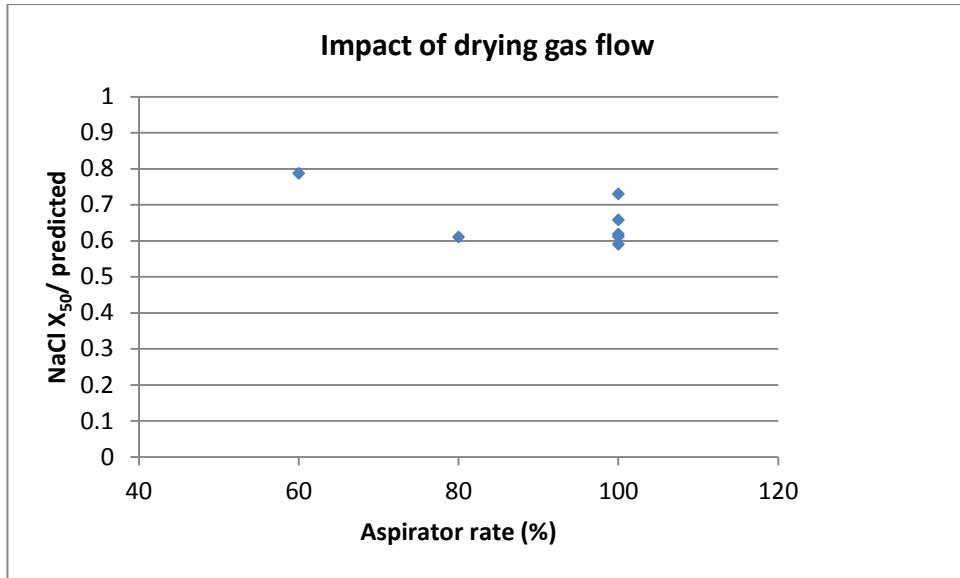
**Figure 4.4** Electron micrograph of sodium chloride produced at 5%w/w, c. 70µm droplet size

## Spray Drying

The predominantly cuboid morphology observed may present challenges with respect to deconvolution of the scattering pattern during laser diffraction. The deconvolution algorithm used to provide dimensional data from the intensity of light at the detector of the laser diffraction instrument is based upon Fraunhofer theory, and assumes diffraction of light by a sphere to be the source of the diffraction pattern (Xu & Di Guida, 2003). Deviations from sphericity could therefore make the derived particle size measurement less accurate, however spheres have been shown to approximate cuboids well for laser diffraction analysis (Heffels *et al.*, 1996, Yamamoto *et al.*, 2002). An alternative explanation is that the offset between actual and predicted particle size is as a result of the inter-run variability when atomizing aqueous solutions observed in section 3.2.3.2.1. The reproducibility was however observed to be random about the predicted target value for the operating pressure employed for this work; hence the systematic over-prediction of size observed during sodium chloride spray drying would be unlikely.

The consistently low value for measured median size of spray dried sodium chloride with no obvious cause other than processing conditions indicates a reduction in predicted droplet size when operated under the conditions experienced within a spray dryer. A set of experimental runs was conducted at reduced drying gas flow to compare the impact of aspirator settings of 100 %, 80 % and 60 %. Normalised dried particle median sizes measured by laser diffraction analysis for these runs are presented as Figure 4.5.

## Spray Drying



**Figure 4.5** Median size of sodium chloride produced at reduced dry gas flow rate

A clear trend is difficult to identify given that the difference in normalised particle size is similar across the change in aspirator rate due to the variability at the 100% setting; however there appears to be evidence of an increase in dried particle size with a decrease in drying gas flow. If the drying gas stream is responsible for reduced droplet size, then subsequent calculation of relationships between operating parameters and dried particle characteristics will be difficult to establish in absolute terms. The strong correlation between measured and predicted size shown in Figure 4.2 demonstrates however that the impact of operating parameters upon output particle characteristics is likely to be able to be elucidated on a relative basis.

The spray drying studies using sodium chloride have therefore established that the flow focusing atomizer is producing droplet populations that are aligned to the operating conditions and consistent with the relationships between droplet population and operating condition discussed in section 3.2. The good correlation between predicted

and actual dried particle  $X_{50}$  for sodium chloride gives confidence that the atomizer is capable of producing similar droplet distributions to those apparent in Chapter 3 when used for spray drying in the Buchi B-290.

### **4.3. Spray drying of active pharmaceutical ingredients**

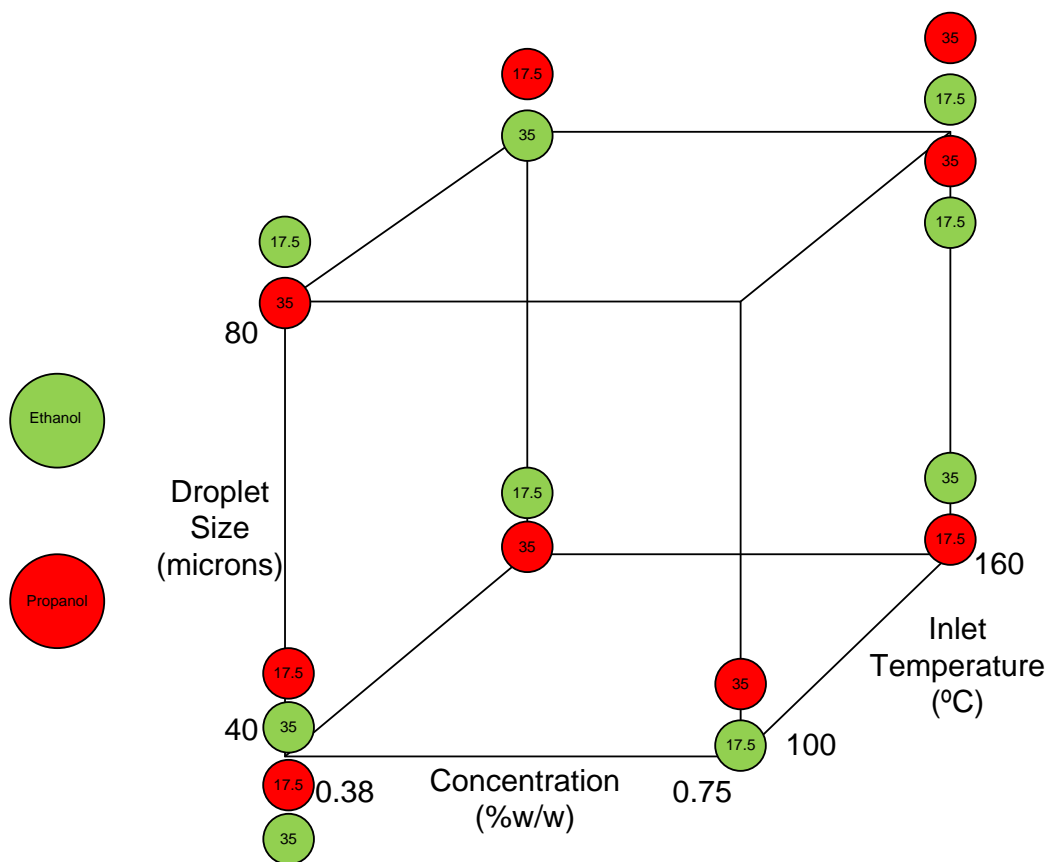
The operating parameters of the spray dryer and the attributes of the solution to be spray dried have a direct impact upon the physicochemical properties of the recovered dry particles, as described in the Introduction. In order to evaluate the magnitude of the effect of the processing variables a two-level factorial experiment was devised using Design Expert 7 ("DX7", Stat-Ease Inc., Minnesota, USA). Five factors - droplet size, solution concentration, drying gas flow and inlet temperature as numerical variables and solvent type as a categorical variable were investigated in the spray drying study; a full factorial experiment would require a minimum of 32 runs so a fractional factorial design was adopted as an efficient way of obtaining the information. A half-factorial (resolution V) design was chosen to allow identification of main effects and two-factor interactions without confounding of factors or interactions. A similar design has been used previously to successfully investigate the impact of spray drying process variables upon the formation of composite particles (Tajber, Corrigan, & Healy, 2009).

Inclusion of centre-points, typically used to estimate curvature and experimental error, was not possible given the lack of an intermediate droplet size condition so repeat runs were conducted at selected experimental points. Experimental ranges employed are shown in Table 4.1 and a graphical representation of the design is given as Figure 4.6.

## Spray Drying

**Table 4.1 Factors and ranges for experimental design**

Factor	Type	Minimum	Maximum
Droplet size ( $\mu\text{m}$ )	Numeric	40	80
Solution concentration (%w/w)	Numeric	0.375	0.75
Aspirator setting (%)	Numeric	50	100
Inlet temperature ( $^{\circ}\text{C}$ )	Numeric	100	160
Solvent	Categoric	Ethanol	2-Propanol



**Figure 4.6 Experimental design - Gas flow value for each run are detailed within solvent identifier**

Assignment of the statistical significance and relative importance of effects was performed using the analysis of variance (ANOVA) technique (Mason, 2003).

### 4.3.1. Operating parameter ranges

The maximum solution concentration value was chosen with reference to the solubility data presented in Chapter 2, and is the saturation concentration at the chosen operating temperature for the solvent and solute combination with the lowest saturation concentration. The minimum concentration was selected to allow sufficient material to be generated for characterisation whilst maintaining achievable run times. Aspirator maximum and minimum values encompassed the operating range for the spray dryer. The maximum inlet temperature was restricted to 160°C to ensure temperatures in the cyclone collection system were sufficiently below the reported glass transition temperature of mometasone furoate (Cacela *et al.*, 2012) to avoid morphological changes after collection. The minimum inlet temperature of 100°C was selected to provide an outlet temperature sufficiently high to minimise residual solvent content.

Following identification of a relationship between solute concentration and dried particle properties (see section 4.3.3.1) supplementary runs were undertaken using higher solute concentrations to further explore the relationship and examine any additional change in shape and texture. The concentrations used were above the solubility limit at the temperature of operation. Mometasone furoate solutions of 1 %w/w concentration were observed to show good stability when allowed to cool to ambient temperature; hence operation in the metastable state was undertaken given the likelihood of API remaining in solution until atomized and dried. A further run, 31Z, was performed using a concentration intermediate between the low and high concentration used in the experimental design, primarily to provide an additional particle size for use in the formulation studies. The supplementary spray drying runs are detailed in Table 4.2.



## Spray Drying

**Table 4.2 Additional spray drying runs**

Solvent	Droplet size ( $\mu\text{m}$ )	Concentration (%w/w)	Inlet temperature ( $^{\circ}\text{C}$ )	Drying gas flow ( $\text{m}^3 \text{h}^{-1}$ )
Ethanol	40	1.0	100	35
Ethanol	80	1.0	100	35
Ethanol	40	1.25	100	35
Ethanol	80	1.25	100	35
Ethanol	40	0.56	160	35

### 4.3.2. Methods

#### 4.3.2.1. Spray drying

100 or 150 g of solution of the appropriate composition was manufactured for each spray drying run, depending on solution flow rate. The required amount of API was weighed into a 50 mL beaker using a 4 decimal place analytical balance to a 0.1 % tolerance. The correct quantity of solvent was then weighed into a 200 mL beaker and used to wash the API from the beaker into a suitable Duran bottle. The bottle was then sealed with the screw lid and placed into the preheated water bath incorporated in the jacketing circuit of the pump and atomizer. Once all solute had dissolved the solution was drawn into the syringe pump by withdrawal of the piston. The syringe pump was cleaned by twice flushing with solvent before each run (the solvent chosen was the one to be used for the subsequent run); this left the tubing at the outlet of the pump filled with solvent which was used to set operating parameters prior to atomization of solution. The same process was then employed as for atomization of sodium chloride solutions (section 4.2.1.1). The collection pot was removed from the spray dryer at the end of the run, closed using a screw cap and transferred to a safety cabinet for powder recovery. The spray dried API was transferred into a pre-weighed vial using a stainless

## Spray Drying

steel spatula. The powder was predominantly adhered to the side of the collection pot, particularly so for powder produced from 40  $\mu\text{m}$  droplets, necessitating scraping down from the sides of the vessel using a spatula. Once all possible material had been removed the vial was closed with the lid and weighed to determine the amount of powder recovered; the collection vessel was washed thoroughly with ethanol to remove the remaining API particles. The pump and connecting tubing were rinsed twice with ethanol or propanol consistent with which was being used as solvent for the current run on the solution; initially a volume of solvent 5 mL greater than that of the solution was used, then a volume 10 mL greater was employed. The atomizer liquid conduit was flushed twice with 10 mL of ethanol or propanol from a syringe. The lid of each vial was replaced with filter paper and the collected batches of spray dried mometasone furoate were stored in a desiccator with 4A molecular sieve.

### **4.3.2.2. Characterisation of API particles**

Spray dried API particles were characterised using thermal analysis, X-ray powder diffraction, laser diffraction and scanning electron microscopy. X-ray diffraction was used as the primary measure of crystallinity; thermal analysis was then employed to provide information on the thermodynamic state of the particles via the interpretation of thermal events detected during evaluation. Laser diffraction was used to give geometric size distribution data, and scanning electron microscopy provided an understanding of prevailing particle morphology and an additional measure of particle size.

## Spray Drying

### 4.3.2.2.1. Thermal analysis

Two thermal analysis techniques were used to identify energetic events potentially attributable to spray drying operating parameters. Differential scanning calorimetry (DSC) was used to detect latent heat effects, such as those characteristic of crystallization, melting and phase transition. DSC analysis was performed using a Q2000 instrument (TA instruments, New Castle, Delaware, USA) with each sample being run in duplicate. Approximately 3mg of sample was used per run for DSC analysis, and was accurately weighed into a standard aluminium pan and lightly crimped with a lid. An empty standard pan with a crimped lid was prepared and used as the reference for measurement. A temperature ramp of 10°C per minute between 0°C and 220°C was used; mometasone furoate degrades (rather than melts) above 230°C, so an upper temperature of 220°C was chosen to avoid contamination of the equipment with thermal degradation products.

Thermogravimetric analysis (TGA) was used to evaluate weight loss from powder samples with increasing temperature. A Q500 instrument (TA instruments, New Castle, Delaware, USA) was used to evaluate weight loss from approximately 5 mg of sample within an open aluminium pan, using a temperature ramp of 10°C per minute between 25°C and 300°C.

Universal Analysis software (TA instruments, New Castle, Delaware, USA) was used to determine onset temperature and enthalpy of thermal events identified during analysis by DSC, and to quantify weight losses observed in the course of TGA runs.

### **4.3.2.2.2. X-Ray Powder Diffraction (XRPD)**

XRPD analysis was performed using an X'pert Powder diffractometer (PANalytical BV, Almelo, Netherlands) fitted with a copper anode and X'celerator detector. A variable divergence slit was fitted on the incident beam side. Silicon wafers were cleaned using acetone and allowed to dry. The surface of each wafer was coated with a thin layer of silicone grease and a small amount of powder was scattered onto the grease layer. Once prepared the wafers were loaded into a sample holder and loaded onto the diffractometer. Each sample was analysed over the range  $2 - 40^\circ 2\theta$  and the diffraction pattern analysed using proprietary software (PANalytical BV, Almelo, Netherlands).

### **4.3.2.2.3. Laser Diffraction**

Particle size analysis of spray dried mometasone furoate was performed using a similar Sympatec Helos instrument with Rodos/M dispersion system to that used previously for analysis of sodium chloride, however the smaller quantity of powder generated by mometasone furoate spray drying runs necessitated the use of an alternative feed system. The Aspiros system doses dry powder into the Helos from a glass vial, and is able to be used with milligram quantities of powder. A dispersion pressure of 1 bar was found to be sufficient to ensure particle deaggregation when used with a feed velocity (rate of advancement of the Aspiros feed tube into the powder vial) of  $30 \text{ mm s}^{-1}$ . The R2 lens, capable of measuring particles with a diameter of up to  $80 \mu\text{m}$ , was used as it spans a measurement range well beyond the anticipated dry particle size.

10 mg of powder per run was loaded into a clean Aspiros glass vial, the vial capped and transferred to the Aspiros unit. The cap was removed and the vial was loaded onto the transporting sled and the unit cover closed. Dispersion pressure and injector depression

## Spray Drying

were optimised automatically for each run before feeding. Measurement was triggered once the optical concentration exceeded 0.1 % and stopped after 5 seconds or when the optical concentration had remained below 0.2 % for more than 3 seconds.

### **4.3.2.2.4. Scanning Electron Microscopy (SEM)**

Representative images of the spray dried particles were obtained using a Supra 25 scanning electron microscope (Carl Zeiss Microscopy, Jena, Germany), employing an element potential difference of 5 kV. A small amount of powder was dispersed onto an adhesive graphite disc mounted on an aluminium stub for each batch of spray dried mometasone furoate. A clean, disposable brush was used to disperse each sample onto the stub, and the powder was then coated with a thin layer of palladium using a sputter coater (AGB7341, Agar Scientific, Stansted, UK). Images of a population of particles considered representative were obtained at three levels of magnification, in order to assess both within-batch consistency and surface detail.

### **4.3.3. Results and discussion**

The materials generated by the spray drying runs were individually assigned a batch number as detailed in Table 4.3 with associated operating parameters. The experimental design detailed in Table 4.1 and Figure 4.6 was successfully completed for mometasone furoate solutions however difficulties were encountered when fluticasone propionate solutions were used, resulting in the generation of a single batch of dried API (EE636926/32A). Severe pressure fluctuations were observed on the pressure gauge connected to the atomizer gas supply during spray drying runs using fluticasone propionate, with deposition of API around the outlet orifice of the atomizer and eventual blockage.

## Spray Drying

**Table 4.3 Spray drying batch identities**

Batch number	Droplet size (µm)	Concentration (%w/w)	Inlet temperature (°C)	Drying gas flow (m <sup>3</sup> h <sup>-1</sup> )	Solvent
Mometasone Furoate – experimental design runs					
EE686926/31C	80	0.38	100	35	2-propanol
EE686926/31E	40	0.75	100	35	2-propanol
EE686926/31F	80	0.75	100	17.5	2-propanol
EE686926/31G	40	0.75	100	17.5	Ethanol
EE686926/31H	80	0.38	100	17.5	Ethanol
EE686926/31I	80	0.75	160	35	2-propanol
EE686926/31J	80	0.75	100	35	Ethanol
EE686926/31K	40	0.38	100	35	Ethanol
EE686926/31L	40	0.75	160	35	Ethanol
EE686926/31M	40	0.38	160	35	2-propanol
EE686926/31N	80	0.38	160	17.5	2-propanol
EE686926/31P	40	0.75	160	17.5	2-propanol
EE686926/31Q	80	0.75	160	17.5	Ethanol
EE686926/31R	80	0.75	160	17.5	Ethanol
EE686926/31S	80	0.75	160	35	2-propanol
EE686926/31T	40	0.38	100	17.5	2-propanol
EE686926/31U	40	0.38	100	17.5	2-propanol
EE686926/32J	40	0.38	160	17.5	Ethanol
EE686926/32K	80	0.38	160	35	Ethanol
EE686926/32I	40	0.38	100	35	Ethanol
Mometasone Furoate – additional runs					
EE686926/31V	40	1.00	100	35	Ethanol
EE686926/31W	80	1.00	100	35	Ethanol
EE686926/31X	40	1.25	100	35	Ethanol
EE686926/31Y	80	1.25	100	35	Ethanol
EE686926/31Z	40	0.56	160	35	Ethanol
Fluticasone Propionate					
EE686926/32A	80	0.38	160	17.5	Ethanol

## Spray Drying

Saturation solubility, in terms of mass fraction, was determined to be lower for fluticasone propionate in comparison to mometasone furoate, however the pronounced difference in the ability to be spray dried is unexpected. The two APIs are structurally similar and although there is a difference in saturation solubility all spray drying runs attempted using fluticasone were below the solubility limit at 50°C, the jacketing temperature of the pump, atomizer and feed hoses. The cause of the rapid formation of solid material in the case of fluticasone propionate is therefore likely due to differences in the dynamic behaviour of the two APIs during atomization and drying beyond the scope of this thesis. The explanation may lie in a diffusivity difference between the APIs; a lower diffusivity in the case of fluticasone propionate would lead to earlier formation of solid possibly resulting in the blockage observed. The molecular masses of the two APIs are similar (501 Da in the case of fluticasone propionate and 521 Da for mometasone furoate) so any differences would most likely be due to the different ester groupings attached to the steroid nucleus and/ or substituents on the nucleus. A comparison of SEM images for batch EE686926/32A to those for mometasone furoate generated using similar droplet size and concentration reveals a spherical morphology for fluticasone propionate versus crumpled particles for mometasone furoate. This suggests a mechanically robust layer is formed early in the droplet lifetime for fluticasone propionate, consistent with precipitation of relatively large quantities of solute. Examination of particle size results given in Table 4.5 shows a larger median particle size was generated for the batch of spray dried fluticasone propionate than for batches of mometasone furoate produced under similar conditions, again consistent with the formation of solid material early in the droplet lifetime.

### 4.3.3.1. **Mometasone furoate particle morphology**

Electron microscope images, summarised in Table 4.4 and presented in full in Appendix 3, reveal a range of surface textures and morphologies. When produced from the smaller droplet size, spherical particles with a smooth surface were observed exclusively when 2-propanol as the solvent, regardless of solute concentration, inlet temperature or drying gas flow rate. Smooth spherical particles were in general produced using ethanol as solvent when spray drying with the higher inlet temperature, however one run at the lowest solute concentration produced spherical particles at the lower temperature. At the lower inlet temperature increasing the solute concentration appears to cause the particle surface to buckle/ crumple, with the size of the corrugations apparently being a function of the solute concentration used. An 'open' buckled or crumpled texture (large corrugations at the surface) resulted from processing at 0.75 %w/w mometasone furoate concentration; increasing the solute concentration further causes the frequency of corrugations to progressively increase, with the resulting smaller corrugations forming a tightly-crumpled 'closed' surface texture of increased roughness.

Spray drying from 2-propanol at the larger droplet size produced either spherical or open crumpled particles depending upon the inlet temperature used. High inlet temperatures are associated with spherical particles; reducing the temperature yields an increased instance of open crumpled particles. Solute concentration appears to have little effect, acknowledging the small number of batches being available to perform the comparison. Switching the solvent to ethanol has a similar impact on the range of morphologies possible to that seen for the smaller droplet size. The lower inlet temperature generated tightly crumpled particles for all solute concentrations evaluated (0.375 to 1.25 %w/w),



## Spray Drying

whilst at the higher inlet temperature open crumpled particles are prevalent with some instances of spherical particles.

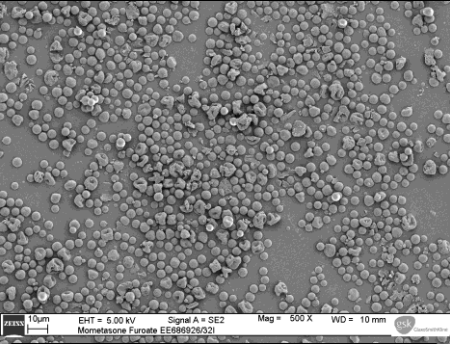
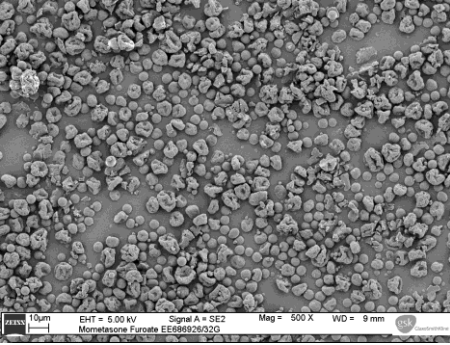
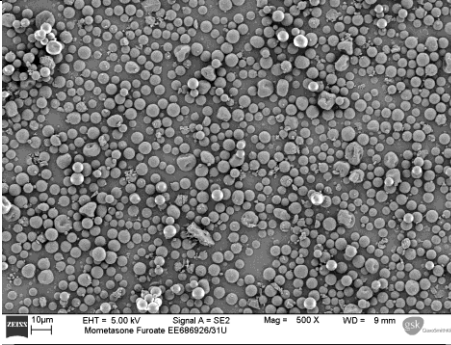
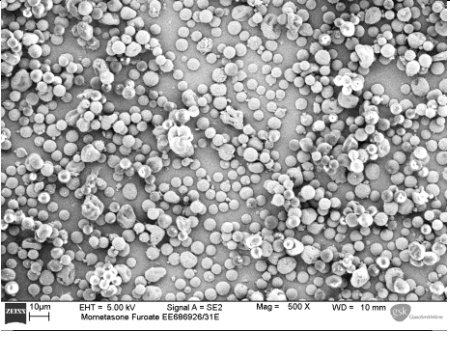
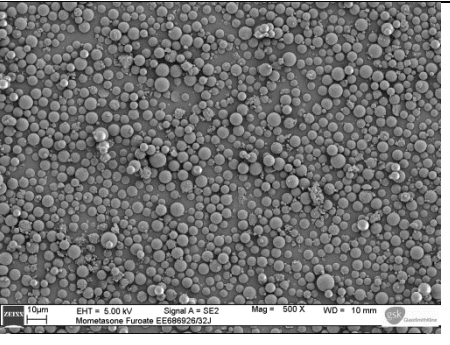
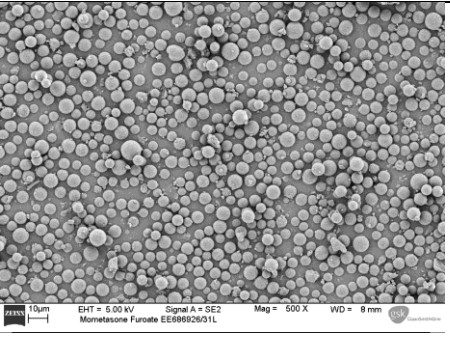
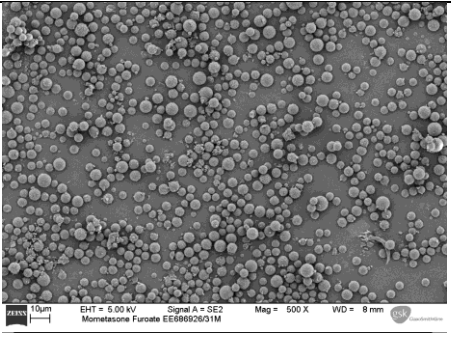
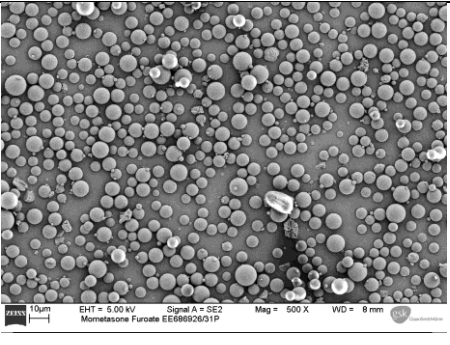
The effect of solvent choice and inlet temperature upon particle morphology indicates that precipitation of solute early within the drying period leads to a smoother surface and therefore spherical morphology. The lower mass fraction at saturation for propanol is likely to translate to earlier deposition that is the case for ethanol, and a higher inlet temperature will lead to more rapid drying, and therefore a higher rate of increase of solute concentration at the droplet surface. As the driving force for drying is decreased, and the saturation concentration is increased, the dry particles recovered become increasingly buckled. Similar tightly-buckled morphologies to those observed here were produced during spray drying experiments using the polymer Eudragit L100 (Raula *et al.*, 2004), attributed to entanglement of polymer molecules in the solidified outer shell of the droplet with polymer molecules precipitating in the interior of the droplet. The postulated mechanism for crumpled particle formation is unlikely to be responsible for the formation of similarly crumpled mometasone furoate particles as precipitation of solute within the bulk of the droplet is likely to lead to crystallization; no evidence of crystallinity was apparent from x-ray diffraction of the relevant batches. Two possible hypotheses were proposed by Vehring and co-workers (Vehring, Foss, & Lechuga-Ballesteros, 2007). One hypothesis notes that surface active molecules will accumulate at the surface thus driving supersaturation; the lack of surface activity for mometasone furoate (see section 2.2.2) indicates this mechanism is unlikely to be of importance in the current scenario. The alternative hypothesis, in the case of low solubility, proposes that the diffusivity difference between solvent and solute leads to an accumulation of solute

## Spray Drying

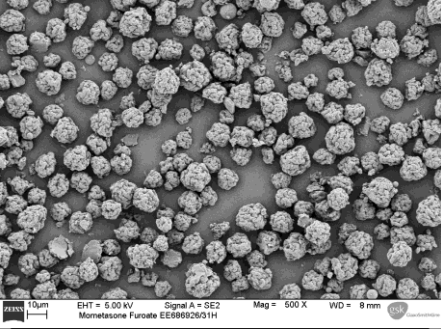
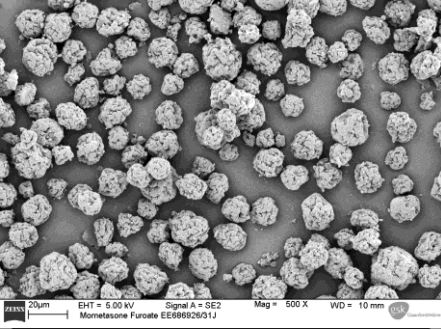
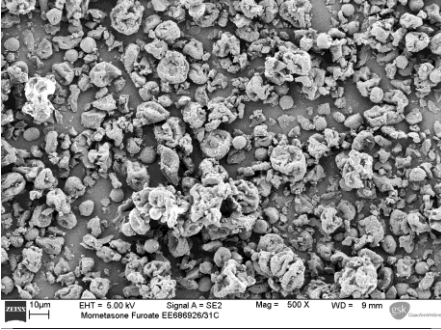
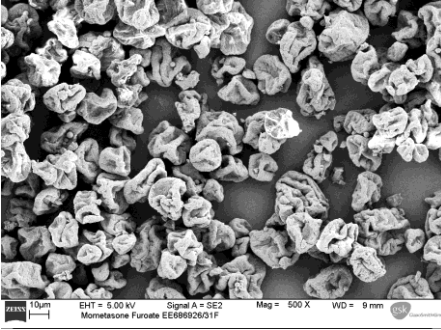
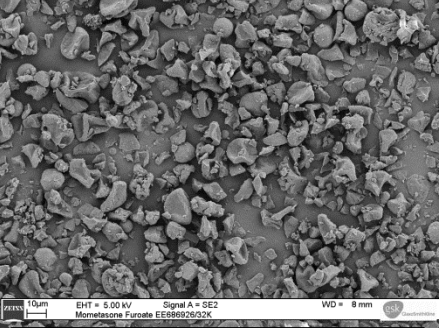
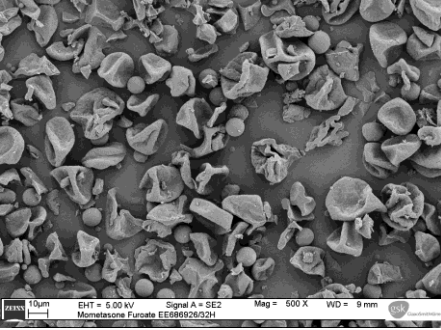
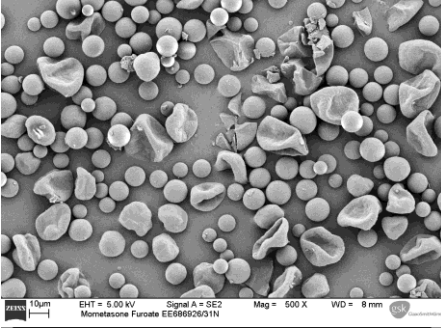
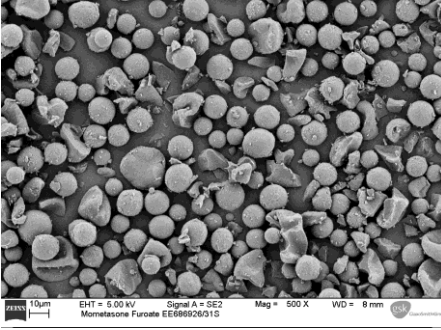
at the droplet surface that rapidly exceeds the solubility limit resulting in formation of a thin solid layer. Depending on the mechanical properties of the surface layer it may then crumple as a result of stresses generated by the retreating droplet surface. This hypothesis provides an explanation to why small molecule solutes do not always produce solid, spherical particles when dried from droplets, contrary to theoretical considerations of the relative diffusivity. That the argument for the formation of buckled or crumpled shells is based upon low solubility of the solute in the solvent would indicate that additional factors must be partially responsible in the present case as the lower solubility solvent, 2-propanol, exhibits a reduced tendency to produce crumpled particles compared to the higher solubility solvent, ethanol. As noted by Vehring et al, the evaporation rate does remain a factor even for high solubility molecules, hence for mometasone furoate the greater volatility of ethanol would appear to have more of an impact upon particle formation than the low solubility in 2-propanol.

# Spray Drying

**Table 4.4 Summary of spray dried mometasone furoate batches**

<b>Particles produced using 40 <math>\mu</math>m droplets</b>			
40 $\mu$ m droplet, 0.375% w/w Ethanol, 100°C inlet temperature	40 $\mu$ m droplet, 0.75% w/w Ethanol, 100°C inlet temperature	40 $\mu$ m droplet, 0.375% w/w 2-propanol, 100°C inlet temperature	40 $\mu$ m droplet, 0.75% w/w 2-propanol, 100°C inlet temperature
			
40 $\mu$ m droplet, 0.375% w/w Ethanol, 160°C inlet temperature	40 $\mu$ m droplet, 0.75% w/w Ethanol, 160°C inlet temperature	40 $\mu$ m droplet, 0.375% w/w 2-propanol, 160°C inlet temperature	40 $\mu$ m droplet, 0.75% w/w 2-propanol, 160°C inlet temperature
			

## Spray Drying

<b>Particles produced using 80 <math>\mu\text{m}</math> droplets</b>			
80 $\mu\text{m}$ droplet, 0.375% w/w Ethanol, 100°C inlet temperature	80 $\mu\text{m}$ droplet, 0.75% w/w Ethanol, 100°C inlet temperature*	80 $\mu\text{m}$ droplet, 0.375% w/w 2-propanol, 100°C inlet temperature	80 $\mu\text{m}$ droplet, 0.75% w/w 2-propanol, 100°C inlet temperature
			
80 $\mu\text{m}$ droplet, 0.375% w/w Ethanol, 160°C inlet temperature	80 $\mu\text{m}$ droplet, 0.75% w/w Ethanol, 160°C inlet temperature	80 $\mu\text{m}$ droplet, 0.375% w/w 2-propanol, 160°C inlet temperature	80 $\mu\text{m}$ droplet, 0.75% w/w 2-propanol, 160°C inlet temperature
			

\* - Note: a 20 micron scale bar has been used for image EE69626/31J; the magnification (500x) is the same as for the other images in Table 4.4

**4.3.3.2. Particle size**

Laser diffraction sizing results for spray dried batches are presented as Table 4.5. Good agreement between repeat samples was observed, as denoted by the small standard deviation for the median particle size.

## Spray Drying

**Table 4.5 Particle size results for spray dried API batches**

Batch number	Droplet size (µm)	Concentration (% w/w)	Solvent	Average percentile (µm)			X <sub>50</sub> SD	Predicted size (µm)
				X <sub>10</sub>	X <sub>50</sub>	X <sub>90</sub>		
EE686926/31C	80	0.38	Propanol	2.3	9.0	16.2	0.2	8.92
EE686926/31E	40	0.75	Propanol	3.3	6.2	9.0	0.1	5.62
EE686926/31F	80	0.75	Propanol	5.2	15.5	25.4	0.1	11.24
EE686926/31G	40	0.75	Ethanol	3.7	6.5	9.7	0.1	5.62
EE686926/31H	80	0.38	Ethanol	7.0	11.8	16.8	0.0	8.93
EE686926/31I	80	0.76	Propanol	5.3	11.7	17.4	0.0	11.27
EE686926/31J	80	0.76	Ethanol	7.5	13.8	19.8	0.0	11.27
EE686926/31K	40	0.38	Ethanol	3.6	6.9	10.1	0.0	4.46
EE686926/31L	40	0.75	Ethanol	2.8	5.9	8.5	0.0	5.62
EE686926/31M	40	0.38	Propanol	1.6	4.5	6.2	0.0	4.47
EE686926/31N	80	0.38	Propanol	6.6	11.2	16.8	0.1	8.93
EE686926/31P	40	0.75	Propanol	3.3	6.3	9.0	0.0	5.63
EE686926/31Q	80	0.75	Ethanol	4.5	11.4	22.6	0.2	11.25
EE686926/31R	80	0.76	Ethanol	4.0	10.2	19.0	0.1	11.26
EE686926/31S	80	0.75	Propanol	5.4	11.7	17.5	0.0	11.25
EE686926/31T	40	0.38	Propanol	2.8	4.8	6.9	0.0	4.46
EE686926/31U	40	0.38	Propanol	2.8	5.0	7.3	0.0	4.46
EE686926/31V	40	1.01	Ethanol	4.3	8.6	13.0	0.1	6.20
EE686926/31W	80	1.01	Ethanol	9.7	16.3	23.0	0.1	12.39
EE686926/31X	40	1.25	Ethanol	5.7	15.9	23.7	0.0	6.66
EE686926/31Y	80	1.25	Ethanol	8.3	16.9	24.1	0.1	13.32
EE686926/31Z	40	0.56	Ethanol	1.8	5.4	7.4	0.0	5.11
EE686926/32A	80	0.38	Ethanol	7.4	14.3	21.3	0.0	8.93
EE686926/32I	40	0.38	Ethanol	2.9	4.8	7.0	0.0	4.46
EE686926/32J	40	0.38	Ethanol	2.6	5.0	7.3	0.0	4.46
EE686926/32K	80	0.38	Ethanol	2.5	8.3	15.0	0.2	8.92

Evaluation of the results via ANOVA using Design Expert 7 is summarised in Table 4.6.

Droplet size ( $P < 0.0001$ ) and concentration ( $p = 0.0062$ ,  $0.0065$  and  $0.0027$  for  $X_{10}$ ,  $X_{50}$  and  $X_{90}$  respectively) as significant factors in dried particle size, as is intuitively expected.

**Table 4.6 Significant processing factors for particle size distribution of spray dried mometasone furoate.**

Batch characteristic	Significant factors	F ratio	P value
X <sub>10</sub>	Droplet size	230.73	0.0001
	Concentration	27.75	0.0062
	Inlet temperature	23.24	0.0085
	Drying gas flow	22.67	0.0089
X <sub>50</sub>	Droplet size	92.72	<0.0001
	Concentration	10.19	0.0065
	Inlet temperature	4.95	0.043
X <sub>90</sub>	Droplet size	147.80	<0.0001
	Concentration	13.24	0.0027

Inlet temperature was also observed to be significant ( $p=0.0085$  and  $0.043$  respectively) for  $X_{10}$  and  $X_{50}$ . In addition, drying gas flow ( $p=0.0089$ ) is seen to be an important factor in determining the fine end of the distribution denoted by  $X_{10}$ . An increase in the inlet temperature results in a reduction in the tenth percentile ( $X_{10}$ ) size, and may be associated with the differences in morphology for dried mometasone furoate apparent at the two inlet temperatures discussed in section 4.3.3.1. The impact of drying gas flow upon  $X_{10}$  is greater for particles produced from 2-propanol than for ethanol. A negative correlation between  $X_{10}$  and drying gas flow is observed for propanol, with a larger gradient apparent at  $160^{\circ}\text{C}$  inlet temperature. A similar gradient observed for ethanol at the higher inlet temperature however little difference is observed at  $100^{\circ}\text{C}$ . An increase in drying gas flow is likely to lead to more rapid drying, and the diffusivity difference between solvent and solute should have a greater impact under conditions of rapid drying to give early formation of a solid shell and so a larger particle size should be expected, unlike the observations made as a result of analysis of the experimental results. The droplet size produced by the atomizer appears to be affected by the gas

## Spray Drying

flow (see section 4.2), with increased gas flow giving potentially smaller droplets; the effect on droplet size would therefore appear to be more important than drying kinetics on the finer end of the droplet distribution.

The high level of significance probability for droplet size and concentration as factors in output particle size indicates that the atomizer produces the expected droplet distributions when used within the dynamic environment of a spray dryer.

### 4.3.3.3. **Crystallinity**

No reflections were determined during XRPD analysis of the spray dried mometasone furoate batches, denoting a lack of long-range molecular order consistent with the generation of amorphous, rather than crystalline material. Diffractograms for all batches produced are presented as Appendix 5. Molecules with a degree of conformational flexibility are often difficult to crystallize (Yu *et al.*, 2000) and isolation of steroid molecules in the amorphous state following spray drying has been previously reported in the scientific literature (Sakagami *et al.*, 2002, Tewes *et al.*, 2013). Evaluation of the spray dried batches by DSC revealed an exothermic event for each batch with an onset between 128°C and 154°C attributed to recrystallization of mometasone furoate (Cacela *et al.*, 2012); thus confirming the non-crystalline particle structure for all batches.

Recrystallization of mometasone furoate in the region of 150°C is understood to be as a result of exceeding the glass transition temperature ( $T_g$ ) of the amorphous state (Cacela *et al.*, 2012). The heat of crystallization and onset temperature of the exotherm are noted to vary between batches and, assuming the onset temperature is indicative of  $T_g$ , may be evidence of variation of the properties of the amorphous API consistent with the



## Spray Drying

processing history of each batch. Onset temperature and enthalpy of crystallization for the experimental design batches are presented in Table 4.7.

**Table 4.7 Thermal events for experimental design batches**

Batch number	Droplet size ( $\mu\text{m}$ )	Concentration (% w/w)	Solvent	Drying gas flow ( $\text{m}^3 \text{h}^{-1}$ )	Inlet temperature ( $^{\circ}\text{C}$ )	Onset temperature ( $^{\circ}\text{C}$ )	Enthalpy ( $\text{J g}^{-1}$ )
EE686926/31C	80	0.38	Propanol	35	100	121.1	11.7
EE686926/31E	40	0.75	Propanol	35	100	109.1	14.4
EE686926/31F	80	0.75	Propanol	17.5	100	120.4	12.9
EE686926/31G	40	0.75	Ethanol	17.5	100	142.0	19.3
EE686926/31H	80	0.38	Ethanol	17.5	100	171.2	26.4
EE686926/31I	80	0.76	Propanol	35	160	137.8	7.9
EE686926/31J	80	0.76	Ethanol	35	100	149.0	21.7
EE686926/31K	40	0.38	Ethanol	35	100	151.3	23.6
EE686926/31L	40	0.75	Ethanol	35	160	134.8	34.0
EE686926/31M	40	0.38	Propanol	35	160	130.6	20.9
EE686926/31N	80	0.38	Propanol	17.5	160	129.0	24.3
EE686926/31P	40	0.75	Propanol	17.5	160	132.1	29.5
EE686926/31Q	80	0.75	Ethanol	17.5	160	173.4	29.8
EE686926/31R	80	0.76	Ethanol	17.5	160	173.9	29.0
EE686926/31S	80	0.75	Propanol	35	160	138.2	13.0
EE686926/31T	40	0.38	Propanol	17.5	100	143.3	33.6
EE686926/31U	40	0.38	Propanol	17.5	100	169.7	35.0
EE686926/32I	40	0.38	Ethanol	35	100	136.0	33.4
EE686926/32J	40	0.38	Ethanol	17.5	160	146.4	40.3
EE686926/32K	80	0.38	Ethanol	35	160	137.7	23.1

The number and nature of the thermal events observed during DSC analysis showed some variation over the entirety of the experimental design, as can be seen in Appendix 4. Common to all thermograms is a broad endotherm below  $100^{\circ}\text{C}$ . Similar endotherms have been observed during the thermal analysis of crystalline forms of mometasone furoate and were attributed to the loss of water of crystallization from the monohydrate

## Spray Drying

(Chen *et al.*, 2005). The mometasone furoate particles produced by spray drying were amorphous, so no stoichiometric solvation is possible, and were spray dried from alcohols, excluding water from the immediate molecular environment during drying and solidification. The endotherm could be as a result of retained solvent dispersed within the amorphous dried mometasone furoate particles rather than as a 'true' solvate; a correlation between weight loss during TGA experiments and  $T_g$  suppression is noted later in this chapter hence this explanation does fit with the experimental evidence gathered.

The crystallization exotherm is predominantly monomodal across the batches, however bimodality of varying modal ratio is observed for runs 31E, 31I, 31S, 31T, 31V, 31W, 31X and 31Y, and an endotherm preceding the exotherm is observed for 31H. Runs 31E, I, S and T were performed using propanol as solvent employing concentrations of 0.75 %w/w or below. Ethanol was used a solvent for runs 31V, W, X and Y, and bimodality is associated with high concentrations in excess of 1.0 %w/w. Exotherm bimodality has been observed in the case of crystalline particles amorphised by milling or cryomilling (Chattoraj *et al.*, 2012, Trasi *et al.*, 2010) and has been attributed to the separate exothermic contributions of surface and bulk crystallization. The increased mobility possible for molecules at the surface compared to those within the bulk results in surface crystallization at a lower temperature than crystallization of the remaining amorphous solid in the mass. Evaluation of amorphous APIs generated by quenching melts showed a single exotherm in comparison to the bimodal exotherms obtained for the same materials produced by milling; the difference was attributed to the presence of small crystalline regions in the predominantly amorphous milled APIs acting as nuclei initiating

## Spray Drying

surface crystallization. The bimodality observed in the exotherms generated for some of the experimental runs may be attributed to a similar phenomenon. With the notable exception of run 31T the bimodal exotherms are produced at high concentrations, and in the case of runs 31V to 31Y at concentrations above the saturation limit. Operation at conditions close to or above the saturation limit may allow small crystalline regions to be produced either during spray drying or during the feed of solution to the atomizer, which become incorporated at the surface of the dried particles and produce the bimodality reminiscent of that observed for milled materials. The endotherm observed for run 31H at an onset of 171°C may be a relaxation endotherm, given that the thermal event occurs above the glass transition temperature. Relaxation endotherms are believed to have two potential causes (Craig *et al.*, 1999):

1. There is a difference in the cooling / solidification rate experienced by the material in the process compared to the heating rate in the DSC. The API molecule relaxation is relative to the slower cooling rate, so when exposed to a relatively rapid heating rate in the DSC the molecules are unable to dissipate the thermal energy by conformational or translation movement so the material heats, resulting in the endotherm. Once the material enters the rubbery state the energy dissipates.
2. Further energetic relaxation occurs following solidification of the material and, similarly to the first cause, the molecules are unable to gain sufficient movement at the rate of heating in the DSC to dissipate the thermal energy supplied. The glass superheats, giving an endotherm.

## Spray Drying

The rapid cooling and solidification rate experienced in the spray dryer compared to the heating rate employed during DSC analysis make the first explanation unlikely. The residence time within the Buchi B-290 is believed to be of the order of one second, during which time droplets are dried to finally yield solid particles. The final part of drying, where the molecules are 'frozen' into their relative positions will take a fraction of this time, hence the required mismatch of rates necessary for the first hypothesis to explain events is unlikely to occur. The second hypothesis requires either a long storage time or sufficient molecular movement to allow relaxation to occur. The storage to test time for sample 31H was within the range described by the other samples, for which no similar endotherm was observed.

Multimodal exotherms are observed for the fluticasone propionate run 32A; under similar conditions mometasone furoate is characterised by a monomodal exotherm. The complexity of the exotherm indicates a non-uniform energetic state within the particles. The processing difficulties observed when spray drying fluticasone propionate were as a result of early solidification of material during atomization; the unstable processing behaviour observed may result in regions within the particles of differing processing history, and therefore varying energetics.

Evaluation of the data using analysis of variance identified statistically significant relationships between the thermal event and processing parameters, as summarised in Table 4.8.

**Table 4.8 Significant processing factors for recrystallization exotherm position and enthalpy**

Batch characteristic	Significant factors	F ratio	P value
Enthalpy of crystallization	Concentration	4.73	0.0473
	Droplet size	11.26	0.0047
	Solvent	10.49	0.0060
	Drying gas flow	10.28	0.0063
Onset temperature	Solvent	7.59	0.0155
	Drying gas flow	5.40	0.0357

The onset temperature and enthalpy of the exotherm varies systematically with the spray drying conditions used and the solvent chosen. Drying gas flow and the choice of solvent have a significant impact upon the onset temperature of the exotherm ( $p = 0.0388$  and  $0.0073$  respectively). Increasing the drying gas flow results in a reduced onset temperature, and higher onset temperatures were seen when analysing particles generated using ethanol as the solvent in comparison to 2-propanol. The glass transition temperature of a material is known to be dependent upon the thermal history (Craig *et al.*, 1999, Matsuda *et al.*, 1992) and is sensitive to the levels of residual solvent within the amorphous solid. Further evaluation of selected samples by thermogravimetric analysis (TGA) revealed a general trend of increased weight loss over the exotherm temperature range ( $130^{\circ}\text{C}$  to  $170^{\circ}\text{C}$ ) for samples demonstrating a lower onset temperature, as summarised in Table 4.9 with experimental data presented as Appendix 6. If the onset temperature is indicative of the position of the  $T_g$ , suppression would appear to result from retained solvent acting as a plasticiser. Comparison of the experimental values to values predicted by the Gordon-Taylor equation reveals that the concentration of retained solvent at the time of measurement would not account for the degree of  $T_g$  suppression measured, however the general trend of measured and predicted values

## Spray Drying

does indicate a correlation. TGA analysis occurred following a prolonged storage period, hence the measured values may not be representative of the initial solvent levels.

Assuming the loss of solvent from the different spray dried MF batches occurs at a similar rate, not an unreasonable assumption as storage was under identical conditions, and the relevant physical properties of the compared batches was appropriately similar giving similar diffusion rates, then the data does support the hypothesis that the differences in  $T_g$  is due to differing amounts of retained solvent.

**Table 4.9 Comparison of DSC exotherm onset and TGA weight loss**

Sample identity	Exotherm onset (°C)	Weight loss (%)	Predicted $T_g$ (°C)
31C	121.4	0.2830	147.7
31F	120.4	0.3477	147.1
31G	142.0	0.3500	146.8
31H	171.2	0.0325	149.7
31I	137.8	0.4620	146.2
31J	149.0	0.0768	149.3
31M	130.6	0.5025	145.9
31R	173.9	0.0923	149.2

Intuitively a proportional relationship between drying gas flow and onset temperature might be expected, assuming a higher drying gas: liquid ratio results in a lower equilibrium solvent content. It should be noted however that a larger drying gas flow will also result in a shorter residence time in the drying chamber, and this would appear to have been more impactful in terms of particle solvent content than the increased equilibrium driving force provided by the larger drying gas flow. Assuming the exotherm observed during thermal analysis is crystallization as the  $T_g$  is reached, then the enthalpy observed can be used as an estimate of the 'excess' internal energy of the amorphous material compared to the thermodynamically stable crystalline state. In addition, a minimum energy state for the glass will exist, so the differences in enthalpy between the

## Spray Drying

runs can be considered reflective of the differences in energetic state resulting from the drying conditions. A smaller enthalpy should therefore result when the solute molecules have the opportunity to relax into a lower energy state during spray drying, due to a reduced drying rate. Droplet size, solvent choice, drying gas flow and concentration were observed to be statistically significant factors in the enthalpy of the exotherm ( $p = 0.006, 0.015, 0.015$  and  $0.029$  respectively). A larger enthalpy is evident when reducing the droplet size, gas flow or concentration and when using ethanol as solvent. An increase in the gas: liquid ratio within the spray dryer is known to lead to more rapid drying, which should in turn cause a more disordered molecular state for the resulting dried particles. An increase in concentration should lead to earlier precipitation during drying, which should be reflected in an increase in enthalpy, assuming relaxation state of the amorphous solid is dependent upon relative supersaturation. The gas flow and concentration relationships with enthalpy therefore appear counterintuitive. Increased levels of retained solvent have been noted for particles produced using high gas flows, which may also have consequences for the enthalpy-gas flow relationship. The reasons behind the inversely proportional relationship between concentration and enthalpy are unclear; the early solidification likely to be encountered when drying higher solute concentrations may result in a larger mass of retained solvent, as the solid layer is likely to present a greater barrier to evaporative loss of solvent. If the mixed system resulting from increased solvent content does decrease the enthalpy measured during thermal analysis then this may provide some explanation of the phenomenon.

Ethanol, being a more volatile solvent than propanol, is likely to dry more rapidly at the same temperature resulting in early solidification of mometasone furoate and a higher

## Spray Drying

free energy. Smaller droplets will evaporate to dryness more rapidly than droplets with larger diameters as a result of the increased surface area: volume ratio; hence precipitation of solid will occur within a higher temperature zone, and therefore at a higher evaporation rate when using a co-current spray dryer as used in this study.

The difference in drying kinetics produced by changes in operating parameters appears to have resulted in differences in energetic state of the mometasone furoate particles; such differences have been noted previously for materials which, similarly to the situation described here, have been isolated in the amorphous state below the glass transition temperature, however systematic attribution to spray drying conditions was not possible (Tajber, Corrigan, & Healy, 2009). The study in question used a similar Buchi spray dryer, however a conventional two-fluid atomizer was used; the wide droplet size diameter likely may have made clear elucidation of trends problematic.

There has been debate previously in the academic literature about the existence of separate amorphous states, analogous to the polymorphic forms often encountered with materials in the crystalline state, and whether there is any relevance to pharmaceutical systems (Craig *et al.*, 1999, Hancock, 2002, Hancock & Zografi, 1997). The trends observed during the spray drying experiments performed here may be characteristic of a material in the glassy state isolated at different stages of relaxation, with the enthalpy being indicative of the degree of molecular rearrangement possible before relative positions and conformations of the molecules become fixed. The evaluation of DSC results is open to a degree of interpretation, given the necessarily manual nature of attributing onset and end of complex thermal events against an often non-linear



baseline. It is therefore acknowledged that the trends identified during this study are tentative, and subject to further confirmation.

#### **4.4. Conclusion**

The relationship between operating conditions and droplet size appears to be preserved when operating the atomizer in the dynamic environment of the spray dryer. Systematic variation of gas and liquid flow rates previously demonstrated to lead to a progressive change in droplet diameter, coupled with the use of suitable solute concentrations is observed to correlate with a proportional increase in output sodium chloride particle size. Good linearity is observed, as demonstrated by the correlation coefficient 0.94 for the relationship between predicted and measured particle size. Absolute proportionality between results generated for the atomizer during droplet measurement by laser diffraction and the output particle size distribution obtained by laser diffraction for sodium chloride was not preserved however, and given the widespread use and acceptance of the measurement systems employed it seems reasonable to conclude that generation of droplets in the spray dryer is subject to additional processing variables.

Structured experimentation has revealed a direct impact of droplet size, solute concentration and spray drying conditions upon the energetics and physical attributes of collected mometasone furoate particles; an enthalpy range of 7.9 to 40.3 J g<sup>-1</sup> was measured by DSC for spray dried mometasone furoate over the twenty runs conducted. Statistically significant relationships have been defined between the processing variables and the exothermic event attributed to crystallization of mometasone furoate once the glass transition temperature has been attained. Use of small droplet sizes and more volatile solvents, likely to lead to rapid evaporation of solvent from the droplets were

## Spray Drying

observed to result in an elevated enthalpy at glass transition being detected during thermal analysis, consistent with an interrupted relaxation process during solidification. Drying gas flow and concentration demonstrated unexpected trends with enthalpy, with increased gas flow and concentration resulting in a reduction in enthalpy change at crystallization. The reasons for this are unclear, however may be associated with an increase in retained solvent resulting from use of these conditions, assuming a relationship between processing conditions and particle energetics exists. Further investigation of the energetics of amorphous mometasone furoate – alcohol systems may provide insight into these unexpected trends, and confirm whether the enthalpic relationship with processing conditions exists.

The temperature of the glass transition for spray dried mometasone furoate has also been observed to vary systematically with differing manufacturing conditions, with a suppression of up to 41°C from the postulated value of 150°C. Interpretation of the relationships between processing conditions and suppression suggests the suppression is due to incomplete drying rather than there being a direct link between  $T_g$  and thermal history.

The texture of the spray dried mometasone furoate particles was observed to be a function of droplet size, solvent and inlet temperature. 40  $\mu\text{m}$  droplets showed an increased tendency to produce smooth particles, particularly when using 2-propanol as the solvent, however use of 100°C inlet temperature and 0.75% w/w concentration with ethanol as solvent caused the particle surface to crumple. At the 80  $\mu\text{m}$  droplet size an increased tendency to form corrugations was observed, with the depth of the corrugations increasing with decreasing concentration consistent with a thinner, less

## Spray Drying

mechanically robust layer precipitating when using low solution concentrations.

Corrugated particle formation was again associated with low inlet temperature, consistent with the trend seen at the smaller droplet size.

The inability to successfully spray dry fluticasone propionate, a molecule with a high degree of structural similarity to mometasone furoate, is unexpected and may present a limitation to the general applicability of flow focussing in the controlled generation of API particles. If, as discussed, the differing substituents of the androstane nucleus are responsible for the large difference in spray drying behaviour then the difference in ester group between the two APIs may be a large factor. Evaluation of fluticasone furoate, a commercially available API, by flow focused spray drying may provide a route to understanding as successful processing of this molecule would indicate the relative significance of the ester group compared to the differences in halogen substituents between fluticasone propionate and mometasone furoate.

## 5. FORMULATION STUDIES

### 5.1. Introduction

Mometasone furoate and fluticasone propionate are often delivered by oral inhalation, a treatment route for which API particle size is of paramount importance in defining the effectiveness of the formulated product. The majority of current research relating to hand-held inhalation dosage forms is undertaken to increase the understanding of dry powder inhalers, as this variant offers a preferential combination of ease of use and broad applicability across particle and compound classes. Research groups have typically investigated API characteristics (Chow *et al.*, 2007, Crowder *et al.*, 2002, Le *et al.*, 2012, Lobo *et al.*, 2005, Weers *et al.*, 2007), carrier particle size distributions (Jones & Price, 2006, Ooi *et al.*, 2011, Smyth & Hickey, 2005, Zeng, Martin, Marriott, & Pritchard, 2001) and interactions between the formulation and device using dry powder inhalers as the delivery system (Chew, Bagster, & Chan, 2000, Chew & Chan, 1999, De Boer *et al.*, 2004a, De Boer *et al.*, 2004b, Donovan *et al.*, 2012, Kubavat *et al.*, 2012, Ngoc *et al.*, 2013, Srichana, Martin, & Marriott, 1998). Capsule based inhalers are generally the device of choice for experimentation to avoid the use of complex primary packaging systems and the need for appreciable amounts of API.

A number of studies have investigated the influence of API particle size on the emitted dose and respirable fraction able to be obtained from passive dry powder inhalers.

Micro-moulded cross-linked polymers were used in a recent study to determine the influence of particle size and shape upon respirable fraction (Fromen *et al.*, 2013). The fabrication technique results in monodisperse particles of predefined shape; differing size particles of similar shape were delivered unformulated using two different devices

## Formulation Studies

into a cascade impactor resulting in a clear relationship between particle size and impaction profile. Louey et al (2004b) prepared spray dried fluticasone propionate particles across the range 1.3 to 9.6  $\mu\text{m}$  and delivered both unformulated and as 2 %w/w blended particles with lactose into a cascade impactor. Aerosolisation from capsules using Inhalator and Rotahaler devices led the authors to conclude a general trend of increasing emitted dose and fine particle fraction with decreasing particle diameter for both API alone and blends, however some device dependency is noted. A clear trend for emitted dose is apparent for the Rotahaler, however no real trend is discernible for the Inhalator. Increasing the API particle size within the formulated blends resulted in a trend of decreasing fine particle fraction, when expressed as a percentage on the loaded API using the Inhalator, with no similar trend for the Rotahaler. A further publication by the same research group (Louey *et al.*, 2004a) explored the use of mannitol particles across the size range 1.4 to 10.3  $\mu\text{m}$  prepared using air-jet milling and spray drying techniques, again delivered from a Rotahaler and Inhalator. An increase in fine particle fraction was observed with increasing size within the 1 to 5  $\mu\text{m}$  range for both particle generation techniques, with a progressive reduction with further increase in particle size. No clear trend of emitted dose with mannitol particle size was apparent for either of the test inhaler devices. A similar trend of increasing fine particle fraction with increasing particle size within the respirable range was identified for jet milled amiloride HCl delivered unformulated from an Aerolizer inhaler; additionally a trend of increasing emitted dose with API particle size was observed (Djokic *et al.*, 2014).

The lack of an unequivocal relationship between API particle characteristics and the mass of API emitted and delivered to the test impactor or impinger in these studies highlights

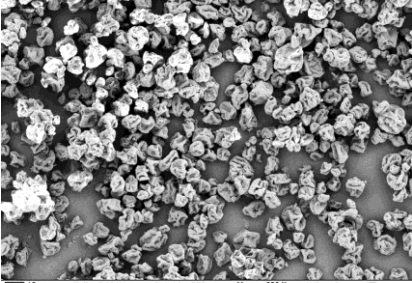
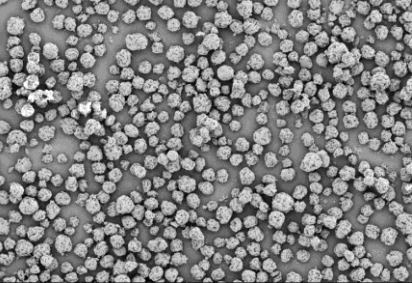
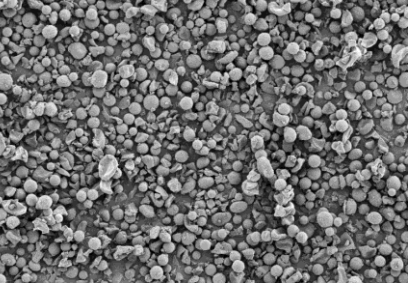
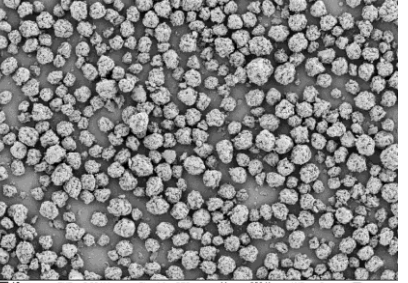
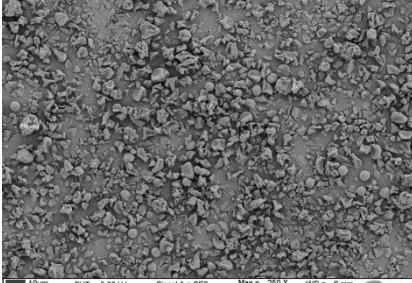
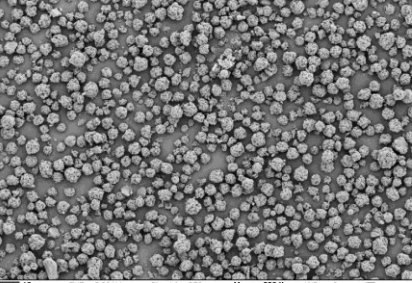
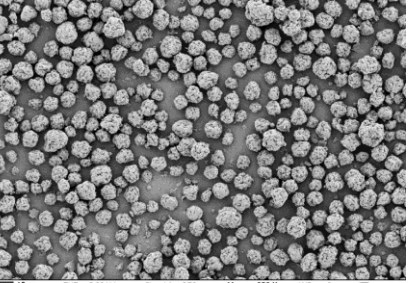
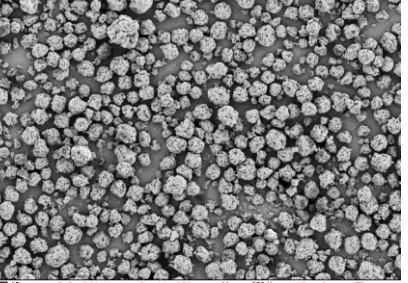
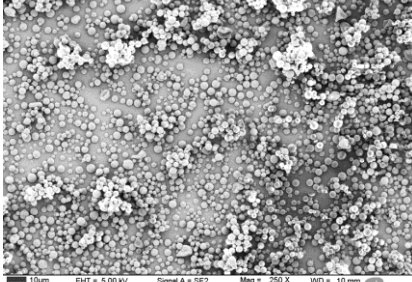
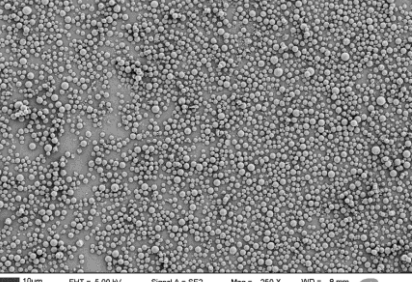
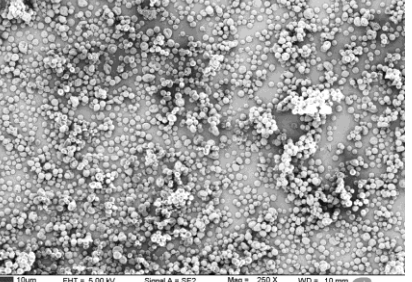
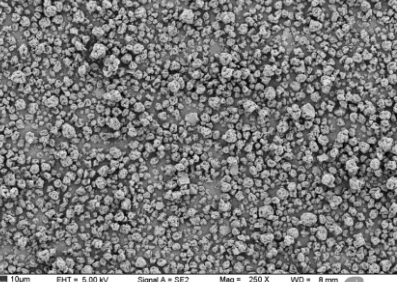
## Formulation Studies

the dependence of the result upon the test conditions employed. The specific device used, as noted in the Introduction chapter, will have large effect upon the results obtained – the internal geometry of the inhaler will define the aerodynamic and mechanical forces experienced by the formulation upon actuation, and the size distribution, morphology and texture of API and carrier particles (if present) will in turn determine the balance of shear and impact-generated fractions of the respirable dose. It is therefore difficult to develop an insight into the behaviour of particles produced using a new processing route by examination of previous studies. An evaluation of the aerosolisation behaviour of spray dried mometasone furoate particles of differing size has not been reported elsewhere in the relevant scientific literature, hence the experiments described in this chapter could provide a useful insight into the importance of API characteristics in determining the emitted dose and resulting aerodynamic particle size distribution.

An oral inhalation formulation and a passive dry powder inhaler delivery system were chosen as the representative case to investigate whether the physicochemical particle differences able to be produced using the flow focussing atomizer had an impact upon patient-relevant dosing characteristics. Twelve batches of spray dried mometasone furoate particles were selected to compare the impact of particle size and surface texture upon aerosolisation performance; representative electron micrographs of particles from the chosen batches are presented in Table 5.1 and API particle size percentiles are detailed in Table 5.2.

## Formulation Studies

**Table 5.1: Spray dried mometasone furoate batches**

<p>EE686926/31F: 80 µm droplet, 0.75% w/w Ethanol, 160°C inlet temperature</p>	<p>EE686926/31J: 80 µm droplet, 0.75% w/w Ethanol, 100°C inlet temperature*</p>	<p>EE686926/31I: 80 µm droplet, 0.75% w/w 2-propanol, 160°C inlet temperature</p>	<p>EE686926/31Y: 80 µm droplet, 1.25% w/w Ethanol, 100°C inlet temperature</p>
 <p>10µm EHT = 5.00 kV Signal A = SE2 Mometasone Furoate EE686926/31F Mag = 250 X WD = 9 mm</p>	 <p>20µm EHT = 5.00 kV Signal A = SE2 Mometasone Furoate EE686926/31J Mag = 250 X WD = 10 mm</p>	 <p>10µm EHT = 5.00 kV Signal A = SE2 Mometasone Furoate EE686926/31I Mag = 250 X WD = 9 mm</p>	 <p>10µm EHT = 5.00 kV Signal A = SE2 Mometasone Furoate EE686926/31Y Mag = 250 X WD = 8 mm</p>
<p>EE686926/32K: 80 µm droplet, 0.375% w/w Ethanol, 160°C inlet temperature</p>	<p>EE686926/31H: 80 µm droplet, 0.375% w/w Ethanol, 100°C inlet temperature</p>	<p>EE686926/31W: 80 µm droplet, 1.0% w/w Ethanol, 100°C inlet temperature</p>	<p>EE686926/31X: 40 µm droplet, 1.25% w/w Ethanol, 100°C inlet temperature</p>
 <p>10µm EHT = 5.00 kV Signal A = SE2 Mometasone Furoate EE686926/32K Mag = 250 X WD = 9 mm</p>	 <p>10µm EHT = 5.00 kV Signal A = SE2 Mometasone Furoate EE686926/31H Mag = 250 X WD = 8 mm</p>	 <p>10µm EHT = 5.00 kV Signal A = SE2 Mometasone Furoate EE686926/31W Mag = 250 X WD = 8 mm</p>	 <p>10µm EHT = 5.00 kV Signal A = SE2 Mometasone Furoate EE686926/31X Mag = 250 X WD = 8 mm</p>
<p>EE686926/31D: 40 µm droplet, 0.375% w/w Ethanol, 160°C inlet temperature</p>	<p>EE686926/31Z: 40 µm droplet, 0.5% w/w Ethanol, 160°C inlet temperature</p>	<p>EE686926/31E: 40 µm droplet, 0.75% w/w 2-propanol, 100°C inlet temperature</p>	<p>EE686926/31V: 40 µm droplet, 1.0% w/w Ethanol, 100°C inlet temperature</p>
 <p>10µm EHT = 5.00 kV Signal A = SE2 Mometasone Furoate EE686926/31D Mag = 250 X WD = 10 mm</p>	 <p>10µm EHT = 5.00 kV Signal A = SE2 Mometasone Furoate EE686926/31Z Mag = 250 X WD = 8 mm</p>	 <p>10µm EHT = 5.00 kV Signal A = SE2 Mometasone Furoate EE686926/31E Mag = 250 X WD = 10 mm</p>	 <p>10µm EHT = 5.00 kV Signal A = SE2 Mometasone Furoate EE686926/31V Mag = 250 X WD = 8 mm</p>

\* - Note: a 20 micron scale bar has been used for the image of EE686926/31J; the magnification (250x) is the same as for the images of compared batches

## Formulation Studies

A Cyclohaler was used as used to deliver formulated spray dried mometasone furoate particles to a next generation impactor (NGI) so aerosolisation characteristics for the chosen batches could be evaluated. The Cyclohaler device (and the closely related Aerolizer) has been extensively used in experimental studies as a capsule is used to contain the formulation, allowing for easy preparation at laboratory scale.

A series of publications by Coates et al describe a thorough characterisation of the contributions of the device and capsule to powder dispersion and resulting respirable dose. Initially the impact of grid structure and mouthpiece was investigated by use of computational fluid dynamics, with the models being validated by Laser Doppler Velocimetry (Coates *et al.*, 2004). Simulation of emitted particle trajectory was then undertaken to understand the effect of the changing flow pattern. Two modified grid configurations were compared to the standard design, to evaluate the difference in airflow, and the resulting impact upon turbulence and aerodynamic particle size distribution of the delivered dose. Additionally, the influence of the mouthpiece length upon the emitted dose was explored, comparing  $\frac{3}{4}$  and  $\frac{1}{2}$  length versions of the inhaler to the standard mouthpiece length. Good agreement between simulated and measured flow rates were observed, giving confidence in subsequent predictions of the flow field at the grid and within the mouthpiece. The main effect of the grid was to straighten the airflow and reduce the swirling airflow generated by the tangential air entry and resulting capsule rotation; additionally the standard low voidage grid was predicted to generate high integral scale strain rates which are understood to aid deagglomeration. Increasing the grid voidage had a significant impact upon straightening of the flow, with increased tangential flow predicted. The fraction of particles impacting the grid



## Formulation Studies

decreased with increasing voidage, however the number of collisions with the inner surface of the mouthpiece is predicted to increase, consistent with the difference in flow field. The similarity in fine particles fraction of the emitted dose for the different voidage grids indicates a compensatory effect – the reduction in grid collisions and lower turbulence experienced with lower grid voidage being offset by an increasing incidence of collisions between particles and the inside of the mouthpiece. The increase in particle – mouthpiece interactions with lower voidage was observed to lead to a lower emitted dose, demonstrating that although an effective deagglomeration mechanism for the ex-device dose, use of mouthpiece collisions will result in a lower emission of respirable particles when expressed in terms of the nominal dose compared to a more effective grid. The length of the mouthpiece was seen to have a much smaller influence upon dosing characteristics, with no impact upon respirable fraction observed. A second publication (Coates *et al.*, 2006) explored the influence of changing the size of the air inlets on the inhaler device, and unlike the previous work, evaluated the influence of test flow rate upon dose emission. When considering the standard inhaler device, as used in the present work, increasing the test flow rate from 30 to 60 L min<sup>-1</sup> results in an increase in fine particle fraction of the loaded dose from 15.0 % to 44.7 %. A smaller increase of 40.1 % to 56.0 % was noted when considering the fine particle fraction of the emitted dose, denoting a lower mass being emitted at the lower flow rate which was attributed to retention within the capsule, rather than upon the inner surfaces of the inhaler.

Particle impact velocities upon collision with the interior surface of the lower regions of the device were estimated at the test flow rate; predicted velocities of 8 and 14 m s<sup>-1</sup> at

## Formulation Studies

30 and 60 L min<sup>-1</sup> were obtained. Capsule rotation rate, determined by high speed photography, increased from 1340 to 2620 revolutions per minute with the increase in flow rate. Both factors were initially considered important in generating both emitted dose and fine particle fraction and were investigated further in a later series of experiments. A third study (Coates *et al.*, 2005a) investigated the impact of flow rate upon the aerosolisation of mannitol, exploring wider range of airflows than the other studies performed by the research group. Three regions of the inhaler were considered using a combination of computer modelling and empirical methods, and their respective roles in deagglomeration of the formulation were examined. The grid of the device was observed to be the key element of the device with regard to deagglomeration, in terms of both the creation of turbulence which causes the stress required to cause deagglomeration, and in providing the surface with the highest energy particle impacts. An increase in dispersion performance was observed from 30 to 75 L min<sup>-1</sup>, but no further increase was apparent up to 120 L min<sup>-1</sup>. Further interrogation of this relationship revealed a maximum, for fine particle fraction of the emitted dose, at 65 L min<sup>-1</sup>. Relationships were defined between the flow rate and level of deposition in the USP throat used with the multi-stage liquid impinger, and also the time required to empty the capsule against the test flow rate. The authors note that at 30 L min<sup>-1</sup> incomplete emptying of the capsule occurs, which reduces the level of device deposition, but at flow rates beyond 60 L min<sup>-1</sup> the increased air velocity leads to a reduced level of deposition as re-entrainment of deposited particles is possible.

The role of the capsule in deagglomeration was explored in a further study (Coates *et al.*, 2005b). High speed photography, computational fluid dynamics and dispersion of

## Formulation Studies

mannitol formulations into a four stage liquid impinger were used to define the importance of capsule size and the presence of a capsule in aerosolisation from the device. The authors concluded that the size of the capsule and particle-capsule impacts were of little importance in determining performance, however the size of the hole pierced in the capsule strongly influenced performance with superior dispersion observed using smaller diameter holes. The authors note that smaller diameter holes increase emptying times, with the hole size produced by the marketed device helping to ensure flow through the inhaler is fully developed and turbulent at the point of dose emission.

In a study similar to the second study conducted by Coates et al, Shur et al investigated the design features of the Cyclohaler, constructing modified versions to match the performance of a reference inhaler (Shur *et al.*, 2012). Using commercial Spiriva capsules containing tiotropium bromide, the authors studied the impact of modified Cyclohaler air inlets upon the aerodynamic particle size distribution of the emitted dose using computerised fluid dynamics, high speed videography and cascade impaction. The flow field and pressure gradients within both the chamber and capsule were defined, indicating the maximum pressure gradient within the capsule is present across the hemispherical ends. The effect of test flow rate was shown to be lower for the low resistance Cyclohaler than the higher resistance reference Handihaler over the range 20 to 55 L min<sup>-1</sup>, with little change in the key aerosolisation parameters noted for the Spiriva formulation at the extremes of the flow rate range.

Donovan *et al* (2010, 2012) evaluated the Cyclohaler whilst studying the interactions between device and formulations, with particular reference to the characteristics of the

## Formulation Studies

carrier particles in the formulation (Donovan, Kim, Raman, & Smyth, 2012, Donovan & Smyth, 2010). The authors investigated the relative importance of aerodynamic forces and those generated during impact upon the generation of respirable API particles from carrier based formulations. Anhydrous (smooth) and granulated (particles containing asperities) lactose particles were compared when used as the carrier for budesonide, with the particle size of the carrier forming an additional variable. The authors concluded that impaction was an important mechanism in the generation of the respirable dose, particularly in the case of the type of inhaler used within the present study, and the magnitude of effect increased with the greater momentum associated with larger carrier particle sizes.

The emitted dose and aerodynamic particle size distribution obtained from a DPI are therefore strongly correlated to the particular formulation and device employed. A lactose-carrier based formulation has been employed to remain consistent in approach with the majority of studies, and the particle size distribution of lactose used has been similarly selected to be consistent. The Cyclohaler used for the experiments described in Chapter 5 has been selected as a consequence of prevalence of this variant of inhaler in the studies described in the academic literature, and the depth of knowledge generated on the mode of operation. A good comparison should therefore be possible between results at produced by the studies described in this thesis and those generated by the work of the research groups summarised in the preceding paragraphs, at equivalent flow rate and pressure drop by using a similar device. The similarity of trends identified during these studies with published results will form part of the discussion of results presented in section 5.3.

### **5.2. Methods**

#### **5.2.1. Manufacture of inhalation blends**

5 %w/w blends using lactose as a carrier/ diluent were produced using a tumbling mixer (Turbula T-2C, Glen Creston, UK) employing a rotation speed of 42 rpm for 60 minutes. Blends were manufactured at 200 mg scale, using a 20 mL vial and lid to contain each blend. Filled vials were packed into a larger cylindrical container in a common orientation and the free space in the container was packed out with tissue to prevent movement of the vials relative to each other or the container. Lactose monohydrate from a single manufactured batch with a median particle size of 77  $\mu\text{m}$ , and fines content ( $\% < 5 \mu\text{m}$  by weight) of 5 % was used for all formulated mometasone furoate blends to ensure consistency. As described in Section 1.4.1 the optimum lactose particle size distribution for use in inhaled blends has been the subject of much debate and research, with little in the way of consensus. A 1:1 ratio of API particles to lactose fines has been suggested (Islam *et al.*, 2004b) and the lactose used was selected to approximate this ratio for the chosen API content within the blends. Aliquots of blend were hand filled into size 3 gelatin capsules. Each capsule shell was tared on an analytical balance and  $10.5 \pm 0.5$  mg of blend was transferred into one half of the shell using a small stainless steel spatula. The capsule was then closed and stored for between 24 and 48 hours between 35 and 60 %RH before dosing into the NGI. The spray dried batches formulated as blends and the corresponding blend batches are detailed in Table 5.2.

**Table 5.2: Blend batch identities**

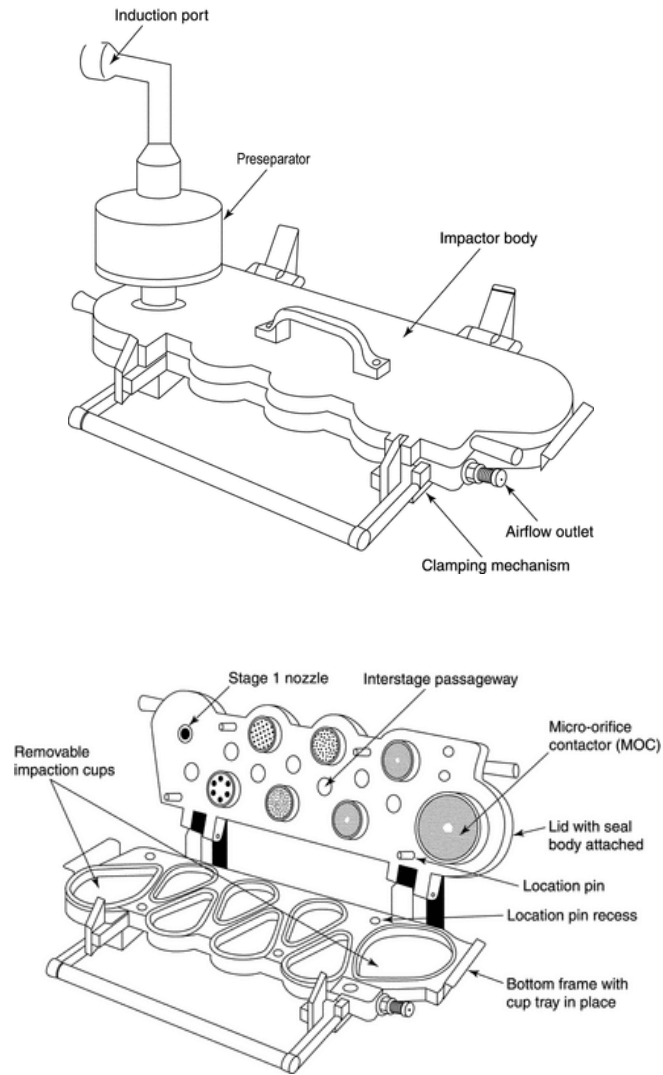
Input spray dried MF batch	Intended droplet size ( $\mu\text{m}$ )	Solution concentration (%w/w)	API Particle Size Distribution undersize percentile ( $\mu\text{m}$ )			Blend batch number
			X <sub>10</sub>	X <sub>50</sub>	X <sub>90</sub>	
EE686926/31E	40	0.75	3.3	6.2	9.0	EE758544/2
EE686926/31D	40	0.375	3.3	6.5	9.4	EE758544/3
EE686926/31F	80	0.75	5.2	15.5	25.4	EE758544/4
EE686926/31H	80	0.375	7.0	11.8	16.8	EE758544/5
EE686926/31I	80	0.75	5.3	11.7	17.4	EE758544/6
EE686926/31J	80	0.75	7.5	13.8	19.8	EE758544/7
EE686926/31V	40	1.00	4.3	8.6	13.0	EE758544/8
EE686926/31W	80	1.00	9.7	16.3	23.0	EE758544/9
EE686926/31X	40	1.25	5.7	15.9	23.7	EE758544/10
EE686926/31Y	80	1.25	8.3	16.9	24.1	EE758544/11
EE686926/31Z	40	0.5	1.8	5.4	7.4	EE758544/12
EE383926/32K	80	0.375	2.5	8.3	15.0	EE758544/13

### 5.2.2. Cascade Impaction

Each batch was evaluated at 20 and 60 L min<sup>-1</sup> flow rate using a next generation impactor; the same impactor components and Cyclohaler device were used for all tests. Three tests were performed for each blend at each flow rate and two capsules were actuated into the NGI for each impaction test. One impaction test was performed for each blend during a single impaction session to ensure the twelve blends were evaluated under similar conditions. The Cyclohaler was washed in distilled water and blown dry with compressed air at least 48 hours before being used to deliver the blends to the NGI, and blown clean until visibly free of powder between evaluation of different batches.

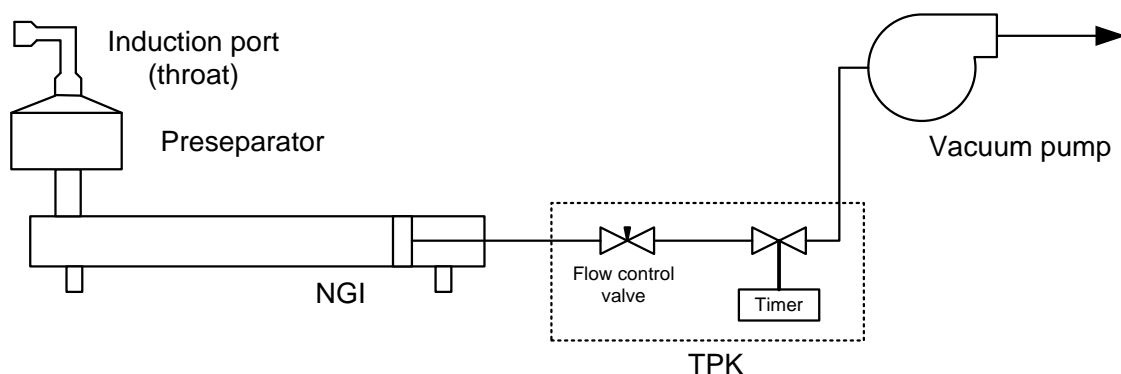
A next generation impactor with a preseparator and USP induction port was used to evaluate the mometasone furoate blends; a diagram of the impactor is given as Figure 5.1 (United States Pharmacopeia Convention, 2014).

## Formulation Studies



**Figure 5.1** Next Generation Impactor

Air flow through the impactor was induced using a vacuum pump ( HCP5, Copley Scientific, Nottingham, UK ) connected to a critical flow controller (TPK, Copley Scientific, Nottingham, UK); a diagram of the experimental configuration used is presented as Figure 5.2:



**Figure 5.2 Cascade impaction configuration**

Each impaction cup was washed with acetone, coated with 19.25 % PEG200 solution in acetone, and the acetone allowed to evaporate to provide an adhesive layer to minimise impactor bounce. 2 mL of PEG200 solution was used to coat the impaction cups for stages 2 to filter; 4 mL of solution was used to coat the stage 1 cup. Once assembled, the preseparator reservoir was filled with 15 mL of deionised water and the air flow rate through the impactor was adjusted using the controller on the pump to give the required volumetric flow as indicated by a calibrated rotameter connected to the induction port. The P3/P2 ratio was checked at this point to ensure it was below 0.5 and that sonic flow was being achieved; the test flow time was then set to give an inspiratory volume of 4 L.

One capsule was selected and inserted into the chamber of the Cyclohaler using steel tweezers. The Cyclohaler was closed and the capsule pierced using the integral pins by depressing the buttons on the side of the device. The Cyclohaler was connected to the NGI induction port using a purpose-designed polymer connector, the vacuum pump switched on and the inspiratory air volume was route through the device by switching the flow controller valve. A second actuation period of equivalent air volume was then



## Formulation Studies

directed through the inhaler to ensure full emptying of capsule contents. The capsule shell was removed from the Cyclohaler, visually checked for residual powder and the second capsule of the same batch was placed into the chamber. Two further actuation periods were then used to entrain and deposit the contents of the capsule into the NGI. The second capsule shell was checked for residual powder, removed and the Cyclohaler was blown with filtered compressed air until visibly clean within a safety cabinet.

The NGI was disassembled and the material present upon each impaction plate was washed into 50mL volumetric flask using 65:35 acetonitrile: water as a dissolving solvent. The contents of the induction port and the preseparator were washed into separate 100mL volumetric flasks using the same dissolving solvent. Flasks were allowed to stand overnight and then the contents were made to volume and shaken approximately 1 hour before a 1 – 2 mL aliquot of solution was transferred to a clean HPLC vial and capped.

Analysis of the samples was performed by HPLC (Agilent 1100, Agilent technologies, Santa Clara, CA, USA) employing UV detection at 250nm wavelength; two standard solutions of  $7.5 \text{ mg} \pm 1.0 \text{ mg L}^{-1}$  were prepared and run with the sample solutions to allow quantification. A Zorbax SB-C18 column (4.6 x 50 mm, 3.5  $\mu\text{m}$  packing) maintained at 40°C was used for separation of a 50  $\mu\text{L}$  injected volume of solution. Gradient elution of two mobile phases over a 6 minute run time was used to aid separation; mobile phase identities, phase ratio changes and associated run time points are detailed in Table 5.3.

**Table 5.3 HPLC run parameters**

Mobile phase A: Water acidified with 0.05% TFA  
 Mobile phase B: Acetonitrile acidified with 0.05% TFA

Time	A:B volumetric flow ratio
0	90:10
5	5:95
5.5	90:10
6	90:10

Linearity of response for the HPLC method has been demonstrated up to a column loading of 880 ng, well in excess of the highest concentration produced during analytical work-up in the current study.

### 5.2.3. SEM characterisation

Electron micrograph images were obtained for each of the blends prepared for evaluation by cascade impaction. Images of lactose and API particles within the formulation were obtained using a Supra 25 scanning electron microscope (Carl Zeiss Microscopy, Jena, Germany), employing an element potential difference of 5kV. A small amount of powder was dispersed onto an adhesive graphite disc mounted on an aluminium stub for each batch of spray dried mometasone furoate. A clean, disposable brush was used to disperse each sample onto the stub, and the powder was then coated with a thin layer of palladium using a sputter coater (AGB7341, Agar Scientific, Stansted, UK). Images of a population of particles considered representative were obtained at three levels of magnification in order to assess both within-batch consistency and surface detail.

### 5.3. Results and discussion

The spray dried mometasone furoate particles appear unaffected by the blending operation, as good comparability is observed between the particles seen in Table 5.1 and API particles within the blends in the electron micrographs presented as Appendix 7.

Cascade impaction analysis results are summarised as Emitted Dose (ED, the sum of API mass deposited on the inlet port, preseparator and stages 1 to filter), Impactor Size Mass (ISM, sum of API mass deposited on stages 2 to filter) and Respirable Mass (RM, sum of API deposited on stages 3 to filter at 20 L min<sup>-1</sup>, and 2 to filter at 60 L min<sup>-1</sup>) as Figure 5.3, Figure 5.4 and Figure 5.5. Mean values for the three results at each flow rate are represented by columns with error bars indicating the standard deviation.

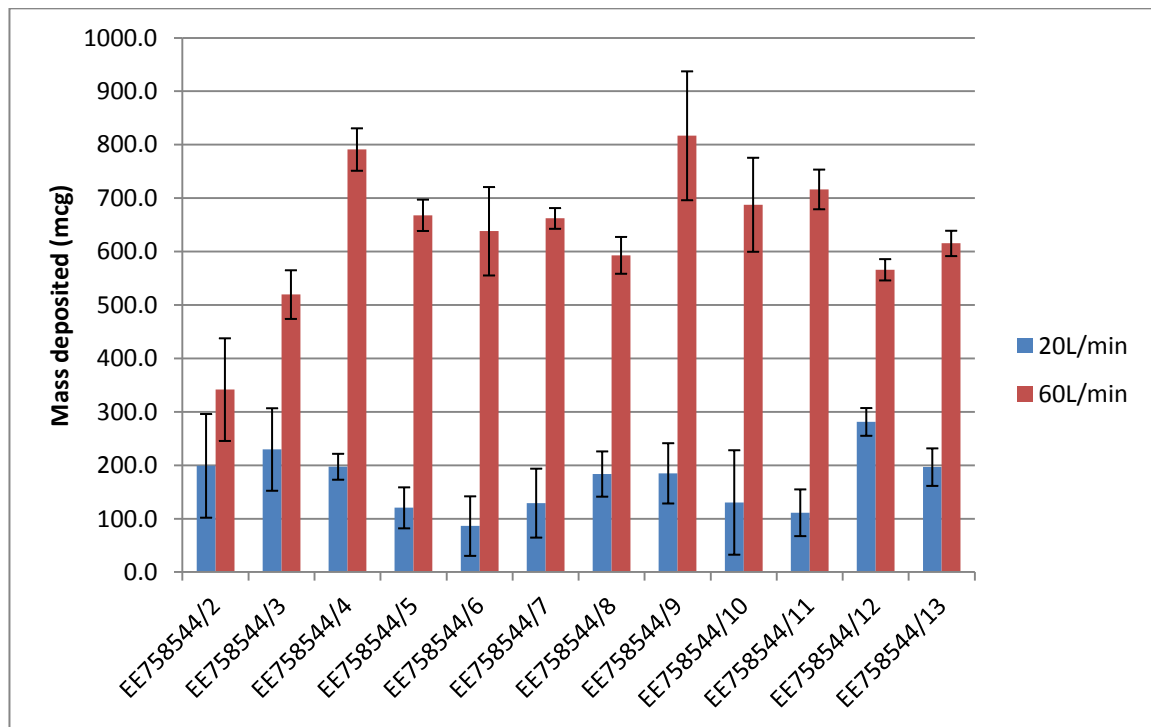
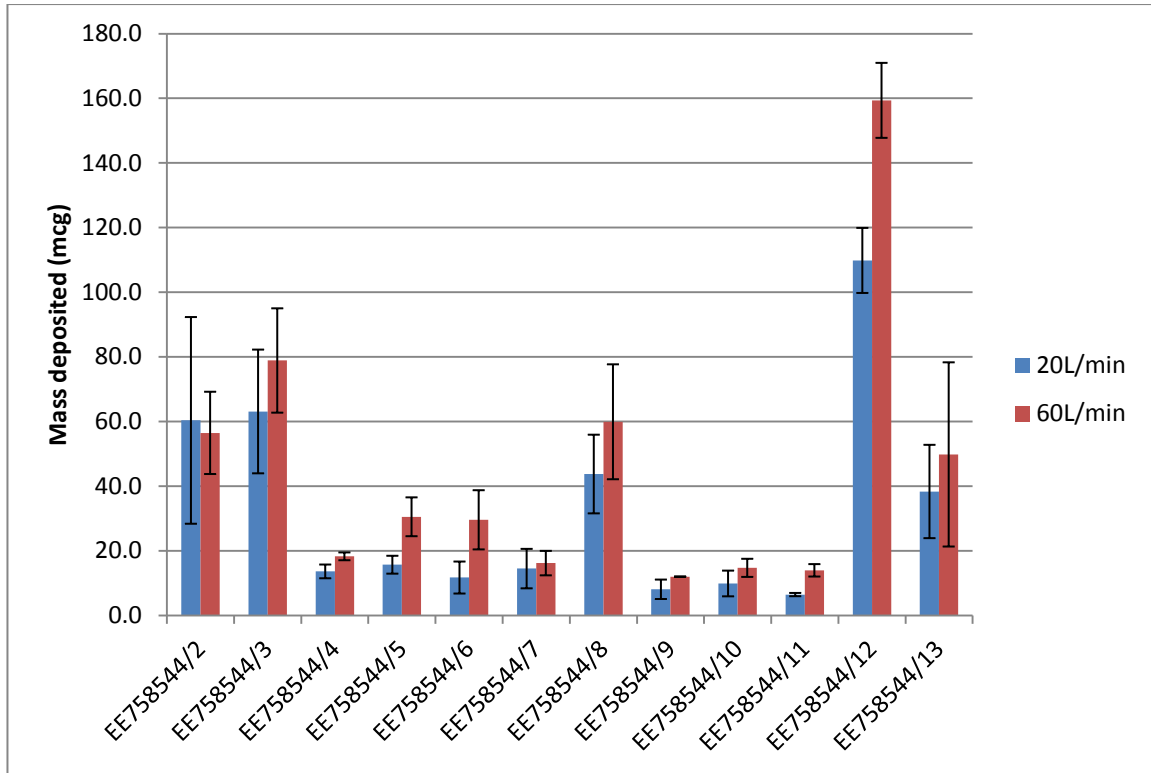
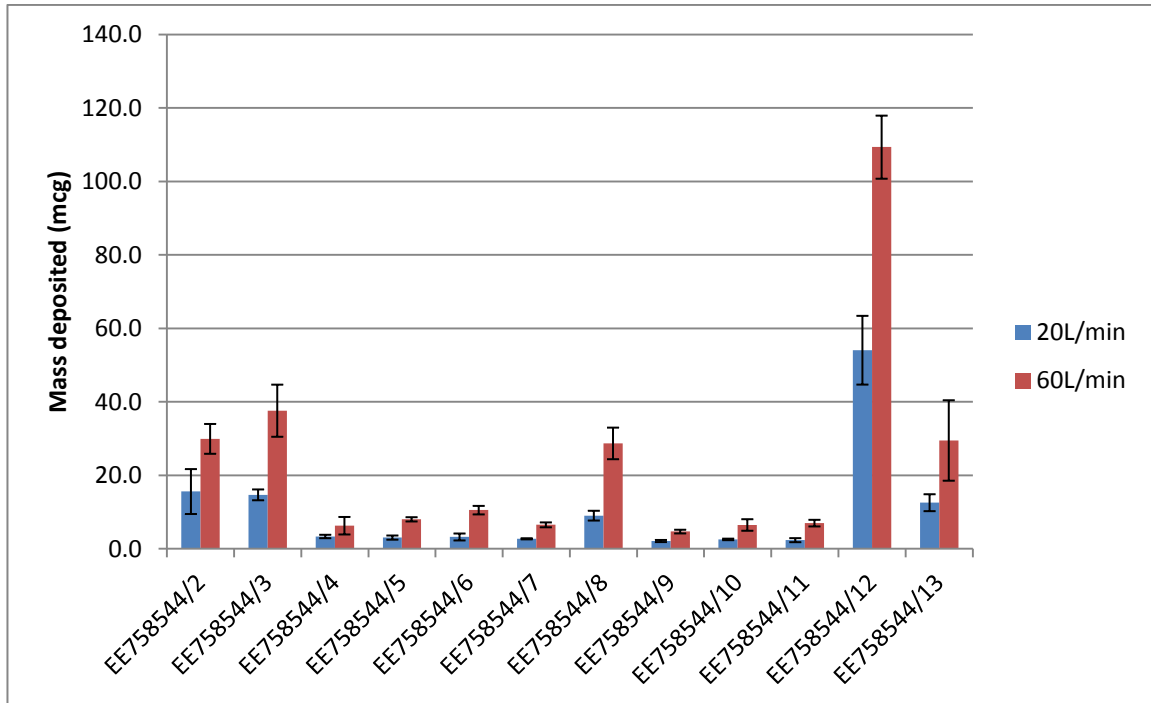


Figure 5.3 Batch comparison of average mometasone furoate emitted dose

## Formulation Studies



**Figure 5.4** Batch comparison of average mometasone furoate impactor sized mass



**Figure 5.5** Batch comparison of average mometasone furoate respirable mass

## Formulation Studies

The proportion of the dose emitted from the Cyclohaler is dependent upon the test flow rate, with higher ex-device deposition observed for all batches at the 60 L min<sup>-1</sup> air flow rate. Emitted dose also exhibits a flow-rate dependent trend with mometasone furoate particle size, as shown in Figure 5.6, with higher values obtained for the batches containing relatively large mometasone furoate particles at 60 L min<sup>-1</sup>. Higher ex-device masses are however produced by blends containing smaller mometasone furoate particles at the lower flow rate of 20 L min<sup>-1</sup>, suggesting a complex relationship between powder physical properties and entrainment of the dose. Increased ED values with greater flow rates have been observed previously when using the Cyclohaler (Srichana, Martin, & Marriott, 1998), however the magnitude of difference observed with the spray dried mometasone furoate formulations is larger than has been observed with formulations containing crystalline APIs. It should be noted that the API particle sizes used within this study are larger than those typically used within inhaled formulations; the low particle formation rate for the equipment configuration used made the generation of sub-five micron particles unachievable within a practical timeframe. The trends identified here may represent those present for smaller particles but are possibly easier to define with the greater range of API particle sizes evaluated. Flow rate dependence of emitted dose was observed for formulations containing micronised and SEDS generated budesonide particles (Lobo *et al.*, 2005), again without the absolute differences observed for spray dried mometasone furoate particles. Jet milled amiloride HCl particles of median particle sizes ranging from 1.7 to 3.0 µm demonstrated a trend of increasing ED with particle size for unformulated API particles delivered from an Aerolizer device (Djokic *et al.*, 2014 ). The authors attributed the difference in ED to an increased agglomeration with smaller particle size, indicating a difference in

## Formulation Studies

agglomerative tendency between the two lower median size batches (1.71 and 2.07  $\mu\text{m}$ ) and the larger batches of jet milled API (2.62 and 2.94  $\mu\text{m}$ ). Whilst this provides a possible explanation of the ED difference between the two groups of materials the categorisation seems arbitrary, with little physical reasoning as to why the size range 2.07 to 2.62  $\mu\text{m}$  should produce a difference in agglomerative behaviour to that of the larger sized particles. The ED data presented may be indicative of a general trend of increasing emitted dose with particle size, as seen for spray dried mometasone furoate particles at the higher test flow rate. A study conducted using spray dried fluticasone propionate revealed a trend of decreasing emitted dose with increasing API particle size for lactose blends delivered from two devices of differing resistance at 60 L min<sup>-1</sup> (Louey, Van Oort, & Hickey, 2004b). Drug-alone dosing showed a device dependent ED trend, with a directly-proportional relationship seen with API particles size when delivered from an Inhalator, and the opposite trend observed when using a Rotahaler, a lower resistance device. A second study by the same research group, this time using unformulated spray dried mannitol with the same two devices revealed no trend of emitted dose with particle size (Louey, Van Oort, & Hickey, 2004a). The impact of particle size upon emitted dose appears therefore to be dependent upon the particular API used, and is influenced by the interaction between API, device resistance and test conditions. Of the work referenced, the evaluation of formulated spray-dried FP most closely matches the present study, however the trend at 60L/min is the opposite of that seen for spray dried mometasone furoate. Electron micrograph images of the fluticasone propionate blends in the referenced work indicate an adhesive mixture was created upon mixing, however similar images taken of the mometasone furoate blends (Appendix 7) show interactions between API and carrier particles that are dependent

## Formulation Studies

upon the API particle size. Mometasone furoate particles with median particle sizes below 10  $\mu\text{m}$  form an adhesive mixture, whereas those above 10  $\mu\text{m}$  show in general a decreasing tendency to adhere to the carrier with increasing API median size. The emitted dose trends illustrate the relative ability of API particles of different sizes to avoid deposition on the surfaces of the Cyclohaler during actuation. Emission from the capsule during actuation is by a combination of aerodynamic and centrifugal forces; avoidance of deposition on the Cyclohaler is then reliant upon the entraining air flow to be sufficiently large for the particles momentum to relax into the prevailing airflow direction. At the higher flow rate this would appear to favour the largest API particles – the increased adhesion of the smaller particles to large carrier particles may result in enhanced impaction for the proportion of mometasone furoate particles remaining attached to the carrier. A reduction in flow rate reduces the air velocity but has a smaller impact upon the ejection velocity from the capsule, resulting in a higher level of deposition upon the Cyclohaler device. Smaller API particles will relax into the airstream more rapidly, so for the fraction able to be separated from the carrier a lower incidence of deposition will be experienced resulting in an inversion of the trend seen at 60  $\text{L min}^{-1}$  for the 20  $\text{L min}^{-1}$  flow condition.

Comparison of the emitted dose results with those for impactor sized mass and respirable mass shows a greater proportion of the API emitted at 20  $\text{L min}^{-1}$  is able to reach the lower stages of the impactor than at 60  $\text{L min}^{-1}$  flow rate, regardless of particle size. By observation (occasional incidence of the capsule shells splitting and fragmenting upon piercing in the Cyclohaler made weighing impractical) only trace amounts of powder remained associated with the capsule shells after use, hence sufficient energy

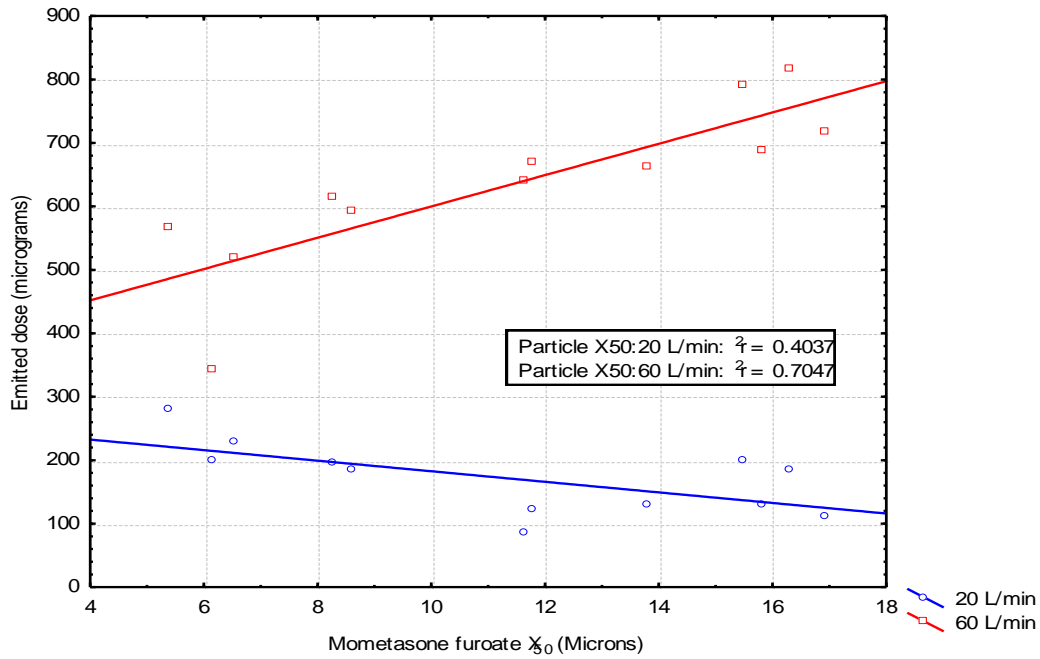
## Formulation Studies

was provided at either flow rate to allow entrainment and aerosolisation of the powder charge. A greater proportion of the powder entrained at  $20 \text{ L min}^{-1}$  must therefore impact upon the Cyclohaler device, as shown by the smaller emitted dose values in Figure 5.3. A larger fraction of the remaining powder cloud is then able to penetrate into the impactor, thus the inhaler device would appear to preferentially classify for smaller particle sizes at the lower flow rate.

The data indicate that the increased energy supplied at the higher flow rate provides sufficient momentum for larger particles to exit the capsule, become entrained in the air flow and deposit within the impactor. Larger particles with greater mass develop more momentum, hence are less likely to be retained within the device by wall adhesion, resulting the proportional relationship between API particle  $X_{50}$  and emitted dose. Conversely at the lower flow rate of  $20 \text{ L min}^{-1}$  smaller particles with lower mass are more likely to be entrained in the air stream and avoid impaction upon the inner surfaces of the inhaler than more massive particles, resulting in the inversely-proportional relationship between size and emitted dose. The trends are illustrated by Figure 5.6:



## Formulation Studies



**Figure 5.6 Effect of mometasone furoate X<sub>50</sub> on Emitted Dose**

Inter-batch comparison of emitted dose using a pairwise T-test to determine statistical significance ( $\alpha = 0.05$ ) between particles formed using large and small droplets and at varying solute concentration is presented as Table 5.4, with statistical significance denoted in red. Significant difference in emitted dose between the two droplet sizes is shown for both air flow rates when considering all concentrations, however at individual concentrations difference is able to be demonstrated at the higher test flow rate. The effect of solute concentration used at the point of spray drying upon emitted dose is noticeably less marked than that observed for droplet size, with difference only proven at the higher flow rate for particles formed from 40  $\mu\text{m}$  droplets.

**Table 5.4 Significance probability (p) values for Emitted Dose differences**

Droplet size ( $\mu\text{m}$ )	Concentration (%w/w)	Emitted Dose	
		20 L min <sup>-1</sup>	60 L min <sup>-1</sup>
80 vs. 40	All	0.0172	<0.001
	0.375	0.143	0.003
	0.75	0.236	<0.001
	1.0	0.976	0.037
	1.25	0.771	0.630
80	0.375 vs. 0.75	0.528	0.161
40	0.375 vs. 0.75	0.691	0.044

The combination of solvent and spray drying conditions was observed to have a direct impact upon the texture of output particles at the 80  $\mu\text{m}$  droplet size, as discussed in Section 4.3.3.1. A comparison of the emitted dose differences for relevant batches is presented as Table 5.5.

**Table 5.5 Significance probability (p) values for Emitted Dose difference, 80 micron droplet size batches**

Droplet size ( $\mu\text{m}$ )	Concentration (%w/w)	Batches compared		Emitted Dose	
				20 L min <sup>-1</sup>	60 L min <sup>-1</sup>
80	0.75	EE758544/4	EE758544/7	0.162	0.007
		EE758544/4	EE758544/6	0.034	0.044
		EE758544/6	EE758544/7	0.432	0.650
	0.375	EE758544/5	EE758544/13	0.064	0.073
	0.375 vs. 0.75	EE758544/4	EE758544/13	0.979	0.003
		EE758544/5	EE758544/7	0.848	0.787
	0.75 vs. 1.0	EE758544/7	EE758544/9	0.323	0.093
	1.0 vs. 1.25	EE758544/9	EE758544/11	0.148	0.240

Higher emitted dose values are seen for batches containing particles with a larger median particle size where significant emitted dose differences exist, consistent with the overall trends observed in Table 5.4. Particle size differences also exist however for the inter-batch comparisons shown in Table 5.5 where significant differences are not observed, and in the case of batches EE758544/7 and EE758544/9 the  $X_{50}$  difference is of the same order as that for EE758544/4 and EE758544/7, where a difference in ED was

## Formulation Studies

demonstrated. It is arguable that the difference in texture between the open crumpled particles of EE758544/4 and the tightly crumpled particles of EE758544/7 and EE758544/9 is to some extent responsible for the emitted dose differences – a difference in emitted dose between corrugated and spherical particles was observed by Chew & Chan (2001) with corrugated bovine serum albumin particles responsible for lower device deposition. The surface texture will have an influence on the geometric particle size for particles of equivalent mass, as a greater deviation from sphericity will result in a larger geometric size, hence the  $X_{50}$  differences observed between the various batches compared here may not completely describe absolute differences in mean diameter by mass. Insufficient material was generated during spray drying to allow specific surface area and density measurements to be conducted, hence it has not been possible to deconvolute the effects of particle mass and texture. Blend structure may also have an influence upon the emitted dose, particularly at the lower test air flow rate. The electron micrographs presented as Appendix 7 show an increased prevalence of adhesion to carrier particles for the three batches containing API particles with  $X_{50}$  below 10  $\mu\text{m}$ .

The effect of particle size upon deposition is clearly evident from the inter-batch comparison of RM and ISM. Greater amounts are deposited in the case of batches containing particles with an  $X_{50}$  below 10  $\mu\text{m}$  particles (batches EE758544/2, 3, 8, 12 and 13) than for batches with larger  $X_{50}$  values, and the expected correlation between  $X_{50}$  and mass deposited is observed for the sub-10  $\mu\text{m}$   $X_{50}$  batches. Students T-test was used to determine the significance (at 95% confidence) of the differences between the deposition masses attributable to droplet sizes and concentrations over the twelve

## Formulation Studies

formulated batches; significance probability (p) values are presented in Table 5.6 with significant differences highlighted in red. The droplet size used to produce mometasone furoate particles has a highly significant impact upon ISM and RM at both 20 and 60 L min<sup>-1</sup> when considering the entire range of mometasone furoate concentrations employed. Significant differences in impactor sized mass between batches containing particles formed at the two droplet sizes are also observed at individual concentrations with the exception of particles formed at 1.25 %w/w solution concentration, where similar particle sizes were unexpectedly obtained during spray drying. Respirable mass shows a similar trend with no significant difference observed at 1.25 %w/w; statistical significance between droplet sizes was also unable to be demonstrated at the 0.375 %w/w solution concentration. The effect of solution concentration used to produce the API particles upon APSD is demonstrated for blends containing API generated at 80 µm droplet size, with significant differences for both ISM and RM. No significant difference is observed at 40 µm droplet diameter however, unsurprisingly given the similarity in mometasone furoate particle size and morphology between the input API batches.

**Table 5.6: Significance probability (p) values for effect of experimental parameters on APSD**

Droplet size (µm)	Concentration (%w/w)	ISM		RM	
		20 L min <sup>-1</sup>	60 L min <sup>-1</sup>	20 L min <sup>-1</sup>	60 L min <sup>-1</sup>
80 vs. 40	All	<0.001	<0.001	0.001	0.001
	0.375	0.018	0.029	0.0743	0.0644
	0.75	0.001	<0.001	<0.001	<0.001
	1.0	0.008	0.010	0.001	0.001
	1.25	0.212	0.716	0.588	0.658
80	0.375 vs. 0.75	0.024	0.029	0.021	0.032
40	0.375 vs. 0.75	0.904	0.132	0.817	0.180

## Formulation Studies

A batch-wise comparison of results was undertaken to assess the possible impact of particle morphology and surface texture upon aerosolisation performance, as presented in Table 5.7. Statistically significant differences in APSD results between batches are denoted using red text.

**Table 5.7: Significance probability (p) values for batch-wise comparison of morphology on APSD**

Droplet size ( $\mu\text{m}$ )	Concentration (%w/w)	Batches compared		ISM		RM	
				20 L min <sup>-1</sup>	60 L min <sup>-1</sup>	20 L min <sup>-1</sup>	60 L min <sup>-1</sup>
80	0.75	EE758544/4	EE758544/7	0.827	0.412	0.827	0.878
		EE758544/4	EE758544/6	0.574	0.101	0.470	0.050
		EE758544/6	EE758544/7	0.575	0.079	0.549	0.007
	0.375	EE758544/5	EE758544/13	0.056	0.315	0.034	0.027
	0.375 vs. 0.75	EE758544/4	EE758544/13	0.043	0.128	0.018	0.023
		EE758544/5	EE758544/7	0.772	0.025	0.062	0.042
	0.75 vs. 1.0	EE758544/7	EE758544/9	0.179	0.127	0.058	0.019
1.0 vs. 1.25	EE758544/9	EE758544/11	0.40	0.151	0.592	0.018	
40	0.5 vs. 0.75	EE758544/2	EE758544/12	0.063	0.001	0.063	<0.001
	0.375 vs. 0.5	EE758544/3	EE758544/12	0.020	0.002	0.002	0.0004
	0.375 vs. 0.75	EE758544/2	EE758544/3	0.904	0.132	0.816	0.180

Differences in the mass of API impacted when comparing concentrations within a droplet

size can be identified. At the 40  $\mu\text{m}$  droplet size differences in ISM and RM exist between 0.5 and 0.375 %w/w or 0.75 %w/w concentrations at 60 L min<sup>-1</sup>; significant difference is also observed at 20 L min<sup>-1</sup> between 0.5 and 0.375 %w/w. The particles generated at 0.5 %w/w concentration produced a larger ISM and RM than those generated at either 0.375 or 0.75 %w/w, however this is unsurprising given that a smaller particle size was produced by the 0.5 %w/w run than for 0.375 %w/w. Some variability between atomization runs at nominally identical conditions was noted in Section 3.2.3, and may be the cause of the unexpectedly smaller particle size percentiles measured for the API used in formulated blend EE758544/12 compared to that used in EE758544/3.

## Formulation Studies

A number of batches manufactured using mometasone furoate particles generated at the larger droplet size have been compared where operating parameters other than concentration are kept constant. Significant differences in RM at  $60 \text{ L min}^{-1}$  are evident for the three groups of batches compared, with the difference also observed at  $20 \text{ L min}^{-1}$  between batches EE758544/4 and EE758544/13, which showed the greatest divergence in result for the batches produced using a target droplet size of  $80 \mu\text{m}$  batches. The RM differences between the batches compared are intuitive for all concentrations with the exception of the comparison between 1.0 and 1.25 %w/w. Inspection of the particle size determination results reveals a similar geometric size for particles produced using 1.0 and 1.25 %w/w concentrations, again possibly due to subtle differences in droplet size distributions between runs at the same atomizer operating parameters.

Comparison of batches containing particles generated at the same droplet size and concentration show significant differences. Two of the batches, EE758544/5 and EE758544/13, contained mometasone furoate particles with distinctly different morphologies as shown in the electron micrographs presented in Table 4.4. The resulting differences in respirable mass between the two batches is similar to that seen between either batch and the RM for batch EE758544/3 containing API produced using  $40 \mu\text{m}$  droplets. Similar arguments on the relative impact of geometric size and particle texture can be made as for the emitted dose differences between batches EE758544/4 and 7; notable differences in particle texture are present but the difference in geometric size is consistent with the relative difference in ISM and RM.

Three formulations (EE758544/4, 6 and 7) utilised particles produced using nominally  $70 \mu\text{m}$  droplets at a solute concentration of 0.75 %w/w. Differences in aerosolisation

## Formulation Studies

performance, assuming similarity in geometric PSD, can be attributed to mometasone furoate particle property differences resulting from the use of different solvent and changes to the inlet temperature and drying gas flow rate of the spray dryer. Visual inspection of the electron micrographs presented as Table 4.4 reveals pronounced differences in particle morphology produced upon drying – particles spray dried from ethanol are corrugated, the degree of which appears related to the drying temperature. In contrast particles produced using propanol as solvent exhibit corrugation to a much lower extent with smooth, spherical particles being prevalent. Differences in aerosolisation behaviour were identified at  $60 \text{ L min}^{-1}$  with emitted dose for EE758544/4 being significantly higher than EE758544/6 and EE758544/7, and respirable mass for EE758544/6 being greater than that for EE758544/4 and EE758544/7. The trends RM results also correspond to the average particle mass trends that would be expected from the measured diameters presented in Table 4.5, however the generation of corrugated particles is likely to result in a larger characteristic particle dimension than for a solid sphere of the same mass of material, similarly to the ED results as discussed earlier.

### **5.4. Conclusion**

The differences in particle properties able to be obtained for mometasone furoate by spray drying with the flow focusing nozzle have had a direct impact upon the performance of formulated product. Statistically-significant differences in both the emitted dose and respirable fraction have been determined during this study, indicating that atomization using controlled droplet distribution is a viable method for optimising the API particle size distribution for use in an inhaled dosage form. A direct relationship between respirable mass and the droplet size used to produce the mometasone furoate

## Formulation Studies

particles has been demonstrated, with respirable masses of 28.7 to 109.3 mcg obtained for particles from 35  $\mu\text{m}$  droplets, compared to 4.7 to 10.5 mcg for 70  $\mu\text{m}$  droplets (for blends containing particles generated from 0.375 to 1.0 %w/w solution concentration, tested at 60 L  $\text{min}^{-1}$ ). The absolute effect of size upon delivery efficiency is illustrated with reference to the API particles produced using 40  $\mu\text{m}$  droplets – a 13 % decrease in MF particle diameter from 6.2 to 5.4  $\mu\text{m}$  has resulted in a three-fold increase in respirable mass from 29.9 to 109.3 mcg.

Emitted doses were also dependent upon the droplet size used to form particles, with lower emitted doses (341.7 to 593.1 mcg) determined at 60 L  $\text{min}^{-1}$  for 35  $\mu\text{m}$  droplets compared to 70  $\mu\text{m}$  droplets (615.4 to 819.7 mcg) at solution concentrations at or below 1.0% w/w. Flow dependency of cascade impaction results is clearly evident, with impactor sized masses and respirable masses all greater at 60 L  $\text{min}^{-1}$  compared to 20 L  $\text{min}^{-1}$ . The relationship between emitted dose and flow rate is similar, additionally divergence in the relationship between mometasone furoate size and emitted dose was noted with a change in flow: smaller mometasone furoate particles produced a comparatively larger emitted dose at 20 L  $\text{min}^{-1}$ , however at 60 L  $\text{min}^{-1}$  larger particles were seen to increase the emitted dose.

The cascade impaction results suggest particle texture may play a role in the differences in respirable mass observed - three API particle batches generated at the same nominal droplet size and concentration under different drying conditions yielded different particle textures which subsequently produced subtle but significant differences in device performance. A respirable mass of 10.3mcg was determined for the smooth mometasone furoate particles within formulation EE758544/6, compared with 6.3 and



## Formulation Studies

6.5 mcg for the open crumpled particles within EE758544/4 and tight crumpled particles in EE758544/7.

The mometasone furoate particles used in this study were generated with the intention of studying the energetic impact of spray drying with controlled droplet sizes, as described in Chapter 3, hence were not optimised for exploring inhaled delivery. The optimal batch produced, containing mometasone furoate particles of 5.4  $\mu\text{m}$   $X_{50}$ , however compares well in terms of respirable fraction to those described by Donovan et al for micronized budesonide from a Cyclohaler using similar lactose – 19.3% of emitted dose for spray dried mometasone furoate versus 15.2 for budesonide.

The data presented here therefore provide only a small insight into what is achievable via narrow droplet distribution spray drying using flow-focusing, and the univariate approach taken to formulation necessitated by the small quantities of API available leaves much scope for optimising the formulation approach. Similarly the use of single device did not fully explore the interplay between deagglomeration potential and API particle properties in respirable dose generation.

Further studies targeted at producing particles within the respirable range, particularly those employing a range of solvents capable of inducing varying texture, will provide additional information regarding the utility of this technique and the potential for subsequent performance gains for inhaled formulations.

## 6. CONCLUSION AND FURTHER WORK

The studies described in this thesis have highlighted the effectiveness of simple flow-focussing technology in improving the uniformity of output from an industrially-representative spray dryer. Regulation of target droplet size and the associated droplet size variance using two control parameters, gas pressure and liquid flow rate, has been successful in delivering meaningful differences in the particle size, morphology and molecular arrangement of a representative active pharmaceutical ingredient. The use of two droplet sizes and multiple solute concentrations allowed sodium chloride particles across the  $X_{50}$  range 3 – 13  $\mu\text{m}$  to be produced; amorphous mometasone furoate particles were generated within the  $X_{50}$  range 5 – 17  $\mu\text{m}$  with a variety of textures. Drying of 40  $\mu\text{m}$  diameter mometasone furoate solution droplets led to the formation of smooth particles, except when using ethanol as a solvent and drying at 100°C inlet temperature which yielded corrugated particles. At 80  $\mu\text{m}$  droplet size the depth of the corrugations was observed to increase with decreasing concentration and 100°C inlet temperature; increasing the concentration or use of 160°C inlet temperature increased the number of corrugations and reduced the corrugation depth, with some instances of spherical particles when using 2-propanol as the solvent. The formation of spherical particles is indicative of a mechanically robust layer being formed during initial precipitation of solid, hence the generation of corrugations would appear to indicate a greater degree of flexibility resulting in deformation upon further drying. Deep corrugations are consistent with increased flexibility given their formation when using low solute concentrations, with increased corrugation frequency and smaller amplitude being observed upon concentration increase.

## Conclusion and Further Work

The differences in the texture able to be produced during spray drying with narrow droplet distributions further exemplify the particle characterisation differences possible by careful control of the spray drying operation, without always having to resort to the inclusion of excipients.

A comparison to experiments employing the standard two-fluid nozzle supplied with the Buchi B-290 demonstrates a reduced span. The flow-focusing atomizer produced particle size distributions with an average span (range in parentheses) of 1.1 (0.8 – 1.6) compared to 1.7 (1.2 – 1.9) (Paluch *et al.*, 2012). Perhaps more important is the range of average particle size the flow-focusing atomizer is capable of generating; minimum and maximum  $X_{50}$  values of 4.5 to 16.9  $\mu\text{m}$  were able to be produced compared to 1.6 to 3.4  $\mu\text{m}$  for the Buchi two-fluid atomizer (Paluch *et al.*, 2012).

Flow rates within the experimental equipment configuration used were modest, however multiplexing of atomizers would offer a route to scale-up and commercial viability. The technology has been observed to be robust to use in the demanding environment within the spray dryer, and is not believed to be subject to the limitations presented by the full range of solution systems encountered with more complex systems. An inability to process fluticasone propionate, one of the APIs selected for evaluation was observed however; further work has been suggested using a similar API with modified ester groupings to attempt to elucidate the root cause for the processing difficulties experienced.

Valuable insights into the thermodynamic and kinetic properties of mometasone furoate in the amorphous state were also able to be gained by use of the flow-focusing technology within the spray drying configuration. A relationship was defined between

## Conclusion and Further Work

the enthalpy observed as the spray dried mometasone furoate passed the glass transition temperature, attributed to latent heat of crystallization, and drying conditions. The correlation between the enthalpy range ( $8 - 40 \text{ J g}^{-1}$ ) and processing conditions suggests a link between the free energy of the particles and the kinetics of drying. The in-vivo dissolution and so bioavailability may therefore be able to be improved whilst maintaining a stable product, given that suitably high glass transition temperatures ( $109 - 150^\circ\text{C}$ ) were determined across the processing ranges used. Some counterintuitive relationships between variables and enthalpy have been identified, with increased gas flow and solute concentration giving unexpected reductions in enthalpy perhaps associated with retained solvent upon drying. Further investigation of these variables would help establish the validity of these relationships and explore whether, if confirmed, they are generic or specific to mometasone furoate. The possible impact of residual solvent on the mometasone glass transition has also been noted; complete drying will be required to ensure no suppression in this attribute and so lend stability to the particles generated.

Formulation experiments using the mometasone furoate particles have demonstrated a meaningful difference in the delivery of API from a pharmaceutical dosage form. The systematic variation in impaction profile with mometasone particle size, spanning the respirable mass range  $5 - 109 \text{ mcg}$  when tested at  $60 \text{ L min}^{-1}$ , indicates a difference in clinical dosing performance should be expected across the range of particles produced by flow-focusing spray drying, and if the differing thermodynamic properties of the particles translate to dissolution and transport differences, an additional dimension in efficacy change may be available.

## Conclusion and Further Work

The work performed has also identified some topics that would benefit from further research. The understanding of flow focusing continues to develop, and the systematic offset from predicted droplet size with varying flow and pressure identified in Section 3.2.3 indicates the current theory based predominantly upon Weber number may require augmentation. The increased variance and decreased reproducibility associated with aqueous solutions compared to those encountered when using alcohols suggests additional attributes in addition to surface tension are impactful and should be accounted for.  $X_{50}$  coefficient of variation values of 4.5 % for sodium chloride solutions and 2.8 % for mometasone furoate were apparent within runs. The discrepancy for between run variability is greater: 5.3 and 3.5 % for 40 and 80  $\mu\text{m}$  mometasone furoate solution droplets versus 26.9 and 10% for 35 and 70  $\mu\text{m}$  sodium chloride solution droplets.

From a processing perspective the over-prediction of output sodium chloride particle diameter (approximately 65 % of predicted) when flow focussing within a high-velocity gas stream indicates the external environment directly effects the formation of droplets, possibly by increasing the degree of extension of the liquid thread initially formed leading to reduced droplet size. Additional investigational work into the influence of external gas flows upon the average droplet size and variance would be of benefit to the successful implementation of the technology.

Insights gained into the behaviour of the two corticosteroid molecules selected for experimentation during practical work also highlights further area of study from a physicochemical perspective. The substantial difference in ability to spray dry the two

## Conclusion and Further Work

APIs was unexpected given their structural similarity, and is indicative of potentially large differences in transport properties that extend beyond their use in spray drying.

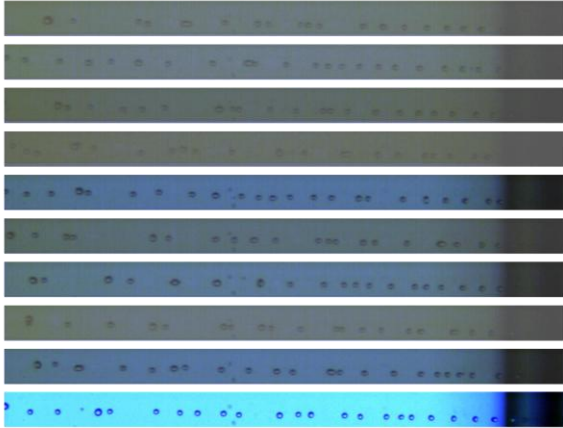
Finally, additional work can be identified that would add to the current knowledge of dry powder inhalation formulations. The variation in texture observed is likely to change the adhesion and aerodynamic properties of the particles compared to an equivalent sphere, however decoupling this factor from size has been difficult in the present study. A more complete understanding of the range of textures possible, and verification of these being produced at similar aerodynamic size would be an important development. The thermodynamic differences indicated by the range of enthalpies and varying textures obtained during experiments may translate into differences in transport across the lung; studies using cultured cell lines are likely to provide an understanding of the efficacy differences attributable to these attribute changes.

7. APPENDICES

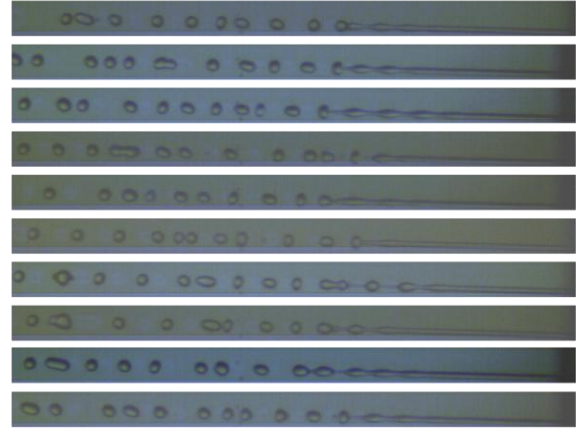
Appendix 1 Images of droplet break-up

Water

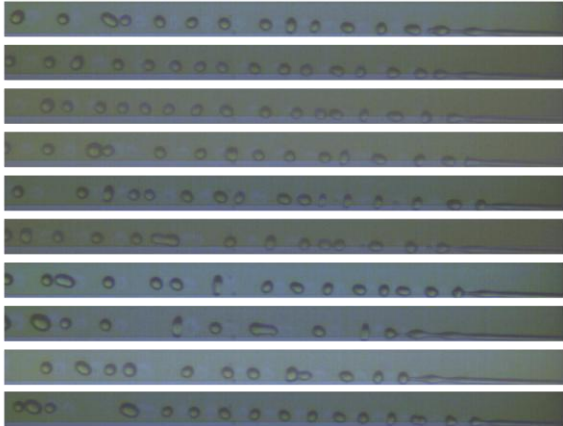
10ml/hr 130mbar (We = 8)



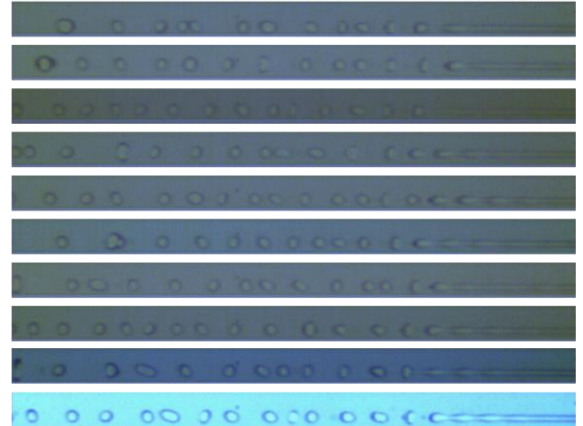
32ml/hr 80mbar (We = 10)



27ml/hr 60mbar (We = 8)

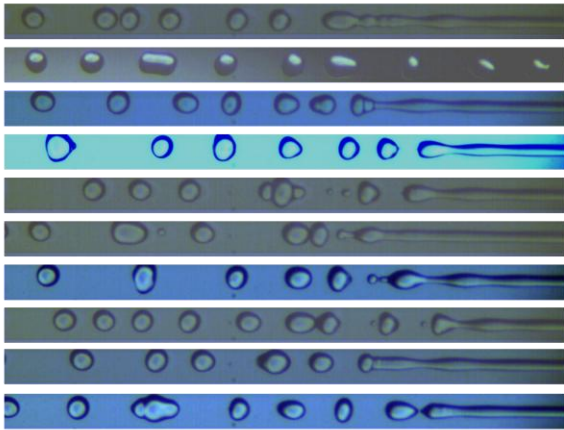


40ml/hr 130mbar (We = 17)

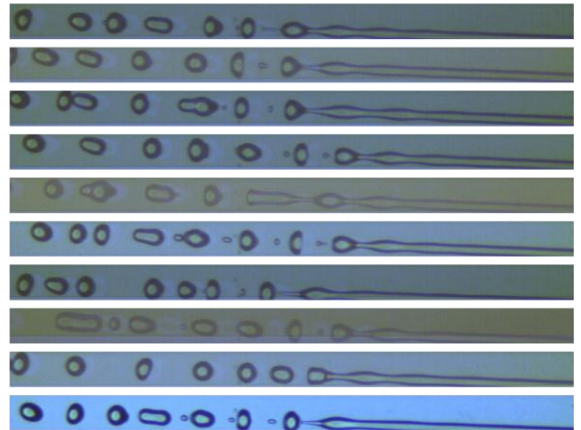


Appendix 1

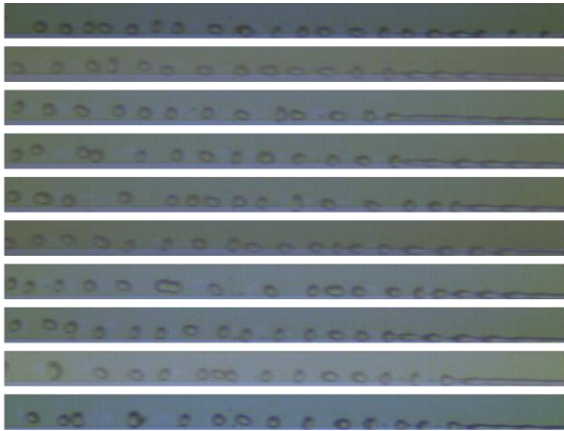
62ml/hr 60mbar (We = 12)



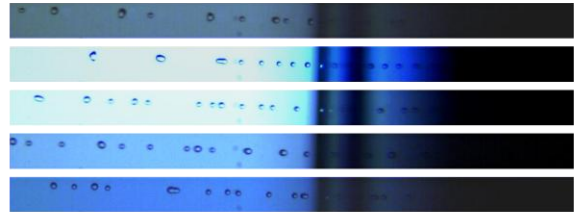
80ml/hr 100mbar (We = 19)



63ml/hr 300mbar (We = 39)



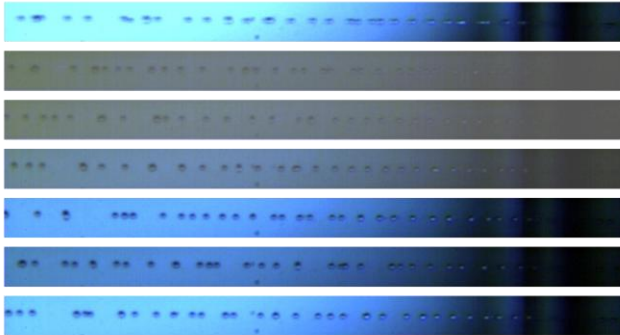
7ml/hr 60mbar (We = 4)



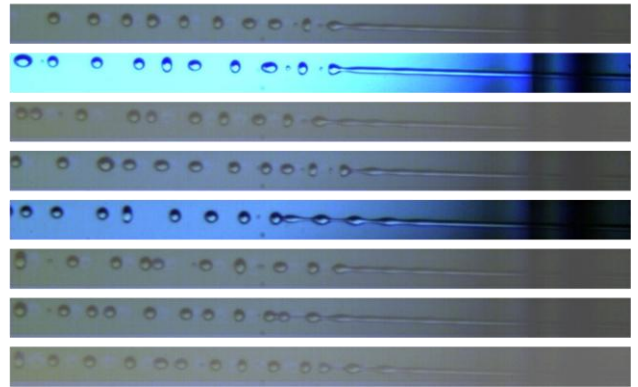


Ethanol

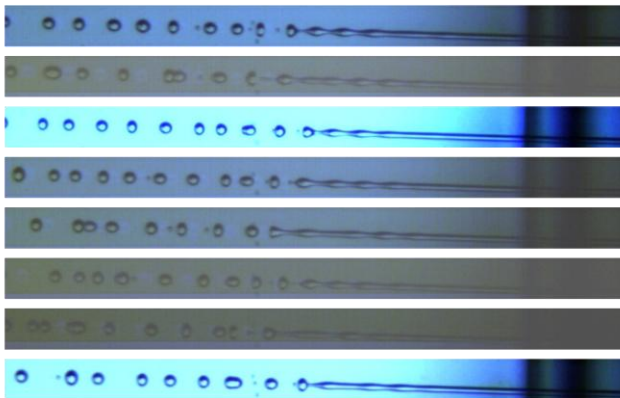
10ml/hr 100mbar (We = 21)



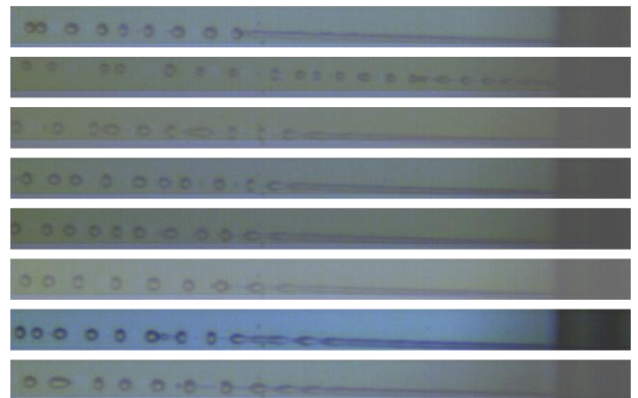
20ml/hr 25mbar (We = 11)



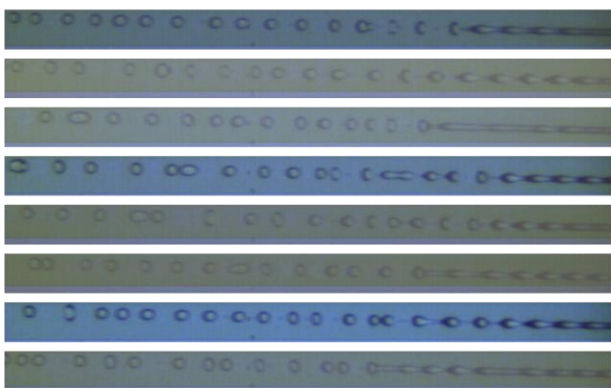
22ml/hr 30mbar (We = 13)



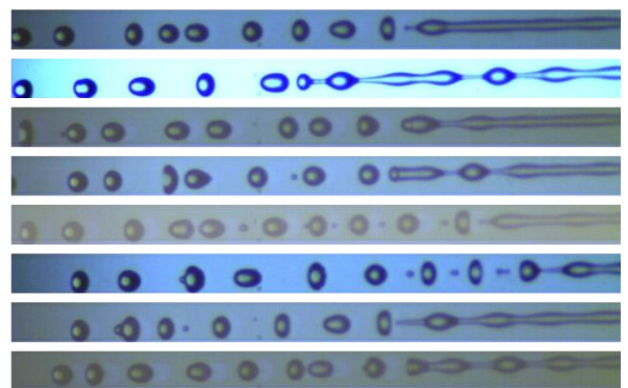
28ml/hr 50mbar (We = 21)



40ml/hr 100mbar (We = 43)

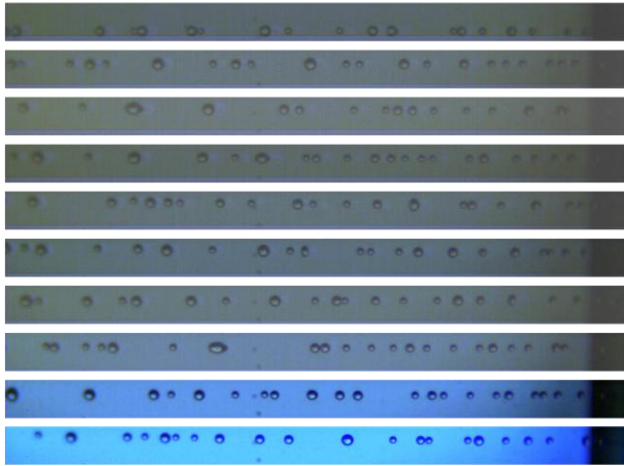


64ml/hr 50mbar (We = 32)

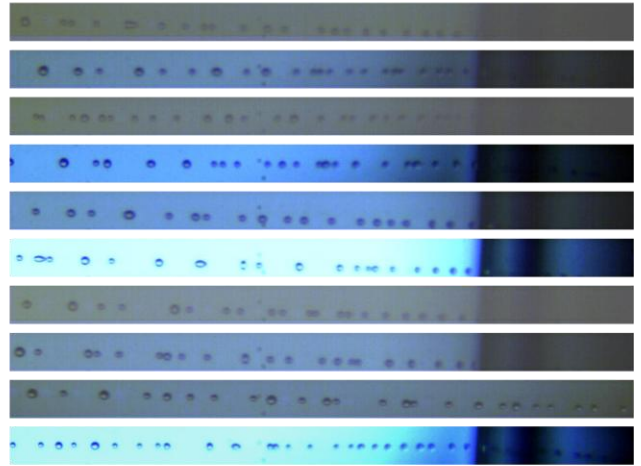


2-Propanol

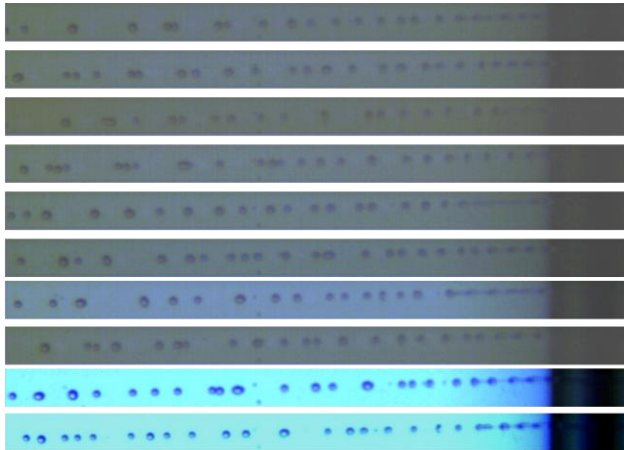
5ml/hr 25 mbar (We = 6)



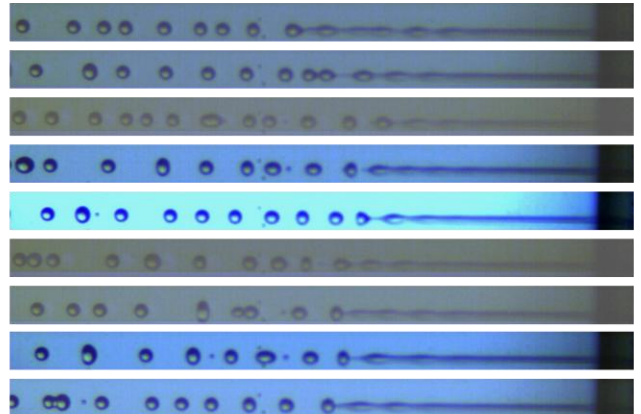
7.5ml/hr 55mbar (We = 14)



12ml/hr 150mbar (We = 37)



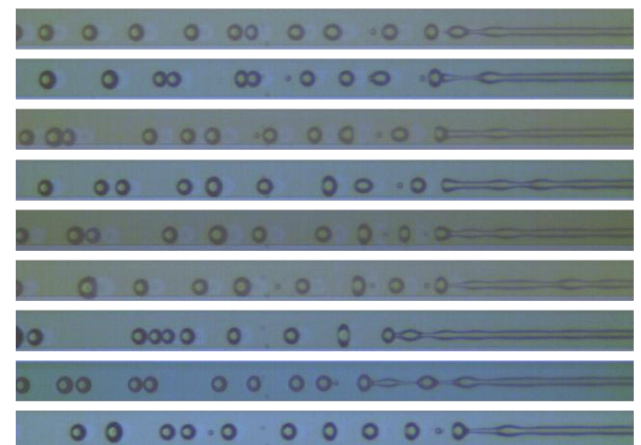
20ml/hr 25mbar (We = 12)



24ml/hr 35mbar (We = 17)

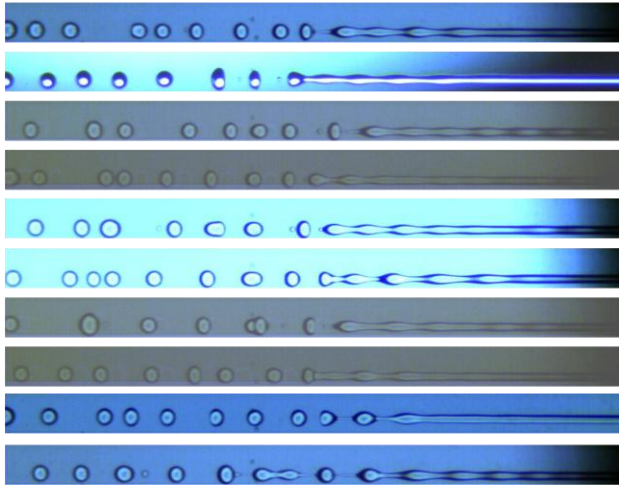


30ml/hr 55mbar (We = 27)

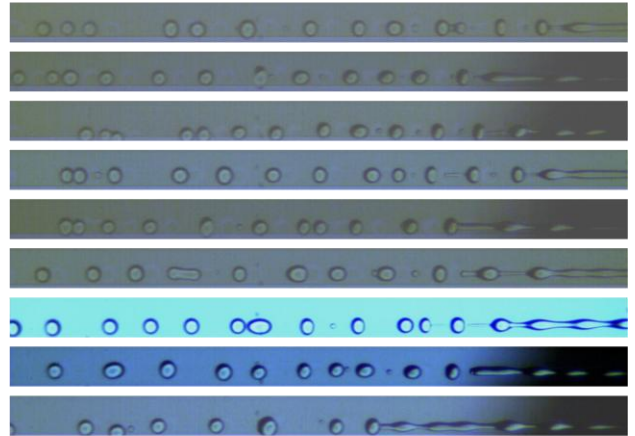


Appendix 1

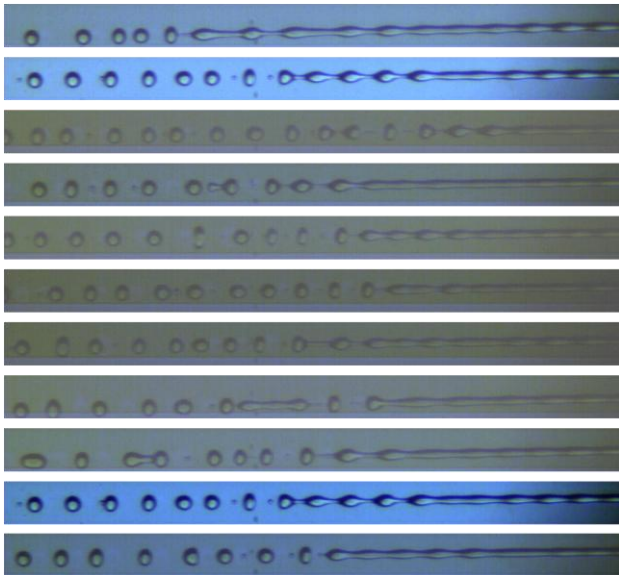
35ml/hr 75mbar (We = 37)



40ml/hr 100mbar (We = 50)

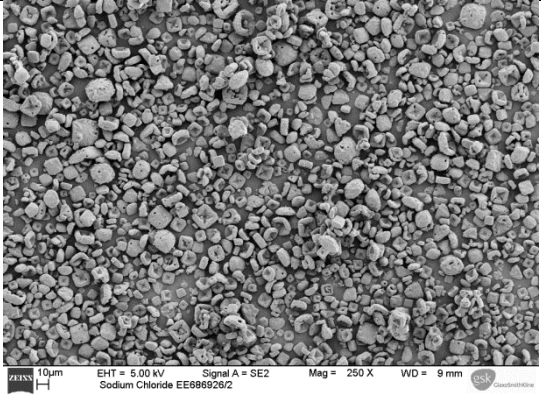
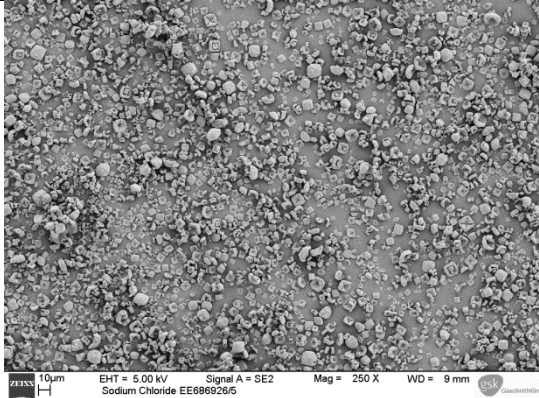
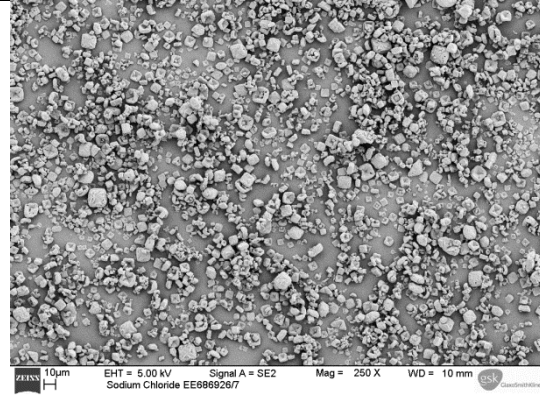
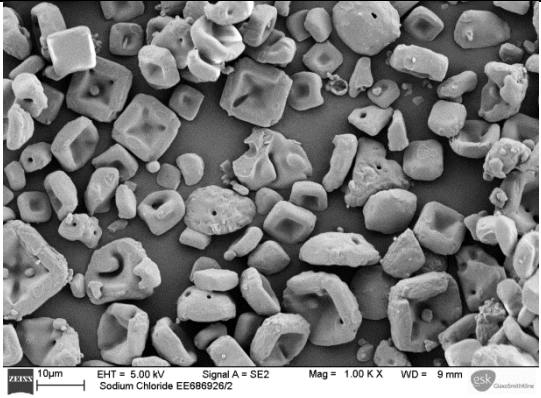
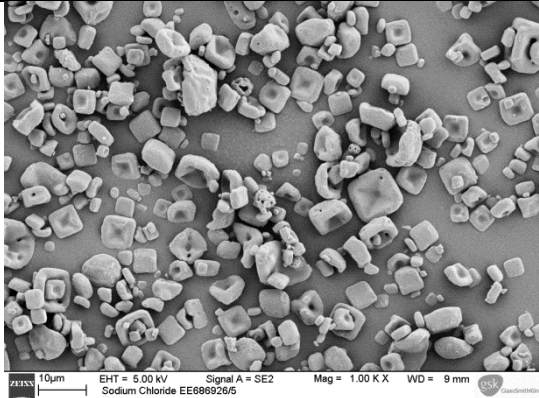
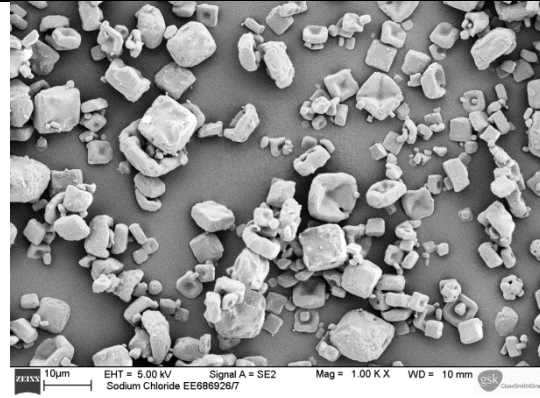


49ml/hr 150mbar (We = 74)

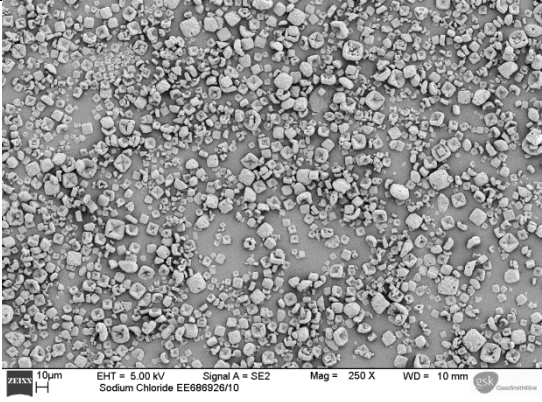
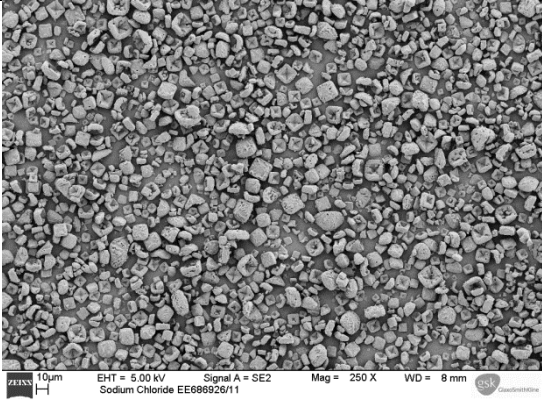
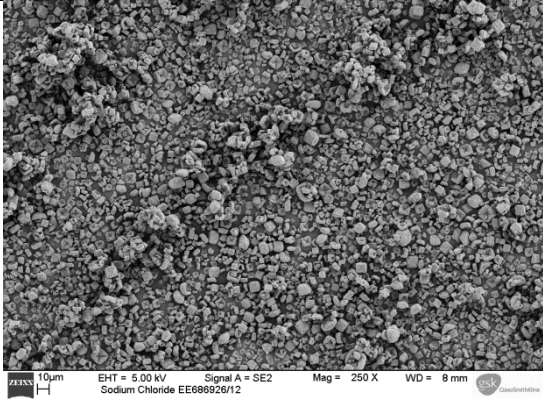
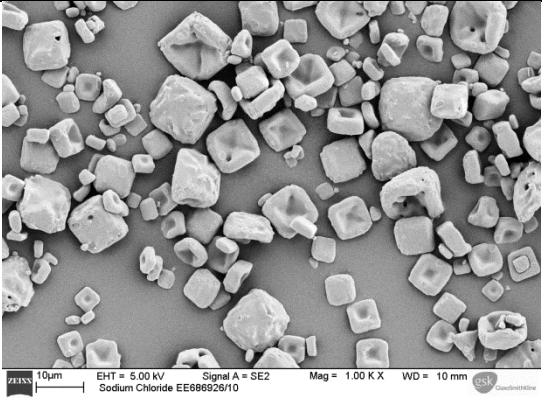
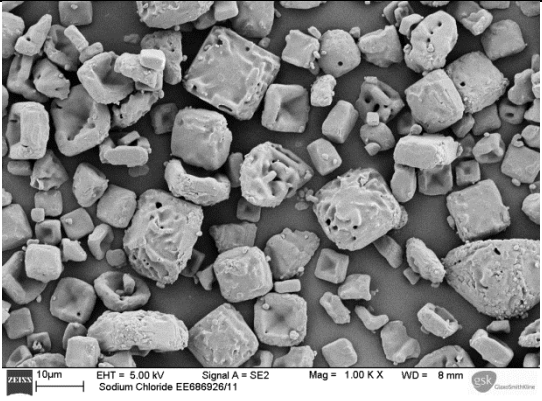
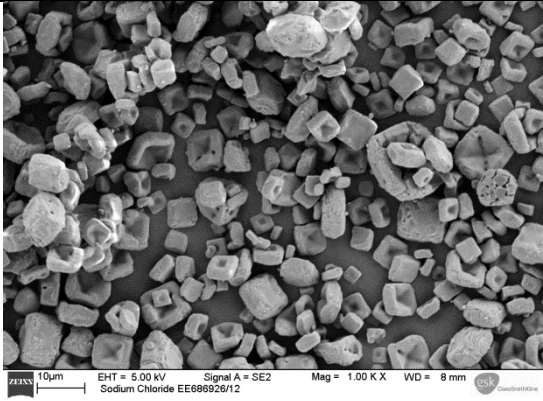




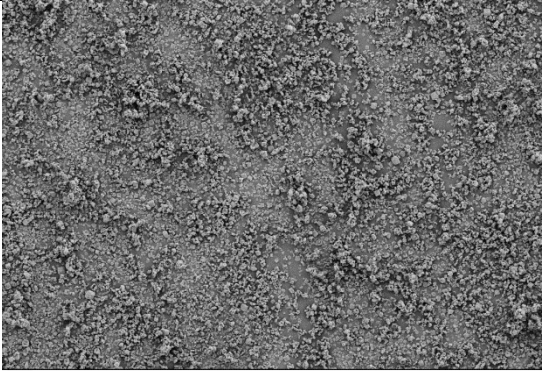
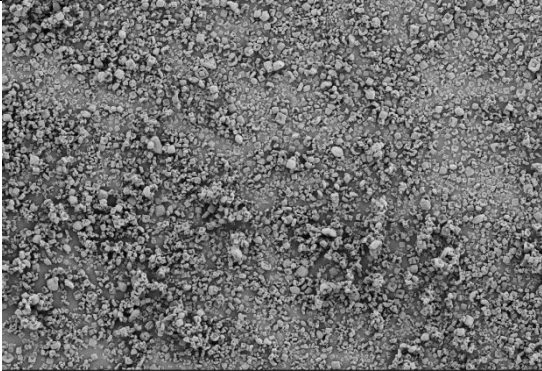
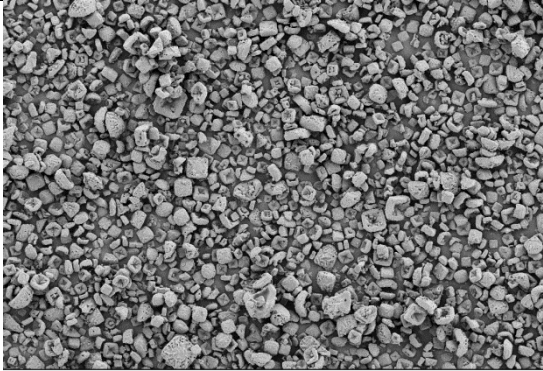
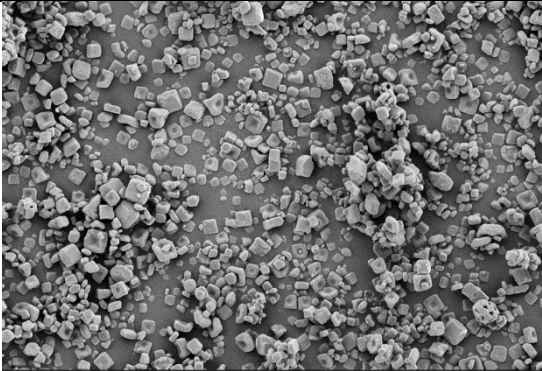
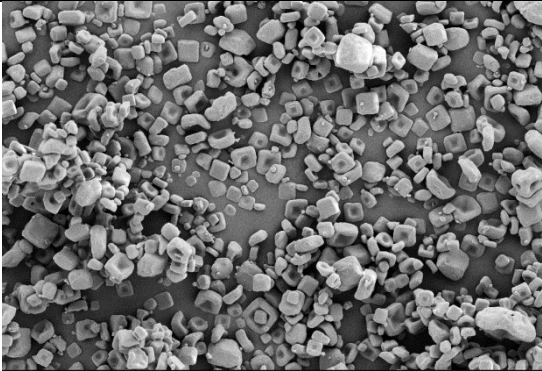
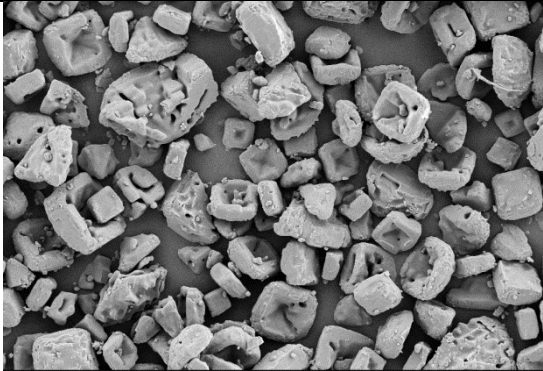
**Appendix 2 SEM images of spray dried NaCl**

Magnification	Batch number, predicted diameter (microns)		
	EE686926/2, 20 microns	EE686926/5, 7 microns	EE686926/7, 9 microns
250			
1000			

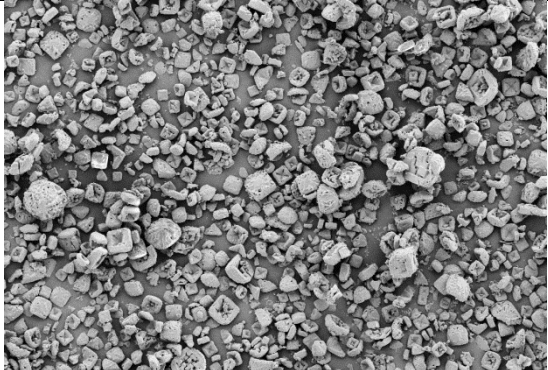
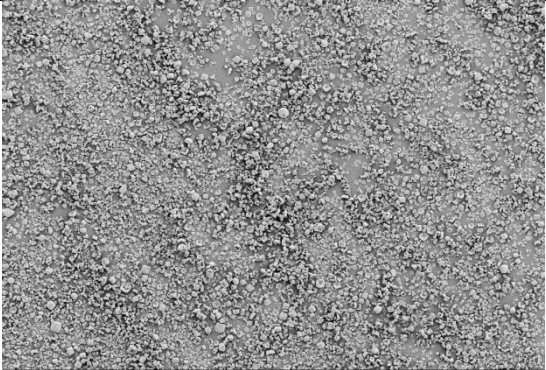
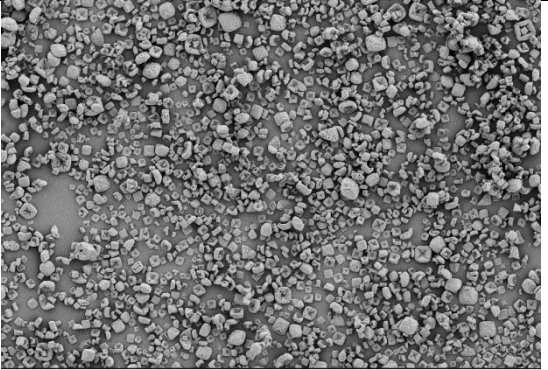
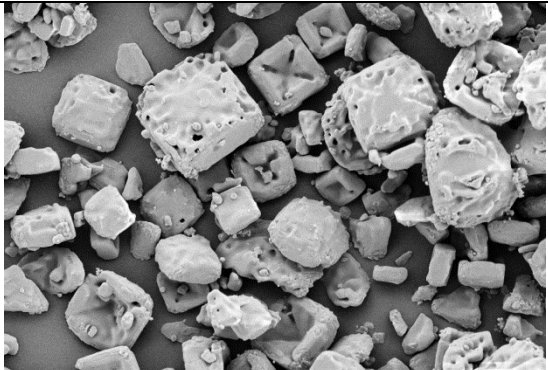
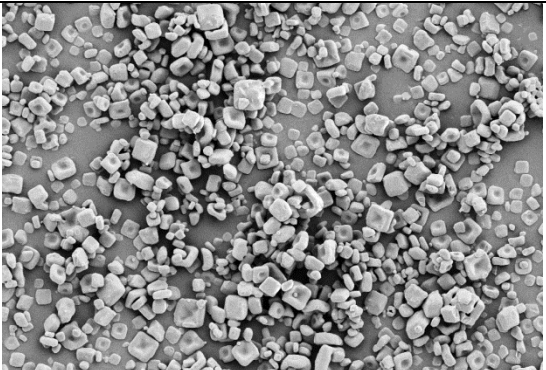
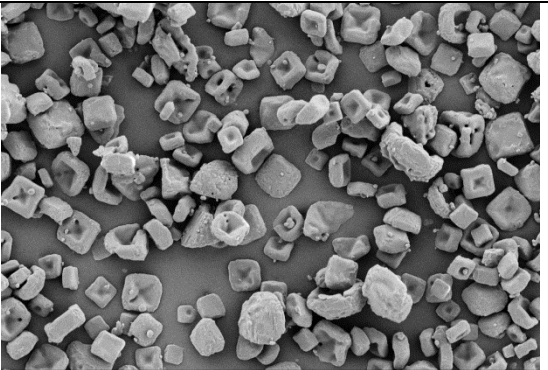
## Appendix 2

Magnification	Batch number, predicted diameter (microns)		
	EE686926/10, 9 microns	EE686926/11, 17 microns	EE686926/12, 12 microns
250			
1000			

## Appendix 2

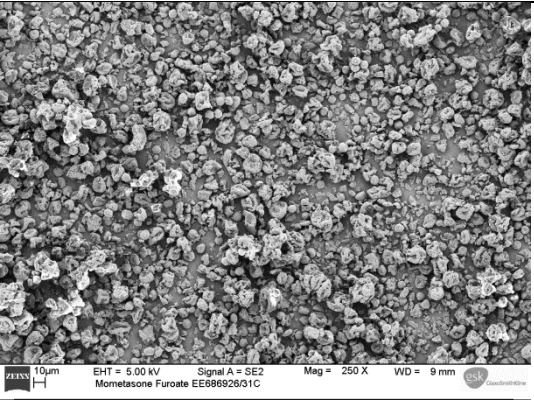
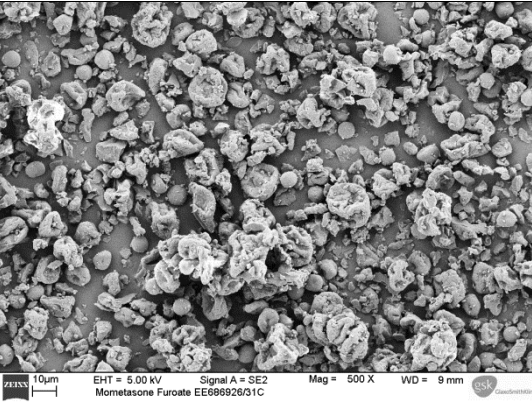
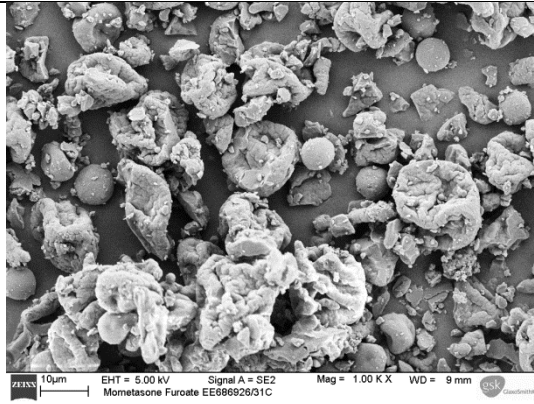
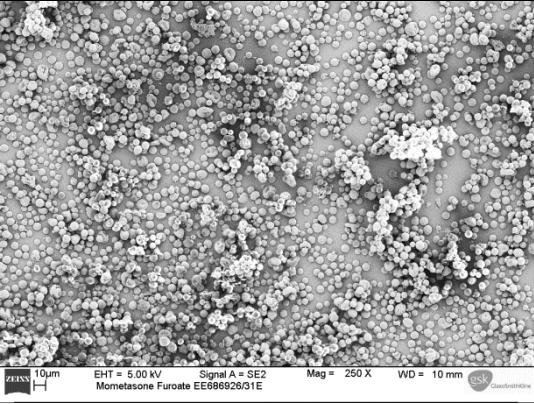
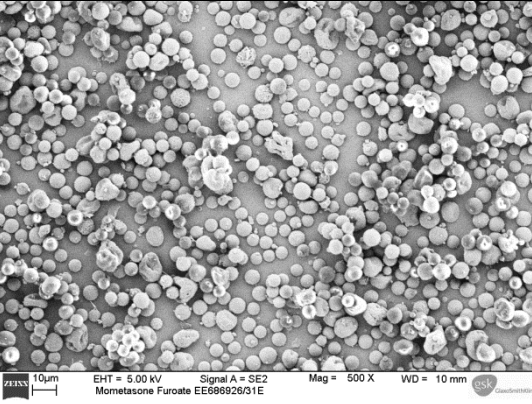
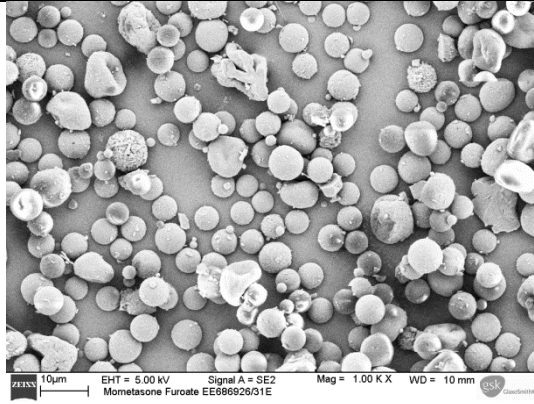
Magnification	Batch number, predicted diameter (microns)		
	EE686926/13, 5 microns	EE686926/14, 7 microns	EE686926/16, 16 microns
250	 <p>ZEISS 10µm EHT = 5.00 kV Signal A = SE2 Mag = 250 X WD = 8 mm Sodium Chloride EE686926/13</p>	 <p>ZEISS 10µm EHT = 5.00 kV Signal A = SE2 Mag = 250 X WD = 9 mm Sodium Chloride EE686926/14</p>	 <p>ZEISS 10µm EHT = 5.00 kV Signal A = SE2 Mag = 250 X WD = 9 mm Sodium Chloride EE686926/16</p>
1000	 <p>ZEISS 10µm EHT = 5.00 kV Signal A = SE2 Mag = 1.00 K X WD = 8 mm Sodium Chloride EE686926/13</p>	 <p>ZEISS 10µm EHT = 5.00 kV Signal A = SE2 Mag = 1.00 K X WD = 9 mm Sodium Chloride EE686926/14</p>	 <p>ZEISS 10µm EHT = 5.00 kV Signal A = SE2 Mag = 1.00 K X WD = 9 mm Sodium Chloride EE686926/16</p>

## Appendix 2

Magnification	Batch number, predicted diameter (microns)		
	EE686926/17, 20 microns	EE686926/19, 5 microns	EE686926/20, 12 microns
250	 <p>ZEISS 10µm EHT = 5.00 kV Signal A = SE2 Mag = 250 X WD = 10 mm Sodium Chloride EE686926/17</p>	 <p>ZEISS 10µm EHT = 5.00 kV Signal A = SE2 Mag = 250 X WD = 10 mm Sodium Chloride EE686926/19</p>	 <p>ZEISS 10µm EHT = 5.00 kV Signal A = SE2 Mag = 250 X WD = 8 mm Sodium Chloride EE686926/20</p>
1000	 <p>ZEISS 10µm EHT = 5.00 kV Signal A = SE2 Mag = 1.00 K X WD = 10 mm Sodium Chloride EE686926/17</p>	 <p>ZEISS 10µm EHT = 5.00 kV Signal A = SE2 Mag = 1.00 K X WD = 10 mm Sodium Chloride EE686926/19</p>	 <p>ZEISS 10µm EHT = 5.00 kV Signal A = SE2 Mag = 1.00 K X WD = 8 mm Sodium Chloride EE686926/20</p>

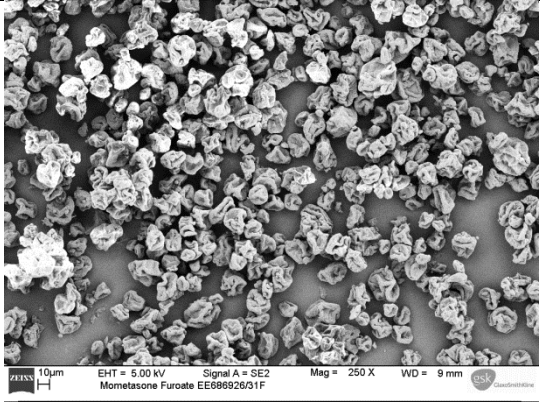
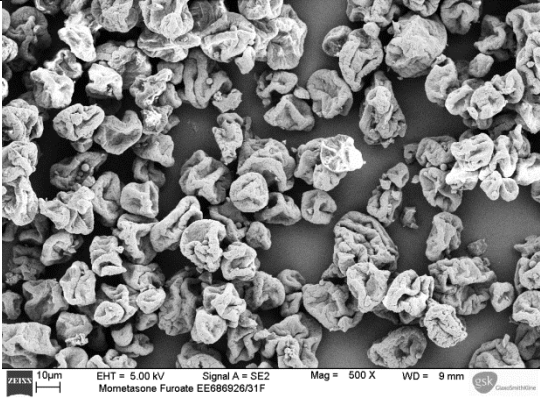
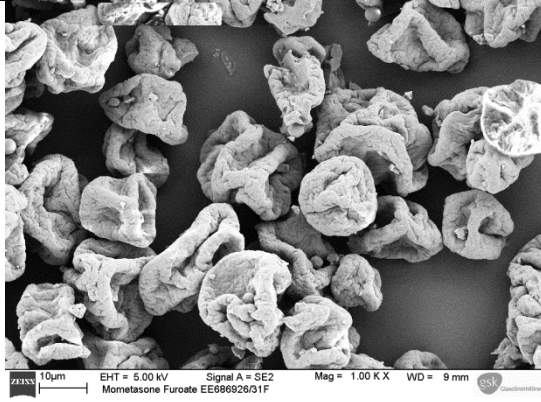
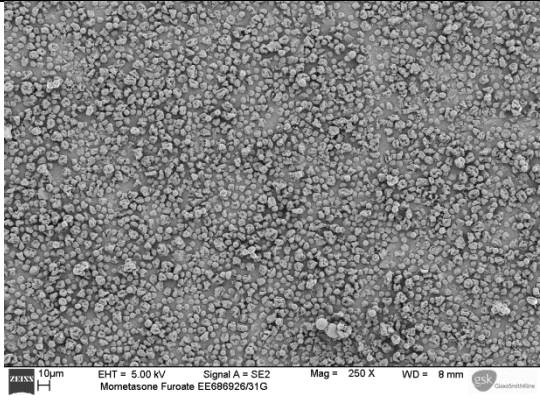
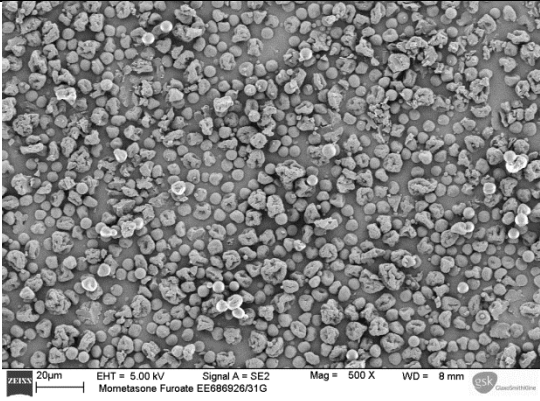
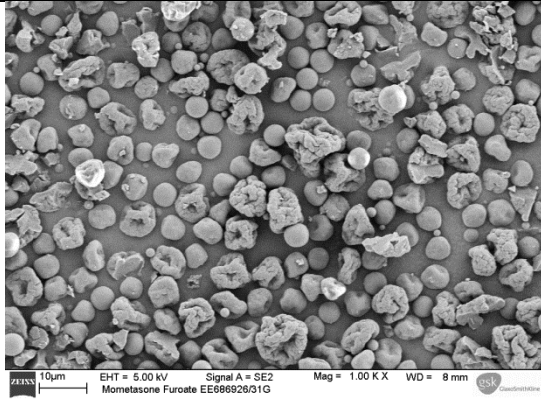


**Appendix 3 SEM images of spray dried MF**

Batch number	Magnification		
	250	500	1000
EE686926/31C			
EE686926/31E			

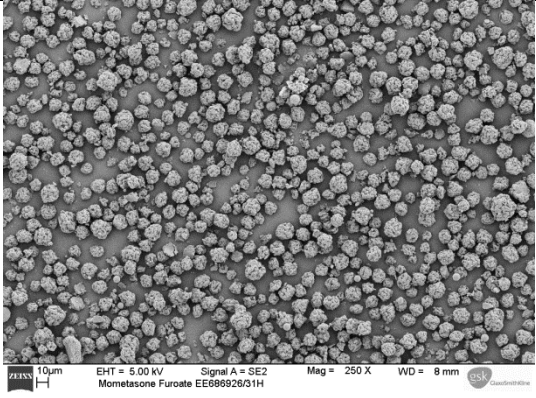
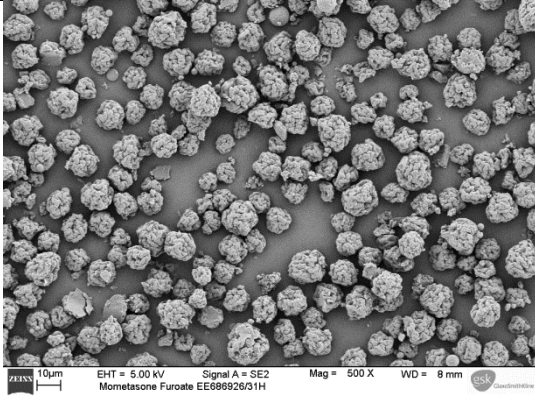
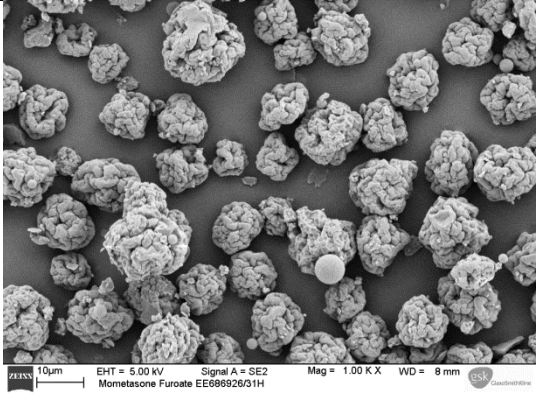
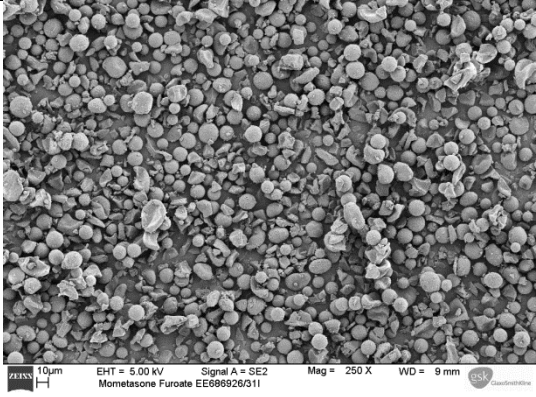
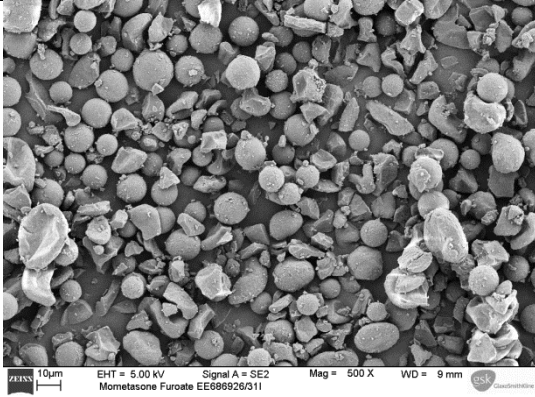
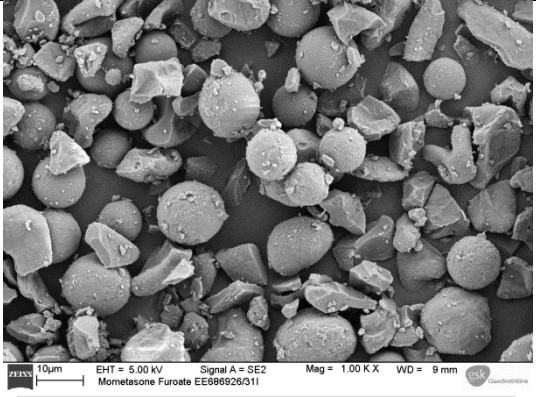


### Appendix 3

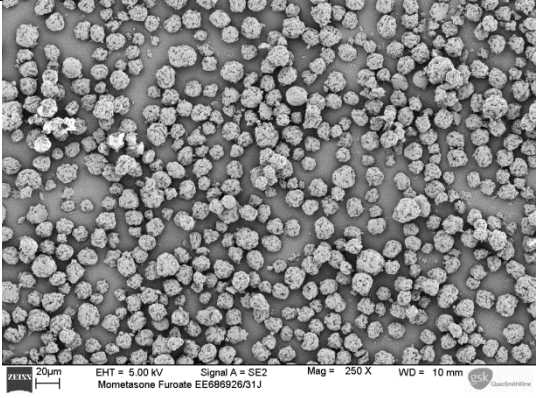
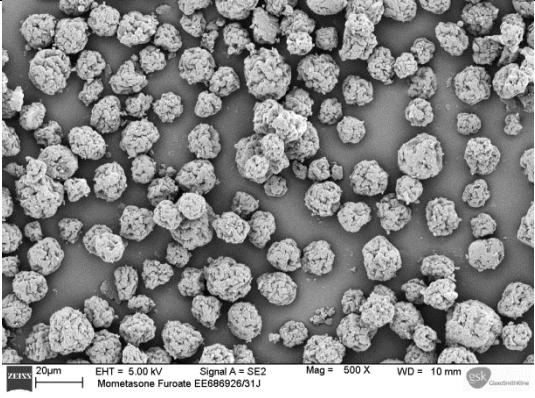
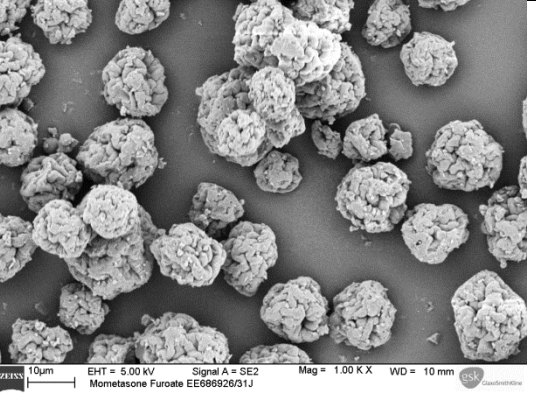
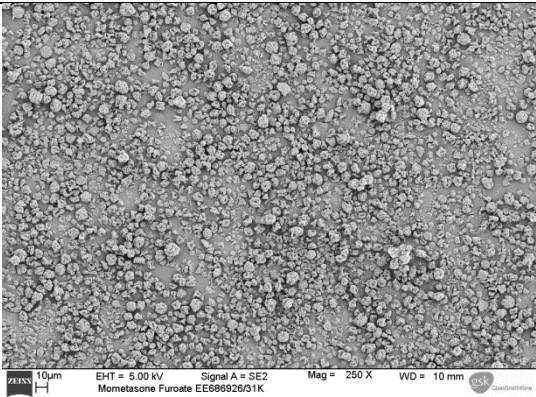
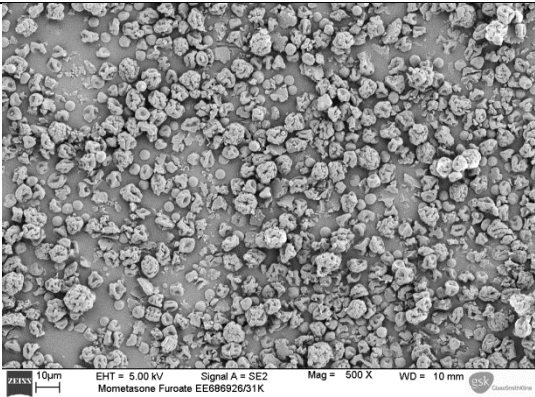
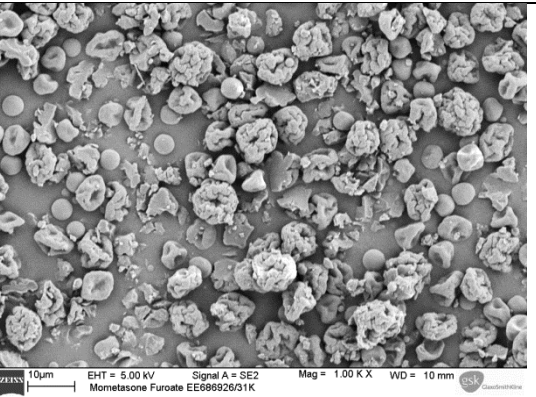
Batch number	Magnification		
	250	500	1000
EE686926/31F			
EE686926/31G*			

\* - Note: a 20 micron scale bar has been used for one image of EE696926/31G; the magnification (500x) is the same as for the images of compared batches

### Appendix 3

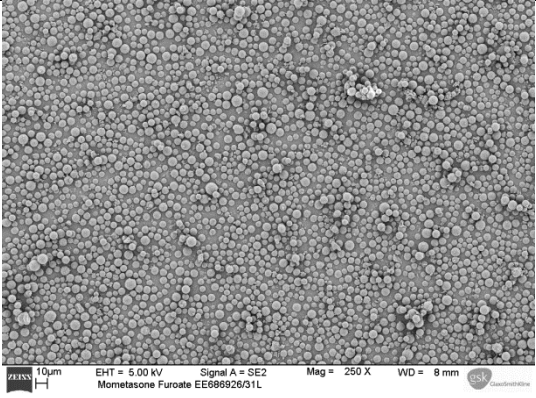
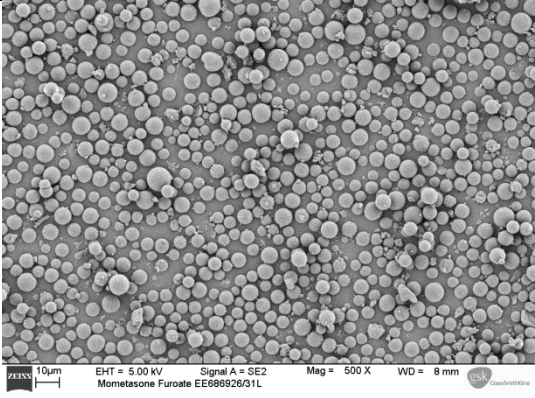
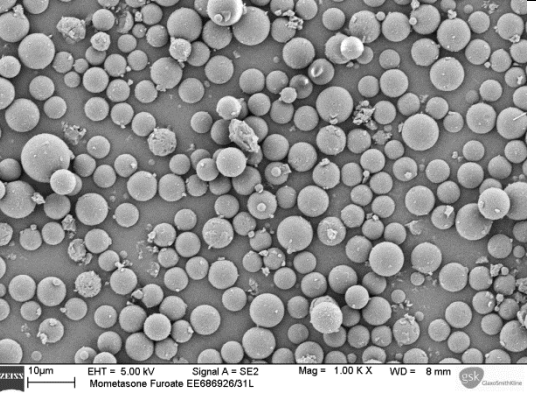
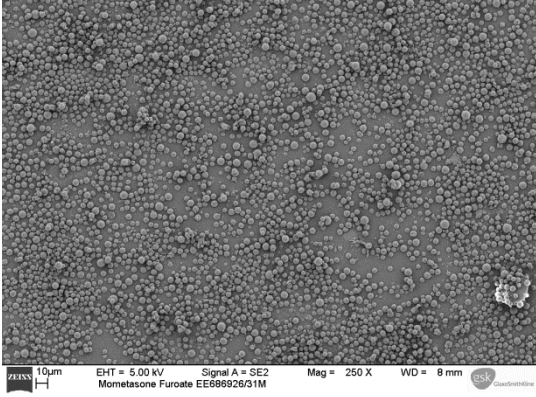
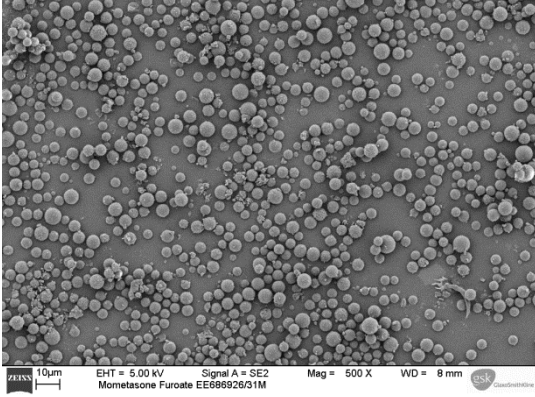
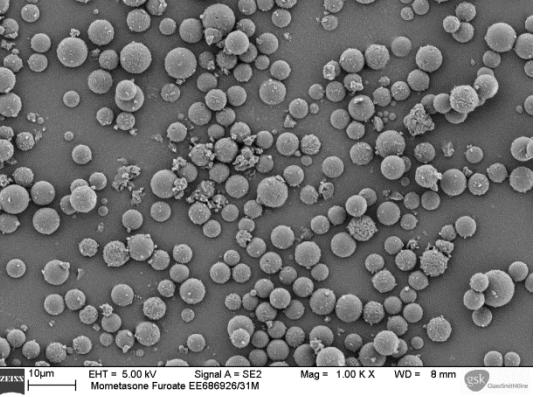
Batch number	Magnification		
	250	500	1000
EE686926/31H	 <p>ZEISS 10µm EHT = 5.00 kV Signal A = SE2 Mag = 250 X WD = 8 mm Mometasone Furoate EE686926/31H</p>	 <p>ZEISS 10µm EHT = 5.00 kV Signal A = SE2 Mag = 500 X WD = 8 mm Mometasone Furoate EE686926/31H</p>	 <p>ZEISS 10µm EHT = 5.00 kV Signal A = SE2 Mag = 1.00 K X WD = 8 mm Mometasone Furoate EE686926/31H</p>
EE686926/31I	 <p>ZEISS 10µm EHT = 5.00 kV Signal A = SE2 Mag = 250 X WD = 9 mm Mometasone Furoate EE686926/31I</p>	 <p>ZEISS 10µm EHT = 5.00 kV Signal A = SE2 Mag = 500 X WD = 9 mm Mometasone Furoate EE686926/31I</p>	 <p>ZEISS 10µm EHT = 5.00 kV Signal A = SE2 Mag = 1.00 K X WD = 9 mm Mometasone Furoate EE686926/31I</p>

### Appendix 3

Batch number	Magnification		
	250	500	1000
EE686926/31J*	 <p>ZEISS 20µm EHT = 5.00 kV Signal A = SE2 Mag = 250 X WD = 10 mm Mometasone Furoate EE686926/31J</p>	 <p>ZEISS 20µm EHT = 5.00 kV Signal A = SE2 Mag = 500 X WD = 10 mm Mometasone Furoate EE686926/31J</p>	 <p>ZEISS 10µm EHT = 5.00 kV Signal A = SE2 Mag = 1.00 K X WD = 10 mm Mometasone Furoate EE686926/31J</p>
EE686926/31K	 <p>ZEISS 10µm EHT = 5.00 kV Signal A = SE2 Mag = 250 X WD = 10 mm Mometasone Furoate EE686926/31K</p>	 <p>ZEISS 10µm EHT = 5.00 kV Signal A = SE2 Mag = 500 X WD = 10 mm Mometasone Furoate EE686926/31K</p>	 <p>ZEISS 10µm EHT = 5.00 kV Signal A = SE2 Mag = 1.00 K X WD = 10 mm Mometasone Furoate EE686926/31K</p>

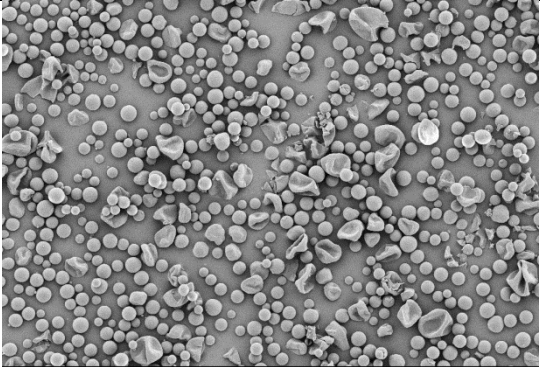
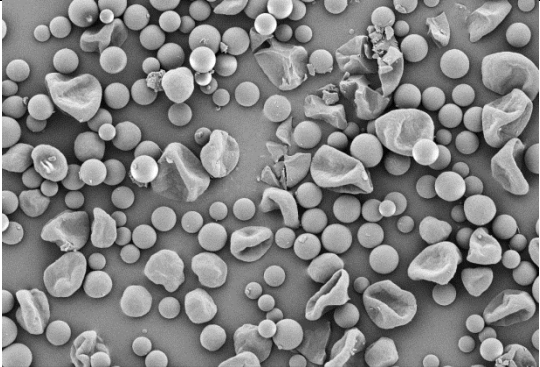
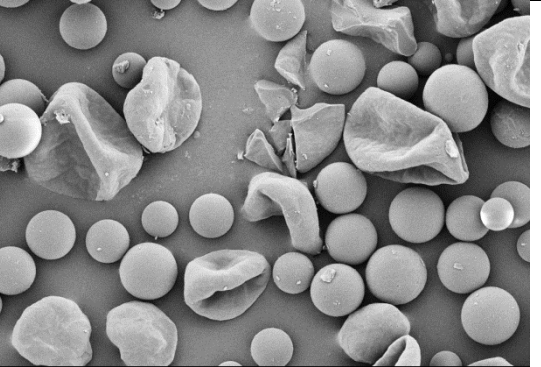
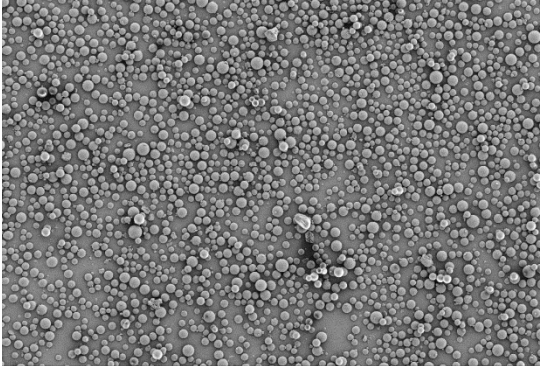
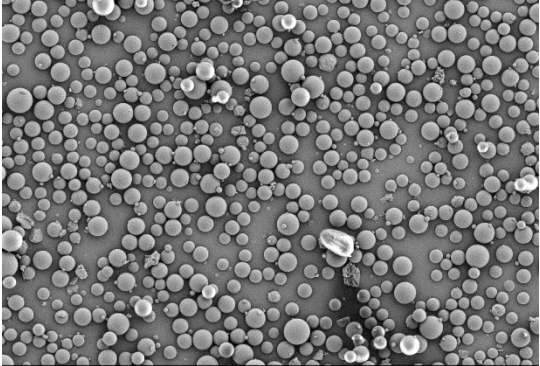
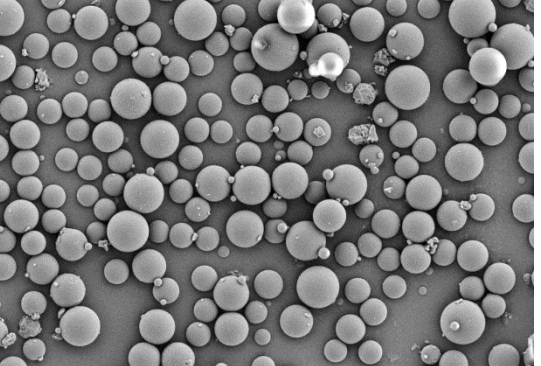
\* - Note: a 20 micron scale bar has been used for one image of EE696926/31J; the magnification (500x) is the same as for the images of compared batches

### Appendix 3

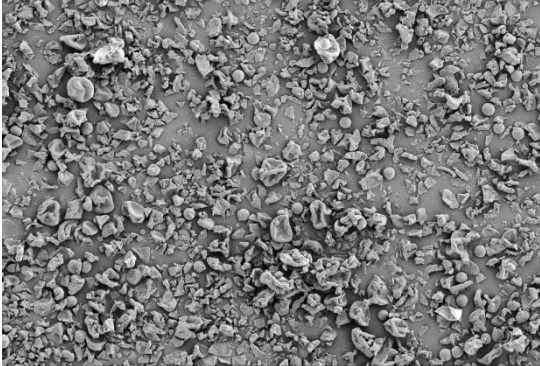
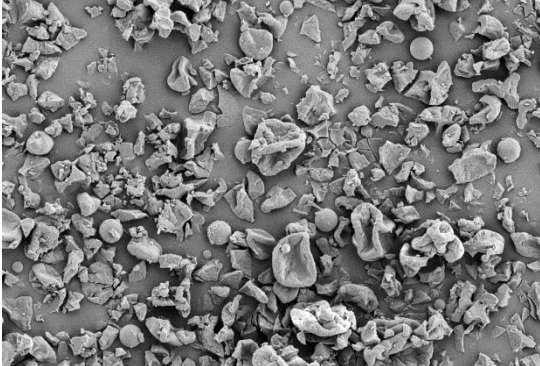
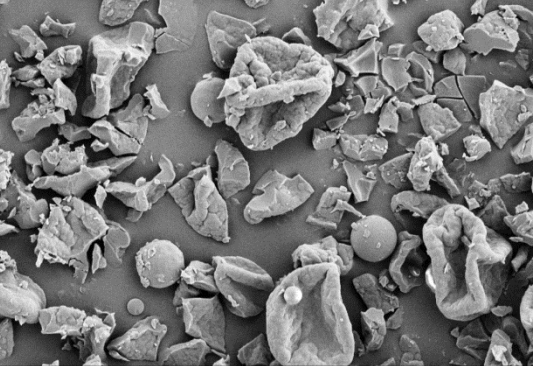
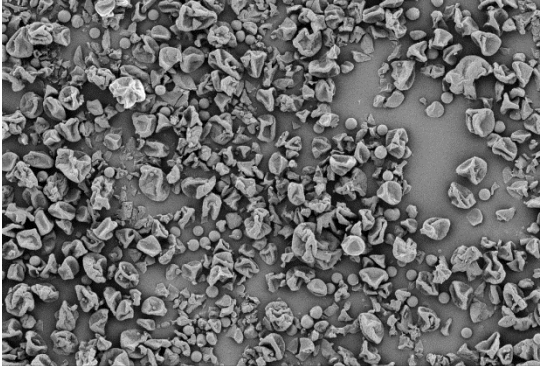
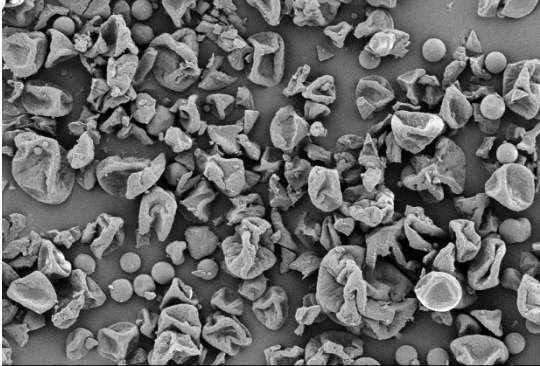
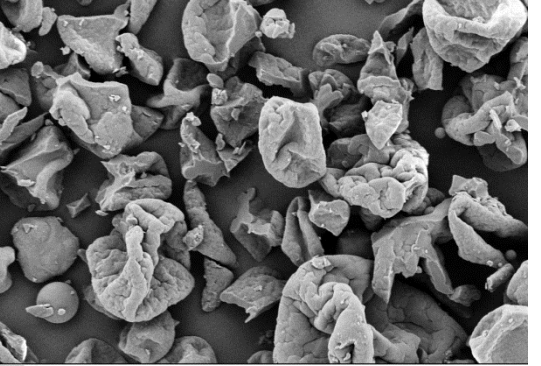
Batch number	Magnification		
	250	500	1000
EE686926/31L	 <p>ZEISS 10µm EHT = 5.00 kV Signal A = SE2 Mometasone Furoate EE686926/31L Mag = 250 X WD = 8 mm</p>	 <p>ZEISS 10µm EHT = 5.00 kV Signal A = SE2 Mometasone Furoate EE686926/31L Mag = 500 X WD = 8 mm</p>	 <p>ZEISS 10µm EHT = 5.00 kV Signal A = SE2 Mometasone Furoate EE686926/31L Mag = 1.00 K X WD = 8 mm</p>
EE686926/31M	 <p>ZEISS 10µm EHT = 5.00 kV Signal A = SE2 Mometasone Furoate EE686926/31M Mag = 250 X WD = 8 mm</p>	 <p>ZEISS 10µm EHT = 5.00 kV Signal A = SE2 Mometasone Furoate EE686926/31M Mag = 500 X WD = 8 mm</p>	 <p>ZEISS 10µm EHT = 5.00 kV Signal A = SE2 Mometasone Furoate EE686926/31M Mag = 1.00 K X WD = 8 mm</p>



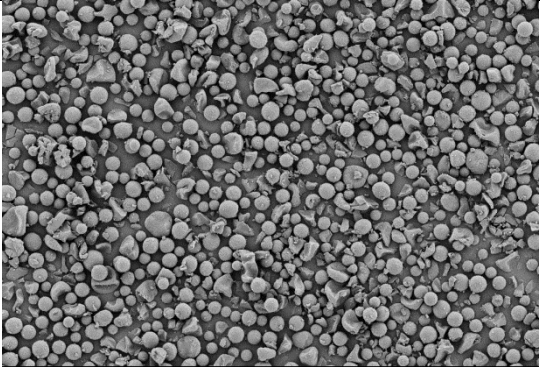
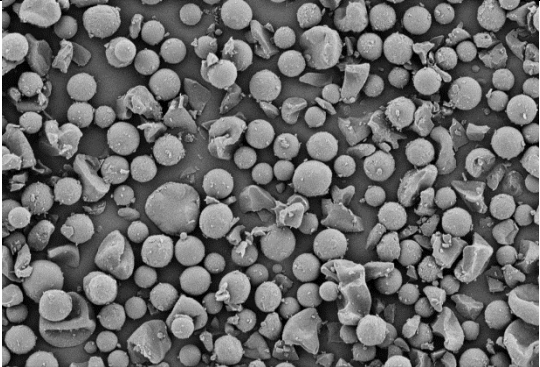
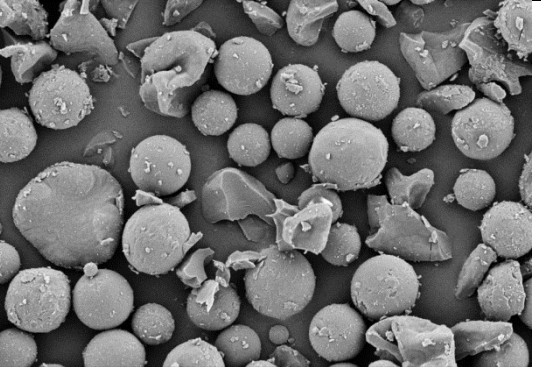
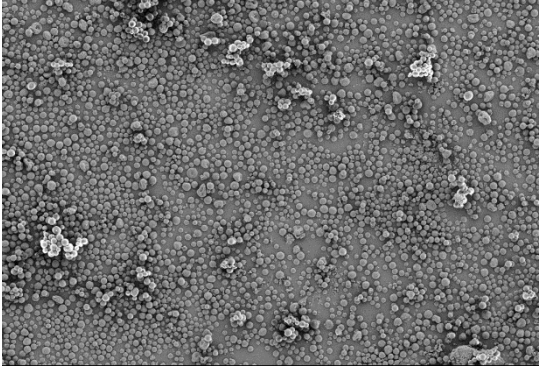
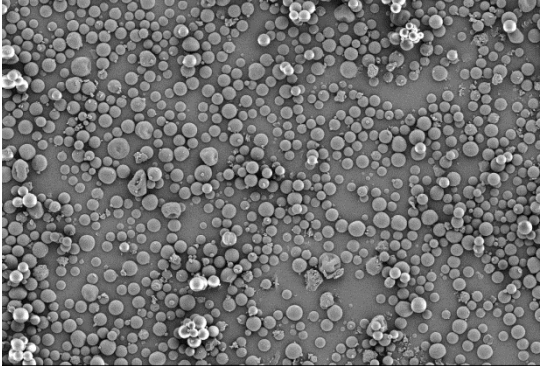
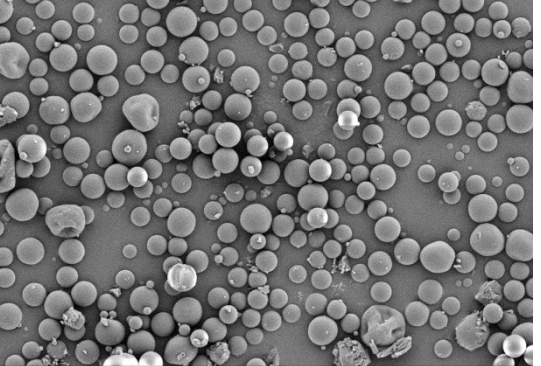
### Appendix 3

Batch number	Magnification		
	250	500	1000
EE686926/31N	 <p>ZEISS 10µm EHT = 5.00 kV Signal A = SE2 Mag = 250 X WD = 8 mm Mometasone Furoate EE686926/31N</p>	 <p>ZEISS 10µm EHT = 5.00 kV Signal A = SE2 Mag = 500 X WD = 8 mm Mometasone Furoate EE686926/31N</p>	 <p>ZEISS 10µm EHT = 5.00 kV Signal A = SE2 Mag = 1.00 K X WD = 8 mm Mometasone Furoate EE686926/31N</p>
EE686926/31P	 <p>ZEISS 10µm EHT = 5.00 kV Signal A = SE2 Mag = 250 X WD = 8 mm Mometasone Furoate EE686926/31P</p>	 <p>ZEISS 10µm EHT = 5.00 kV Signal A = SE2 Mag = 500 X WD = 8 mm Mometasone Furoate EE686926/31P</p>	 <p>ZEISS 10µm EHT = 5.00 kV Signal A = SE2 Mag = 1.00 K X WD = 8 mm Mometasone Furoate EE686926/31P</p>

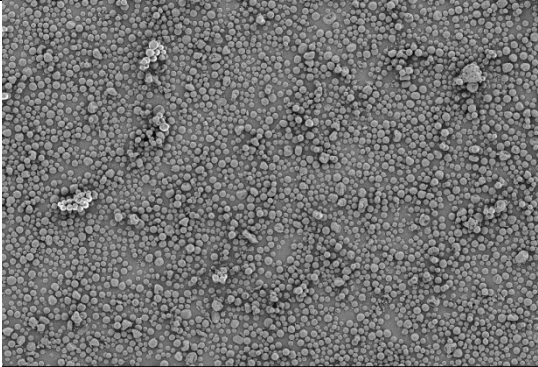
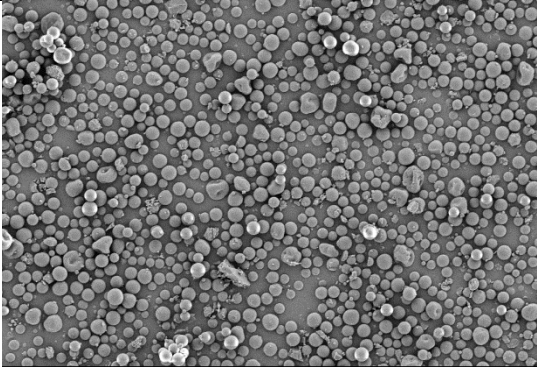
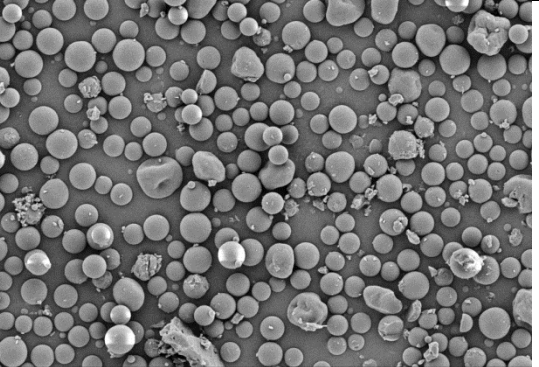
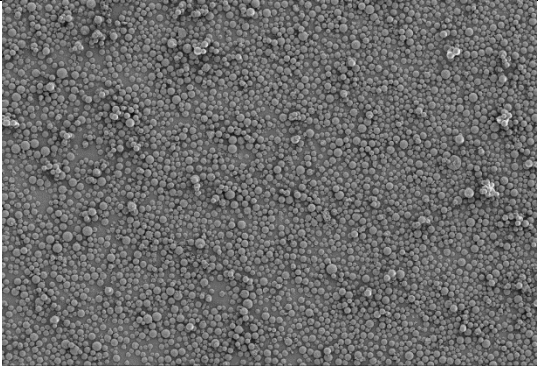
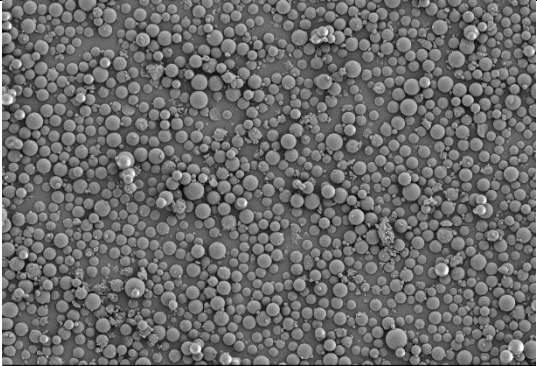
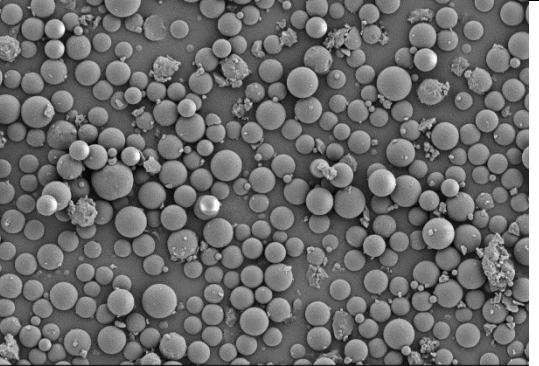
Appendix 3

Batch number	Magnification		
	250	500	1000
EE686926/31Q	 <p>ZEISS 10µm EHT = 5.00 kV Signal A = SE2 Mag = 250 X WD = 10 mm Mometasone Furoate EE686926/31Q</p>	 <p>ZEISS 10µm EHT = 5.00 kV Signal A = SE2 Mag = 500 X WD = 10 mm Mometasone Furoate EE686926/31Q</p>	 <p>ZEISS 10µm EHT = 5.00 kV Signal A = SE2 Mag = 1.00 K X WD = 10 mm Mometasone Furoate EE686926/31Q</p>
EE686926/31R	 <p>ZEISS 10µm EHT = 5.00 kV Signal A = SE2 Mag = 250 X WD = 10 mm Mometasone Furoate EE686926/31R</p>	 <p>ZEISS 10µm EHT = 5.00 kV Signal A = SE2 Mag = 500 X WD = 10 mm Mometasone Furoate EE686926/31R</p>	 <p>ZEISS 10µm EHT = 5.00 kV Signal A = SE2 Mag = 1.00 K X WD = 10 mm Mometasone Furoate EE686926/31R</p>

### Appendix 3

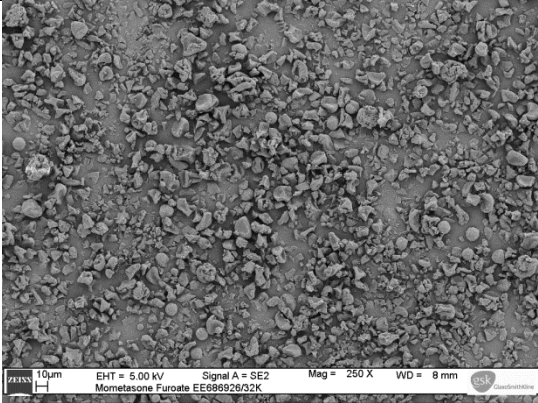
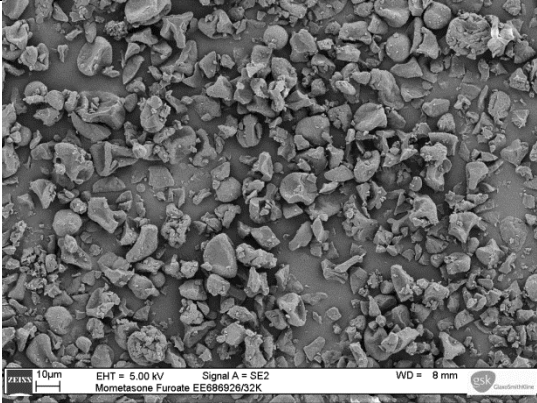
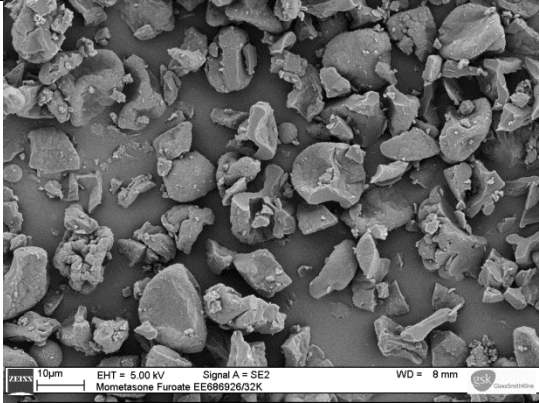
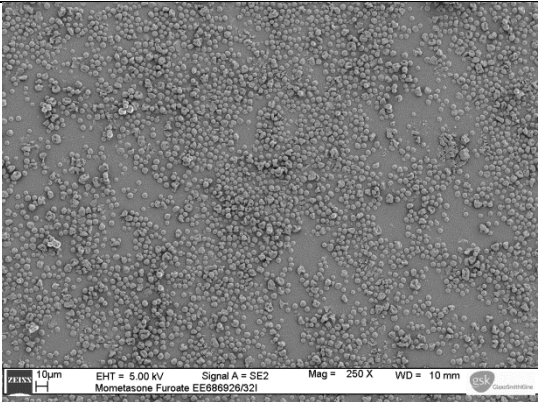
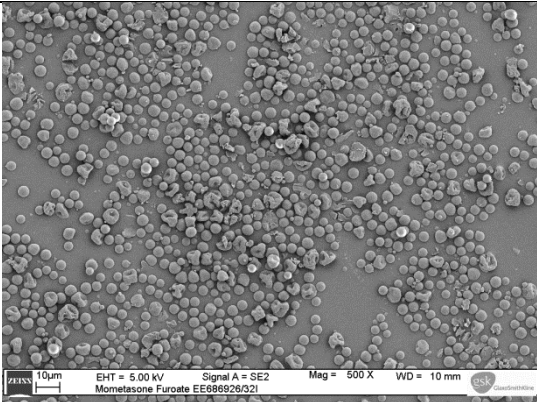
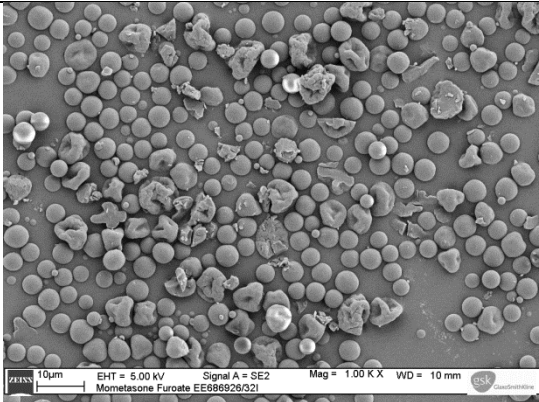
Batch number	Magnification		
	250	500	1000
EE686926/31S	 <p>ZEISS 10µm EHT = 5.00 kV Signal A = SE2 Mag = 250 X WD = 8 mm Mometasone Furoate EE686926/31S</p>	 <p>ZEISS 10µm EHT = 5.00 kV Signal A = SE2 Mag = 500 X WD = 8 mm Mometasone Furoate EE686926/31S</p>	 <p>ZEISS 10µm EHT = 5.00 kV Signal A = SE2 Mag = 1000 X WD = 8 mm Mometasone Furoate EE686926/31S</p>
EE686926/31T	 <p>ZEISS 10µm EHT = 5.00 kV Signal A = SE2 Mag = 250 X WD = 8 mm Mometasone Furoate EE686926/31T</p>	 <p>ZEISS 10µm EHT = 5.00 kV Signal A = SE2 Mag = 500 X WD = 8 mm Mometasone Furoate EE686926/31T</p>	 <p>ZEISS 10µm EHT = 5.00 kV Signal A = SE2 Mag = 1000 X WD = 8 mm Mometasone Furoate EE686926/31T</p>

### Appendix 3

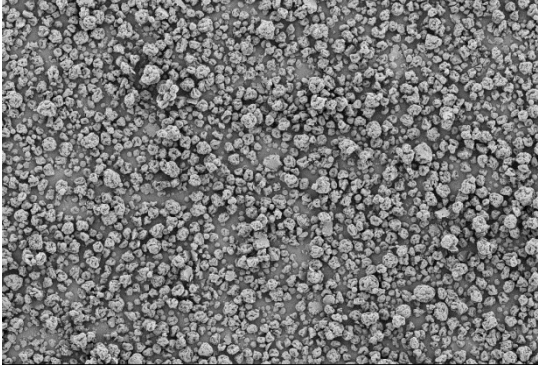
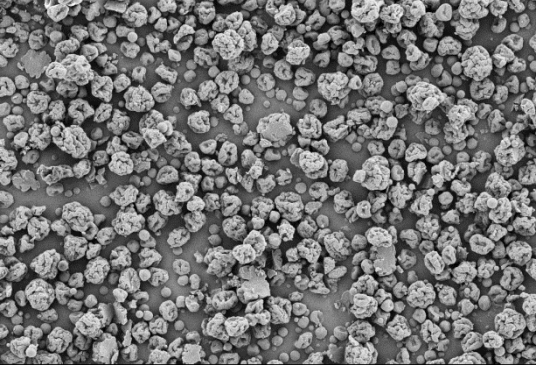
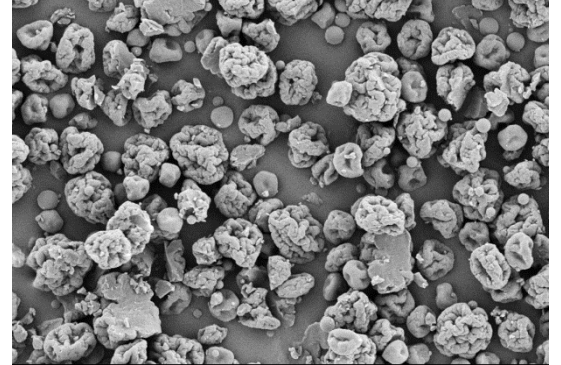
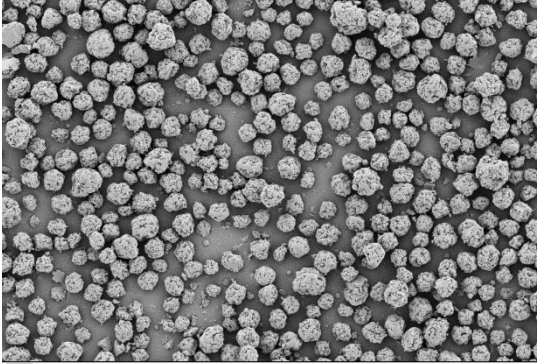
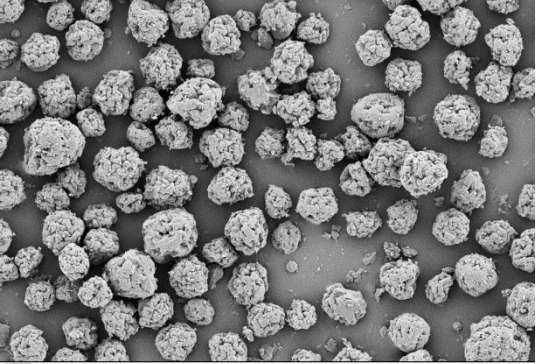
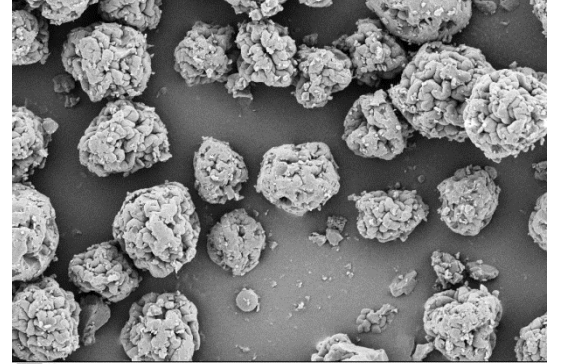
Batch number	Magnification		
	250	500	1000
EE686926/31U	 <p>ZEISS 10µm EHT = 5.00 kV Signal A = SE2 Mag = 250 X WD = 9 mm Mometasone Furoate EE686926/31U</p>	 <p>ZEISS 10µm EHT = 5.00 kV Signal A = SE2 Mag = 500 X WD = 9 mm Mometasone Furoate EE686926/31U</p>	 <p>ZEISS 10µm EHT = 5.00 kV Signal A = SE2 Mag = 1.00 K X WD = 9 mm Mometasone Furoate EE686926/31U</p>
EE686926/32J	 <p>ZEISS 10µm EHT = 5.00 kV Signal A = SE2 Mag = 250 X WD = 10 mm Mometasone Furoate EE686926/32J</p>	 <p>ZEISS 10µm EHT = 5.00 kV Signal A = SE2 Mag = 500 X WD = 10 mm Mometasone Furoate EE686926/32J</p>	 <p>ZEISS 10µm EHT = 5.00 kV Signal A = SE2 Mag = 1.00 K X WD = 10 mm Mometasone Furoate EE686926/32J</p>



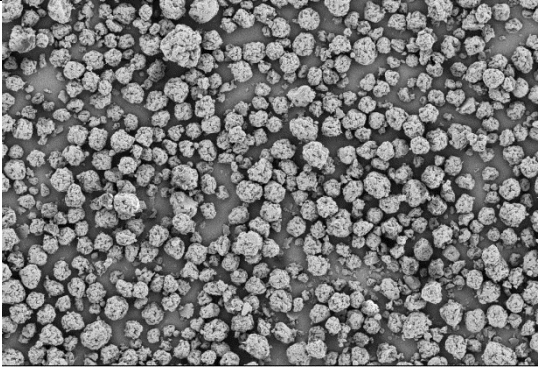
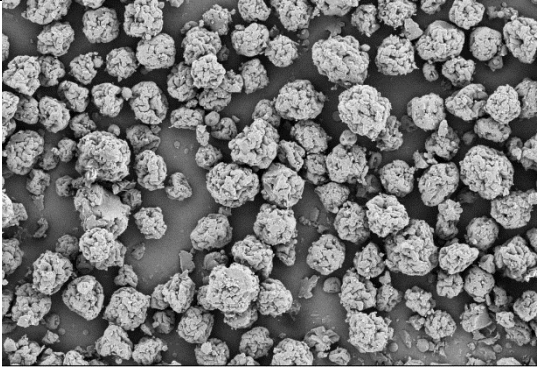
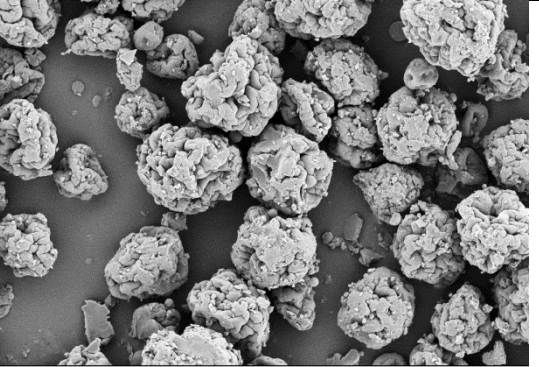
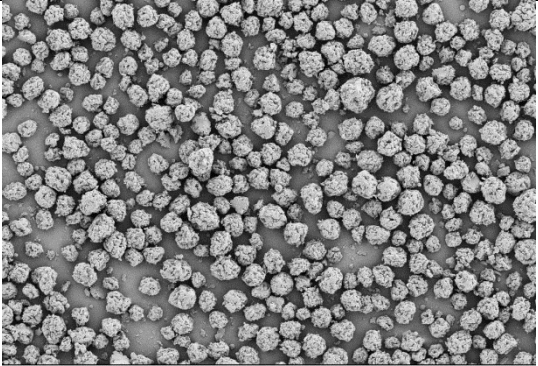
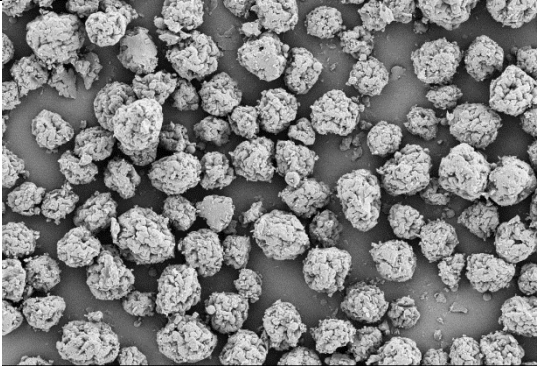
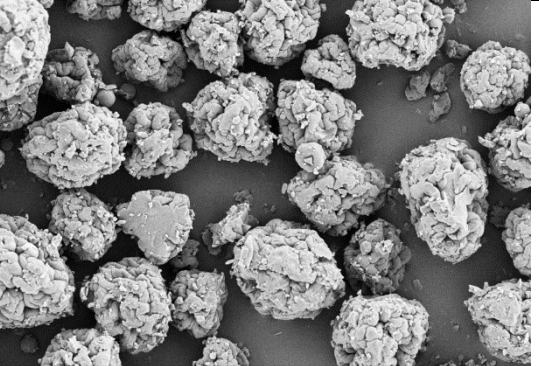
### Appendix 3

Batch number	Magnification		
	250	500	1000
EE686926/32K			
EE686926/32I			

### Appendix 3

Batch number	Magnification		
	250	500	1000
EE686926/31V	 <p data-bbox="376 707 911 738">ZEISS 10µm EHT = 5.00 kV Signal A = SE2 Mag = 250 X WD = 8 mm Mometasone Furoate EE686926/31V</p>	 <p data-bbox="949 707 1485 738">ZEISS 10µm EHT = 5.00 kV Signal A = SE2 Mag = 500 X WD = 8 mm Mometasone Furoate EE686926/31V</p>	 <p data-bbox="1500 707 2058 738">ZEISS 10µm EHT = 5.00 kV Signal A = SE2 Mag = 1.00 K X WD = 8 mm Mometasone Furoate EE686926/31V</p>
EE686926/31W	 <p data-bbox="376 1145 911 1177">ZEISS 10µm EHT = 5.00 kV Signal A = SE2 Mag = 250 X WD = 8 mm Mometasone Furoate EE686926/31W</p>	 <p data-bbox="949 1145 1485 1177">ZEISS 10µm EHT = 5.00 kV Signal A = SE2 Mag = 500 X WD = 8 mm Mometasone Furoate EE686926/31W</p>	 <p data-bbox="1500 1145 2058 1177">ZEISS 10µm EHT = 5.00 kV Signal A = SE2 Mag = 1.00 K X WD = 8 mm Mometasone Furoate EE686926/31W</p>

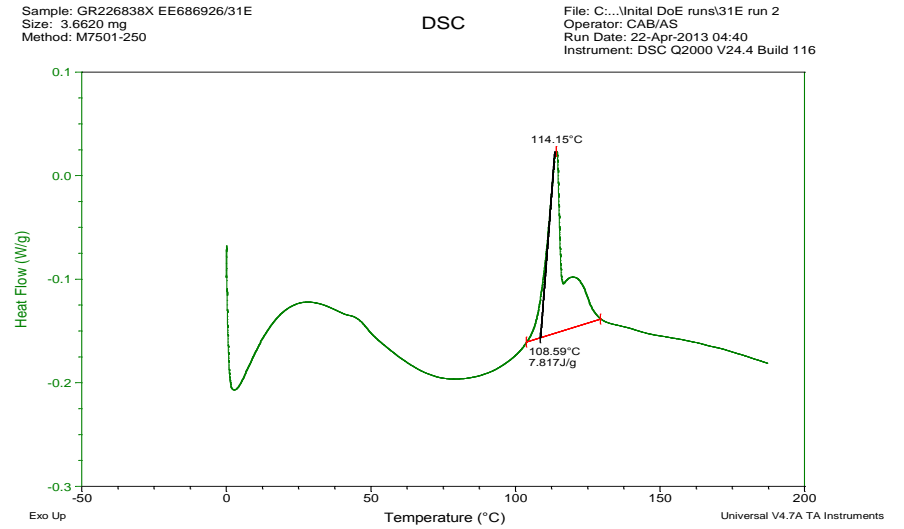
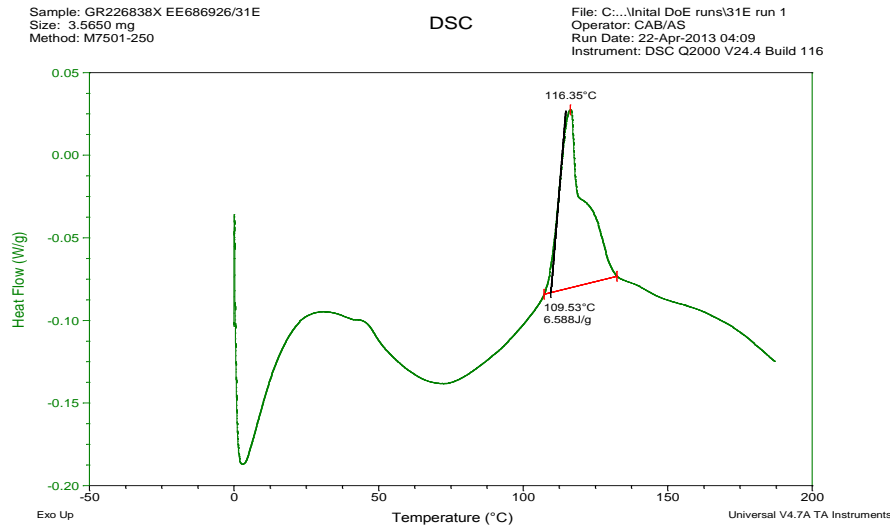
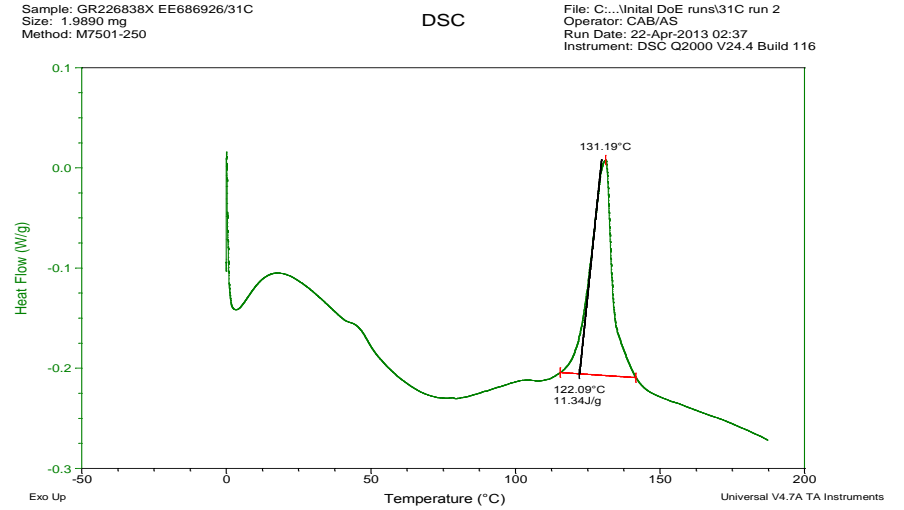
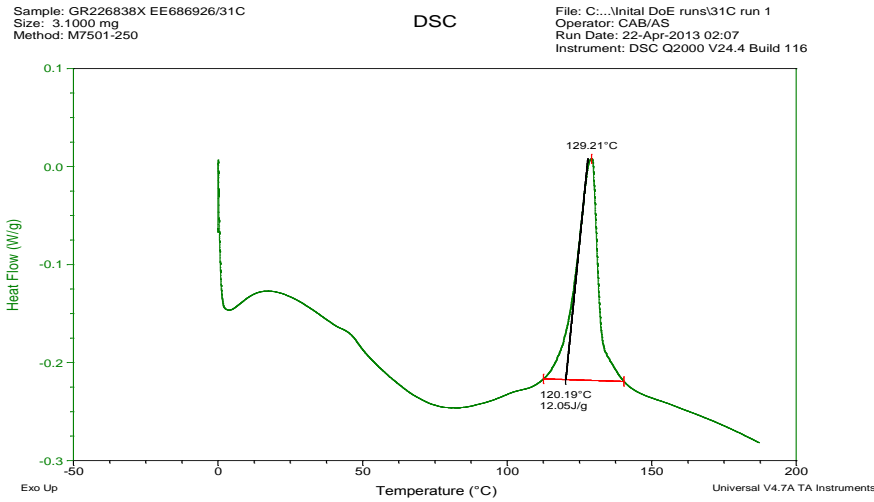
### Appendix 3

Batch number	Magnification		
	250	500	1000
EE686926/31X	 <p>ZEISS 10µm EHT = 5.00 kV Signal A = SE2 Mometasone Furoate EE686926/31X Mag = 250 X WD = 8 mm</p>	 <p>ZEISS 10µm EHT = 5.00 kV Signal A = SE2 Mometasone Furoate EE686926/31X Mag = 500 X WD = 8 mm</p>	 <p>ZEISS 10µm EHT = 5.00 kV Signal A = SE2 Mometasone Furoate EE686926/31X Mag = 1.00 K X WD = 8 mm</p>
EE686926/31Y	 <p>ZEISS 10µm EHT = 5.00 kV Signal A = SE2 Mometasone Furoate EE686926/31Y Mag = 250 X WD = 8 mm</p>	 <p>ZEISS 10µm EHT = 5.00 kV Signal A = SE2 Mometasone Furoate EE686926/31Y Mag = 500 X WD = 8 mm</p>	 <p>ZEISS 10µm EHT = 5.00 kV Signal A = SE2 Mometasone Furoate EE686926/31Y Mag = 1.00 K X WD = 8 mm</p>

### Appendix 3

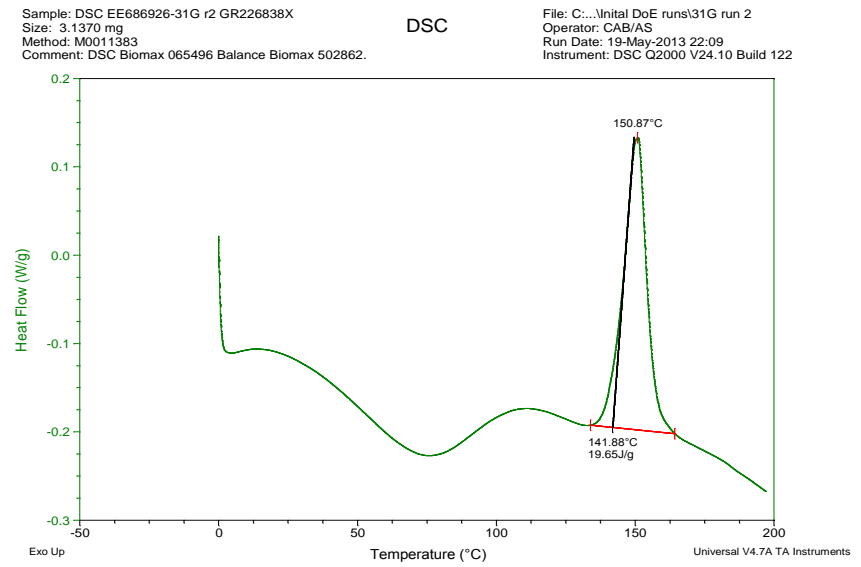
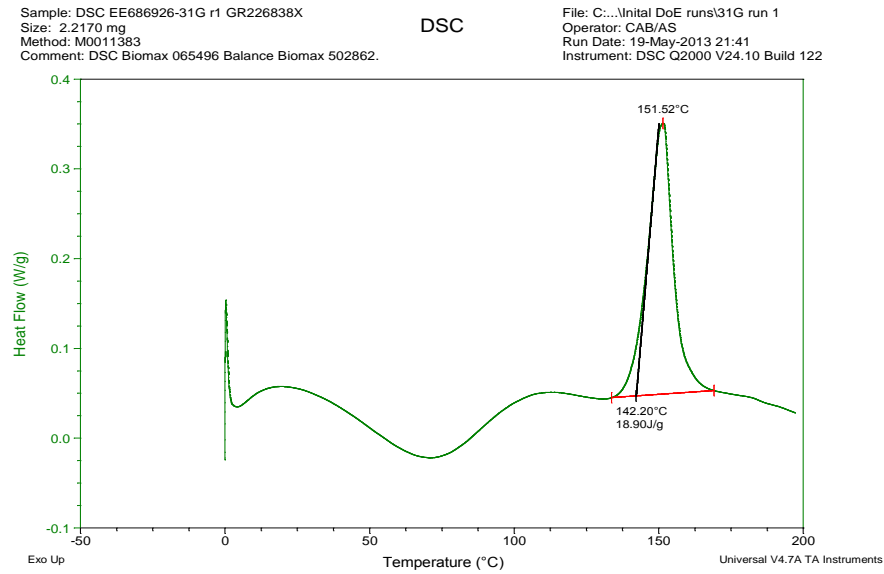
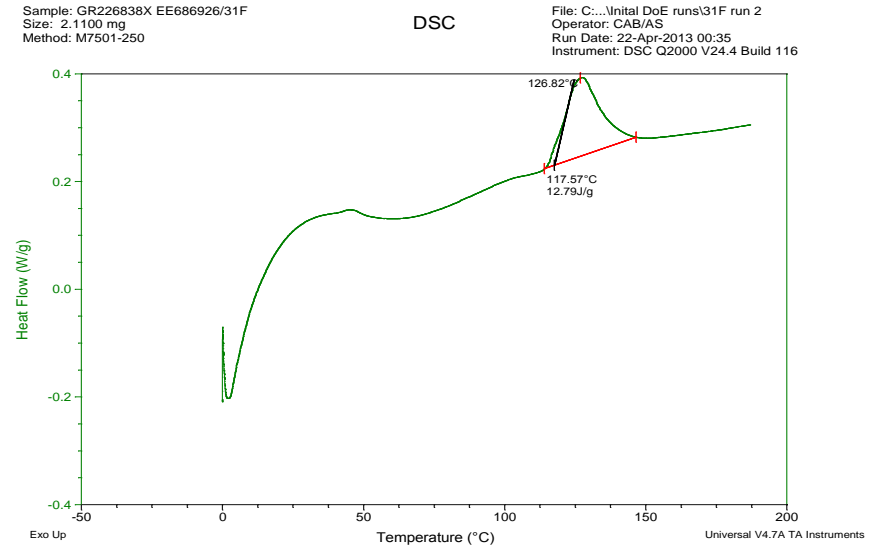
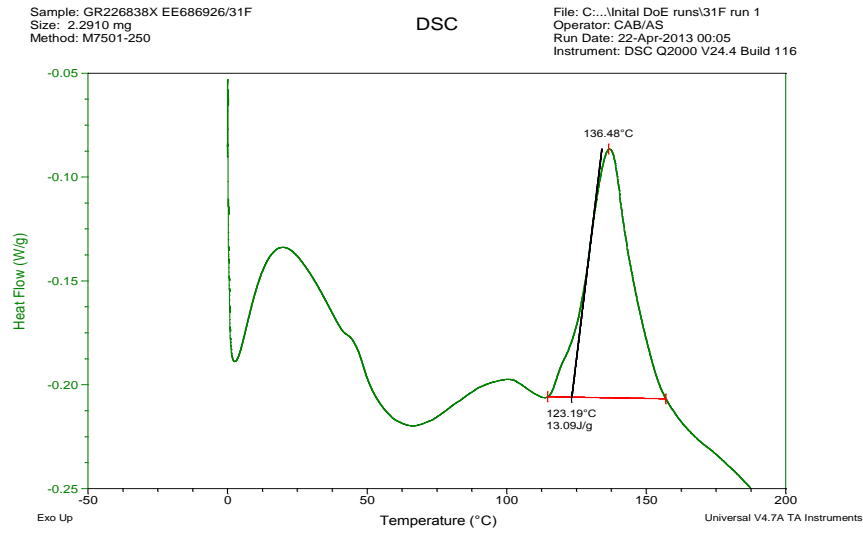
Batch number	Magnification		
	250	500	1000
EE686926/31Z			
EE686926/32A			

Appendix 4 Thermal analysis results

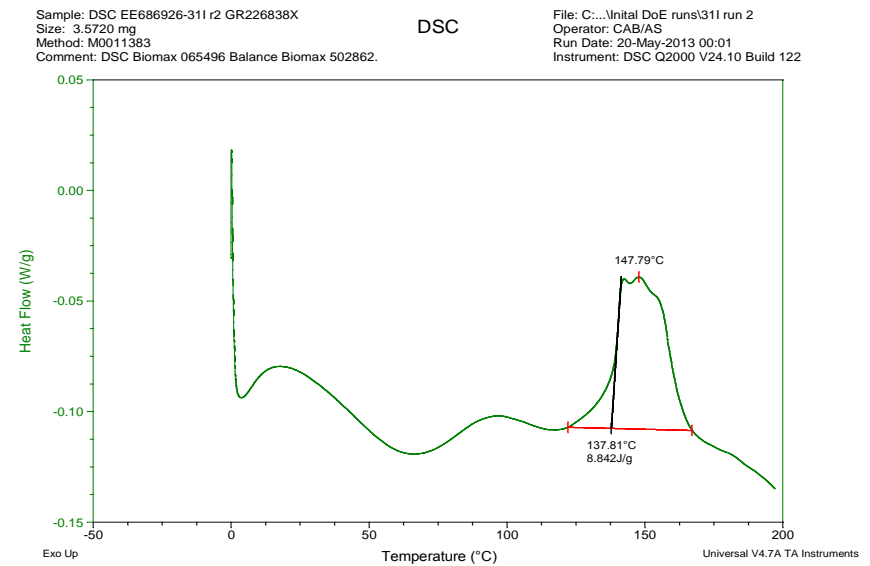
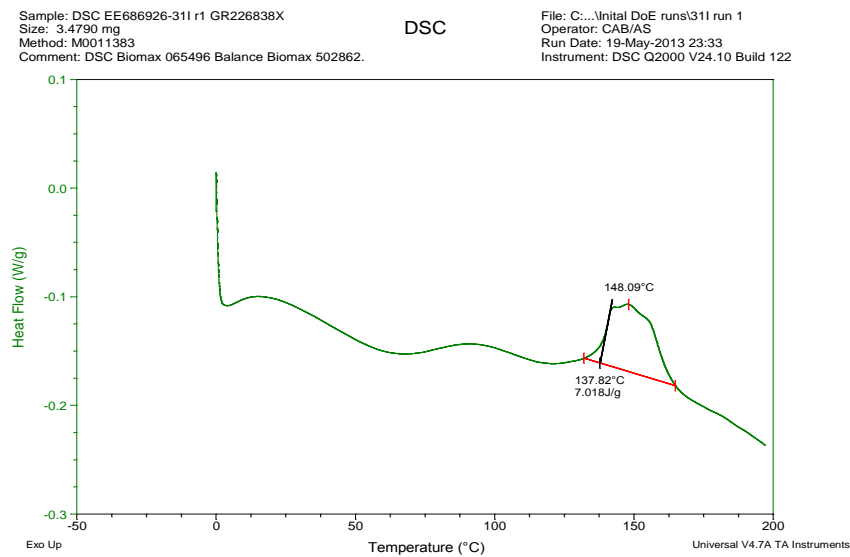
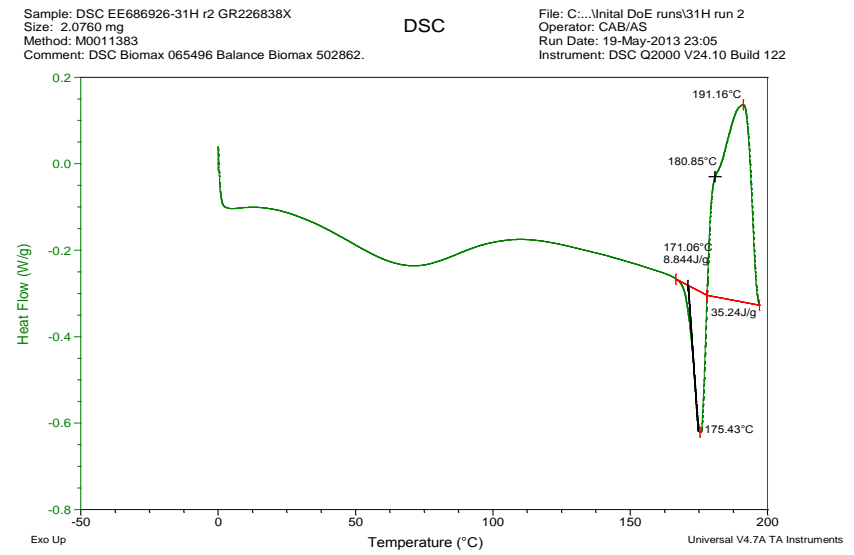
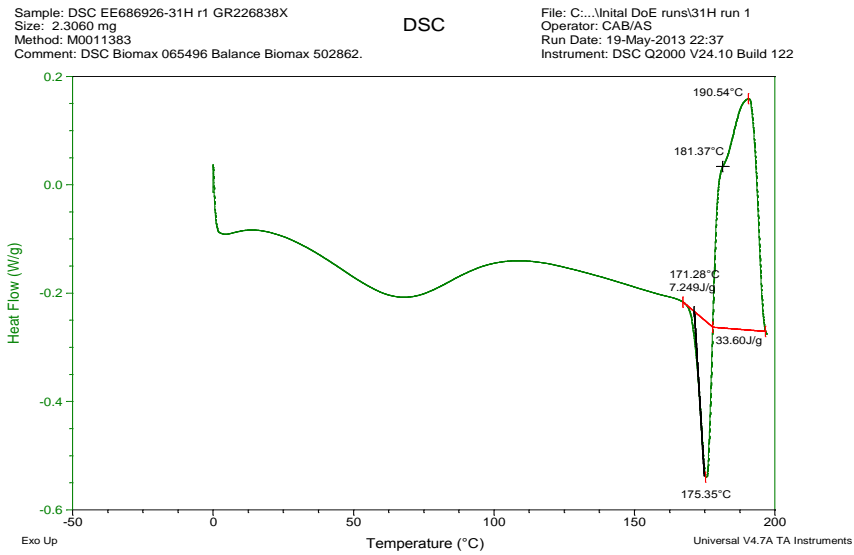




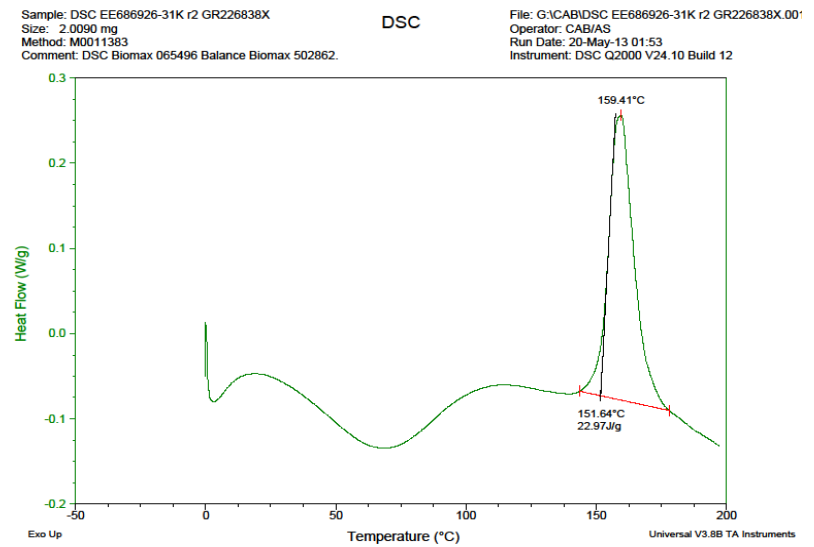
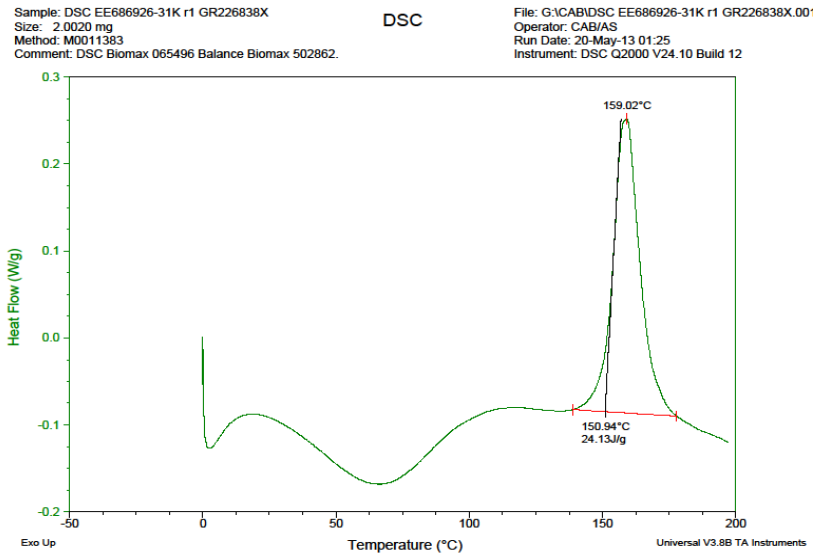
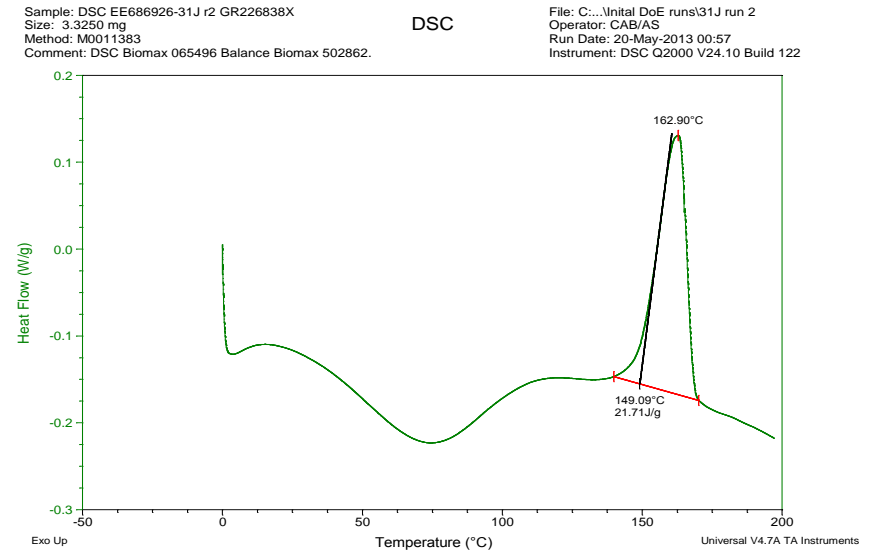
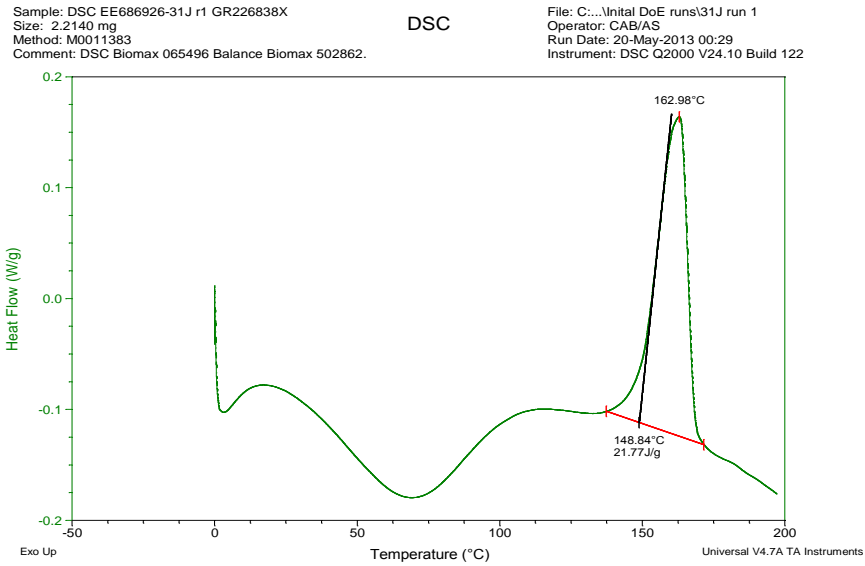
# Appendix 4



# Appendix 4

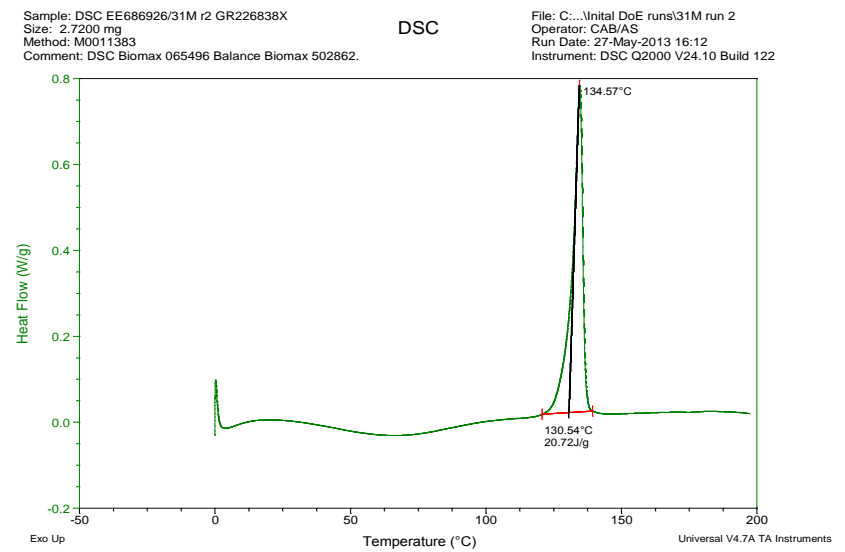
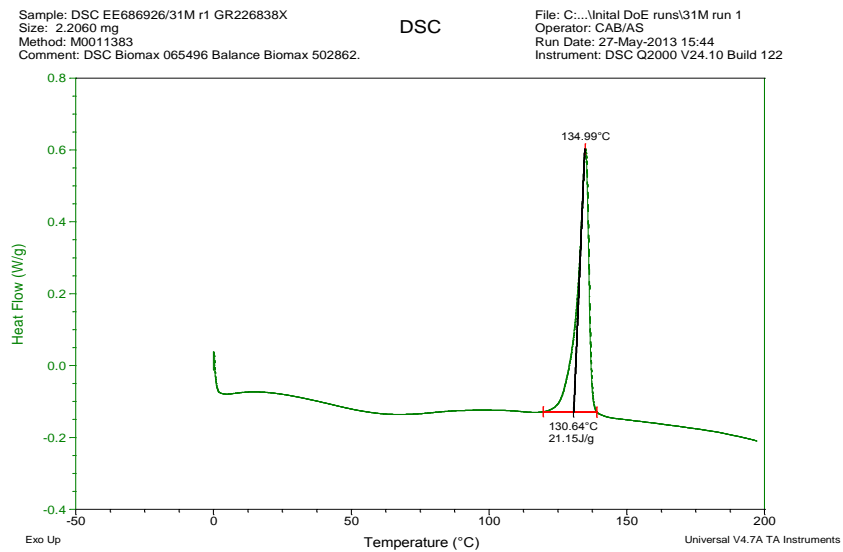
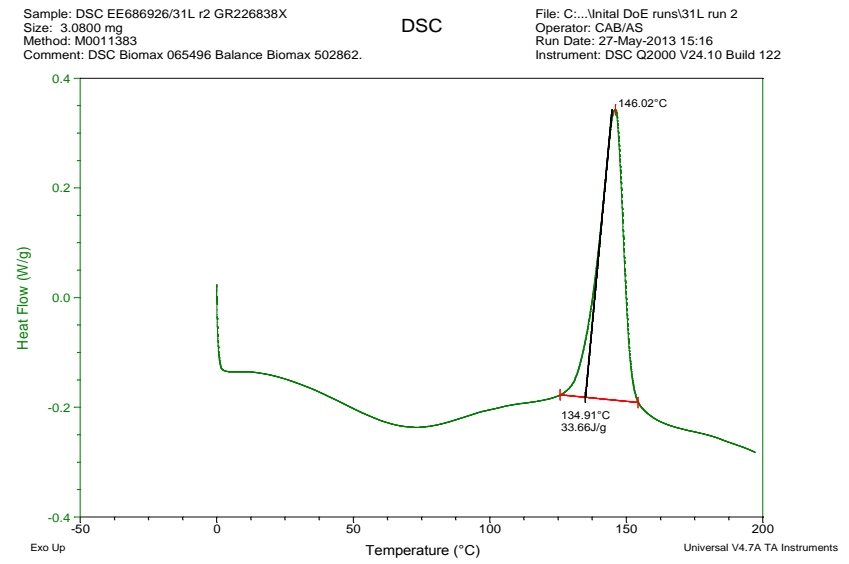
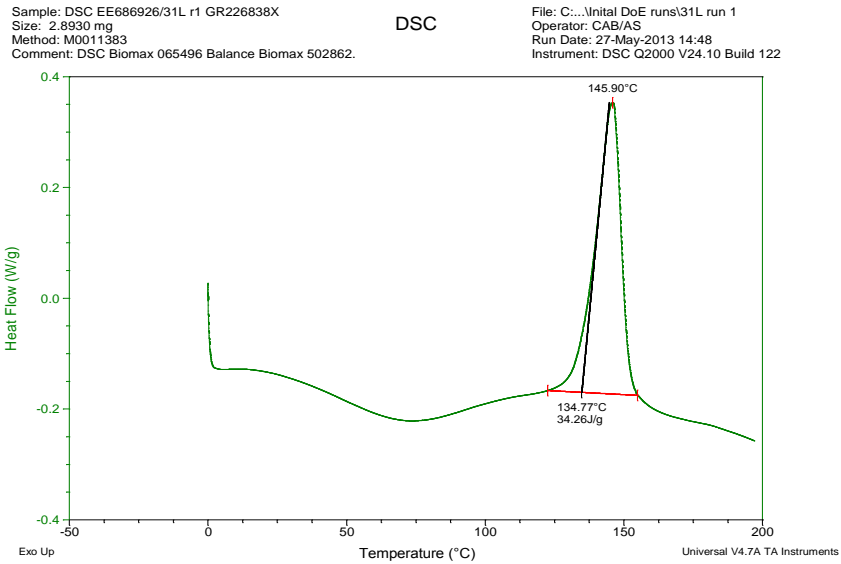


# Appendix 4

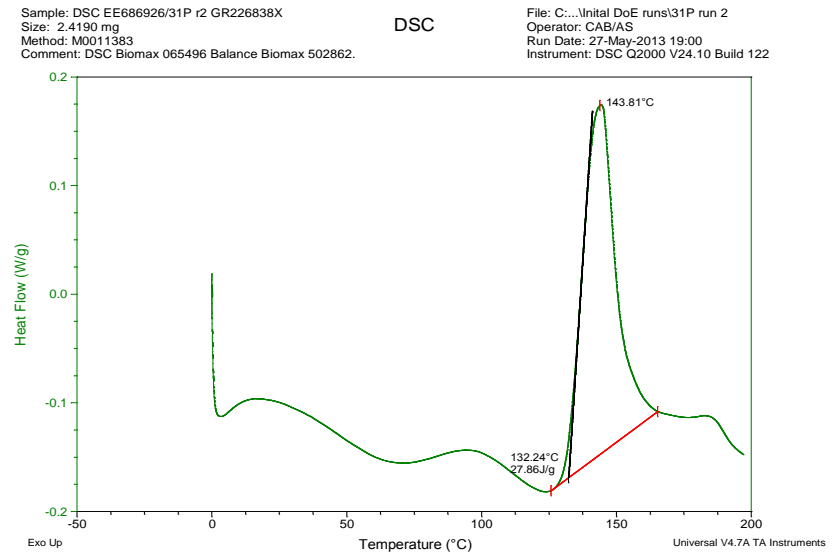
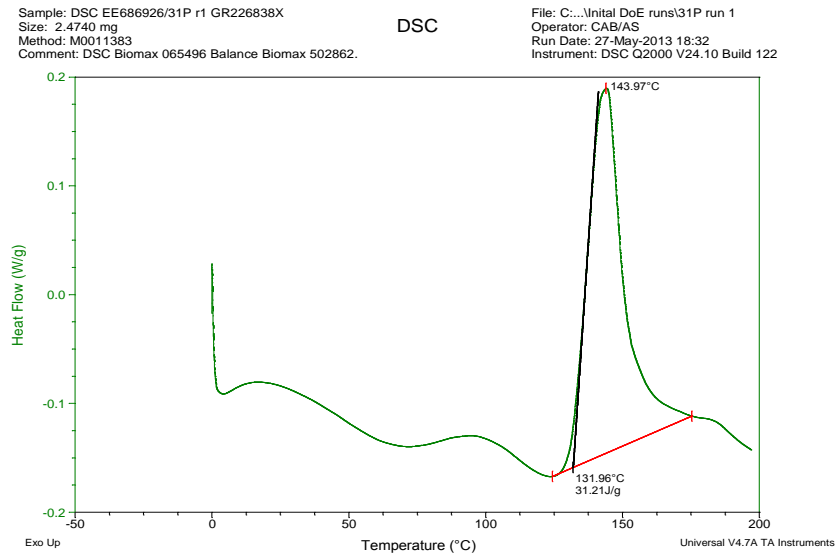
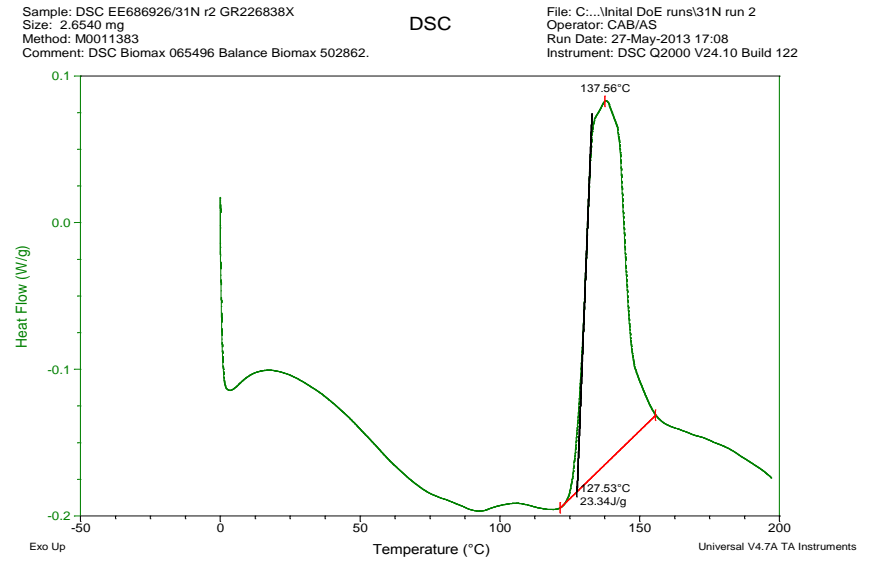
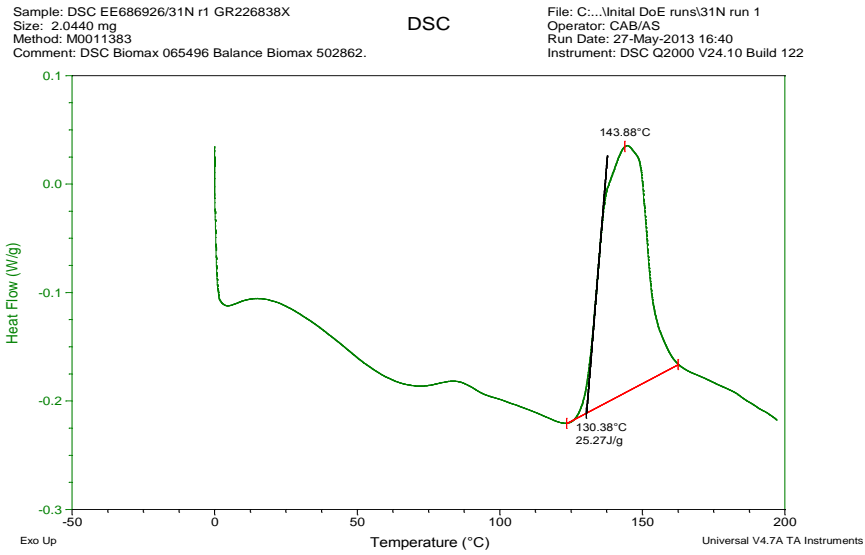




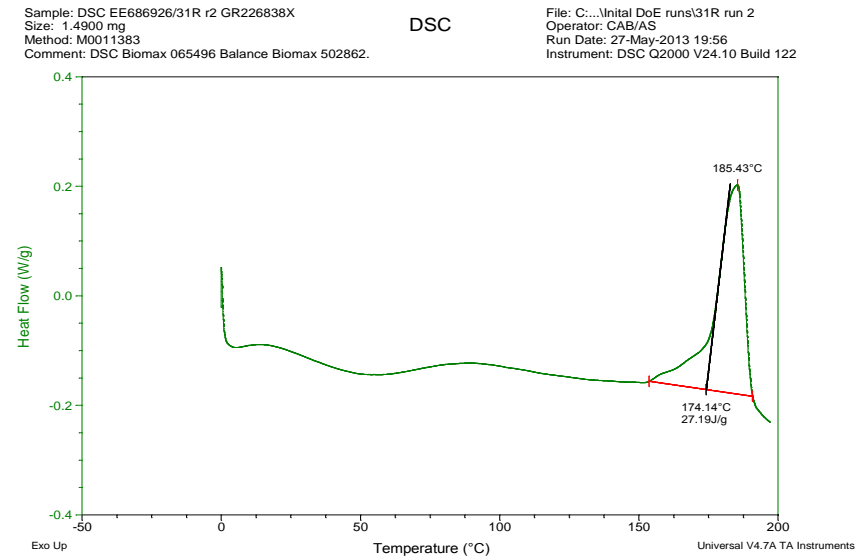
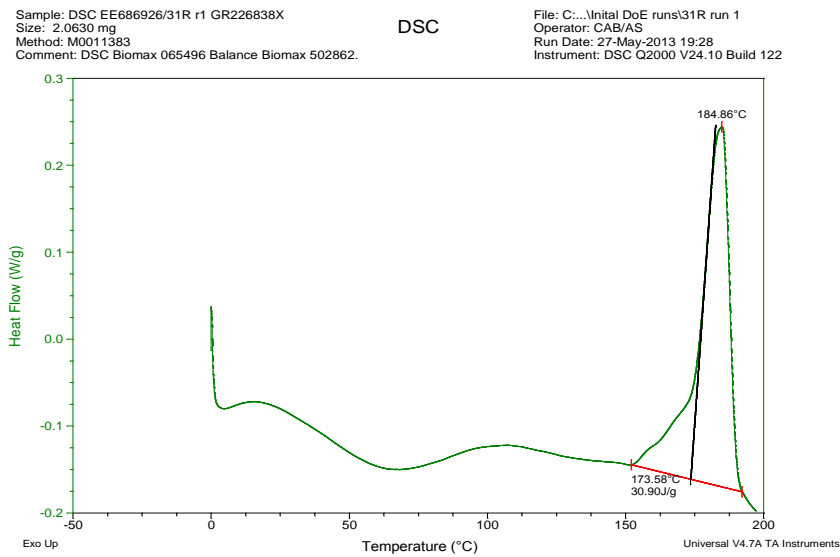
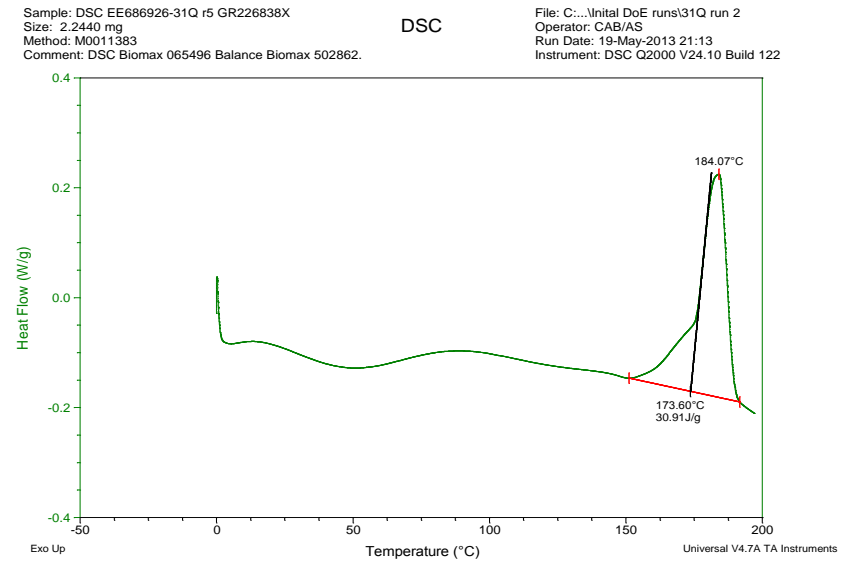
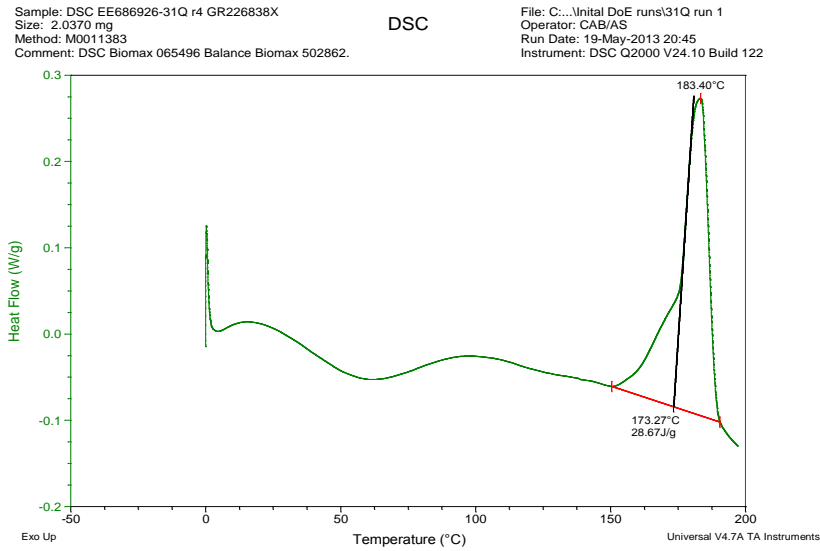
# Appendix 4



# Appendix 4



# Appendix 4

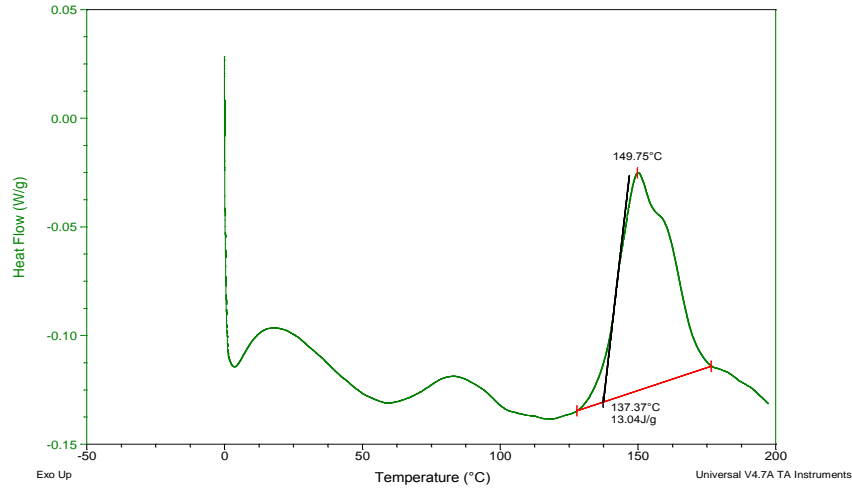


# Appendix 4

Sample: DSC EE686926/31S r1 GR226838X  
 Size: 1.8600 mg  
 Method: M0011383  
 Comment: DSC Biomax 065496 Balance Biomax 502862.

DSC

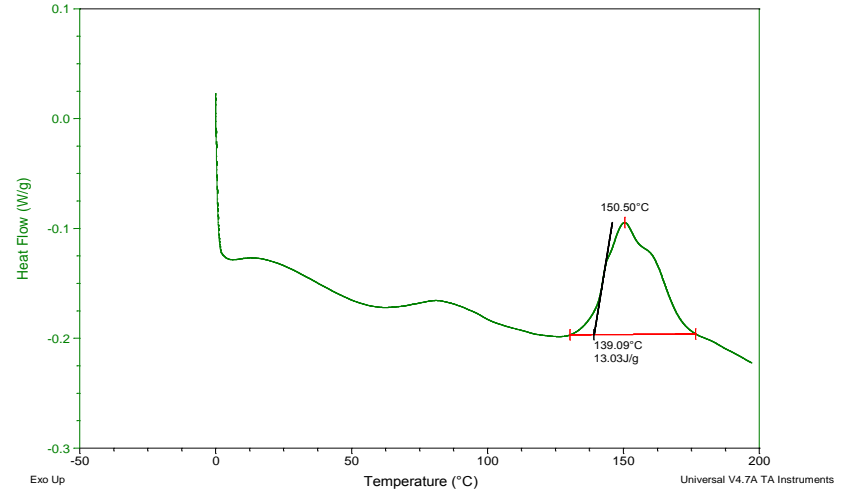
File: C:\...l\lital DoE runs\31S run 1  
 Operator: CAB/AS  
 Run Date: 27-May-2013 20:23  
 Instrument: DSC Q2000 V24.10 Build 122



Sample: DSC EE686926/31S r2 GR226838X  
 Size: 2.5970 mg  
 Method: M0011383  
 Comment: DSC Biomax 065496 Balance Biomax 502862.

DSC

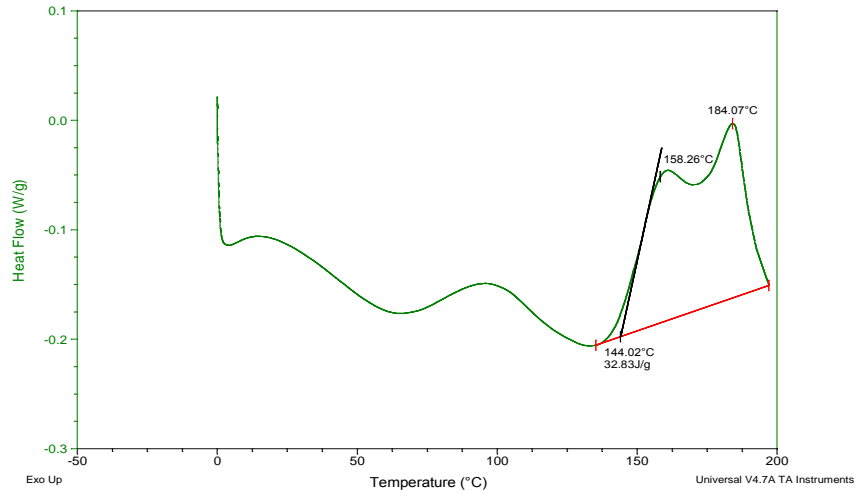
File: C:\...l\lital DoE runs\31S run 2  
 Operator: CAB/AS  
 Run Date: 27-May-2013 20:51  
 Instrument: DSC Q2000 V24.10 Build 122



Sample: DSC EE686926/31T r1 GR226838X  
 Size: 2.4240 mg  
 Method: M0011383  
 Comment: DSC Biomax 065496 Balance Biomax 502862.

DSC

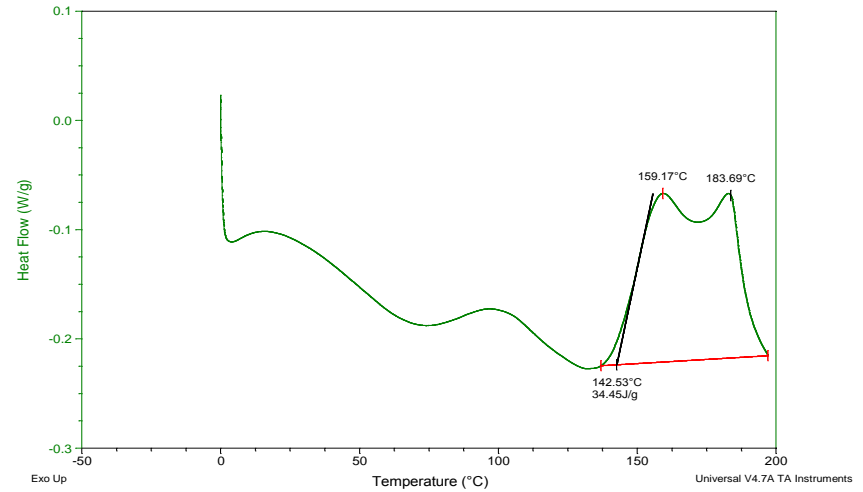
File: C:\...l\lital DoE runs\31T run 1  
 Operator: CAB/AS  
 Run Date: 27-May-2013 21:19  
 Instrument: DSC Q2000 V24.10 Build 122



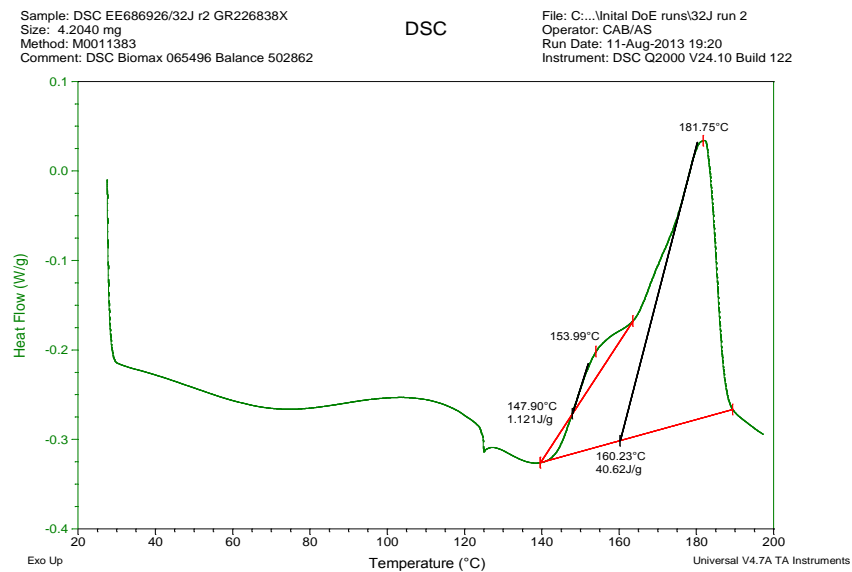
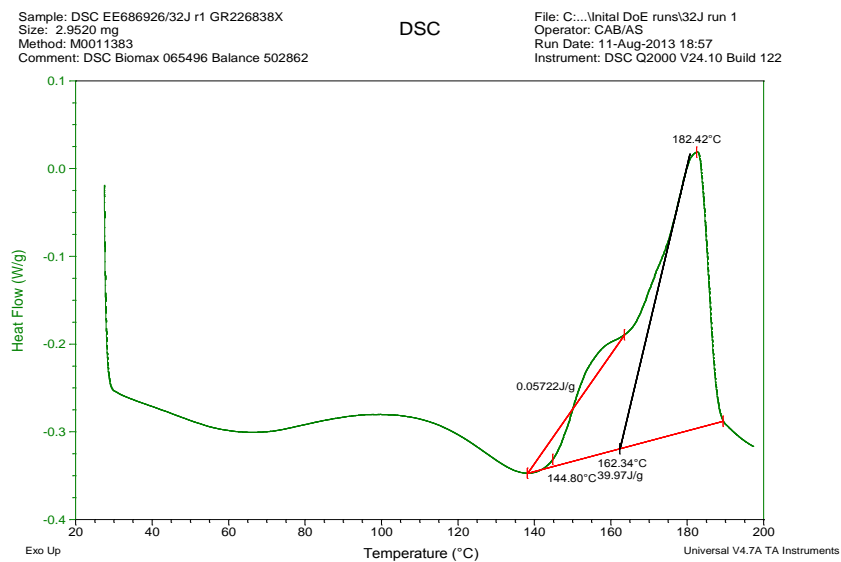
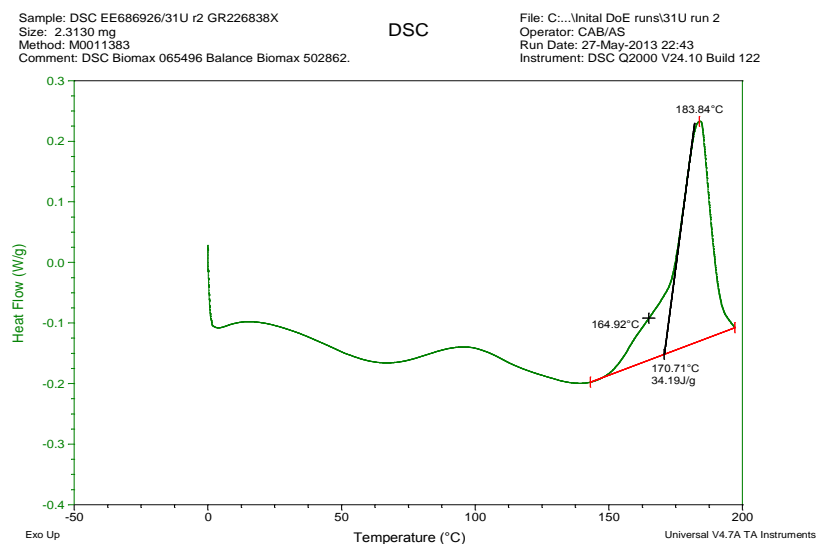
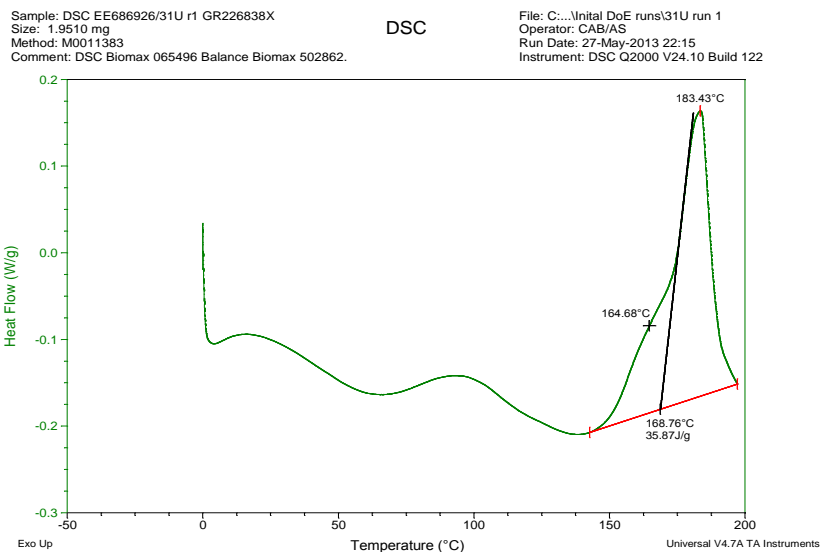
Sample: DSC EE686926/31T r2 GR226838X  
 Size: 2.5260 mg  
 Method: M0011383  
 Comment: DSC Biomax 065496 Balance Biomax 502862.

DSC

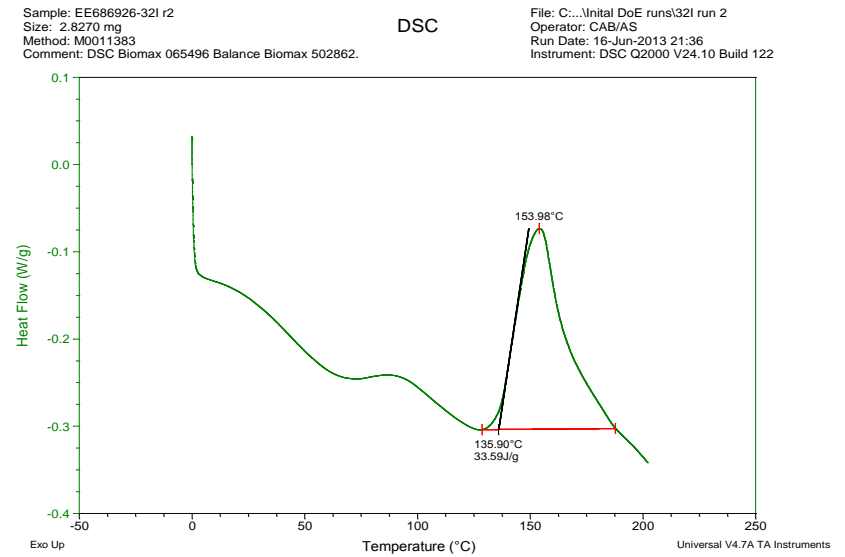
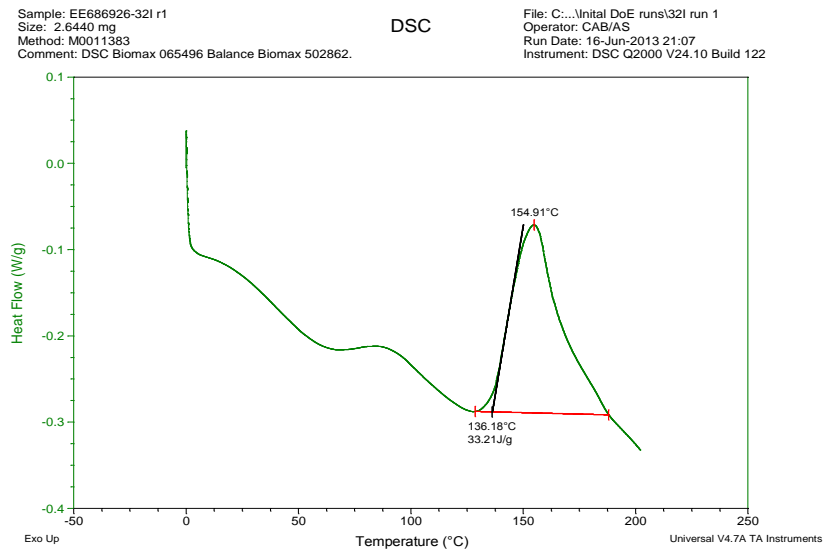
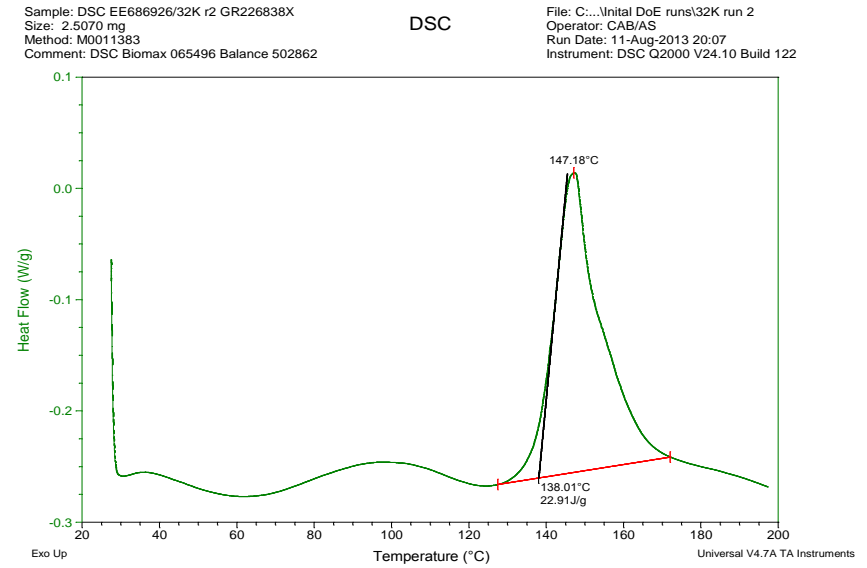
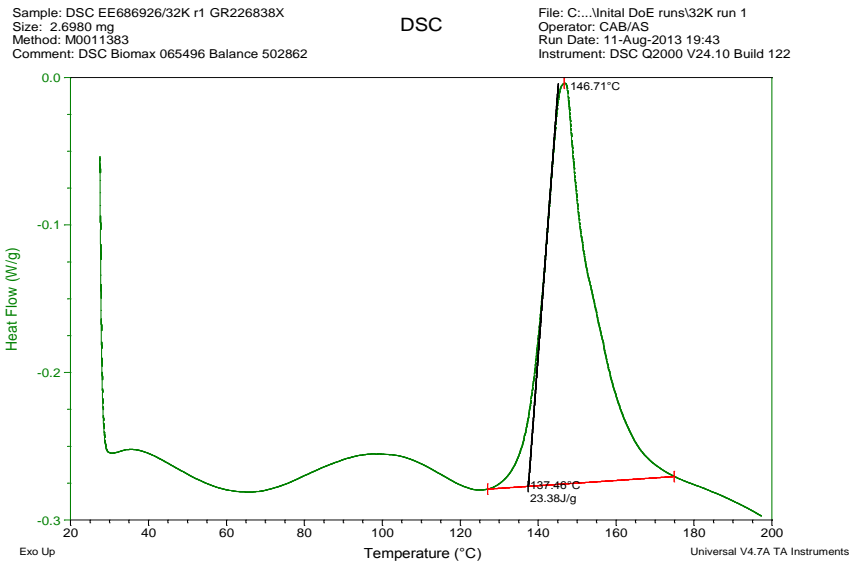
File: C:\...l\lital DoE runs\31T run 2  
 Operator: CAB/AS  
 Run Date: 27-May-2013 21:47  
 Instrument: DSC Q2000 V24.10 Build 122



# Appendix 4

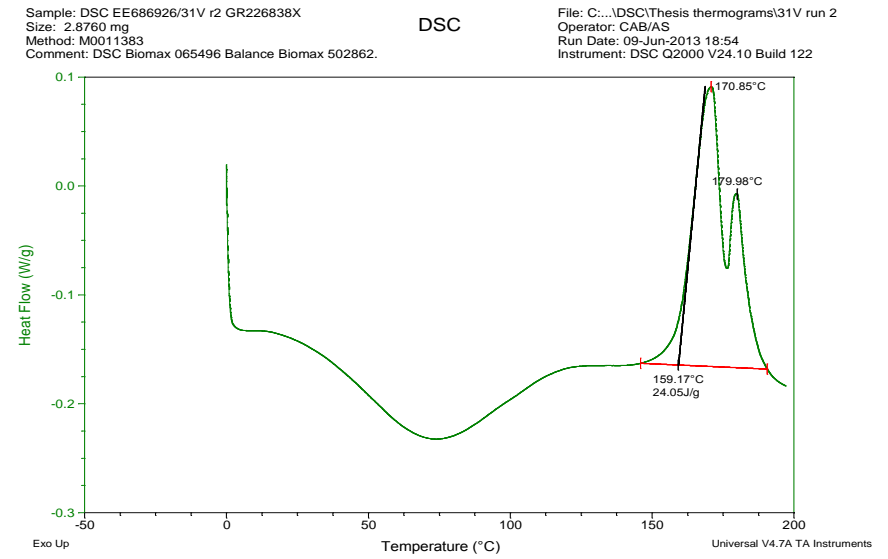
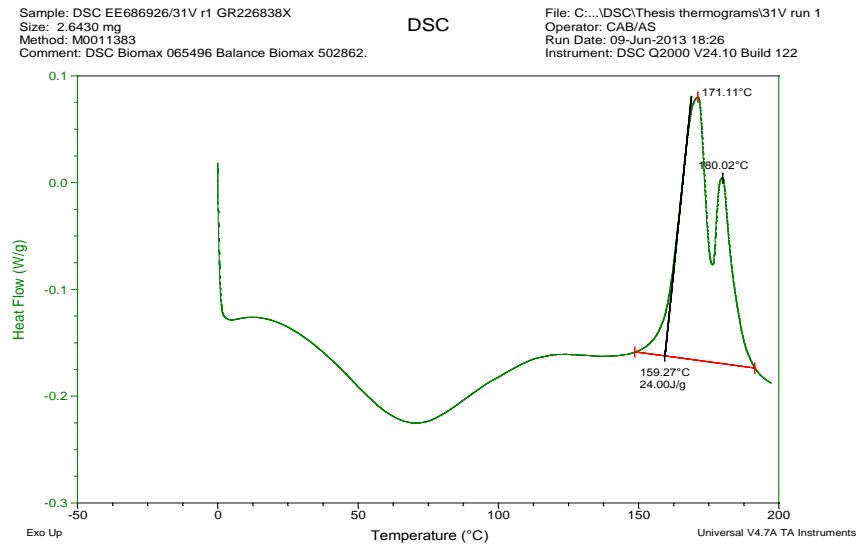


# Appendix 4

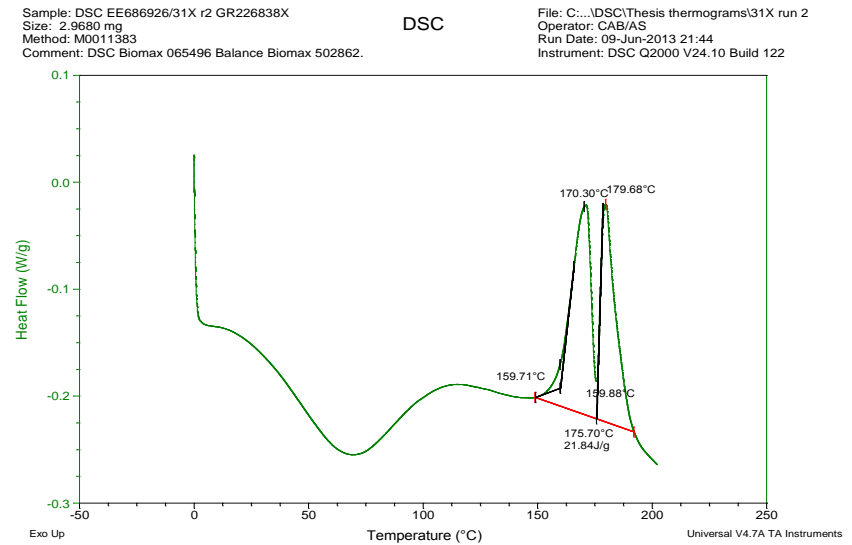
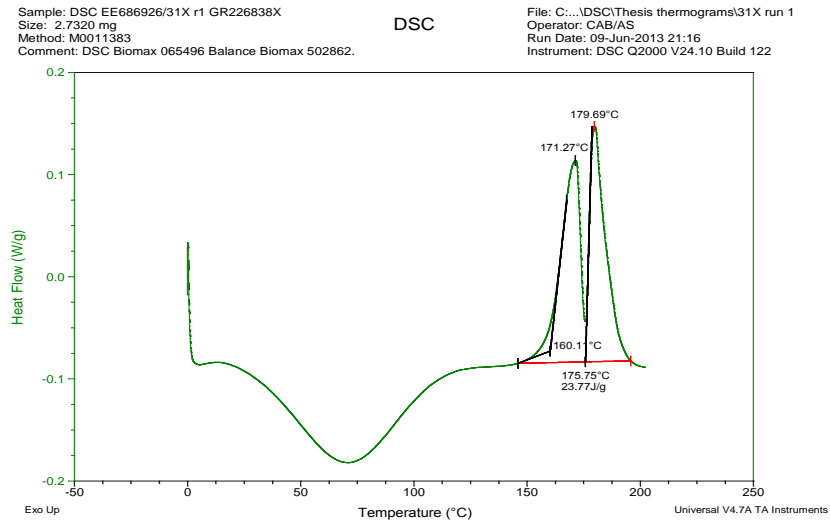
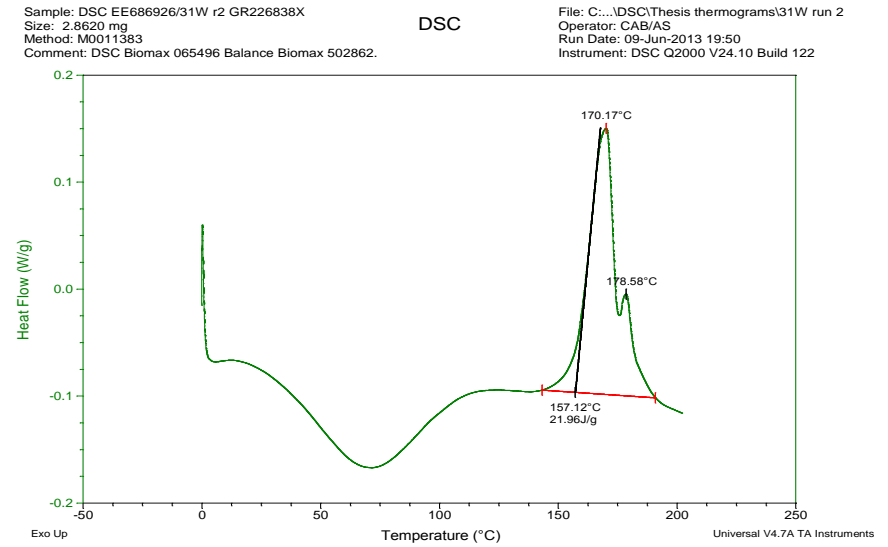
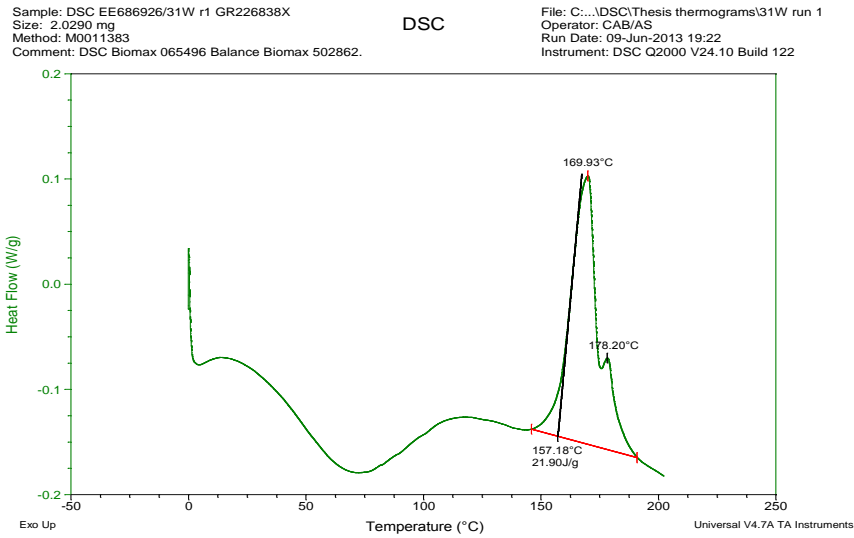


## Appendix 4

Additional runs – 0.56, 1.00 and 1.25%w/w mometasone furoate and 0.375%w/w fluticasone propionate

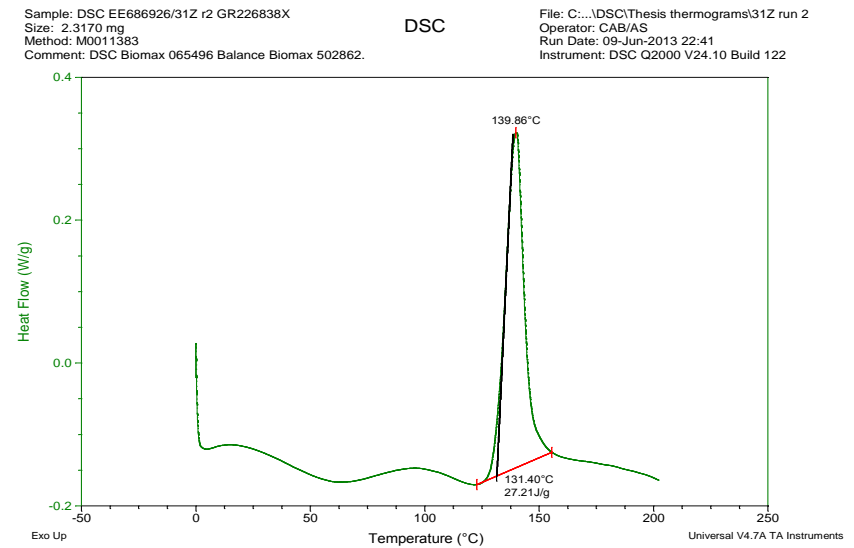
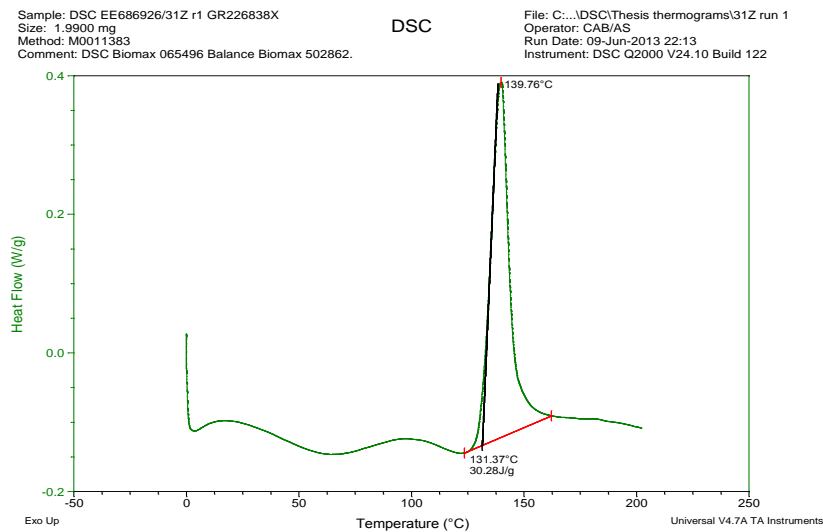
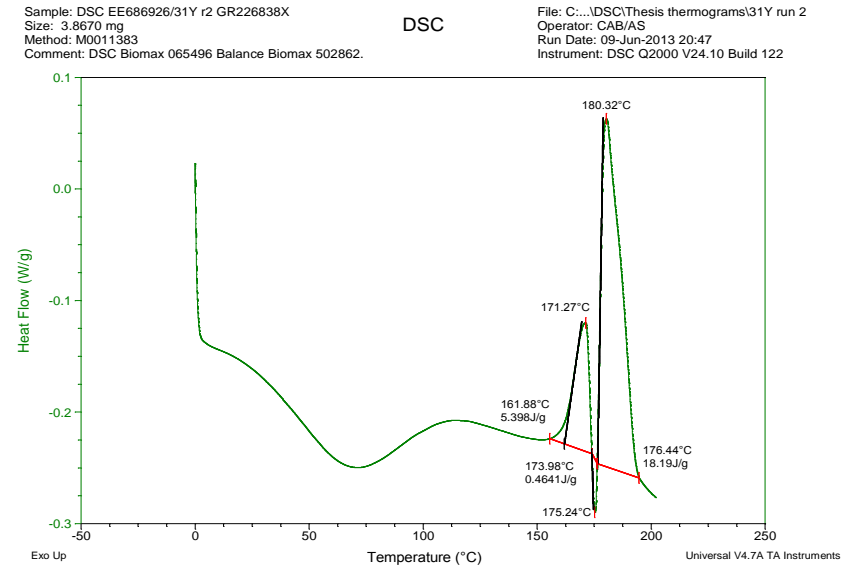
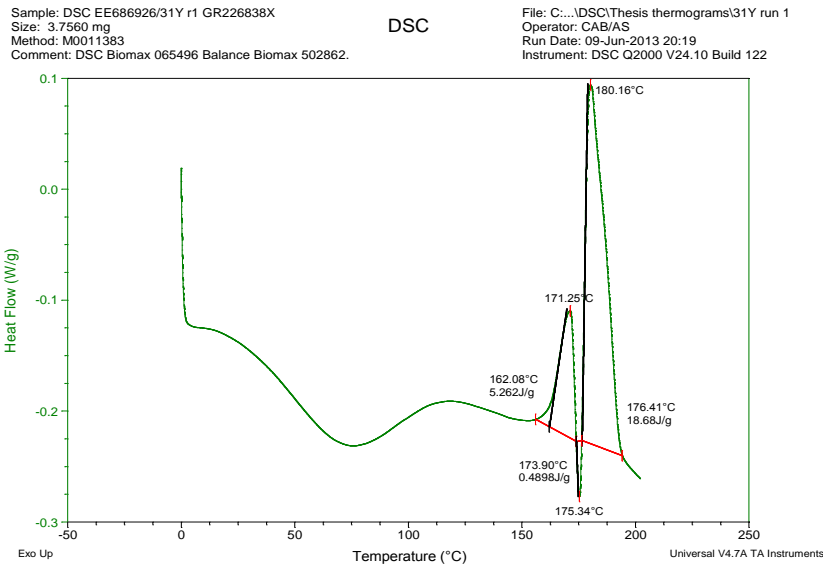


# Appendix 4

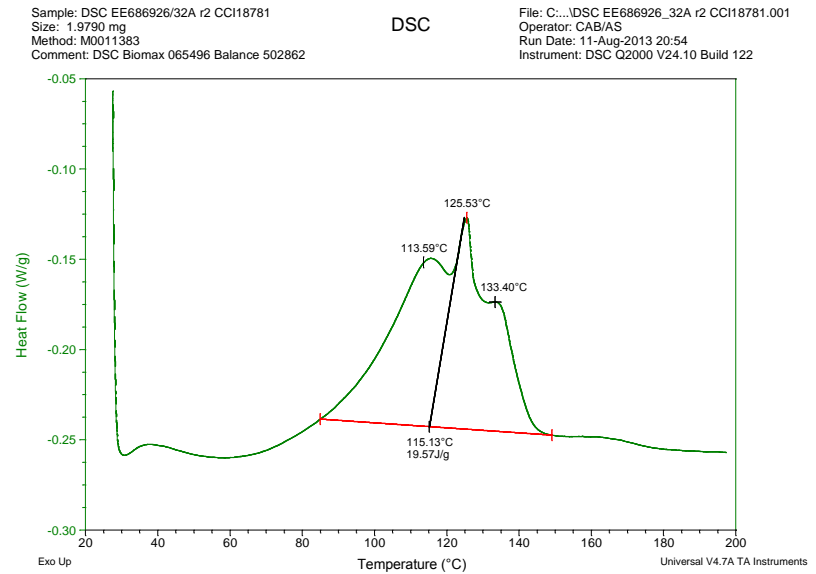
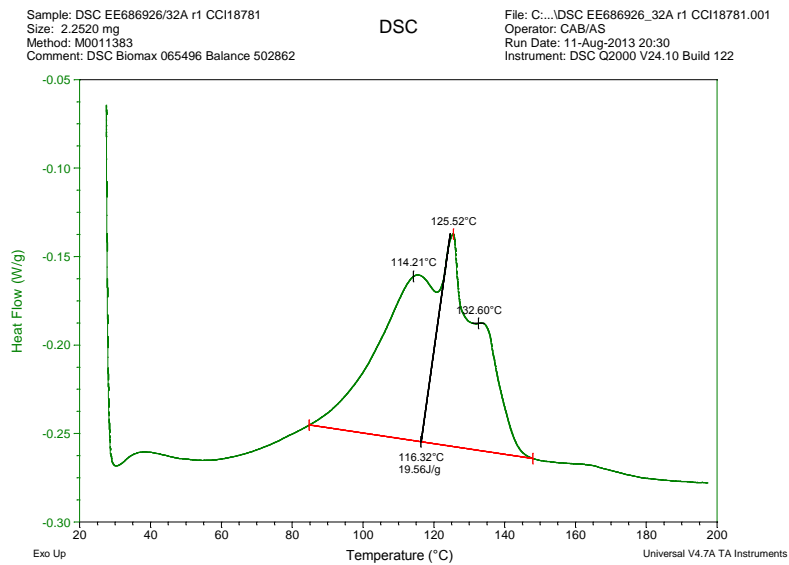
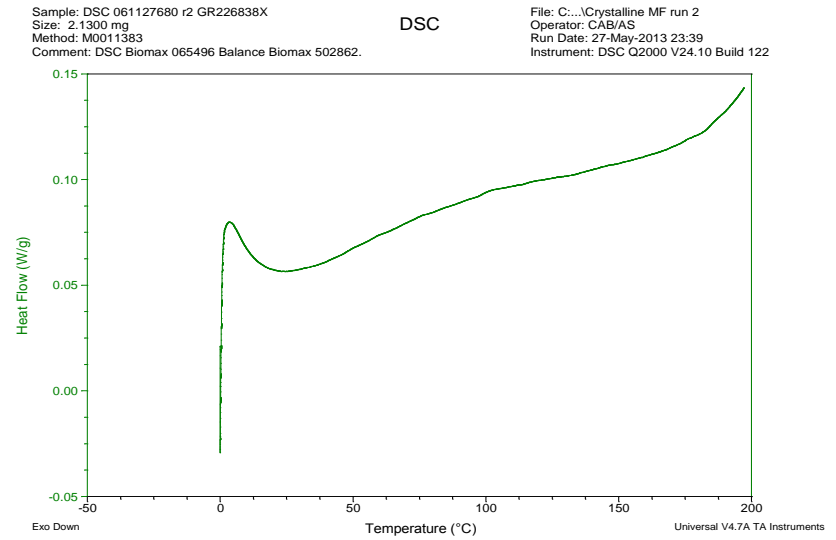
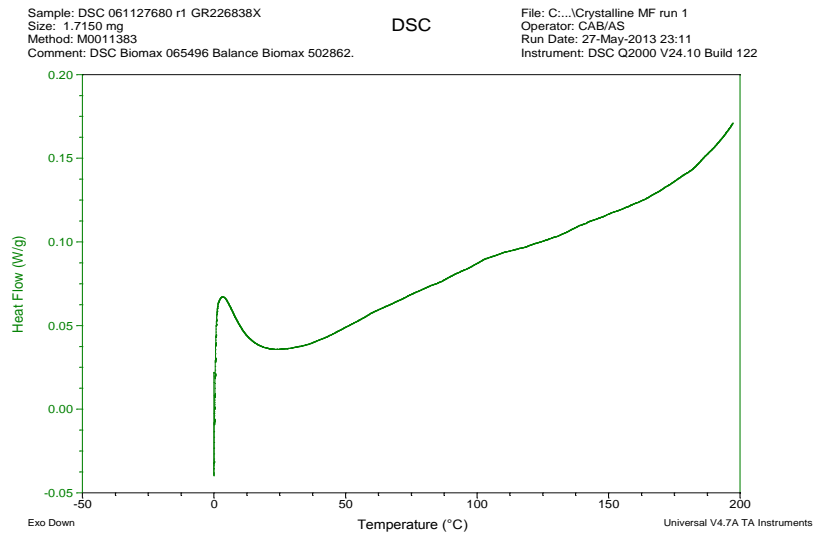




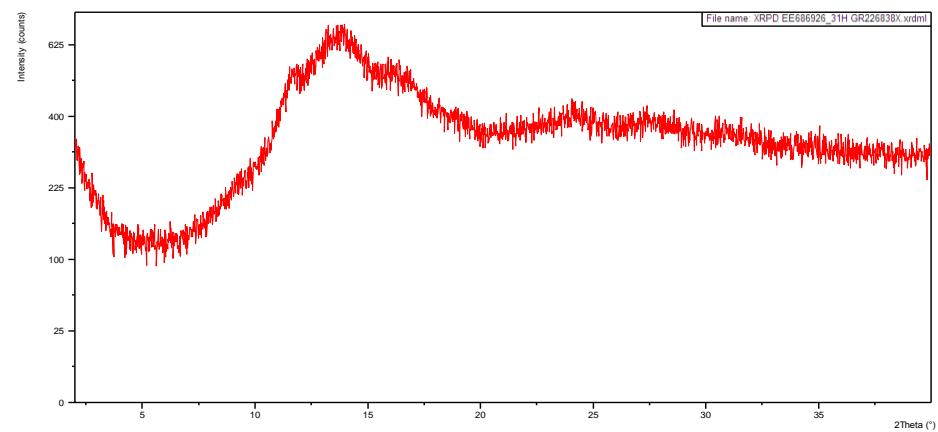
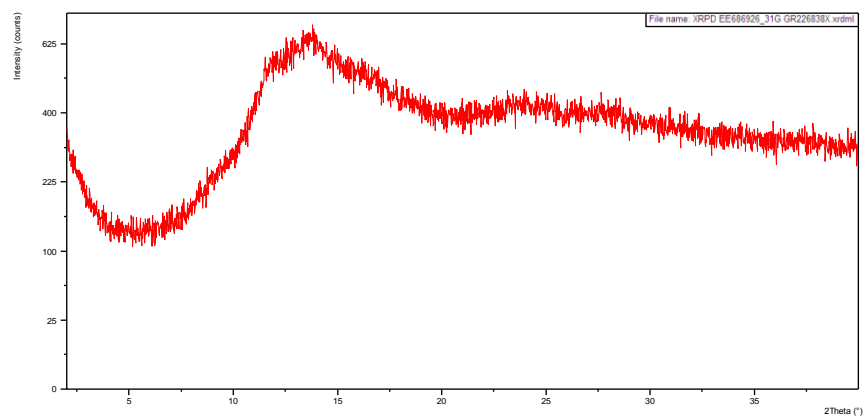
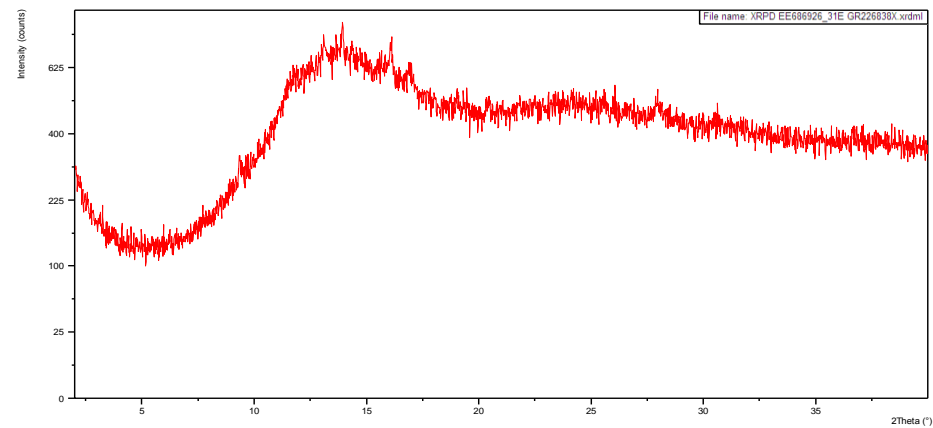
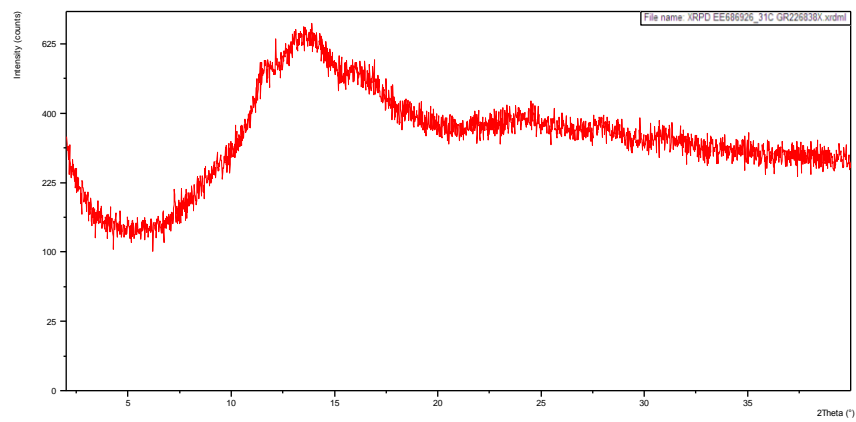
# Appendix 4



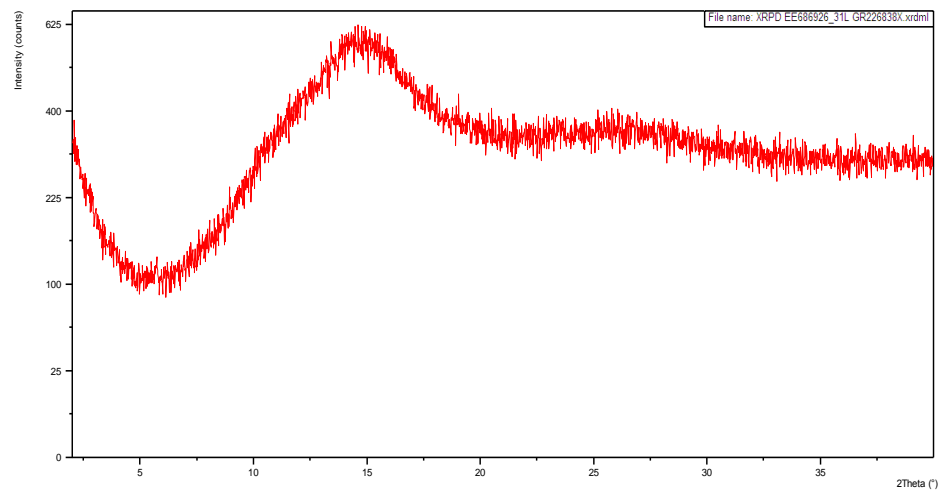
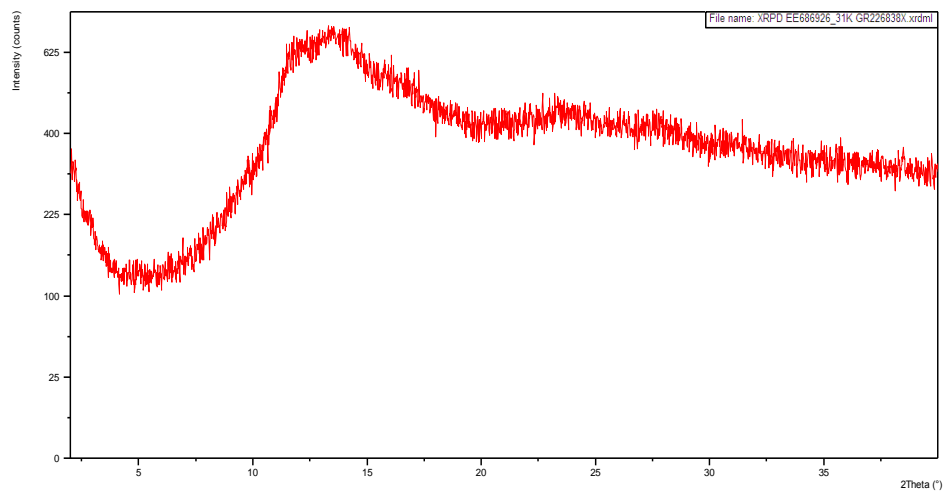
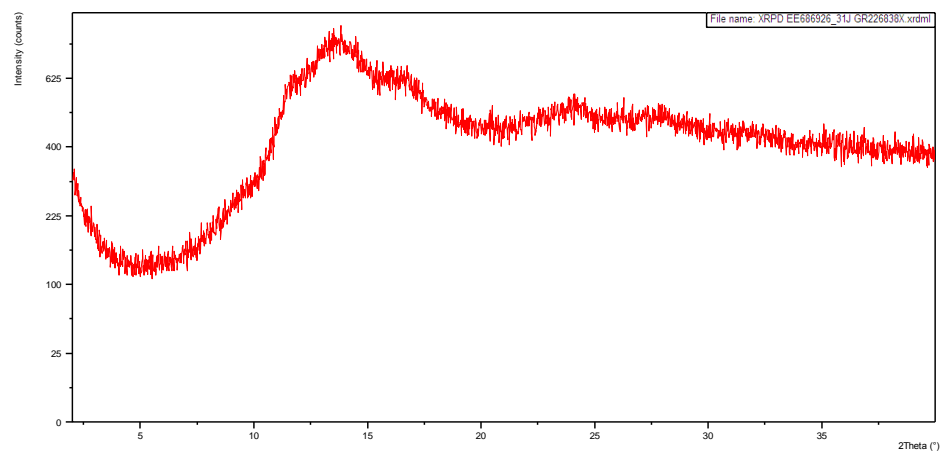
# Appendix 4



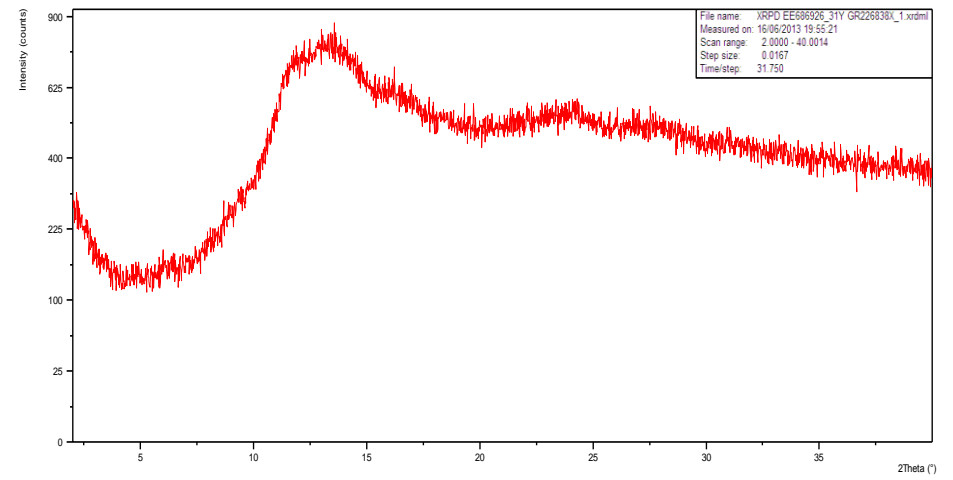
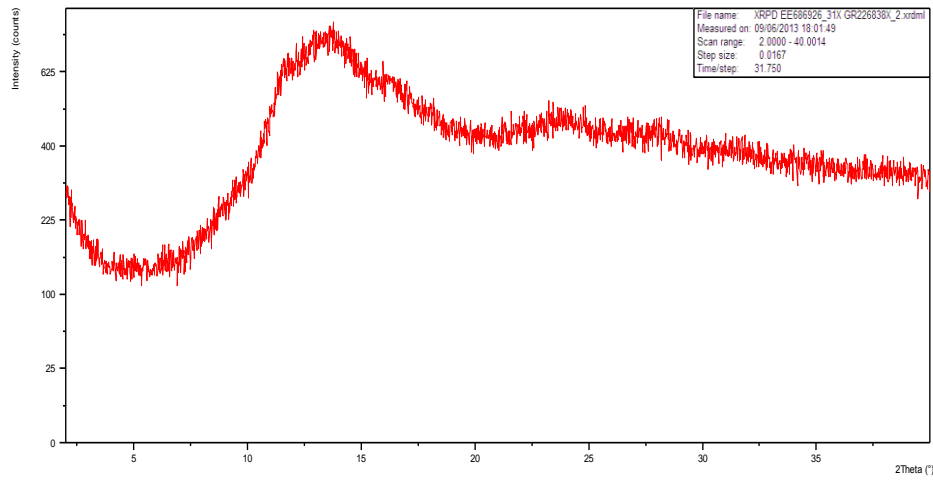
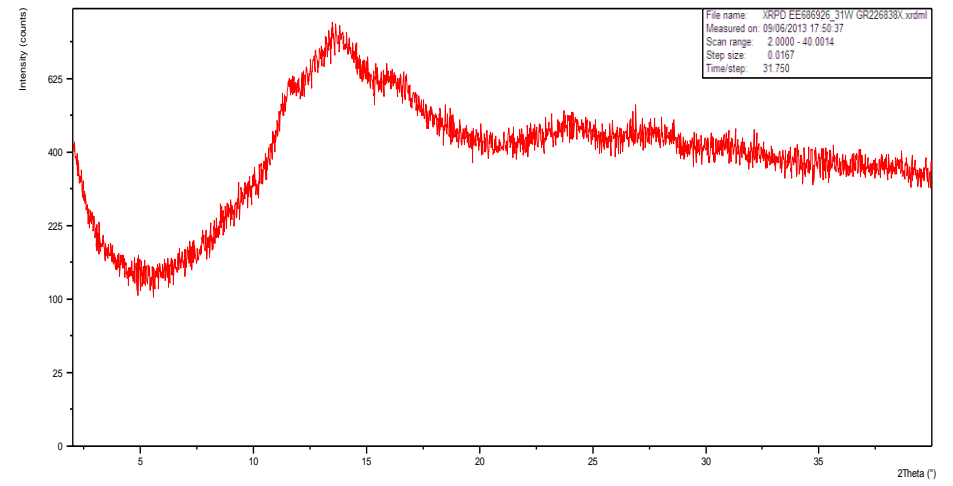
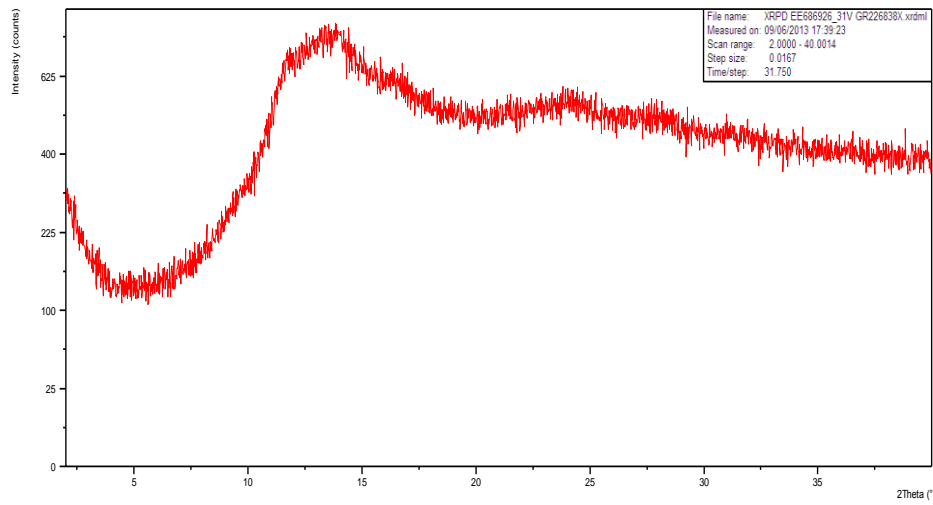
## Appendix 5 X-ray powder diffractograms



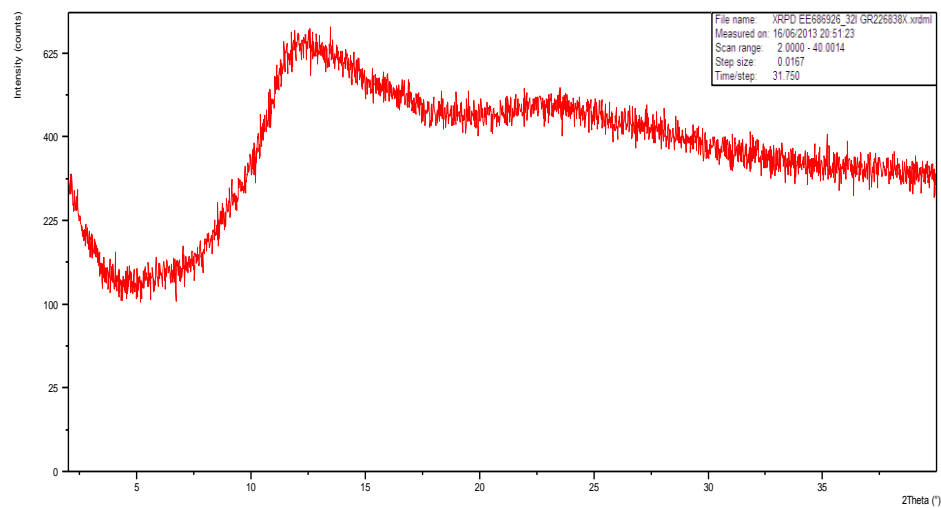
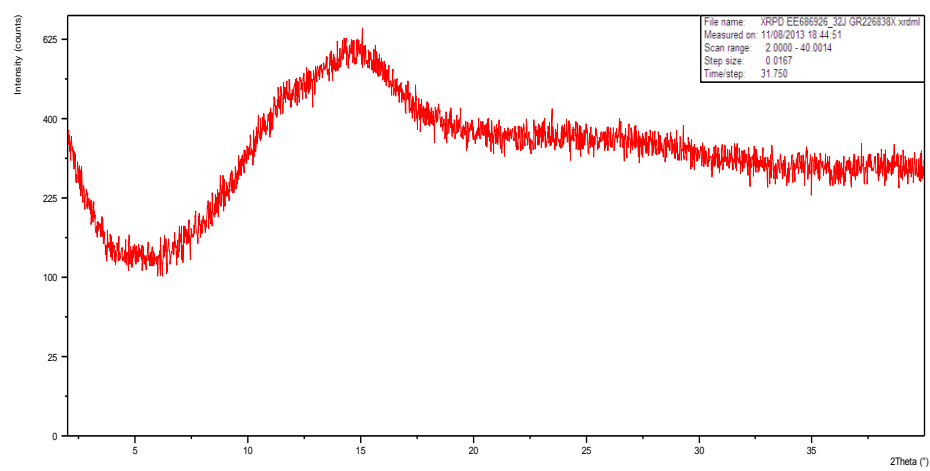
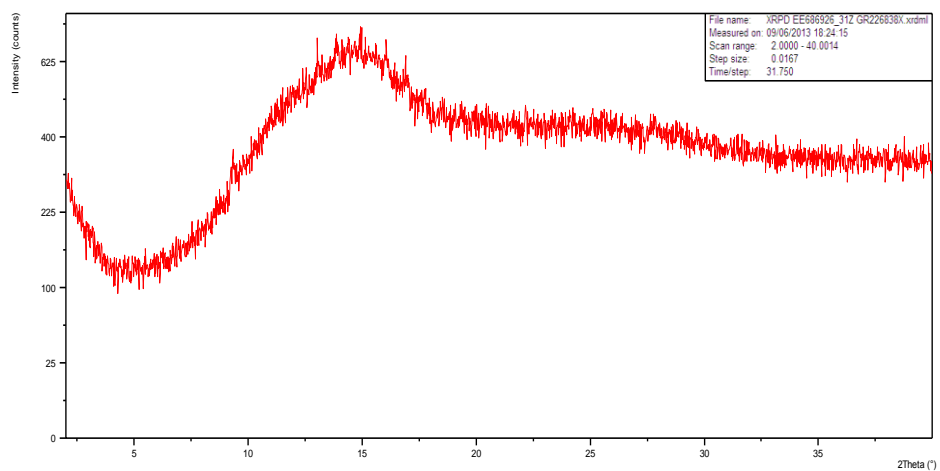
## Appendix 5



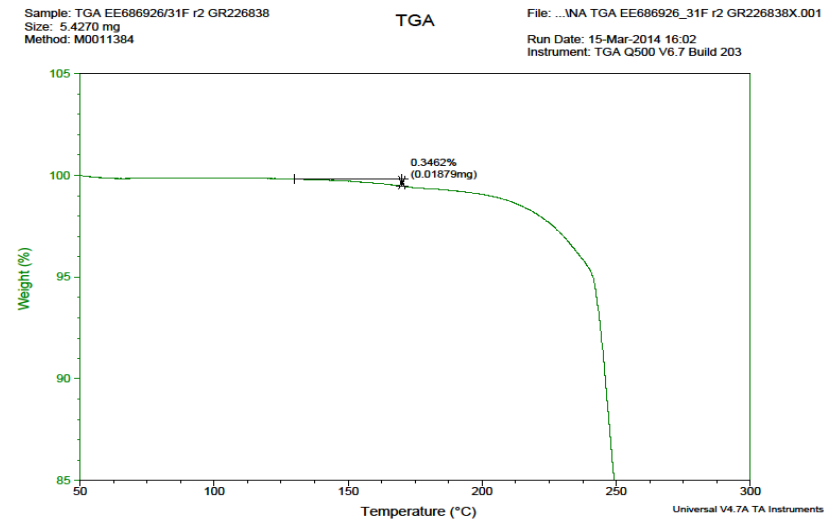
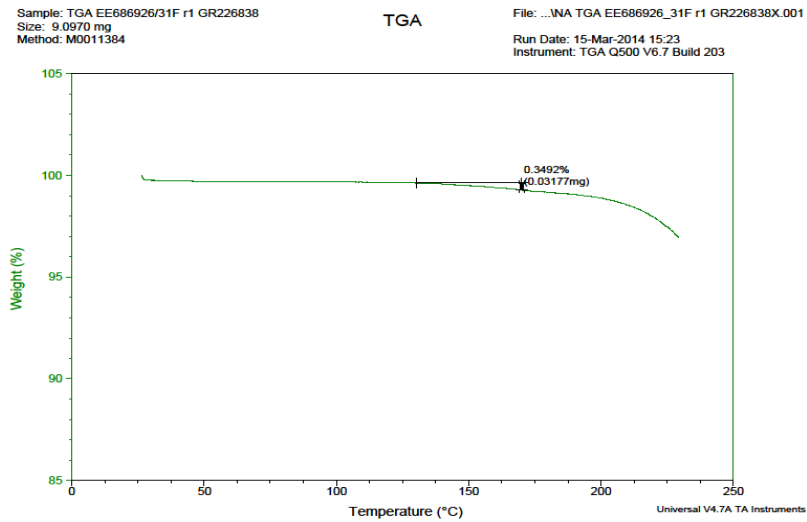
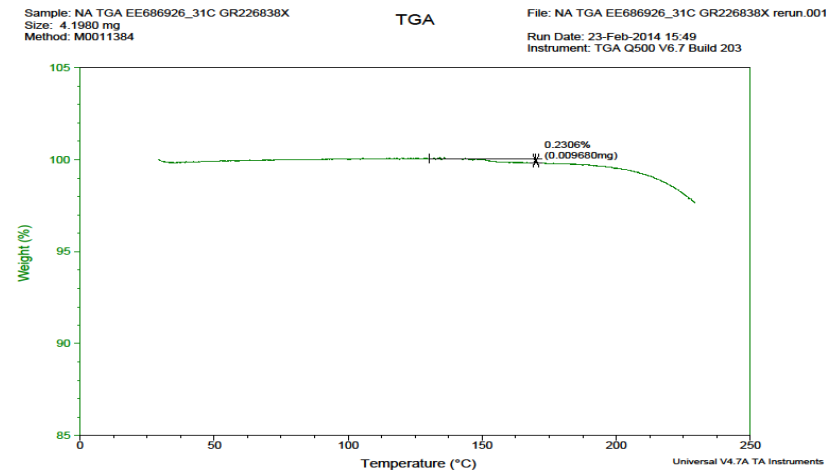
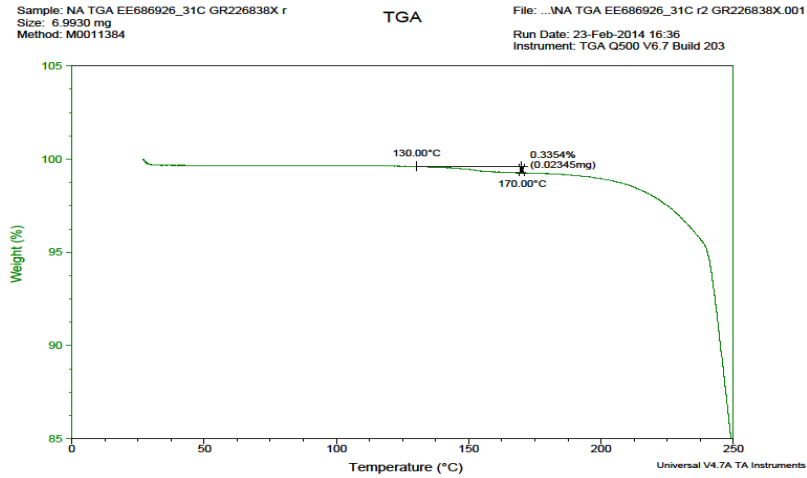
# Appendix 5



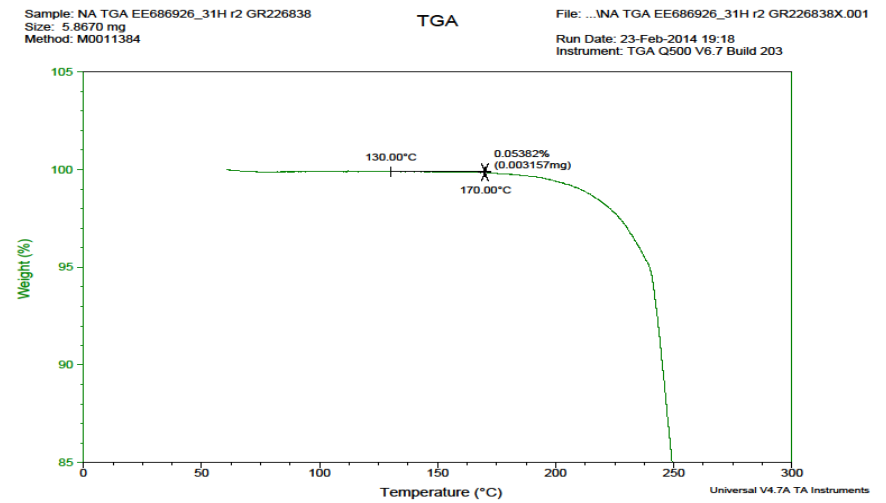
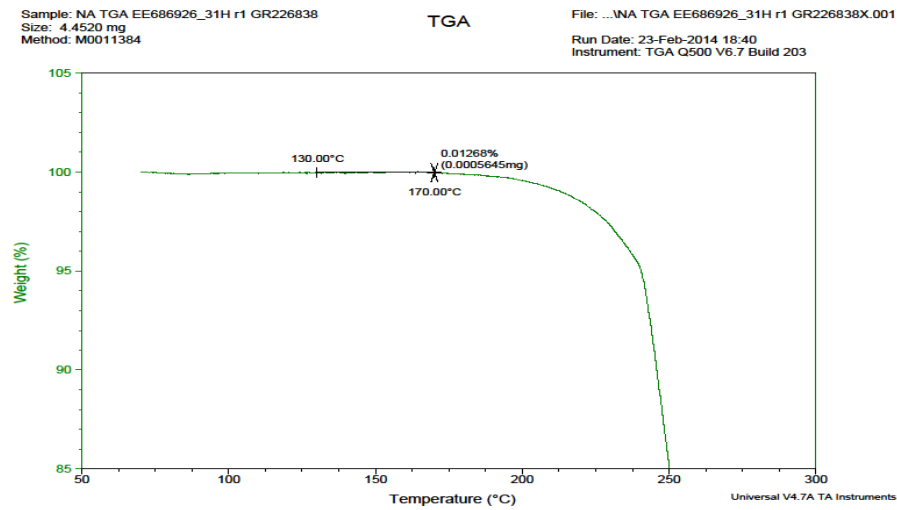
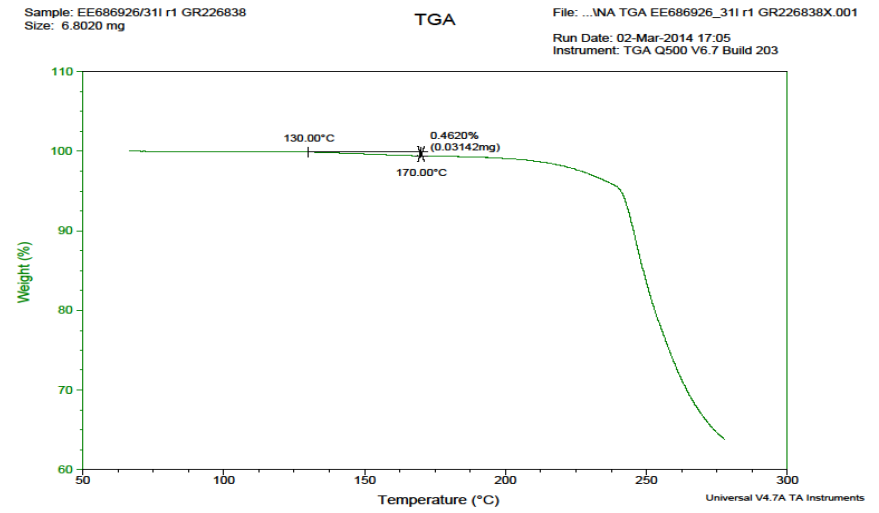
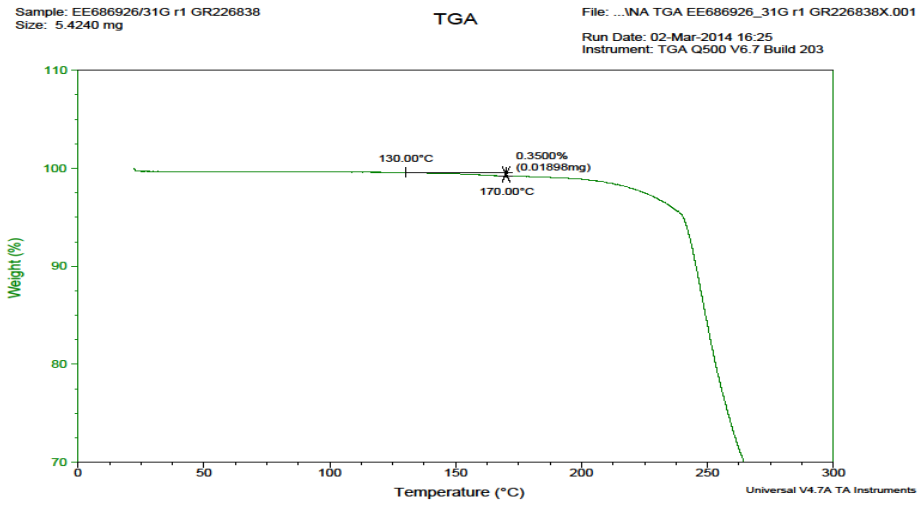
## Appendix 5



Appendix 6 Thermogravimetric analysis data

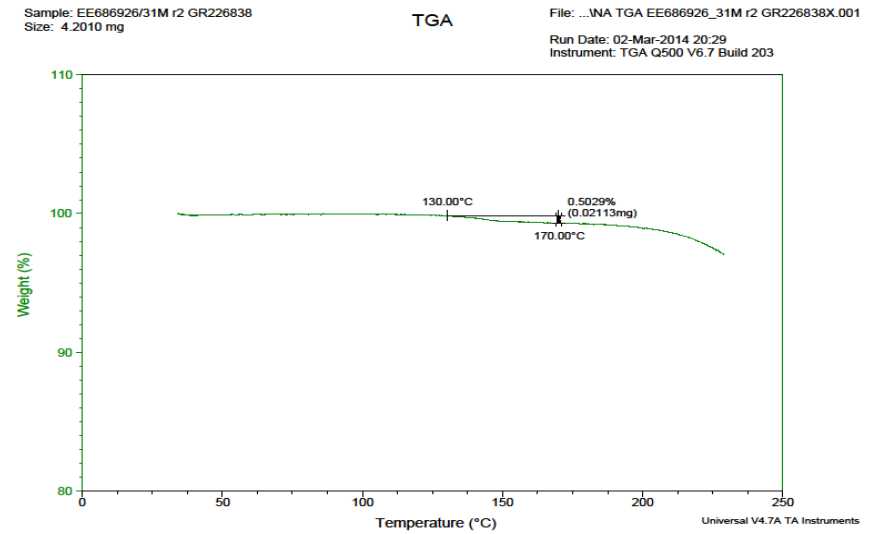
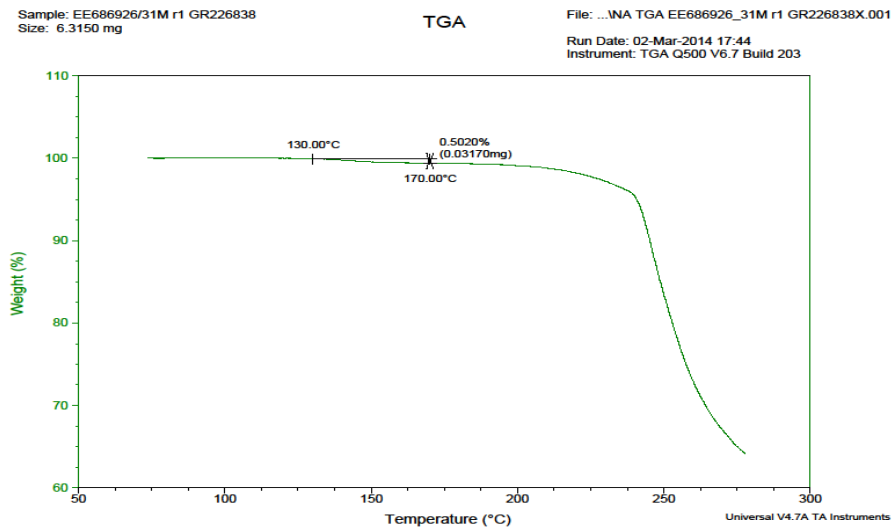
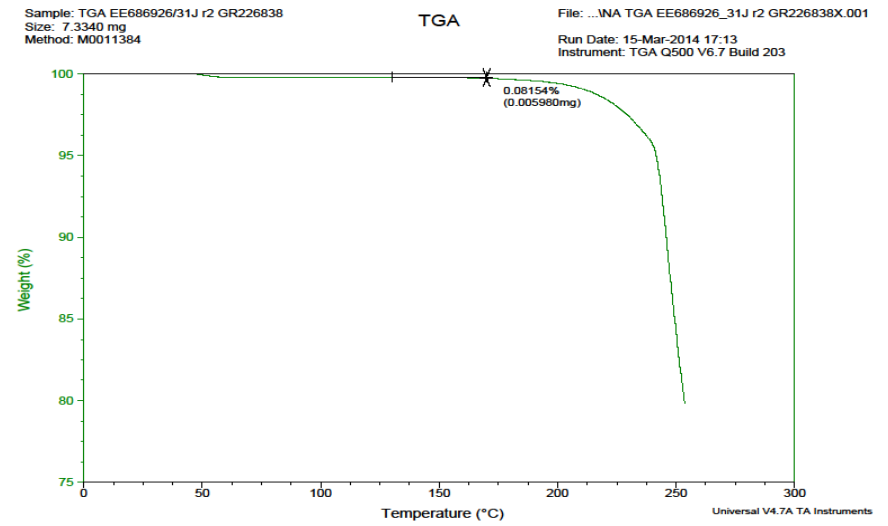
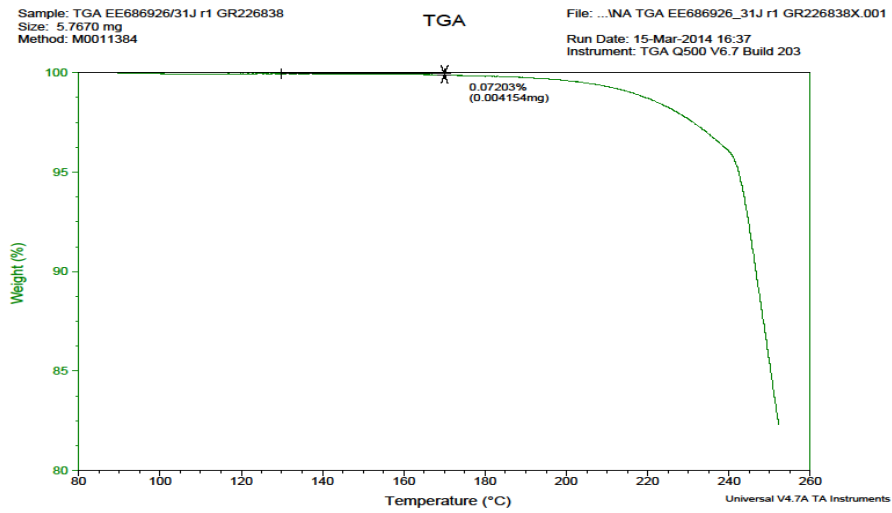


# Appendix 6





# Appendix 6

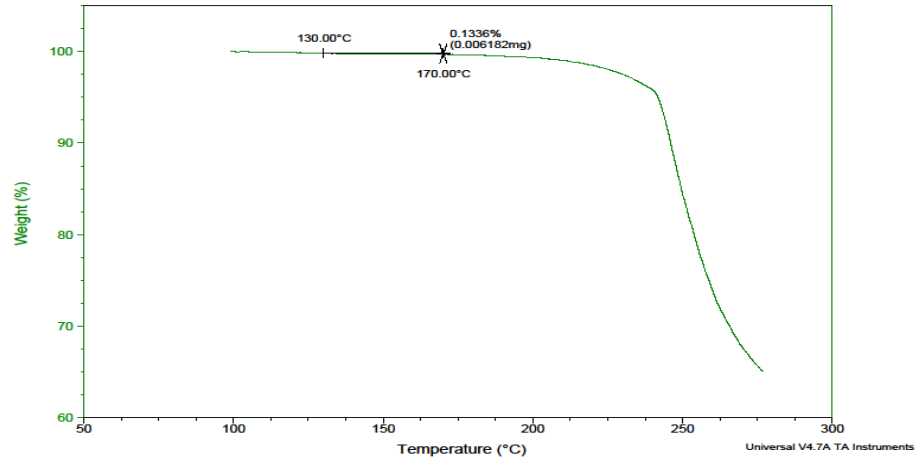


# Appendix 6

Sample: NA TGA EE686926\_31R r1 GR226838  
Size: 4.6270 mg  
Method: M0011384

TGA

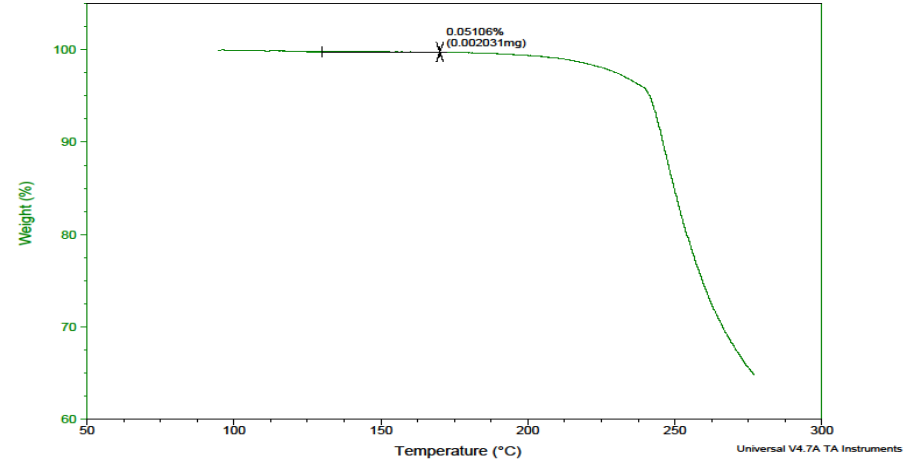
File: ...NA TGA EE686926\_31R r1 GR226838X.001  
Run Date: 23-Feb-2014 19:51  
Instrument: TGA Q500 V6.7 Build 203



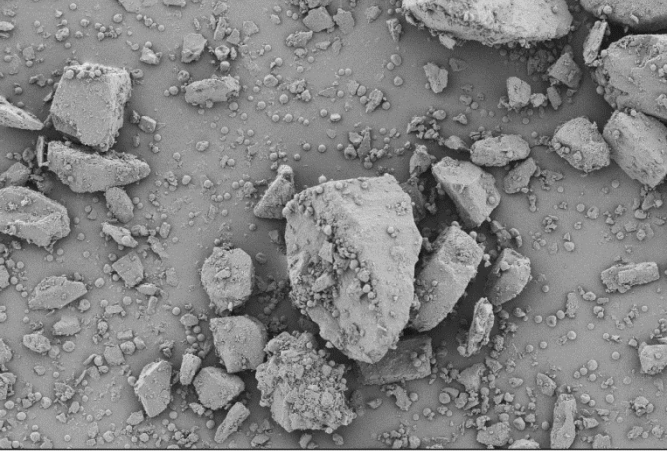
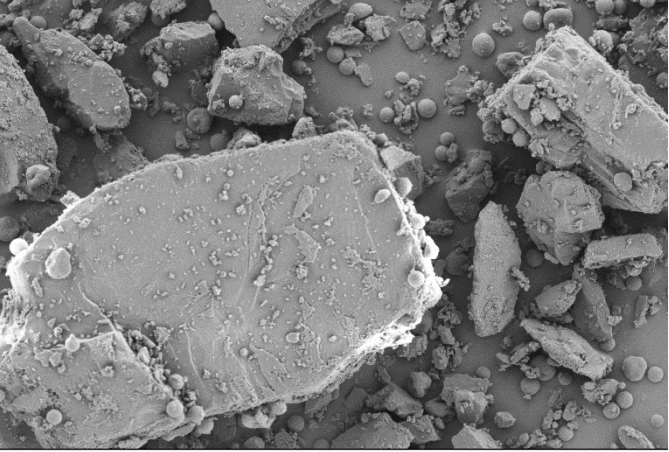

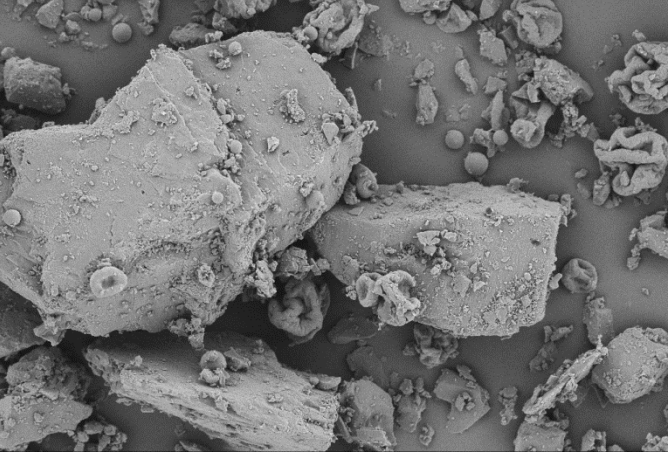
Sample: NA TGA EE686926\_31R r2 GR226838  
Size: 3.9780 mg  
Method: M0011384

TGA

File: ...NA TGA EE686926\_31R r2 GR226838X.001  
Run Date: 23-Feb-2014 20:21  
Instrument: TGA Q500 V6.7 Build 203

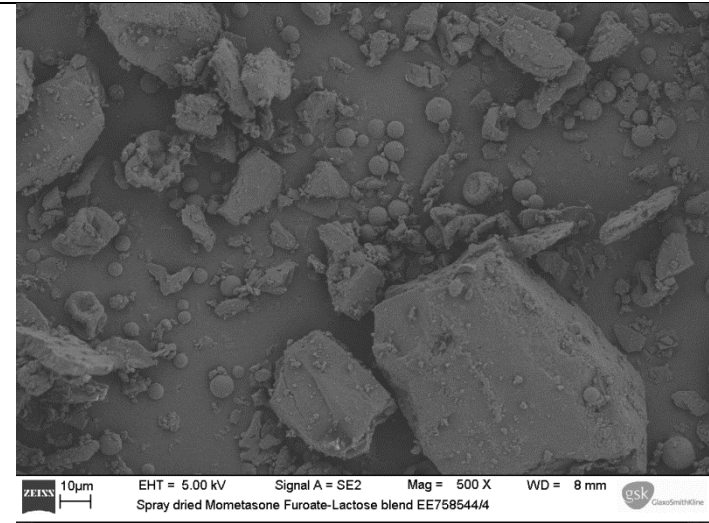
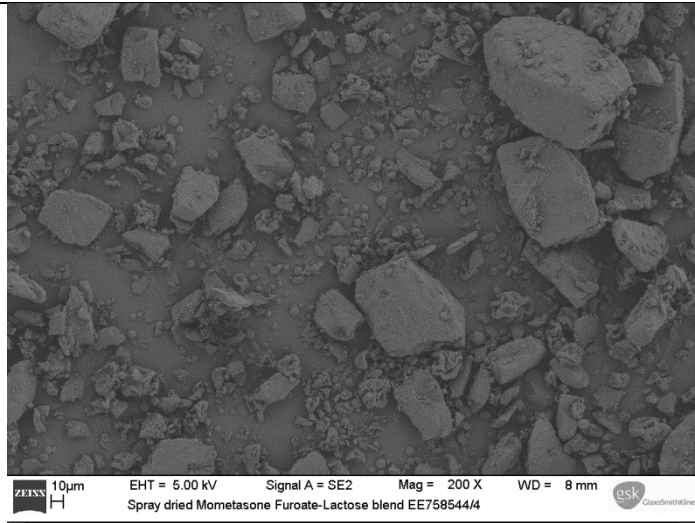


**Appendix 7 SEM images of MF-lactose blends**

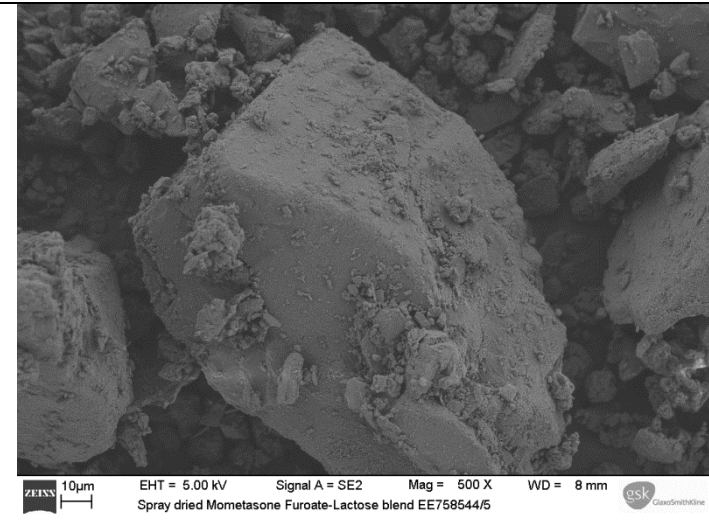
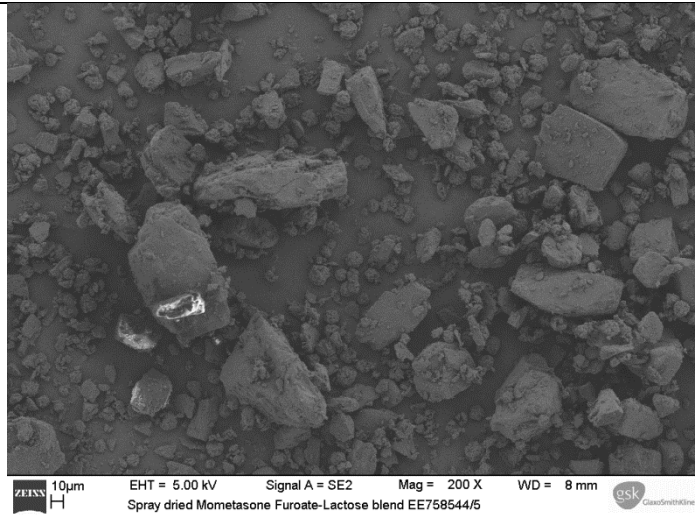
Batch number	Image 1	Image 2
EE758544/2	 <p data-bbox="450 842 1115 887">ZEISS 10µm EHT = 5.00 kV Signal A = SE2 Mag = 200 X WD = 9 mm esk Spray dried Mometasone Furoate-Lactose blend EE758544/2</p>	 <p data-bbox="1305 842 1971 887">ZEISS 20µm EHT = 5.00 kV Signal A = SE2 Mag = 500 X WD = 9 mm esk Spray dried Mometasone Furoate-Lactose blend EE758544/2</p>
EE758544/3	 <p data-bbox="450 1345 1115 1391">ZEISS 10µm EHT = 5.00 kV Signal A = SE2 Mag = 500 X WD = 9 mm esk Spray dried Mometasone Furoate-Lactose blend EE758544/3</p>	 <p data-bbox="1305 1345 1971 1391">ZEISS 10µm EHT = 5.00 kV Signal A = SE2 Mag = 500 X WD = 9 mm esk Spray dried Mometasone Furoate-Lactose blend EE758544/2</p>

Appendix 7

EE758544/4

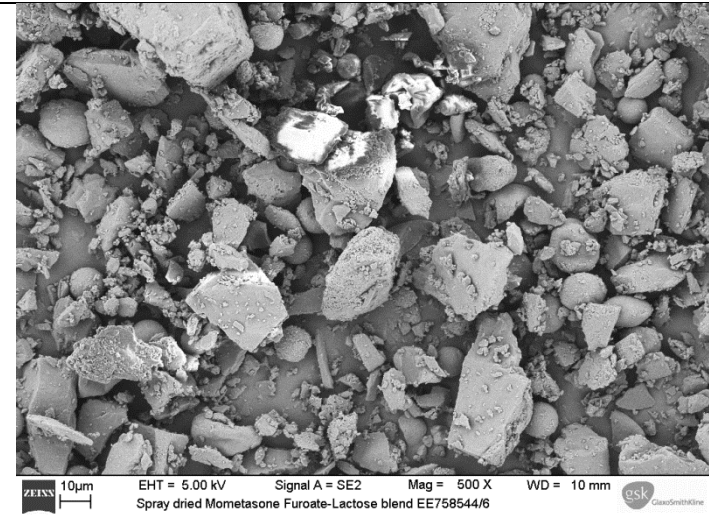
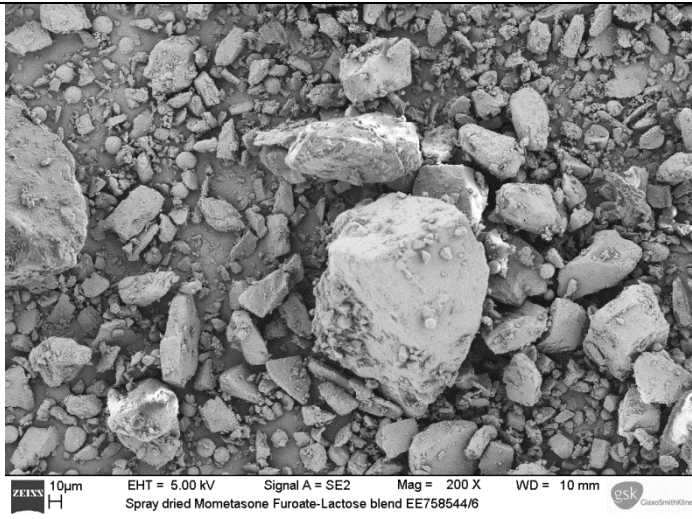


EE758544/5

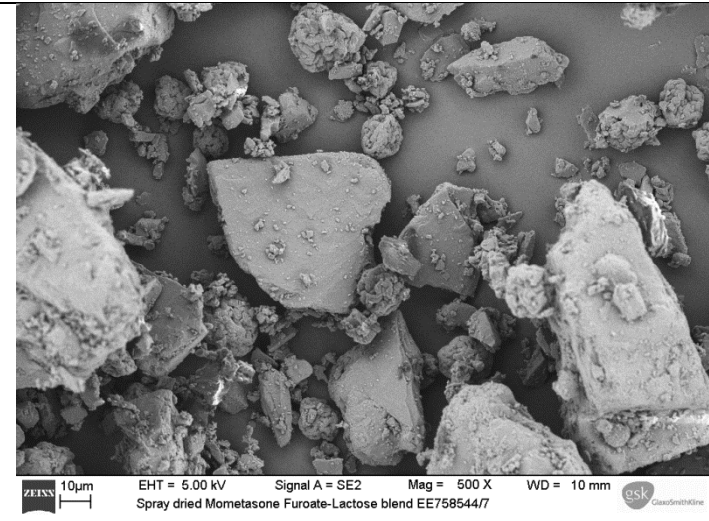
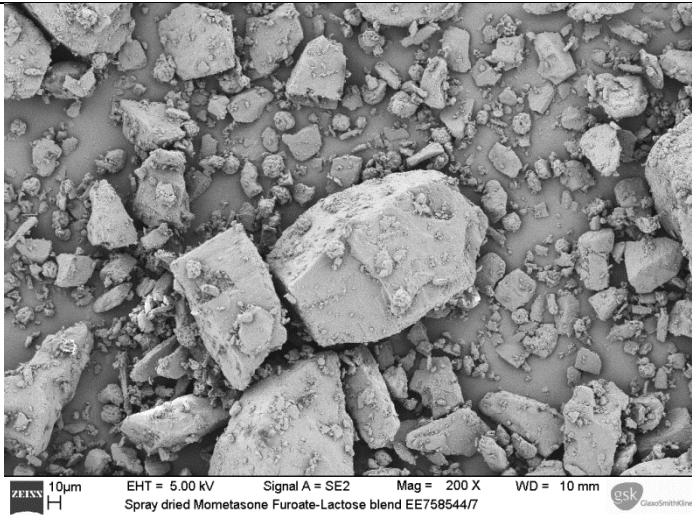


Appendix 7

EE758544/6

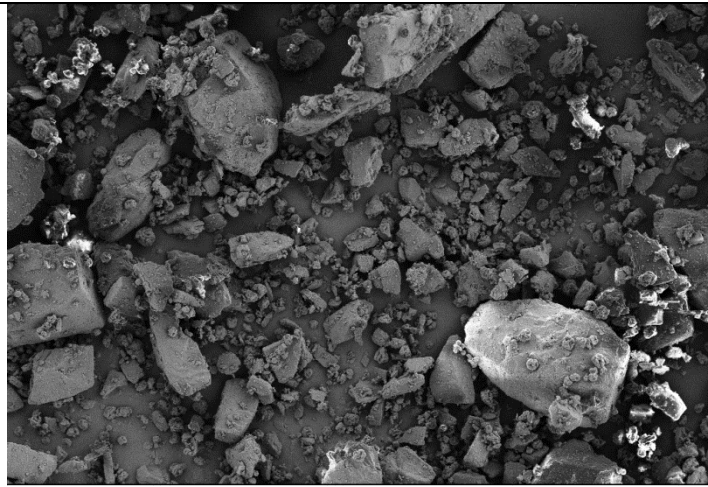


EE758544/7

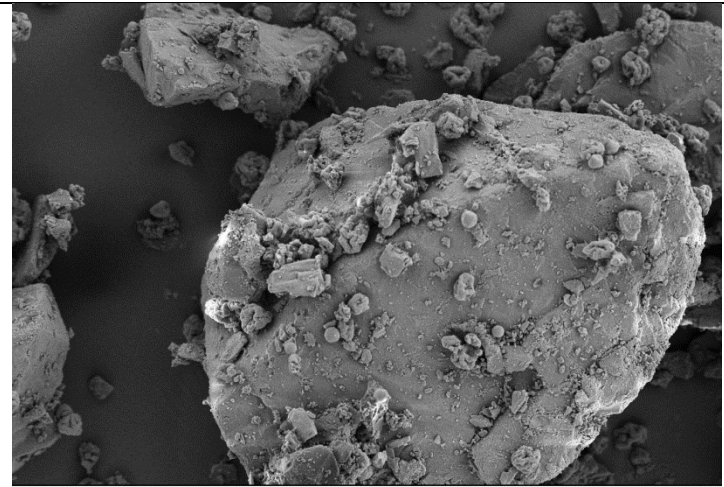


Appendix 7

EE758544/8

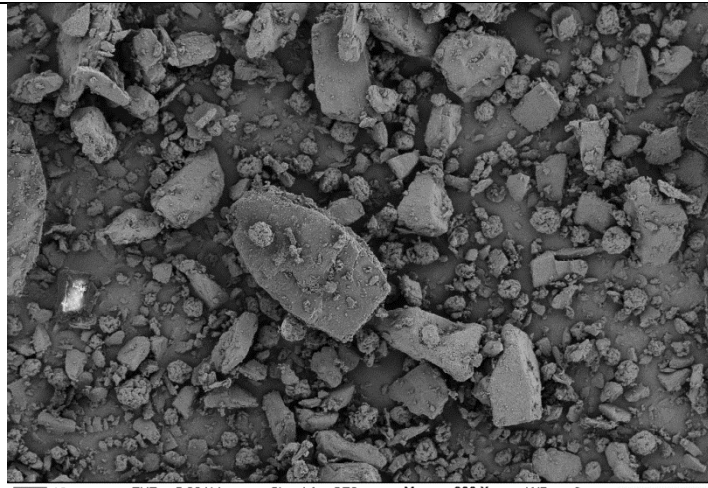


ZEISS 10µm EHT = 5.00 kV Signal A = SE2 Mag = 200 X WD = 8 mm esk  
Spary dried Mometasone Furoate-Lactose blend EE758544/8

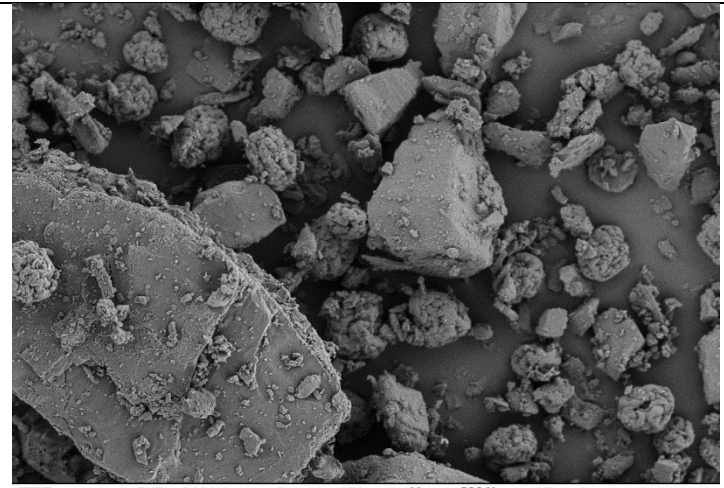


ZEISS 10µm EHT = 5.00 kV Signal A = SE2 Mag = 500 X WD = 8 mm esk  
Spary dried Mometasone Furoate-Lactose blend EE758544/8

EE758544/9



ZEISS 10µm EHT = 5.00 kV Signal A = SE2 Mag = 200 X WD = 9 mm esk  
Spary dried Mometasone Furoate-Lactose blend EE758544/9

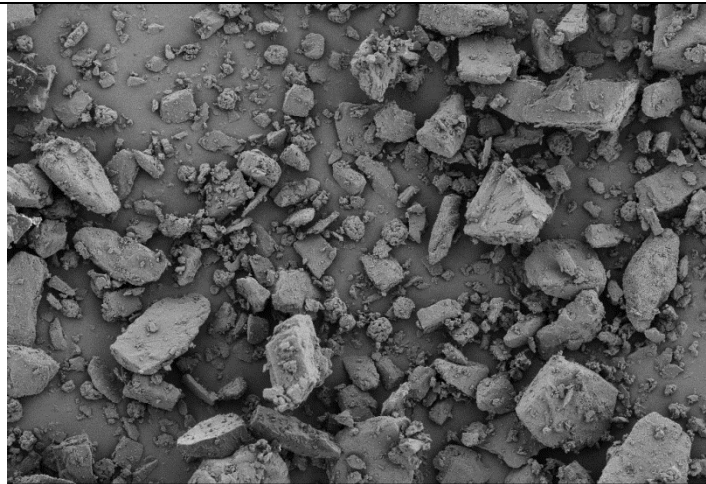


ZEISS 10µm EHT = 5.00 kV Signal A = SE2 Mag = 500 X WD = 9 mm esk  
Spary dried Mometasone Furoate-Lactose blend EE758544/9

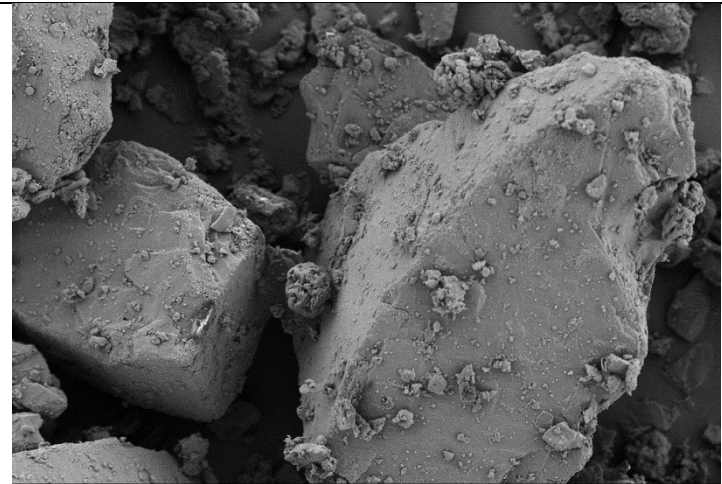


Appendix 7

EE758544/10

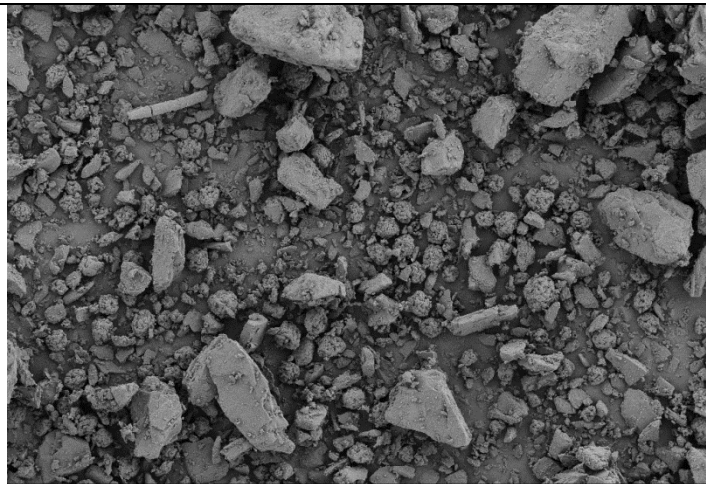


ZEISS 10µm EHT = 5.00 kV Signal A = SE2 Mag = 200 X WD = 9 mm esk GlaxoSmithKline  
Spary dried Mometasone Furoate-Lactose blend EE758544/10

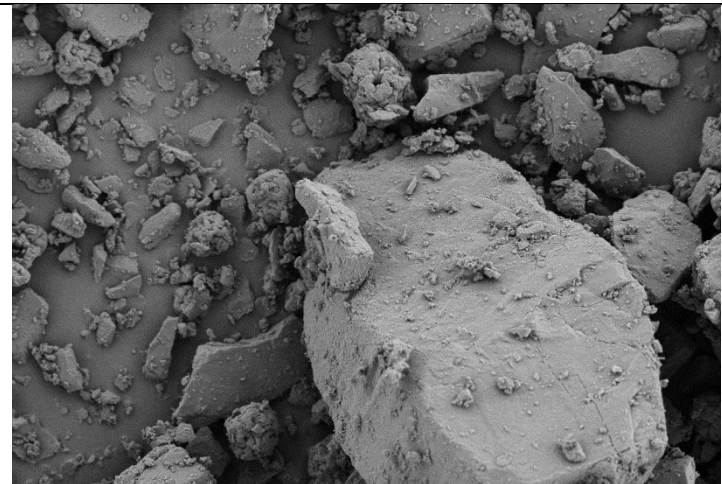


ZEISS 10µm EHT = 5.00 kV Signal A = SE2 Mag = 500 X WD = 8 mm esk GlaxoSmithKline  
Spary dried Mometasone Furoate-Lactose blend EE758544/10

EE758544/11



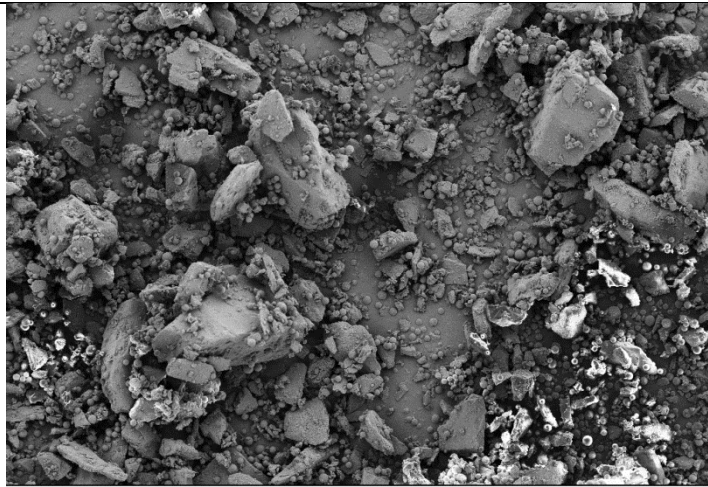
ZEISS 10µm EHT = 5.00 kV Signal A = SE2 Mag = 200 X WD = 9 mm esk GlaxoSmithKline  
Spary dried Mometasone Furoate-Lactose blend EE758544/11



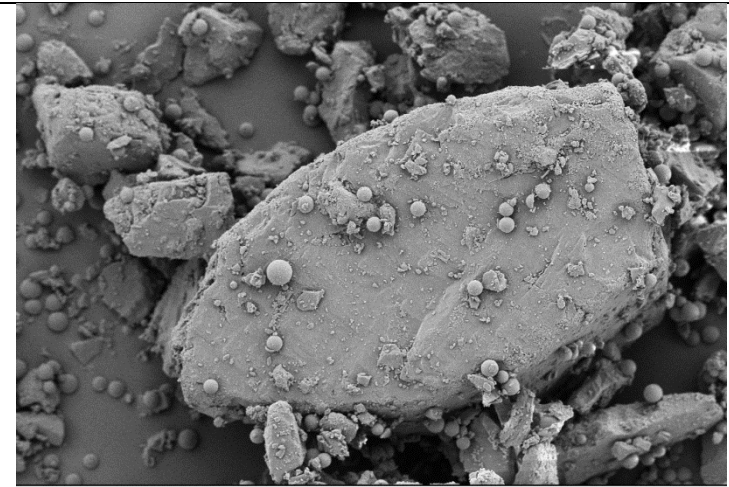
ZEISS 10µm EHT = 5.00 kV Signal A = SE2 Mag = 500 X WD = 9 mm esk GlaxoSmithKline  
Spary dried Mometasone Furoate-Lactose blend EE758544/11

Appendix 7

EE758544/12

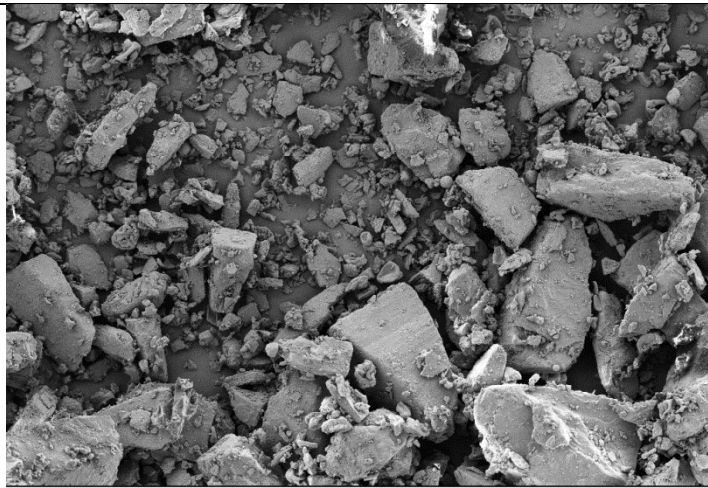


10µm EHT = 5.00 kV Signal A = SE2 Mag = 200 X WD = 10 mm  
Spary dried Mometasone Furoate-Lactose blend EE758544/12

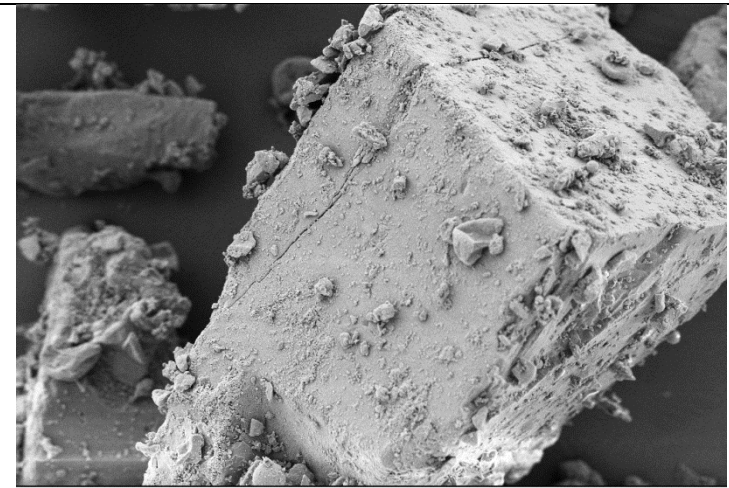


10µm EHT = 5.00 kV Signal A = SE2 Mag = 500 X WD = 10 mm  
Spary dried Mometasone Furoate-Lactose blend EE758544/12

EE758544/13



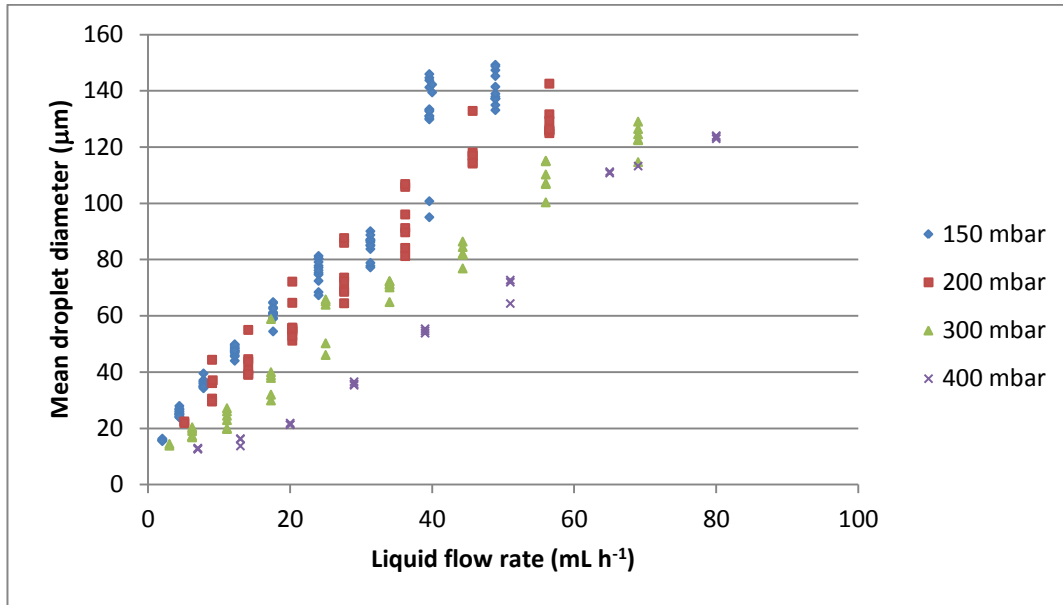
10µm EHT = 5.00 kV Signal A = SE2 Mag = 200 X WD = 10 mm  
Spary dried Mometasone Furoate-Lactose blend EE758544/13



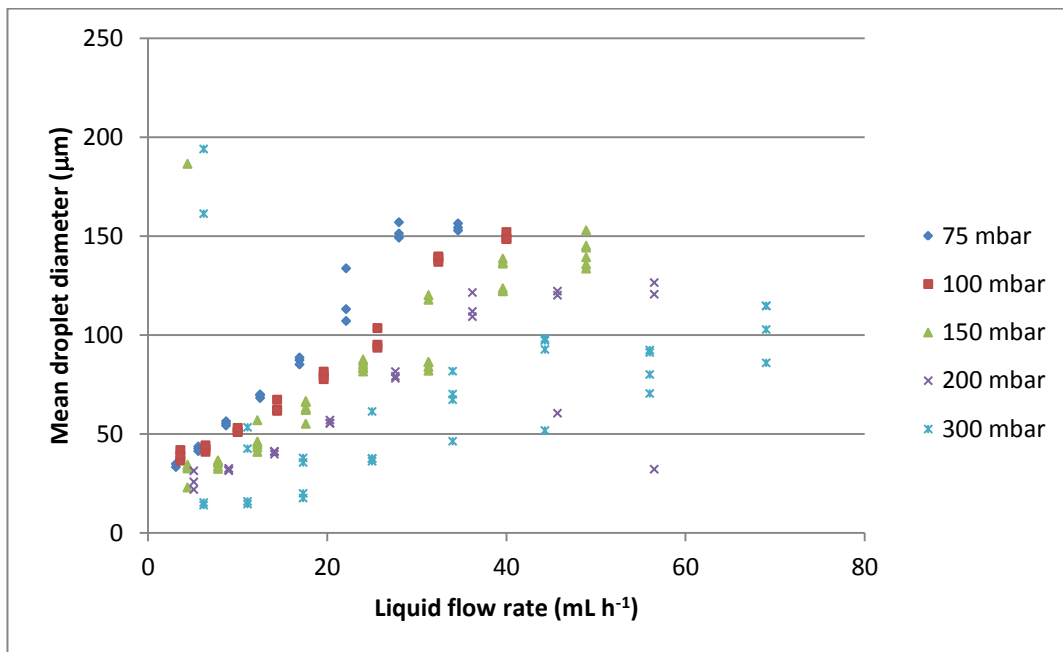
10µm EHT = 5.00 kV Signal A = SE2 Mag = 500 X WD = 10 mm  
Spary dried Mometasone Furoate-Lactose blend EE758544/13



**Appendix 8 Droplet size, flow rate and pressure drop relationships for flow focusing atomization**

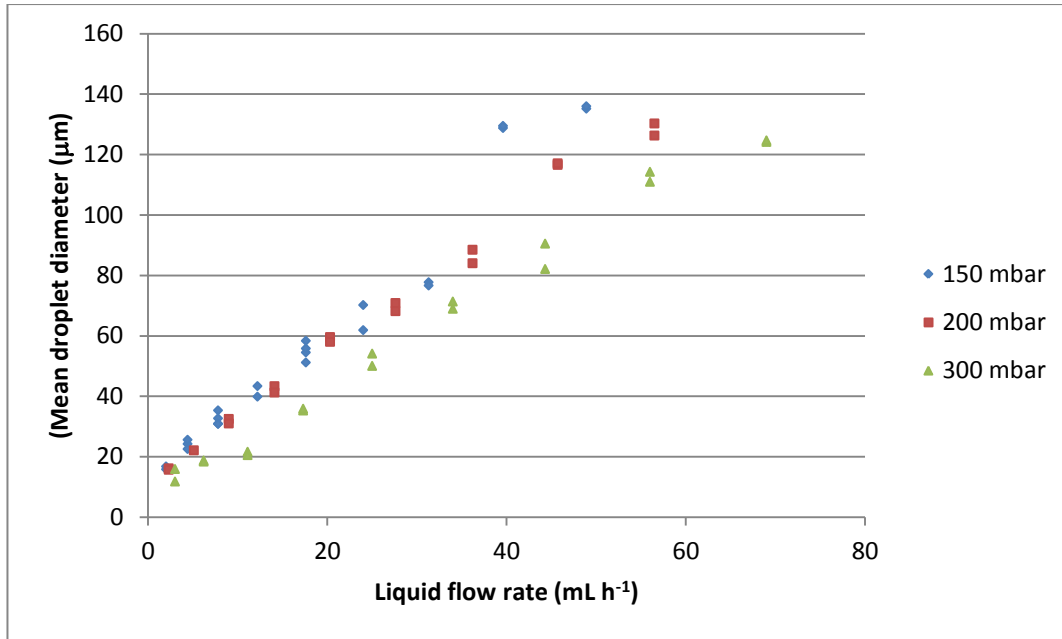


2-Propanol, 25°C

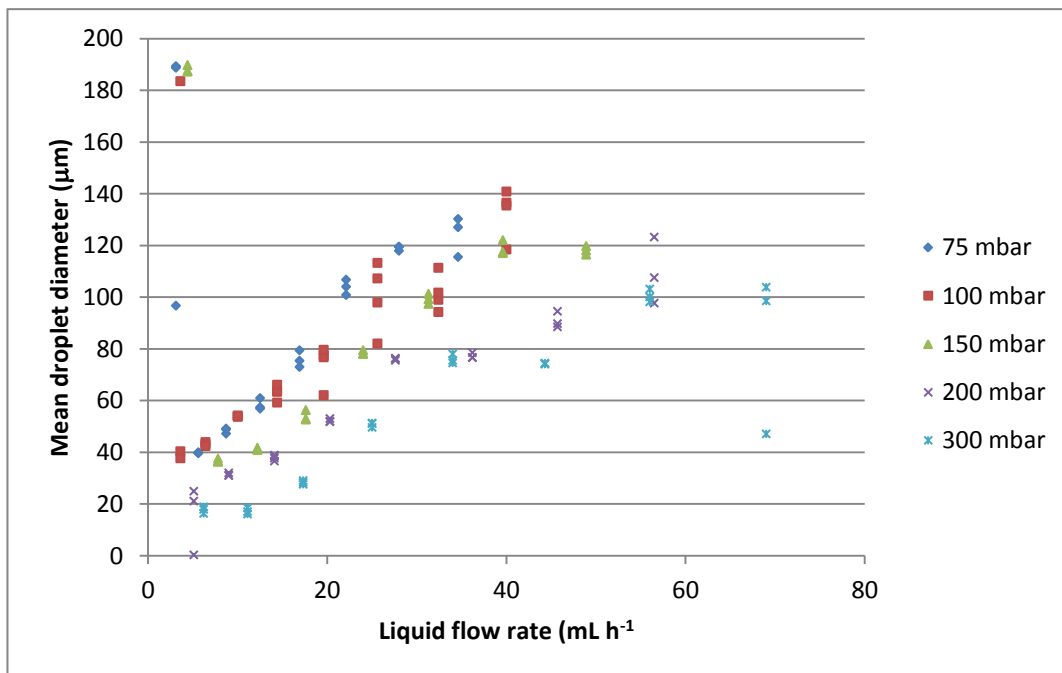


2-Propanol, 50°C

## Appendix 8



Ethanol, 25°C



Ethanol, 50°C

## References

## References

- Adamson, A. W. (1982). *Physical Chemistry of Surfaces*. New York: J. Wiley.
- Adi, H., Kwok, P. C. L., Crapper, J., Young, P. M., Traini, D., & Chan, H. K. (2010). Does electrostatic charge affect powder aerosolisation? *J. Pharm. Sci.* *99*, 2455-2461.
- Adi, H., Larson, I., Chiou, H., Young, P., Traini, D., & Stewart, P. (2006). Agglomerate strength and dispersion of salmeterol xinafoate from powder mixtures for inhalation. *Pharm. Res.* *23*, 2556-2565.
- Anderson, P. J. (2005). History of aerosol therapy: Liquid nebulization to MDIs to DPIs. *Respir. Car.* *50*, 1139-1149.
- Angell, C. A. (1995). The old problems of glass and the glass transition, and the many new twists. *Proceedings of the National Academy of Sciences* *92*, 6675-6682.
- Atkins, P. (1998). *Physical Chemistry*, 6th ed. Oxford: Oxford University Press.
- Azizian, S. & Hemmati, M. (2003). Surface tension of binary mixtures of ethanol + ethylene glycol from 20 to 50°C. *J. Chem. Eng Data* *48*, 662-663.
- Barzegar-Jalali, M., Alaei-Beirami, M., Javadzadeh, Y., Mohammadi, G., Hamidi, A., Andalib, S., & Adibkia, K. (2012). Comparison of physicochemical characteristics and drug release of diclofenac sodium-eudragit- RS100 nanoparticles and solid dispersions. *Powder Technol.* *219*, 211-216.
- Basaran, O. A. (2002). Small-scale free surface flows with breakup: Drop formation and emerging applications. *AIChE J.* *48*, 1842-1848.
- Beckett, S. T. (1996). *Physico-Chemical Aspects of Food Processing*, Berlin: Springer Science and Business Media.
- Begat, P., Morton, D. A. V., Shur, J., Kippax, P., Staniforth, J. N., & Price, R. (2009). The role of force control agents in high-dose dry powder inhaler formulations. *J. Pharm. Sci.* *98*, 2770-2783.
- Bell, J. & Newman, S. (2007). The rejuvenated pressurised metered dose inhaler. *Expert Opin. Drug Deliv.* *4*, 215-234.
- Bell, J. H., Hartley, P. S., & Cox, J. S. (1971). Dry powder aerosols. I. A new powder inhalation device. *J. Pharm. Sci.* *60*, 1559-1564.
- Berard, V., Lesniewska, E., Andres, C., Pertuy, D., Laroche, C., & Pourcelot, Y. (2002). Affinity scale between a carrier and a drug in DPI studied by atomic force microscopy. *Int. J. Pharm.* *247*, 127-137.

## References

- Biddiscombe, M. F., Barnes, P. J., & Usmani, O. S. (2006). Generating monodisperse pharmacological aerosols using the spinning-top aerosol generator. *J. Aerosol Med. Deposition Clear. Eff. Lung* 19, 245-253.
- Bohr, A., Kristensen, J., Stride, E., Dyas, M., & Edirisinghe, M. (2011). Preparation of microspheres containing low solubility drug compound by electrohydrodynamic spraying. *Int. J. Pharm.* 412, 59-67.
- Bosquillon, C., Lombry, C., Preat, V., & Vanbever, R. (2001). Influence of formulation excipients and physical characteristics of inhalation dry powders on their aerosolization performance. *J. Control. Release* 70, 329-339.
- Brenn, G., Helpiö, T., & Durst, F. (1997). A new apparatus for the production of monodisperse sprays at high flow rates. *Chem. Eng. Sci.* 52, 237-244.
- Bridson, R. H., Robbins, P. T., Chen, Y., Westerman, D., Gillham, C. R., Roche, T. C., & Seville, J. P. K. (2007). The effects of high shear blending on lactose monohydrate. *Int. J. Pharm.* 339, 84-90.
- Burnell, P. K. P., Malton, A., Reavill, K., & Ball, M. H. E. (1998). Design, validation and initial testing of the Electronic Lung device. *J. Aerosol Sci.* 29, 1011-1025.
- Cacela, C., Gil, M., & Temtem, M. (2012). Advances in size reduction process for Mometasone Furoate Monohydrate. *Respiratory Drug Delivery* 2, 535-538.
- Cal, K. & Sollohub, K. (2010). Spray drying technique. I: Hardware and process parameters. *J. Pharm. Sci.* 99, 575-586.
- Carter, P. A., Cassidy, O. E., Rowley, G., & Merrifield, D. R. (1998). Triboelectrification of fractionated crystalline and spray-dried lactose. *Pharm. Pharmacol. Commun.* 4, 111-115.
- Chattoraj, S., Bhugra, C., Telang, C., Zhong, L., Wang, Z., & Sun, C. C. (2012). Origin of two modes of non-isothermal crystallization of glasses produced by milling. *Pharm. Res.* 29, 1020-1032.
- Chawla, A.; Taylor, K. M. G.; Newton, J. M.; Johnson, M. C. R. (1994). Production of spray dried salbutamol sulphate for use in dry powder aerosol formulations. *Int. J. Pharm.* 108, 233 - 240
- Chen, X., Carillo, M., Haltiwanger, R. C., & Bradley, P. (2005). Solid state characterization of mometasone furoate anhydrous and monohydrate forms. *J. Pharm. Sci.* 94, 2496-2509.
- Chew, N. Y. K., Bagster, D. F., & Chan, H. K. (2000). Effect of particle size, air flow and inhaler device on the aerosolisation of disodium cromoglycate powders. *Int. J. Pharm.* 206, 75-83.
- Chew, N. Y. K. & Chan, H. K. (1999). Influence of particle size, air flow, and inhaler device on the dispersion of mannitol powders as aerosols. *Pharm. Res.* 16, 1098-1103.

## References

- Chew, N. Y. K. & Chan, H. K. (2001). Use of solid corrugated particles to enhance powder aerosol performance. *Pharm. Res.* 18, 1570-1577.
- Chiou, D. & Langrish, T. A. G. (2008). A comparison of crystallisation approaches in spray drying. *J. Food Eng.* 88, 177-185.
- Chow, A. H. L., Tong, H. H. Y., Chattopadhyay, P., & Shekunov, B. Y. (2007). Particle engineering for pulmonary drug delivery. *Pharm. Res.* 24, 411-437.
- Chow, K. T., Zhu, K., Tan, R. B. H., & Heng, P. W. S. (2008). Investigation of electrostatic behavior of a lactose carrier for dry powder inhalers. *Pharm. Res.* 25, 2822-2834.
- Chrystyn, H. (2007). The Diskus<sup>TM</sup>: a review of its position among dry powder inhaler devices. *International Journal of Clinical Practice* 61, 1022-1036.
- Clark, A. R. & Hollingworth, A. M. (1993). The relationship between powder inhaler resistance and peak inspiratory conditions in healthy volunteers - Implications for in vitro testing. *J. Aerosol Med. Deposition Clear. Eff. Lung* 6, 99-110.
- Coates, M. S., Chan, H. K., Fletcher, D. F., & Raper, J. A. (2005a). Influence of air flow on the performance of a dry powder inhaler using computational and experimental analyses. *Pharm. Res.* 22, 1445-1453.
- Coates, M. S., Chan, H. K., Fletcher, D. F., & Raper, J. A. (2006). Effect of design on the performance of a dry powder inhaler using computational fluid dynamics. Part 2: Air inlet size. *J. Pharm. Sci.* 95, 1382-1392.
- Coates, M. S., Fletcher, D. F., Chan, H. K., & Raper, J. A. (2004). Effect of design on the performance of a dry powder inhaler using computational fluid dynamics. Part 1: Grid structure and mouthpiece length. *J. Pharm. Sci.* 93, 2863-2876.
- Coates, M. S., Fletcher, D. F., Chan, H. K., & Raper, J. A. (2005b). The role of capsule on the performance of a dry powder inhaler using computational and experimental analyses. *Pharm. Res.* 22, 923-932.
- Codrons, V., Vanderbist, F., Verbeeck, R. K., Arras, M., Lison, D., Preat, V., & Vanbever, R. (2003). Systemic delivery of parathyroid hormone (1-34) using inhalation dry powders in rats. *J. Pharm. Sci.* 92, 938-950.
- Cooper, S. M. (2003). Particle design of fluticasone propionate by supercritical fluid processing for inhalation drug delivery. *Ph.D Thesis*, University of Bradford.
- Craig, D. Q. M., Royall, P. G., Kett, V. L., & Hopton, M. L. (1999). The relevance of the amorphous state to pharmaceutical dosage forms: Glassy drugs and freeze dried systems. *Int. J. Pharm.* 179, 179-207.
- Crim, C., Pierre, L. N., & Daley-Yates, P. T. (2001). A review of the pharmacology and pharmacokinetics of inhaled fluticasone propionate and mometasone furoate. *Clin. Ther.* 23, 1339-1354.

## References

- Crowder, T. M., Rosati, J. A., Schroeter, J. D., Hickey, A. J., & Martonen, T. B. (2002). Fundamental effects of particle morphology on lung delivery: Predictions of Stokes' law and the particular relevance to dry powder inhaler formulation and development. *Pharm. Res.* *19*, 239-245.
- Das, D. & Langrish, T. A. G. (2012). An activated-state model for the prediction of solid-phase crystallization growth kinetics in dried lactose particles. *J Food Eng* *109*, 691-700.
- Davis, M. E., Chen, Z., & Shin, D. M. (2008). Nanoparticle therapeutics: An emerging treatment modality for cancer. *Nat. Rev. Drug Disc.* *7*, 771-782.
- Dayal, P., Shaik, M. S., & Singh, M. (2004). Evaluation of different parameters that affect droplet-size distribution from nasal sprays using the Malvern Spraytec. *J. Pharm. Sci.* *93*, 1725-1742.
- De Boer, A. H., Chan, H. K., & Price, R. (2012). A critical view on lactose-based drug formulation and device studies for dry powder inhalation: Which are relevant and what interactions to expect? *Adv. Drug Deliv. Rev.* *64*, 257-274.
- De Boer, A. H., Hagedoorn, P., Gjaltema, D., Lambregts, D., Irngartinger, M., & Frijlink, H. W. (2004a). The mode of drug particle detachment from carrier crystals in an air classifier-based inhaler. *Pharm. Res.* *21*, 2167-2174.
- De Boer, A. H., Hagedoorn, P., Gjaltema, D., Lambregts, D., Irngartinger, M., & Frijlink, H. W. (2004b). The rate of drug particle detachment from carrier crystals in an air classifier-based inhaler. *Pharm. Res.* *21*, 2158-2166.
- Dellamary, L. A., Tarara, T. E., Smith, D. J., Woelk, C. H., Adractas, A., Costello, M. L., Gill, H., & Weers, J. G. (2000). Hollow porous particles in metered dose inhalers. *Pharm. Res.* *17*, 168-174.
- Djokic, M., Kachrimanis, K., Solomun, L., Djuris, J., Vasiljević, D., & Ibrić, S. (2014). A study of jet-milling and spray-drying process for the physicochemical and aerodynamic dispersion properties of amiloride HCl. *Powder Technol.* *262*, 170-176.
- Donovan, M. J., Kim, S. H., Raman, V., & Smyth, H. D. (2012). Dry powder inhaler device influence on carrier particle performance. *J. Pharm. Sci.* *101*, 1097-1107.
- Donovan, M. J. & Smyth, H. D. C. (2010). Influence of size and surface roughness of large lactose carrier particles in dry powder inhaler formulations. *Int. J. Pharm.* *402*, 1-9.
- Dumouchel, C., Yongyingsakthavorn, P., & Cousin, J. (2009). Light multiple scattering correction of laser-diffraction spray drop-size distribution measurements. *Int J Multiphase Flow* *35*, 277-287.
- Dunbar, C. A., Hickey, A. J., & Holzner, P. (1998). Dispersion and Characterization of Pharmaceutical Dry Powder Aerosols. *Kona Powder Part. J.* *16*, 7-45.

## References

- Eastoe, J. & Dalton, J. S. (2000). Dynamic surface tension and adsorption mechanisms of surfactants at the air-water interface. *Adv. Colloid Interface Sci.* *85*, 103-144.
- Edwards, D. A., Hanes, J., Caponetti, G., Hrkach, J., Ben-Jebria, A., Eskew, M. L., Mintzes, J., Deaver, D., Lotan, N., & Langer, R. (1997). Large porous particles for pulmonary drug delivery. *Science* *276*, 1868-1871.
- Eggers, J. (1997). Nonlinear dynamics and breakup of free-surface flows. *Reviews of Modern Physics* *69*, 865-929.
- Eggers, J. & Villermaux, E. (2008). Physics of liquid jets. *Rep. Prog. Phys.* *71*, 1 - 79.
- Elajnaf, A., Carter, P., & Rowley, G. (2006). Electrostatic characterisation of inhaled powders: Effect of contact surface and relative humidity. *Eur. J. Pharm. Sci.* *29*, 375-384.
- Fainerman, V. B., Miller, R., & Joos, P. (1994). The measurement of dynamic surface tension by the maximum bubble pressure method. *Colloid Polym Sci* *272*, 731-739.
- Finlay, W. H. & Gehmlich, M. G. (2000). Inertial sizing of aerosol inhaled from two dry powder inhalers with realistic breath patterns versus constant flow rates. *Int. J. Pharm.* *210*, 83-95.
- Finlay, W. H. (2001). *Mechanics of Inhaled Pharmaceutical Aerosols - An Introduction*. London: Academic Press.
- Fromen, C. A., Shen, T. W., Larus, A. E., Mack, P., Maynor, B. W., Luft, J. C., & Desimone, J. M. (2013). Synthesis and characterization of monodisperse uniformly shaped respirable aerosols. *AIChE J.* *59*, 3184-3194.
- Ganan-Calvo, A. M. (1998). Generation of steady liquid microthreads and micron-sized monodisperse sprays in gas streams. *Phys Rev Lett* *80*, 285-288.
- Ganan-Calvo, A. M. (2008). Unconditional jetting. *Phys. Rev. E Stat. Nonlinear Soft Matter Phys.* *78*.
- Ganan-Calvo, A. M., Ferrera, C., & Montanero, J. M. (2011a). Universal size and shape of viscous capillary jets: Application to gas-focused microjets. *J. Fluid Mech.* *670*, 427-438.
- Ganan-Calvo, A. M., Ferrera, C., Torregrosa, M., Herrada, M. A., & Marchand, M. (2011b). Experimental and numerical study of the recirculation flow inside a liquid meniscus focused by air. *Microfluid. Nanofluid.* *11*, 65-74.
- Ganan-Calvo, A. M. & Riesco-Chueca, P. (2006). Jetting-dripping transition of a liquid jet in a lower viscosity co-flowing immiscible liquid: The minimum flow rate in flow focusing. *J. Fluid Mech.* *553*, 75-84.
- Glover, W., Chan, H. K., Eberl, S., Daviskas, E., & Verschuer, J. (2008). Effect of particle size of dry powder mannitol on the lung deposition in healthy volunteers. *Int. J. Pharm.* *349*, 314-322.

## References

- Gordillo, J. M., Ganan-Calvo, A. M., & Perez-Saborid, M. (2001a). Monodisperse microbubbling: Absolute instabilities in coflowing gas-liquid jets. *Phys. Fluids* *13*, 3839-3842.
- Gordillo, J. M., Perez-Saborid, M., & Ganan-Calvo, A. M. (2001b). Linear stability of co-flowing liquid-gas jets. *J. Fluid Mech.* *448*, 23-51.
- Grisedale, L. C., Jamieson, M. J., Belton, P. S., Barker, S. A., & Craig, D. Q. M. (2011). Characterization and quantification of amorphous material in milled and spray-dried salbutamol sulfate: A comparison of thermal, spectroscopic, and water vapor sorption approaches. *J. Pharm. Sci.* *100*, 3114-3129.
- Guenette, E., Barrett, A., Kraus, D., Brody, R., Harding, L., & Magee, G. (2009). Understanding the effect of lactose particle size on the properties of DPI formulations using experimental design. *Int. J. Pharm.* *380*, 80-88.
- Hancock, B. C. (2002). Disordered drug delivery: Destiny, dynamics and the Deborah number. *J. Pharm. Pharmacol.* *54*, 737-746.
- Hancock, B. C. & Shamblin, S. L. (2001). Molecular mobility of amorphous pharmaceuticals determined using differential scanning calorimetry. *Thermochim. Acta* *380*, 95-107.
- Hancock, B. C. & Zografi, G. (1997). Characteristics and significance of the amorphous state in pharmaceutical systems. *J. Pharm. Sci.* *86*, 1-12.
- Haynes, W. M. (2012). *CRC Handbook of Chemistry and Physics, 93rd Edition*. Boca Raton: Taylor & Francis.
- Heffels, C. M. G., Verheijen, P. J. T., Heitzmann, D., & Scarlett, B. (1996). Correction of the effect of particle shape on the size distribution measured with a laser diffraction instrument. *Particle and Particle Systems Characterization* *13*, 271-279.
- Hoe, S., Traini, D., Chan, H. K., & Young, P. M. (2010). The contribution of different formulation components on the aerosol charge in carrier-based dry powder inhaler systems. *Pharm. Res.* *27*, 1325-1336.
- Hoke, J. & Chen, J. C. (1991). Binary aqueous-organic surface tension temperature dependence. *J. Chem. Eng Data* *36*, 322-326.
- Ijsebaert, J. C., Geerse, K. B., Marijnissen, J. C. M., Lammers, J. W. J., & Zanen, P. (2001). Electro-hydrodynamic atomization of drug solutions for inhalation purposes. *J. Appl. Physiol.* *91*, 2735-2741.
- Islam, N., Stewart, P., Larson, I., & Hartley, P. (2004a). Effect of Carrier Size on the Dispersion of Salmeterol Xinafoate from Interactive Mixtures. *J. Pharm. Sci.* *93*, 1030-1038.



## References

- Islam, N., Stewart, P., Larson, I., & Hartley, P. (2004b). Lactose surface modification by decantation: Are drug-fine lactose ratios the key to better dispersion of salmeterol xinafoate from lactose-interactive mixtures? *Pharm. Res.* *21*, 492-499.
- Jones, M. D. & Price, R. (2006). The influence of fine excipient particles on the performance of carrier-based dry powder inhalation formulations. *Pharm. Res.* *23*, 1665-1674.
- Kawakami, K., Hasegawa, Y., Zhang, S., Yoshihashi, Y., Yonemochi, E., & Terada, K. (2014). Low-density microparticles with petaloid surface structure for pulmonary drug delivery. *J. Pharm. Sci.* *103*, 1309-1313.
- King, M. R. & Leighton, J. (1997). Measurement of the inertial lift on a moving sphere in contact with a plane wall in a shear flow. *Phys. Fluids.* *9*, 1248-1255.
- Kinnunen, H., Hebbink, G., Peters, H., Shur, J., & Price, R. (2014). An investigation into the effect of fine lactose particles on the fluidization behaviour and aerosolization performance of carrier-based dry powder inhaler formulations. *AAPS PharmSciTech.* *15*, 898-909.
- Kou, X., Chan, L. W., Steckel, H., & Heng, P. W. S. (2012). Physico-chemical aspects of lactose for inhalation. *Adv. Drug Deliv. Rev.* *64*, 220-232.
- Kovalchuk, V. I. & Dukhin, S. S. (2001). Dynamic effects in maximum bubble pressure experiments. *Colloids Surf. A Physicochem. Eng. Asp.* *192*, 131-155.
- Kubavat, H. A., Shur, J., Ruecroft, G., Hipkiss, D., & Price, R. (2012). Investigation into the influence of primary crystallization conditions on the mechanical properties and secondary processing behaviour of fluticasone propionate for carrier based dry powder inhaler formulations. *Pharm. Res.* *29*, 994-1006.
- Kufferath, A., Wende, B., & Leuckel, W. (1999). Influence of liquid flow conditions on spray characteristics of internal-mixing twin-fluid atomizers. *International Journal of Heat and Fluid Flow* *20*, 513-519.
- Langrish, T. A. G. (2007). New engineered particles from spray dryers: Research needs in spray drying. *Dry. Technol.* *25*, 971-983.
- Langrish, T. A. G. (2009). Assessing the relative tendency of different materials to crystallize in spray drying: A comparison between sodium chloride and lactose. *J. Food Eng* *91*, 521-525.
- Lapple, C. E. & Shepherd, C. B. (1940). Calculation of particle trajectories. *Ind. Eng. Chem.* *32*, 605-617.
- Le, V. N. P., Robins, E., & Flament, M. P. (2012). Agglomerate behaviour of fluticasone propionate within dry powder inhaler formulations. *Eur. J. Pharm. Biopharm.* *80*, 596-603.

## References

- Lefebvre, A. (1988). *Atomization and Sprays* Boca Raton: CRC Press.
- Liang, Z., Ni, R., Zhou, J., & Mao, S. (2015). Recent advances in controlled pulmonary drug delivery. *Drug Discov. Today* 20, 380-389.
- Litster, J. D., Hapgood, K. P., Michaels, J. N., Sims, A., Roberts, M., & Kameneni, S. K. (2002). Scale-up of mixer granulators for effective liquid distribution. *Powder Technol.* 124, 272-280.
- Lobo, J. M., Schiavone, H., Palakodaty, S., York, P., Clark, A., & Tzannis, S. T. (2005). SCF-engineered powders for delivery of budesonide from passive DPI devices. *J. Pharm. Sci.* 94, 2276-2288.
- Loubiere, K. & Hebrard, G. (2004). Influence of liquid surface tension (surfactants) on bubble formation at rigid and flexible orifices. *Chem. Eng. Process.* 43, 1361-1369.
- Louey, M. D. & Stewart, P. J. (2002). Particle interactions involved in aerosol dispersion of ternary interactive mixtures. *Pharm. Res.* 19, 1524-1531.
- Louey, M. D., Van Oort, M., & Hickey, A. J. (2004a). Aerosol dispersion of respirable particles in narrow size distributions produced by jet-milling and spray-drying techniques. *Pharm. Res.* 21, 1200-1206.
- Louey, M. D., Van Oort, M., & Hickey, A. J. (2004b). Aerosol dispersion of respirable particles in narrow size distributions using drug-alone and lactose-blend formulations. *Pharm. Res.* 21, 1207-1213.
- Mackin, L., Zanon, R., Park, J. M., Foster, K., Opalenik, H., & Demonte, M. (2002). Quantification of low levels (<10%) of amorphous content in micronised active batches using dynamic vapour sorption and isothermal microcalorimetry. *Int. J. Pharm.* 231, 227-236.
- Marple, V. A., Hochrainer, D., Roberts, D. L., Romay, F. J., Miller, N. C., Truman, K. G., Van Oort, M., Olsson, B., Holroyd, M. J., & Mitchell, J. P. (2003). Next Generation Pharmaceutical Impactor (a new impactor for pharmaceutical inhaler testing). Part I: Design. *J. Aerosol Med.* 16, 283-299.
- Marshall, W. R. (1954). *Atomization and Spray Drying* New York: American Institute of Chemical Engineers.
- Mason, R. L. (2003). *Statistical design and analysis of experiments with applications to engineering and science* New Jersey: J. Wiley.
- Masters, K. (1991). *Spray drying handbook* New York: Longman Scientific & Technical.
- Matsuda, Y., Otsuka, M., Onoe, M., & Tatsumi, E. (1992). Amorphism and physicochemical stability of spray-dried frusemide. *J. Pharm. Pharmacol.* 44, 627-633.
- Mayer, W. O. H. (1994). Coaxial atomization of a round liquid jet in a high speed gas stream: A phenomenological study. *Exp Fluids* 16, 401-410.

## References

- Miller, R., Joos, P., & Fainerman, V. B. (1994). Dynamic surface and interfacial tensions of surfactant and polymer solutions. *Adv. Colloid Interface Sci.* 49, 249-302.
- Mitchell, J. P. & Nagel, M. W. (2003). Cascade Impactors for the Size Characterization of Aerosols from Medical Inhalers: Their Uses and Limitations. *J. Aerosol Med.* 16, 341-377.
- Mitchell, J. P., Nagel, M. W., Nichols, S., & Nerbrink, O. (2006). Laser diffractometry as a technique for the rapid assessment of aerosol particle size from inhalers. *J. Aerosol Med.* 19, 409-433.
- Mohammed, H., Roberts, D., Copley, M., Hammond, M., Nichols, S., & Mitchell, J. (2012). Effect of Sampling Volume on Dry Powder Inhaler (DPI)-Emitted Aerosol Aerodynamic Particle Size Distributions (APSDs) measured by the Next-Generation Pharmaceutical Impactor (NGI) and the Andersen Eight-Stage Cascade Impactor (ACI). *AAPS PharmSciTech* 13, 875-882.
- Mullin, J. W. (2001). *Crystallization*. 3<sup>rd</sup> Ed, Oxford: Butterworth Heinemann.
- Newman, S. P., Busse, W. W., Evolution of dry powder inhaler design, formulation, and performance, *Resp. Med.* 96, 293 - 304
- Ngoc, N. T. Q., Chang, L., Jia, X., & Lau, R. (2013). Experimental investigation of design parameters on dry powder inhaler performance. *Int. J. Pharm.* 457, 92-100.
- Nukiyama, S. & Tanasawa, Y. (1940). On liquid spray drying. *Trans. Soc. Mech. Eng. Japan* 6, 7 - 15.
- Ooi, J., Traini, D., Hoe, S., Wong, W., & Young, P. M. (2011). Does carrier size matter? A fundamental study of drug aerosolisation from carrier based dry powder inhalation systems. *Int. J. Pharm.* 413, 1-9.
- Paluch, K. J., Tajber, L., Corrigan, O. I., & Healy, A. M. (2012). Impact of process variables on the micromeritic and physicochemical properties of spray-dried porous microparticles, part I: Introduction of a new morphology classification system. *J. Pharm. Pharmacol.* 64, 1570-1582.
- Panyam, J. & Labhassetwar, V. (2003). Biodegradable nanoparticles for drug and gene delivery to cells and tissue. *Adv. Drug Deliv. Rev.* 55, 329-347.
- Parsian, A. R., Vatanara, A., Rahmati, M. R., Gilani, K., Khosravi, K. M., & Najafabadi, A. R. (2014). Inhalable budesonide porous microparticles tailored by spray freeze drying technique. *Powder Technol.* 260, 36-41.
- Percy, S. R. (1872). Improvement in drying and concentrating liquid substances by atomizing, *US Patent: US125406A*.
- Podczeczek, F., Newton, J. M., & James, M. B. (1996). The adhesion force of micronized Salmeterol Xinafoate particles to pharmaceutically relevant surface materials. *J. Phys. D. Appl. Phys.* 29, 1878-1884.

## References

- Podczeczek, F., Newton, J. M., & James, M. B. (1997). Influence of relative humidity of storage air on the adhesion and autoadhesion of micronized particles to particulate and compacted powder surfaces. *J. Colloid Interf. Sci.* 187, 484-491.
- Price, R., Young, P. M., Edge, S., & Staniforth, J. N. (2002). The influence of relative humidity on particulate interactions in carrier-based dry powder inhaler formulations. *Int. J. Pharm.* 246, 47-59.
- Prime, D., Atkins, P. J., Slater, A., & Sumbly, B. (1997). Review of dry powder inhalers. *Adv. Drug Deliv. Rev.* 26, 51-58.
- Prinn, K. B., Constantino, H. R., & Tracy, M. (2002) Statistical modeling of protein spray drying at the lab scale. *AAPS PharmSciTech*, 3, 32 - 39.
- Raula, J., Eerikainen, H., & Kauppinen, E. I. (2004). Influence of the solvent composition on the aerosol synthesis of pharmaceutical polymer nanoparticles. *Int. J. Pharm.* 284, 13-21.
- Re, M. I. (2006). Formulating drug delivery systems by spray drying. *Dry. Technol.* 24, 433-446.
- Reitz, R. D. (1978). Atomization and Other Breakup Regimes of a Liquid Jet. *Ph.D. Thesis*, Princeton University.
- Rosell-Llompart, J. & Ganan-Calvo, A. M. (2008). Turbulence in pneumatic flow focusing and flow blurring regimes. *Phys. Rev. E Stat. Nonlinear Soft Matter Phys.* 77.
- Sakagami, M., Kinoshita, W., Sakon, K., Sato, J., & Makino, Y. (2002). Mucoadhesive beclomethasone microspheres for powder inhalation: Their pharmacokinetics and pharmacodynamics evaluation. *J. Control. Release* 80, 207-218.
- Santangelo, P. E. (2010). Characterization of high-pressure water-mist sprays: Experimental analysis of droplet size and dispersion. *Exp. Therm. Fluid Sci.* 34, 1353-1366.
- Sedin, D. L. & Rowlen, K. L. (2000). Adhesion forces measured by atomic force microscopy in humid air. *Anal. Chem.* 72, 2183-2189.
- Shur, J., Lee, S., Adams, W., Lionberger, R., Tibbatts, J., & Price, R. (2012). Effect of device design on the in vitro performance and comparability for capsule-based dry powder inhalers. *AAPS J.* 14, 667-676.
- Smyth, H. D. C. & Hickey, A. J. (2005). Carriers in drug powder delivery: Implications for inhalation system design. *Am. J. Drug Deliv.* 3, 117-132.
- Srichana, T., Martin, G. P., & Marriott, C. (1998). Dry powder inhalers: The influence of device resistance and powder formulation on drug and lactose deposition in vitro. *Eur. J. Pharm. Sci.* 7, 73-80.

## References

- Stahlhofen, W., Rudolf, G., & James, A. C. (1989). Intercomparison of experimental regional aerosol deposition data. *Journal of Aerosol Medicine* 2, 285-308.
- Staniforth, J. N. (1987). British Pharmaceutical Conference Science Award Lecture 1986: Order out of chaos. *J. Pharm. Pharmacol.* 39, 329-334.
- Stank, K. & Steckel, H. (2013). Physico-chemical characterisation of surface modified particles for inhalation. *Int. J. Pharm.* 448, 9-18.
- Steckel, H. & Muller, B. W. (1997). In vitro evaluation of dry powder inhalers I: Drug deposition of commonly used devices. *Int. J. Pharm.* 154, 19-29.
- Su, C. S., Lo, W. S., & Lien, L. H. (2011). Micronization of fluticasone propionate using supercritical antisolvent (SAS) process. *Chem. Eng. Technol.* 34, 535-541.
- Suwandecha, T., Wongpoowarak, W., Maliwan, K., & Srichana, T. (2014). Effect of turbulent kinetic energy on dry powder inhaler performance. *Powder Technol.* 267, 381-391.
- Tajber, L., Corrigan, O. I., & Healy, A. M. (2009). Spray drying of budesonide, formoterol fumarate and their composites-II. Statistical factorial design and in vitro deposition properties. *Int. J. Pharm.* 367, 86-96.
- Tang, P., Chan, H. K., Tam, E., De Gruyter, N., & Chan, J. (2006). Preparation of NaCl powder suitable for inhalation. *Ind. Eng. Chem. Res.* 45, 4188-4192.
- Tee, S. K., Marriott, C., Zeng, X. M., & Martin, G. P. (2000). The use of different sugars as fine and coarse carriers for aerosolised salbutamol sulphate. *Int. J. Pharm.* 208, 111-123.
- Telko, M. J. & Hickey, A. J. (2005). Dry powder inhaler formulation. *Respir. Care* 50, 1209-1227.
- Telko, M. J. & Hickey, A. J. (2014). Aerodynamic and Electrostatic Properties of Model Dry Powder Aerosols: a Comprehensive Study of Formulation Factors. *AAPS PharmSciTech* 15, 1378-1397.
- Tewes, F., Paluch, K. J., Tajber, L., Gulati, K., Kalantri, D., Ehrhardt, C., & Healy, A. M. (2013). Steroid/mucokinetic hybrid nanoporous microparticles for pulmonary drug delivery. *Eur. J. Pharm. Biopharm.* 85, 604-613.
- Thybo, P., Hovgaard, L., Andersen, S. K., & Lindelov, J. S. (2008). Droplet size measurements for spray dryer scale-up. *Pharm. Dev. Technol.* 13, 93-104.
- Trasi, N. S., Boerrigter, S. X. M., & Byrn, S. R. (2010). Investigation of the milling-induced thermal behavior of crystalline and amorphous griseofulvin. *Pharm. Res.* 27, 1377-1389.
- Triballier, K., Dumouchel, C., & Cousin, J. (2003). A technical study on the Spraytec performances: Influence of multiple light scattering and multi-modal drop-size distribution measurements. *Exp. Fluids* 35, 347-356.

## References

- United States Pharmacopeia Convention (2014). *USP 38 - NF 33 The United States Pharmacopeia and National Formulary 2015: Main Edition Plus Supplements 1 and 2*, Rockville: US Pharmacopeial Convention.
- Usmani, O. S., Biddiscombe, M. F., & Barnes, P. J. (2005). Regional lung deposition and bronchodilator response as a function of beta 2-agonist particle size. *American Journal of Respiratory and Critical Care Medicine* 172, 1497-1504.
- Vanbever, R., Mintzes, J. D., Wang, J., Nice, J., Chen, D., Batycky, R., Langer, R., & Edwards, D. A. (1999). Formulation and physical characterization of large porous particles for inhalation. *Pharm. Res.* 16, 1735-1742.
- Vazquez, G., Alvarez, E., & Navaza, J. M. (1995). Surface tension of alcohol + water from 20 to 50°C. *J. Chem. Eng Data* 40, 611-614.
- Vehring, R., Foss, W. R., & Lechuga-Ballesteros, D. (2007). Particle formation in spray drying. *J. Aerosol Sci.* 38, 728-746.
- Voss, A. & Finlay, W. H. (2002). Deagglomeration of dry powder pharmaceutical aerosols. *Int. J. Pharm.* 248, 39-50.
- Walters, R. H., Bhatnagar, B., Tchessalov, S., Izutsu, K. I., Tsumoto, K., & Ohtake, S. (2014). Next generation drying technologies for pharmaceutical applications. *J. Pharm. Sci.* 103, 2673-2695.
- Wang, W. N., Purwanto, A., Lenggono, I. W., Okuyama, K., Chang, H., & Jang, H. D. (2008). Investigation on the correlations between droplet and particle size distribution in ultrasonic spray pyrolysis. *Ind. Eng. Chem. Res.* 47, 1650-1659.
- Weers, J. G., Tarara, T. E., & Clark, A. R. (2007). Design of fine particles for pulmonary drug delivery. *Expert Opin. Drug Deliv.* 4, 297-313.
- Weers, J. & Tarara, T. (2014). The PulmoSphere platform for pulmonary drug delivery. *Therapeutic Delivery* 5, 277-295.
- Wetterlin, K. (1988). Turbuhaler: A New Powder Inhaler for Administration of Drugs to the Airways. *Pharm Res* 5, 506-508.
- Wissing, S. A., Kayser, O., & Muller, R. H. (2004). Solid lipid nanoparticles for parenteral drug delivery. *Adv. Drug Deliv. Rev.* 56, 1257-1272.
- Worth Longest, P. & Hindle, M. (2009). Evaluation of the respimat soft mist inhaler using a concurrent cfd and in vitro approach. *J. Aerosol. Med. Pulm. Drug. Deliv.* 22, 99-112.
- Xu, Q., Li, M., Niu, J., & Xia, Z. (2013). Dynamic enhancement in adhesion forces of microparticles on substrates. *Langmuir* 29, 13743-13749.
- Xu, R. & Di Guida, O. A. (2003). Comparison of sizing small particles using different technologies. *Powder Technol.* 132, 145-153.

## References

- Yamamoto, H., Matsuyama, T., & Wada, M. (2002). Shape distinction of particulate materials by laser diffraction pattern analysis. *Powder Technol.* 122, 205-211.
- Yang, T. T., Li, S., Wyka, B., & Kenyom, D. (2001). Drug delivery performance of the mometasone furoate dry powder Inhaler. *J. Aerosol Med.* 14, 487-494.
- Yaws, C. L. (2012). *Yaws' Critical Property Data for Chemical Engineers and Chemists*, New York: Knovel.
- Young, P. M., Sung, A., Traini, D., Kwok, P., Chiou, H., & Chan, H. K. (2007). Influence of humidity on the electrostatic charge and aerosol performance of dry powder inhaler carrier based systems. *Pharm. Res.* 24, 963-970.
- Young, P. M., Wood, O., Ooi, J., & Traini, D. (2011). The influence of drug loading on formulation structure and aerosol performance in carrier based dry powder inhalers. *Int. J. Pharm.* 416, 129-135.
- Yu, L., Reutzel-Edens, S. M., & Mitchell, C. A. (2000). Crystallization and polymorphism of conformationally flexible molecules: Problems, patterns, and strategies. *Org. Process Res. Dev.* 4, 396-402.
- Zanen, P., Go, L. T., & Lammers, J. W. J. (1995). The optimal particle size for parasympatholytic aerosols in mild asthmatics. *Int. J. Pharm.* 114, 111-115.
- Zeng, X. M., Martin, G. P., Marriott, C., & Pritchard, J. (2001). Lactose as a carrier in dry powder formulations: The influence of surface characteristics on drug delivery. *J. Pharm. Sci.* 90, 1424-1434.
- Zeng, X. M., Pandhal, K. H., & Martin, G. P. (2000). The influence of lactose carrier on the content homogeneity and dispersibility of beclomethasone dipropionate from dry powder aerosols. *Int. J. Pharm.* 197, 41-52.